PERFORMANCE OF AN AIR CONVECTION EMBANKMENT OVER ICE-RICH PERMAFROST: INSTRUMENTATION, MONITORING, AND MODELING

By

David D. Jensen

RECOMMENDED:

Dr. Scott L. Huang

Dr. Yuri Shur

Dr. Margaret M. Darrow
Advisory Committee Chair

Dr. Rajive Ganguli
Chair, Department of Mining & Geological Engineering

APPROVED:

Dr. Douglas J. Goering
Dean, College of Engineering and Mines

Dr. John C. Eichelberger
Dean of the Graduate School

28 April 2015
Date

PERFORMANCE OF AN AIR CONVECTION EMBANKMENT OVER ICE-RICH PERMAFROST: INSTRUMENTATION, MONITORING, AND MODELING

A

THESIS

Presented to the Faculty

of the University of Alaska Fairbanks

in Partial Fulfillment of the Requirements

for the Degree of

MASTER OF SCIENCE

By

David D. Jensen, B.S.

Fairbanks, Alaska

May 2015

ABSTRACT

Construction and monitoring of roadway embankments over ice-rich permafrost present unique challenges. The air convection embankment (ACE) is a relatively new design developed to reduce thaw settlement over ice-rich permafrost. Monitoring ACE temperatures and deformation allows for evaluation of embankment performance to improve ACE designs, and numerical modeling of an ACE can be used to estimate long-term thermal stability. For this research, geotechnical instrumentation was installed in an ACE with thermal berm located near Chicken, Alaska. A digital temperature acquisition cable (TAC) and a MEMS-based in-place inclinometer were installed at the base of the embankment and evaluated for performance over a one-year period, and two-dimensional thermal modeling of the ACE and thermal berm was conducted. Temperature and deformation measurements from the site were analyzed to assess embankment performance, while modeled and measured embankment temperatures were compared to assess model validity.

Results suggest that the TAC and in-place inclinometer demonstrate acceptable performance for monitoring embankment temperature and deformation, respectively, over ice-rich permafrost. The modeled embankment temperatures demonstrated a similar trend to measured temperatures, with temperatures beneath the thermal berm warmer than beneath the ACE; however, the mean modeled temperatures differed from those measured by -5°F for the thermal berm and -2°F and -9°F for a snow-covered and plowed ACE, respectively. Model results for a plowed ACE showed increased performance and a 7°F decrease in mean annual temperature compared to a snow covered ACE. Numerical modeling results and measured embankment temperatures and deformation suggest the ACE will remain stable while the thermal berm will experience thaw settlement until thermal equilibrium is reached. Foundation soil temperatures are expected to grow colder beneath the ACE and warmer beneath the thermal berm.

TABLE OF CONTENTS

LIST OF FIGURES

Page

LIST OF TABLES

LIST OF APPENDICES

ACKNOWLEDGEMENTS

First, I would like to express my deepest gratitude to my advisor, Dr. Margaret Darrow, for her steadfast support and guidance throughout this academic journey. Without her exceptional knowledge, technical writing expertise, and hours spent reviewing my thesis, it is unlikely I would have been able to finish. Her insightful lectures, high standards, and unwavering encouragement helped me to succeed in my academic career. I could not have had a better academic advisor for my graduate studies.

In addition to my advisor, I would like to thank the rest of my thesis committee members, Dr. Scott Huang and Dr. Yuri Shur, for their time and excellent knowledge in the field of engineering, which they shared during numerous lectures. Their thought-provoking comments and questions encouraged me to work harder and strive to improve the various aspect of my research.

I would also like to thank Jeff Currey, PE, of ADOT&PF Northern Region Materials Section, for his invaluable time and assistance in facilitating the Lost Chicken project. Last, but not least, I want to thank Jason Zottola for his assistance in installing the geotechnical instrumentation at the Lost Chicken project.

This research was jointly funded by ADOT&PF (RSA ADN2512140) and the Alaska University Transportation Center (Award No. DTRT06-G-0011).

CHAPTER 1 INTRODUCTION AND BACKGROUND

There are numerous environmental challenges associated with construction of civil infrastructure in Alaska. One of the most difficult and costly challenges in roadway construction is building embankments over permafrost, which is defined as any ground (soil or rock, including ice and/or organics) that has remained at or below 32°F for two or more years (International Permafrost Association 2014). Modification of the ground surface from construction activities typically leads to a thermal imbalance, often resulting in increased ground temperatures. When ground temperatures rise enough to thaw the ice-rich permafrost, large amounts of settlement can occur, which then leads to degradation of the pavement and/or failure of the embankment.

This study focuses on a project involving a section of the Taylor Highway, which is one of numerous Alaskan roadways constructed over permafrost soils (see Figure 1.1). According to the Bureau of Land Management (BLM), the history of the Taylor Highway began when gold-bearing gravels were discovered in 1881 on the North Fork of the Fortymile River (BLM 2007). Between 1886 and 1887, trails were worn down between the town of Eagle and other small communities, including Chicken. The trails were developed later into roads, forming part of the Taylor Highway, which was built mostly during the winter of 1945-1946 and finished in 1951 (BLM 2007).

The Taylor Highway begins at Tetlin Junction where it intersects the Alaska Highway just southeast of Tok (see Figure 1.2). It extends northeast approximately 160 miles to the town of Eagle located near the US/Canada border. It is typically open from April to mid-October and is gravel beyond milepost (MP) 64. Lost Chicken Hill, located at MP 69, held a “lost” gold pay streak, and is now privately owned and mined (BLM 2007).

Since its construction, several sections of the Taylor Highway have experienced numerous maintenance issues related to thawing permafrost and settlement of the roadway embankment. The project area, located near Lost Chicken Creek at MP 70 (see Figure 1.2), is one particular location where degradation of ice-rich permafrost led to severe embankment settlement and increased maintenance costs. The area, which has become known as the Lost Chicken Slide, required hundreds of cubic yards of fill annually to maintain embankment elevation (Barney 2010). A photograph of the area, including fresh fill material placed over the embankment, is shown in Figure 1.3.

It was hypothesized that over-steepened slopes along Lost Chicken Creek due to past mining activities, in conjunction with erosion from a relocated culvert that was too short, were largely responsible for the exposure of ice-rich permafrost and subsequent embankment

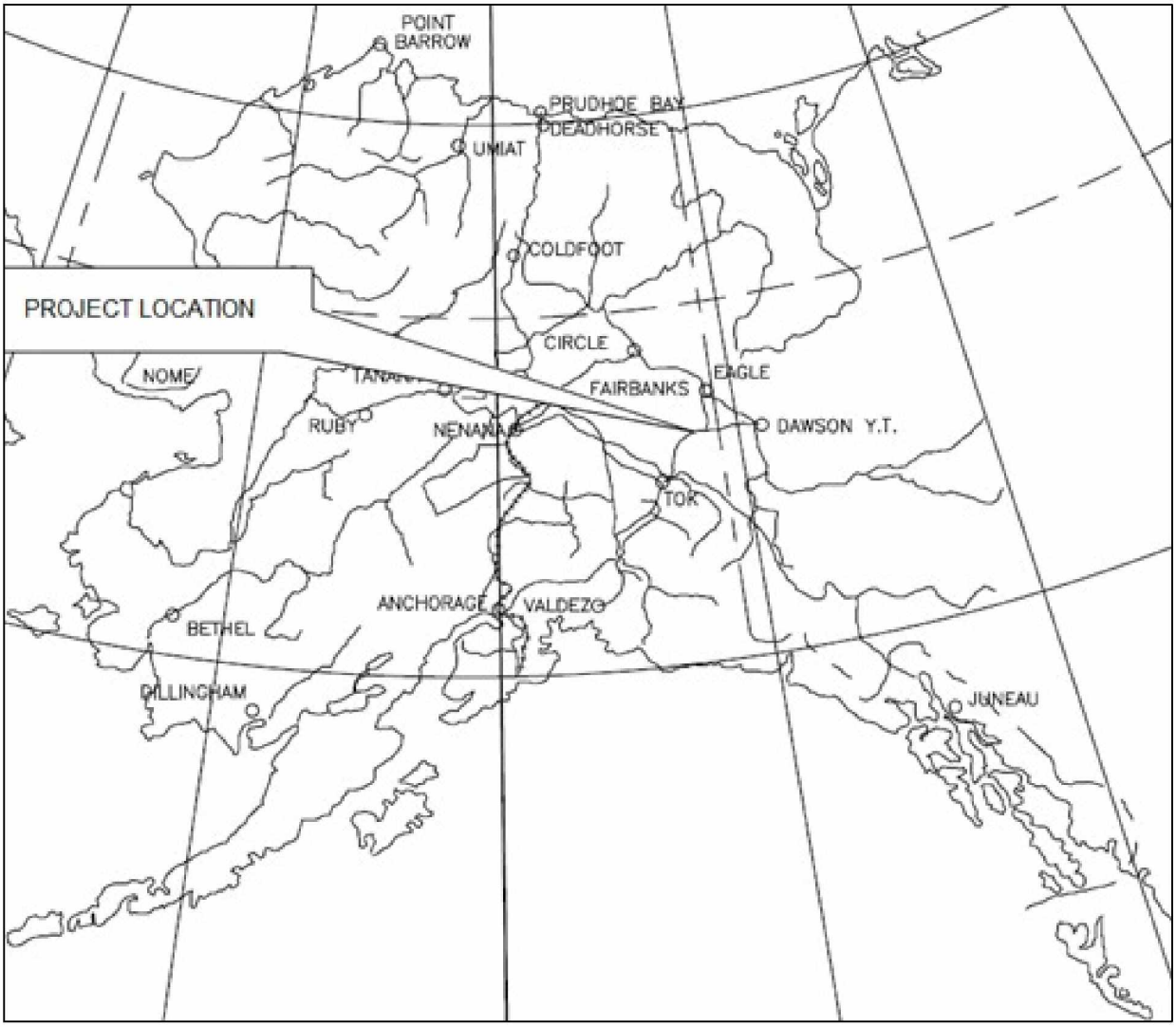

Figure 1.1 General project location map (Barney 2010).

settlement (Darrow 2008). The culvert outlet and eroded gulley are shown in Figure 1.4 and Figure 1.5. A photograph of the exposed ice-rich permafrost below the embankment, along the southern edge, is presented in Figure 1.6.

In 2007 Alaska Department of Transportation and Public Facilities (ADOT&PF) Northern Region Materials Section (NRMS) personnel conducted a geotechnical investigation along the Taylor Highway for the Taylor Highway MP 64 to Canadian Border Rehabilitation project. During the investigation, NRMS personnel drilled several test holes along and adjacent to the existing embankment in the Lost Chicken Slide area. Results of the subsurface exploration revealed the presence of organic, ice-rich silt, and massive ice beneath and adjacent to the embankment (Darrow 2008).

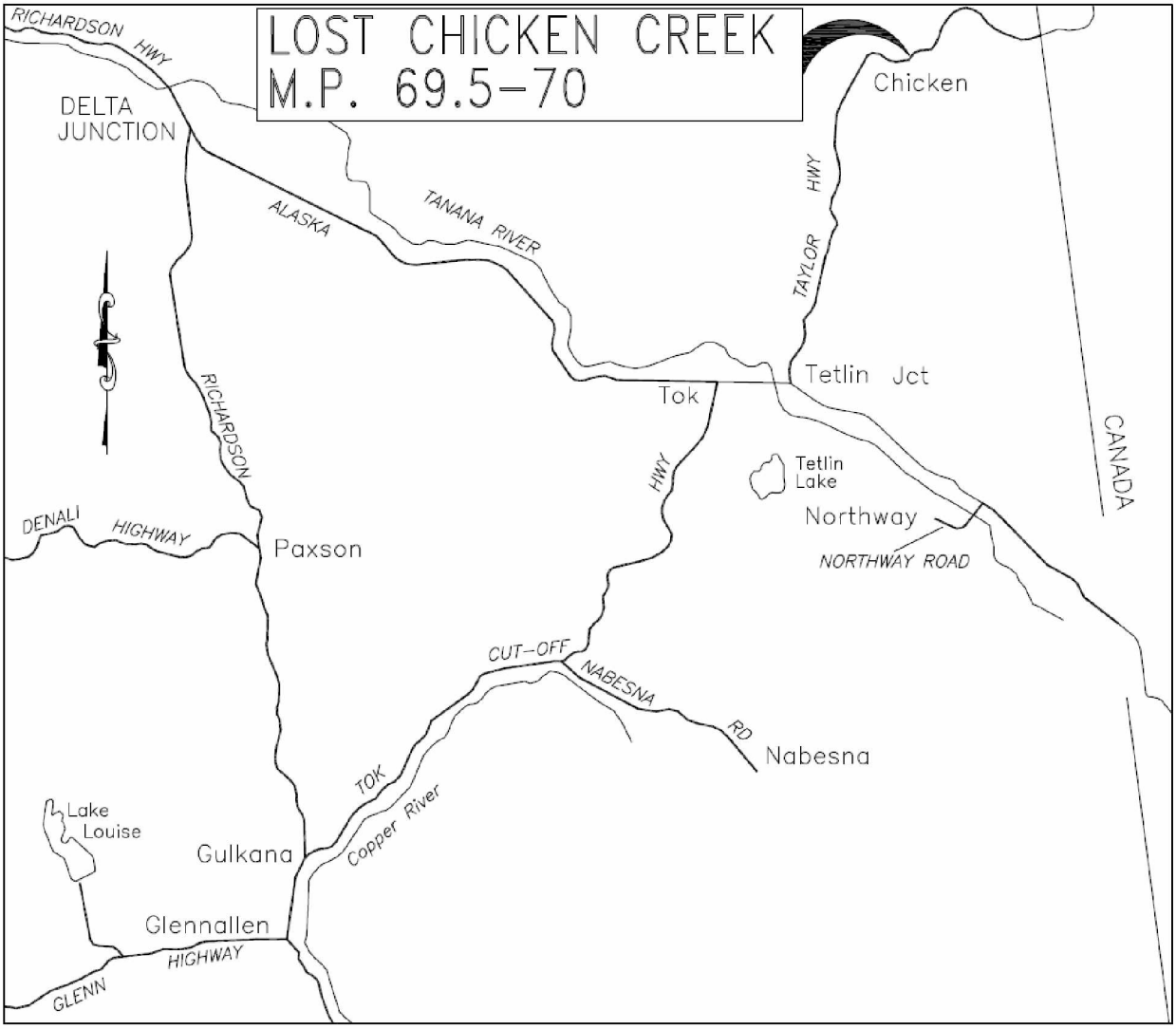

Figure 1.2 Specific project location map (Barney 2010).

In November 2008 NRMS personnel conducted a second geotechnical investigation to explore a proposed realignment route north of the existing embankment, uphill from the eroding slope. The subsurface findings indicated that the proposed route across the valley was underlain by ice-rich permafrost; however, significantly less massive ice was encountered under the proposed route than beneath the existing alignment (Speeter 2010). Test hole logs and laboratory test reports for the investigation are provided in Appendix A.

Based on the results of the investigation, ADOT&PF decided to realign the Taylor Highway at the Lost Chicken Slide area using the proposed alignment route. To avoid upsetting the thermal balance and to prevent future thaw settlement problems beneath the new embankment, the design included an air convection embankment (ACE) using coarse, poorly-

Figure 1.3 Lost Chicken Slide area, showing recent maintenance (photograph taken in May 2007; courtesy of ADOT&PF).

graded rock, across the ice-rich permafrost area. Well-graded gravel was used to construct an embankment lateral berm, or thermal berm, along the south (downslope) side of the ACE to minimize settlement due to thawing at the toe of the structural embankment.

As part of a separate research project evaluating micro-electro-mechanical system (MEMS)-based in-place inclinometers in cold regions, the Lost Chicken site was chosen for the installation of geotechnical instrumentation. Instruments installed in the embankment were used to monitor temperature changes and vertical deformation, as well as to compare the performance of different instruments used to monitor said changes. The geotechnical instrumentation was jointly funded by ADOT&PF and the Alaska University Transportation Center (AUTC) and was installed by University of Alaska Fairbanks (UAF) research personnel during construction of the realignment in the summer of 2012.

Since the ACE is a relatively new method of embankment design for permafrost regions, research involving performance monitoring and numerical modeling can provide valuable information that will aid in ACE design and advancement of ACE numerical modeling techniques. The following literature review introduces the ACE design concept, as well as the numerous methods that have come before it. The majority of the projects discussed were located in Alaska.

Figure 1.4 Erosion of embankment slope and culvert outfall (photograph taken in August 2007; courtesy of M. Darrow).

Figure 1.5 View to the north of the embankment slope and culvert location (photograph taken in October 2008; courtesy of ADOT&PF).

Figure 1.6 Exposed ice-rich permafrost below the culvert outfall (photograph taken in June 2007; courtesy of ADOT&PF).

1.1 LITERATURE REVIEW

Various embankment designs and construction methods have been explored for use in embankment construction over thaw-unstable permafrost. This literature review provides a chronological summary, beginning in the early 1960s, of numerous methods that have been employed to prevent thawing of permafrost beneath roadway embankments. The methods detailed include both experimental ideas as well as those that have become common construction practices. One method discussed in detail is the use of ACE. The theory behind ACE design is explored as well as typical applications and limitations.

1.1.1 History of Embankment Design and Construction over Permafrost

Prior to the conception and implementation of an ACE, numerous design and construction methods were experimented with and employed in the effort to prevent thawing of permafrost beneath roadway embankments. These methods included ground surface modifications and pre-thawing, insulation in the form of polystyrene or peat underlays,

embankment lateral berms, air cooling ducts, snow sheds, thermosyphons, geosynthetic reinforcement, lightweight fills, foundation bridges, and finally ACE (Vinson et al. 1996).

Paint coatings were one of the earliest forms of ground surface modification used to prevent thawing of permafrost. For an embankment with asphalt pavement, the method simply involved applying a coat of light-colored paint to the asphalt surface. The light color increased the albedo of the asphalt and reduced the amount of heat absorbed, thus reducing the depth of seasonal thaw (Bjella 2013).

In the 1950s, paint coatings were utilized by the U.S. Air Force at Thule Air Base, Greenland. The air base was constructed in 1951 and consisted of 4 in. of asphalt atop a 6-ft high gravel embankment. In 1953 and 1954 thaw settlement was evident and an investigation was conducted to determine the cause. It was discovered that insufficient fill thickness allowed thawing of ice-rich soil beneath the embankment. To mitigate the settlement problems, part of the runway surface was painted white between 1957 and 1959; in 1962 additional runway length, taxiways, and ramps were painted (Bjella 2013).

White paint proved to be successful in lowering the thaw depth beneath the airfield at Thule Air Base; however, a painted asphalt surface is not without disadvantages. In order to be fully effective, the white paint must be maintained in near pristine condition. Due to wear from airplane traffic and snow removal, frequent repainting is required, which increases maintenance costs. The painted asphalt surface also can lead to reduced braking ability for aircraft, and thus poses a safety hazard (Bjella 2013).

Plastic foam insulation placed within or at the base of an embankment is another method used to prevent thawing of permafrost foundation soils. The first experimental use of foam insulation by the then-named Alaska Department of Highways was carried out in 1968 for frost heave control. Shortly thereafter, in 1969, the first insulated roadway section was constructed near Chitina, Alaska to prevent thawing of warm permafrost (i.e., approximately +30°F) beneath the embankment (Esch 1986).

Monitoring ground temperatures and embankment settlement revealed that the insulated section of embankment typically performed well, with soils beneath it refreezing completely each year. The embankment side slopes, however, still experienced settlement over time despite the insulation, which resulted in shoulder cracking and slope sloughing. Meanwhile, beneath the adjacent uninsulated sections of embankment, thaw settlement beneath the center and side slopes continued over time (Esch 1986).

In 1973 peat was utilized in the construction of an experimental roadway section located near Fairbanks, Alaska (Esch and Livingston 1978). The unique thermal properties of wet peat

enable it to have a frozen thermal conductivity almost twice as high as its thawed thermal conductivity, thus leading to a thermal diode effect. This property made peat useful in successfully reducing frost heave beneath roads and railways in Norway as far back as 1903 (Esch and Livingston 1978).

The experimental roadway section utilized 4 to 5-ft thick layers of peat beneath the roadway embankment in a cut section in permafrost. The roadway section was observed through 1977 and demonstrated earlier freeze-back beneath the embankment and a decrease in the underlying permafrost temperature when compared to the normal roadway section (Esch and Livingston 1978).

Esch and Livingston (1978) found that for Interior Alaska approximately 2.5 ft of consolidated peat beneath a 4-ft thick, paved roadway embankment is sufficient to prevent thawing of the underlying permafrost. Unfortunately, despite the potential thermal benefits, there are problems associated with peat underlays. First, thawing beneath the slope and ditch areas still can occur despite the insulating properties of peat. Second, it may be difficult to obtain a sufficient amount of peat required for a road section at a reasonable cost if it is not available in the immediate area. Finally, there is significant post-construction consolidation and settlement of peat that has to reach stability before paving can be completed (Esch and Livingston 1978).

Thermal berms, also referred to as embankment lateral berms, consist of additional embankment soil or waste material placed along the toe of the structural embankment. The thermal berm, as shown in Figure 1.7, is supposed to act as an insulating layer to prevent accelerated thawing at the embankment toe.

In 1974 thermal berms were employed at the Parks Highway Bonanza Creek site, located near Fairbanks, Alaska. It was discovered that the thermal berms offered a temporary (1 to 3 year) reduction in thaw depth beneath the embankment toe. The long-term effects of thermal berms at the site were found to be detrimental. After 15 years the thaw settlement and embankment cracking were severe enough to require reconstruction of the lower slopes of the embankment and, after 20 years, the berms settled as much as 6.6 ft (Vinson et al. 1996).

Over a long period of time, the thermal berms resulted in a warming effect of the entire embankment due to the increase in warm surface area of the embankment slope. Even though the thermal berms along the test embankment were constructed of silt and vegetated, ground temperatures still increased enough to thaw the underlying permafrost. Thaw settlement beneath the thermal berms was expected to lead eventually to the development of thaw ponds along the edge of the embankment (Vinson et al. 1996).

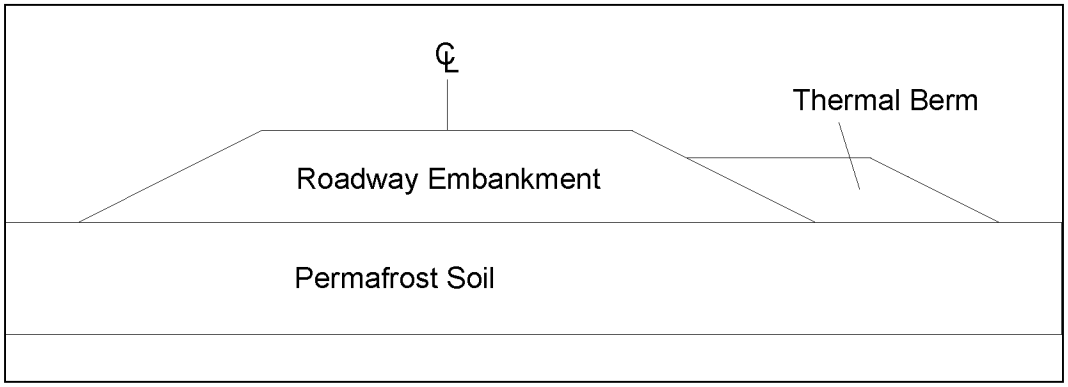

Figure 1.7 Cross section of embankment with thermal berm.

Air cooling ducts also were employed at the Bonanza Creek site in 1974. This method consists of a corrugated metal pipe buried beneath the embankment with a horizontal inlet on one end and a vertical outlet on the other (see Figure 1.8). Air cooling ducts work via the stack or chimney effect wherein the warm air in the duct system is forced upward out the vertical chimney by the surrounding, denser cold air (Zarling et al. 1984).

Air cooling ducts remove heat from the embankment via convective heat transfer and offer the benefit of being passive systems that work during the winter when a sufficient temperature gradient exists, but cease to function in the summer when the ambient temperature rises. Unfortunately, it was concluded that the air cooling duct system installed at Bonanza Creek was not designed properly due to lack of design methodology and thus did not perform well (Zarling et al. 1984).

Through experiments and analysis, Zarling et al. (1984) focused on improved design methodology for air cooling duct systems. Their research results were implemented in the design of an air cooling duct system installed at MP 1240 on the Alaska Highway (Zarling et al. 1984). The site was monitored for settlement from 1984 through 1988 and compared to an adjacent control section with no air cooling ducts. Results of the monitoring indicated that the air cooling ducts significantly reduced the amount of embankment settlement compared to the control section, but did not eliminate it entirely (Reger et al. 2012).

Thawing permafrost soils prior to construction is another method of reducing or eliminating post-construction thaw settlement. In 1980 ADOT&PF experimented with passive methods of pre-thawing permafrost by means of ground surface modifications. Depending on the type of surface modification and the time allowed for pre-thawing, the thickness of embankment required to prevent seasonal thawing into unstable soil can be greatly reduced (Esch 1982).

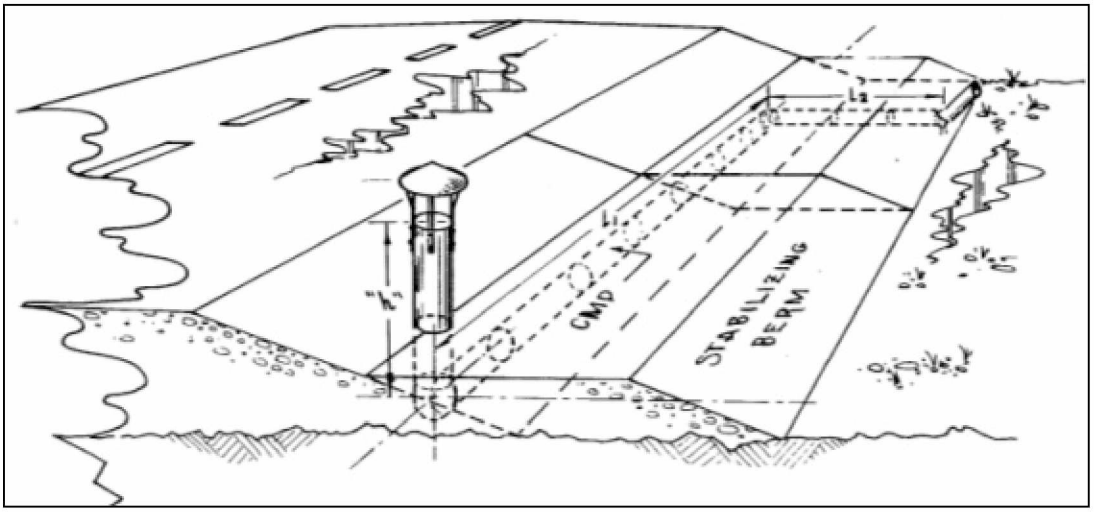

Figure 1.8 Air duct system (Zarling et al. 1984).

A total of six different surface modification methods were used in the 1980 field test. The first method was simply to machine strip the ground of all vegetation. The next was to machine strip the ground and then place a thin sheet of polyethylene film over it to induce a greenhouse effect. The third method involved stripping the ground, placing a layer of gravel, darkening the gravel surface with asphalt spray, and then placing polyethylene sheeting over the surface. The fourth method was the same as the third without the placement of polyethylene sheeting. The next method was to hand clear the area and place a gravel pad with a layer of polyethylene sheeting over it. Finally, the sixth method was to strip the ground and place a gravel layer (Esch 1982).

Results of the field experimentation revealed that from May to Oct. the greatest thaw rate (i.e., 1.16 ft/month) was achieved by the combination of ground stripping, gravel layer, asphalt spray, and polyethylene sheeting. The least effective method was stripping and placing a gravel layer, which had a thaw rate of 0.90 ft/month. Simply stripping the ground resulted in a thaw rate of 1.03 ft/month; however, it was believed that the addition of a gravel layer helped with soil consolidation, erosion control, and trafficability (Esch 1982).

In the early 1980's, structures known as snow-sheds were experimented with as a method to prevent thawing of permafrost beneath embankment side slopes. The shed roof-like structures were constructed of plywood and lumber. They were designed to provide shade along the embankment during the summer months and to keep snow off the embankment during the winter, thus allowing cold winter air to reach the ground surface.

In 1985 and 1986, snow-sheds constructed at the Parks Highway Bonanza Creek site, and along Farmers Loop Road, located in Fairbanks, were monitored using temperature

sensors (Zarling and Braley 1986). A photograph of the snow-sheds employed along an embankment slope during winter is presented in Figure 1.9.

Experimental results indicated that the snow-sheds worked quite well and were able to reduce the mean annual soil surface temperature to 28°F, while the mean annual soil surface temperature of the untreated ground was 39°F (Zarling and Braley 1986). Regardless of the thermal benefits provided by snow-sheds, there were large disadvantages. Snow-sheds were very expensive to construct and required large amounts of material. Long-term durability of the structures was questionable. Finally, snow-sheds also posed a safety concern for vehicles that might run off the road and crash into the structures. Therefore, it was noted that guardrail may be required to provide sufficient safety in areas where snow-sheds were employed, further raising construction costs (Zarling and Braley 1986).

From 1984 to 1988, the use of inclined thermosyphons was investigated at the airport in Bethel, Alaska. Thermosyphons typically consist of a sealed metal tube containing a working fluid such as ammonia, butane, or carbon dioxide. One end of the metal tube (referred to as the "evaporator") is installed in the soil that is to be kept frozen, while the other end of the tube (referred to as the "condenser") exits the ground and is exposed to the air. The working fluid in the tube remains inactive during the summer months until the air temperature is cold enough to cause condensation of the fluid. The condensed fluid flows down the tube and into the section beneath the ground where it absorbs heat from the soil, boils, and evaporates. The fluid, now in gaseous form, flows back up the tube where it releases heat to the outside air, condenses, and flows back down the tube, thus completing the cycle (McFadden 1989). A simple illustration of a thermistor tube installation is depicted in Figure 1.10.

At the Bethel airport, thermosyphons were installed beneath a section of the runway and ground temperatures were monitored using thermistor strings. Analysis of the data indicated that the thermosyphon units performed well and were able to reduce the active layer beneath the runway by approximately 53%. The section of runway with thermosyphons remained stable with the asphalt in good condition, while the remainder of the embankment continued to experience settlement problems (McFadden 1989).

One of the major advantages of thermosyphons is their simplistic design, which requires little to no maintenance, no moving parts, and no external energy for power. Unfortunately there are disadvantages to thermosyphons as well. Since thermosyphons only operate during the winter, they must remove enough heat from the soil during the winter to counter the incoming heat from the summer. They are also prone to leaking, in which case they perform poorly or not

Figure 1.9 Snow sheds along embankment slope (Zarling and Braley 1986).

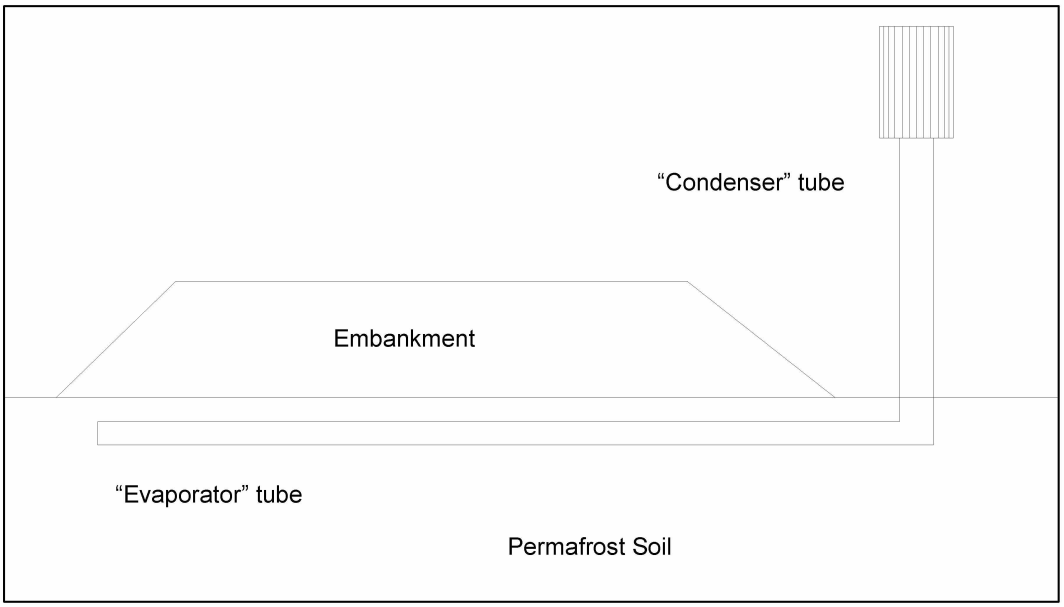

Figure 1.10 Illustration of thermistor tube installation.

at all. Finally, they are quite expensive, both in materials and installation costs (McFadden 1989).

Development of geosynthetic fabrics in the 1970's and 1980's provided another potential solution to embankment settlement over thawing permafrost. Experimental research was conducted by UAF researchers in 1984 to test the effectiveness of geosynthetics to support an embankment over voids created by thawing ice in the foundation soil. Results of the research

suggested that an embankment could be supported over voids up to 3 meters (9.8 ft) in width, but eventual stretching of the fabric would lead to unacceptable settlement and maintenance requirements (Vinson et al. 1996).

1.1.2 Air Convection Embankment (ACE)

ACE is a relatively new roadway embankment design intended to prevent thawing and subsequent settling of underlying permafrost soils. An ACE is constructed using coarse, poorly-graded rock that has a high porosity, thus allowing air to flow freely through the pore spaces. During winter months, the ambient air temperature is typically much colder than the temperature at the base of the embankment. The cold air temperature cools the driving surface and upper portion of the embankment while the temperatures at the base remain relatively warm. The result is an unstable air density gradient, causing pore air circulation to occur and accelerating heat transfer from the base of the embankment to the upper surface (see Figure 1.11) (Saboundjian and Goering 2003).

Theoretically an ACE system can be viewed as a horizontal layer of porous material that will experience natural convection if the critical Rayleigh number of $4\pi^2$ (approximately 40) is exceeded. The Rayleigh number (*Ra*) is defined as follows:

$$Ra = \frac{C\beta gKH\Delta T}{\nu k} \tag{1.1}$$

where C is the volumetric heat capacity of the soil, β is an expansion coefficient, g is acceleration due to gravity, K is intrinsic permeability, H is layer height, ΔT is the temperature difference between the top and bottom of the layer, v is the kinematic viscosity of the pore fluid, and k is thermal conductivity (Saboundjian and Goering 2003).

Given the critical Rayleigh number, Equation 1.1 can be solved for the critical temperature difference as follows:

$$\Delta T_C = \frac{40\nu k}{C\beta gKH} \tag{1.2}$$

where ΔT_C is the critical temperature difference between the top and bottom of the ACE layer (Saboundjian and Goering 2003). When the temperature difference between the top and bottom of the ACE exceeds the critical temperature difference, air convection can occur as shown in Figure 1.11.

During the summer months the upper portion of the ACE is exposed to incoming solar radiation and warm air, thus the upper portion of the embankment becomes warmer than the

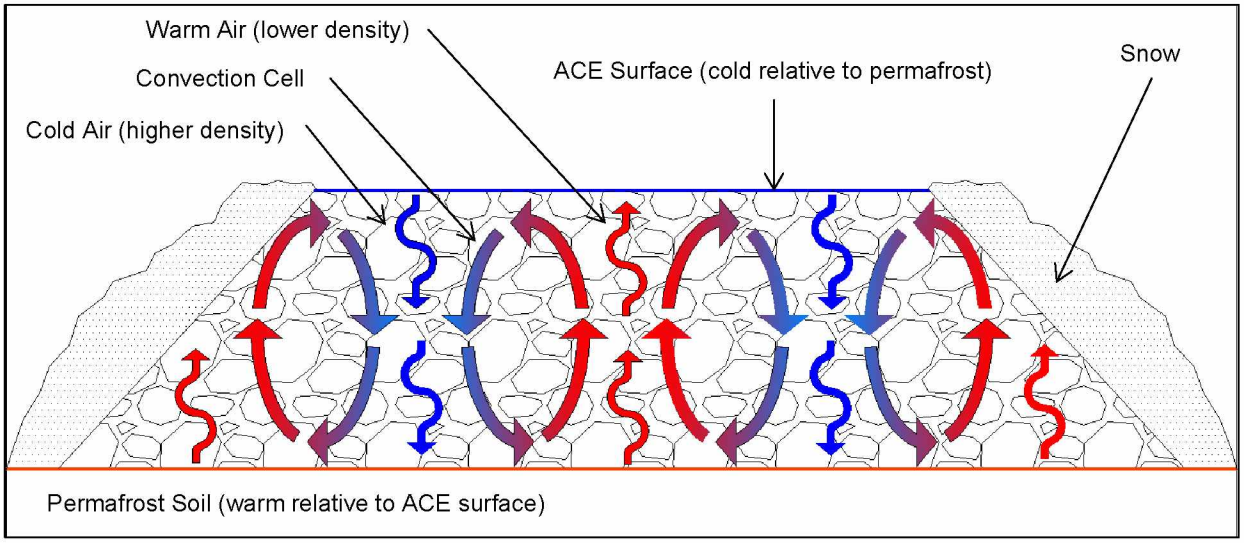

Figure 1.11 ACE during winter months.

lower portion. This leads to a stable air density gradient where the lower density warm air remains in the upper portion of the embankment while the higher density cold air remains at the base of the embankment (see Figure 1.12). Under these conditions, air convection between the upper and lower portions of the embankment ceases and heat transfer occurs primarily through conduction. Since the ACE material has a lower thermal conductivity than a regular gravel embankment, it acts as an insulator and lessens the amount of heat that reaches the underlying soil during the summer.

From 1992 to 1993 an experimental ACE was designed and constructed at Brown's Hill Quarry, near Fairbanks. The ACE was 40-m (131 ft) long and 2.5-m (8 ft) high, with a 6-m (20 ft) wide driving surface and 2H:1V side slopes (see Figure 1.13). The embankment was not part of an actual roadway nor was it designed for traffic. Material used to construct the embankment consisted of coarse, poorly-graded rock with a typical diameter of 5 to 8 cm (2 to 3 in.) (Goering 1998).

The temperature within the embankment was measured using 44 thermistors placed in a grid pattern, while 4 additional sensors were installed vertically within existing ground beneath the embankment centerline (see Figure 1.13). Thermistors also were placed along the side slopes to measure surface temperatures and additional sensors were used to measure air temperatures at the site (Goering 1998).

Temperature data was logged every 15 minutes from Oct. 26, 1993 to Oct. 27, 1995. During the first winter, snow was compacted on the driving surface to create an impermeable layer in order to simulate real world conditions. The following spring, plastic sheeting was placed

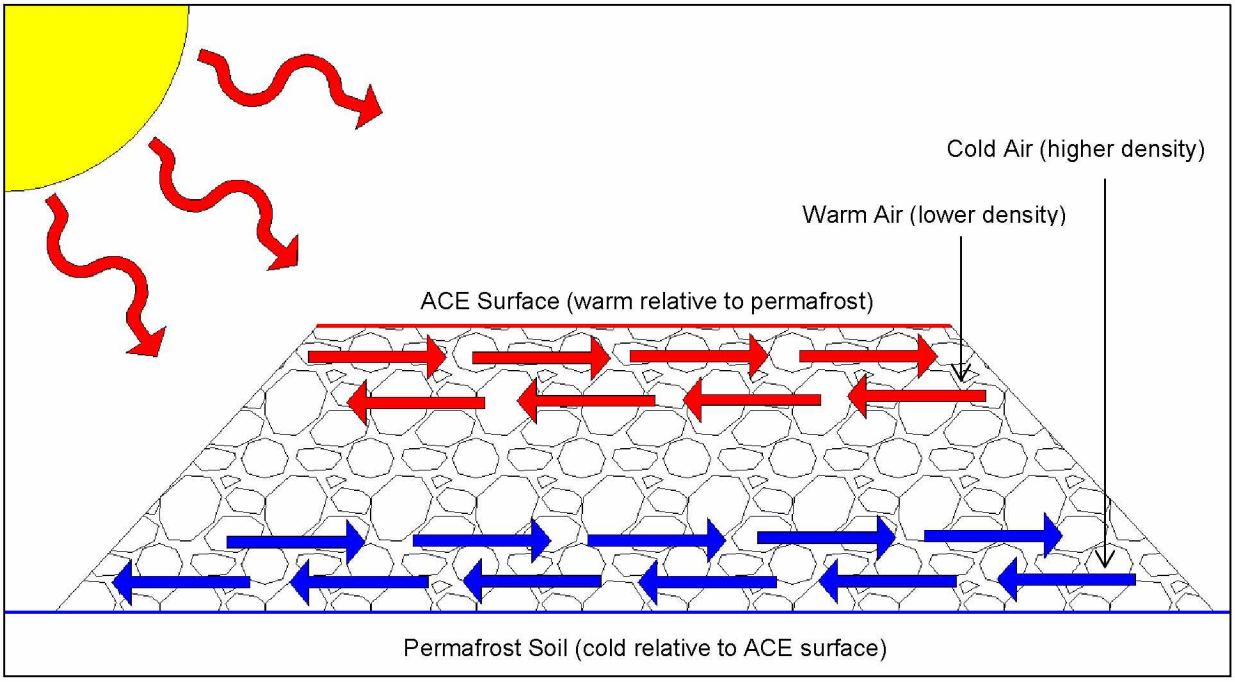

Figure 1.12 ACE during summer months.

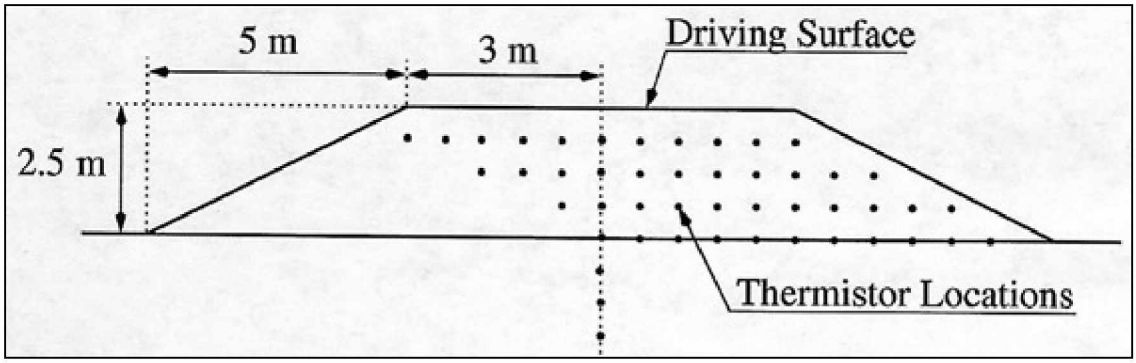

Figure 1.13 Experimental ACE cross section (Goering 1998).

over the entire embankment surface and remained in place until that fall. Then the plastic was removed from the upper surface of the embankment while the sheeting along the side slopes was left in place (Goering 1998).

Results of temperature measurements indicated the presence of convection plumes within the embankment during the winter months. Upper surface temperatures of the embankment averaged 2°C (35.6°F) while at the base of the embankment the mean annual temperature varied from -1.2 to -3.6°C (29.8 to 25.5°F). The experimental embankment provided strong evidence to suggest that an ACE could be effective at minimizing or eliminating thaw settlement of roadway embankments over permafrost (Goering 1998).

Following construction and monitoring of the experimental ACE at Brown's Hill Quarry, the ACE concept was implemented as part of an actual roadway project. From 1995 to 1997, an ACE was designed and constructed as part of the Parks/Chena Ridge Interchange project in Fairbanks. The ACE section was constructed of coarse, poorly-graded rock, ranging from 1 to 6 in. in diameter, while the control section was constructed of standard embankment fill with 4 in. of insulation board placed 4 ft below the asphalt (Saboundjian and Goering 2003).

Thermistor strings were used to monitor temperatures within the ACE and control section from 1996 through 2001. Temperatures within the embankment were measured hourly with six-hour averages stored on a datalogger. In addition to embankment temperatures, air temperature was measured two times per hour and used to determine the mean, maximum, and minimum daily air temperatures (Saboundjian and Goering 2003).

Temperature data indicated that air convection plumes were occurring within the ACE during winter. Mean annual temperatures at the base of the ACE were approximately 7°F less than at the ACE surface, and although the mean annual temperature at the ACE surface was at or above freezing, mean annual temperature at the base remained below freezing. The maximum temperature at the base of the ACE decreased from greater than 40°F to near freezing during the five-year monitoring period. It was expected that the permafrost table would eventually move into the base of the ACE and eliminate any seasonal thawing of the foundation soils (Saboundjian and Goering 2003).

For the control section, the insulation was effective at limiting annual temperature extremes at the embankment base beneath centerline; however, the temperatures beneath the embankment side slopes were warmer and resulted in thawing of the foundation soils and thaw settlement. Field observations showed embankment deformation and shoulder rotation in the control section, while the ACE showed no signs of deformation at the time (Saboundjian and Goering 2003).

1.2 RESEARCH OBJECTIVES

The research discussed herein involves evaluation of geotechnical instrumentation performance, analysis of embankment thermal performance, and development of a numerical model for an ACE with thermal berm. Such research is important in evaluating the applicability of new geotechnical instrumentation technology for monitoring embankments over permafrost. Additionally, the embankment analysis and numerical modeling aspect of this research is

important in expanding our knowledge of ACE modeling methods and how modeling results compare to real world measurements. The objectives of this research were to:

1) compare the results and performance of relatively new geotechnical instruments with well-established instruments used for measuring deformation and temperature;
2) analyze and assess the short-term thermal performance and deformation of the embankment; and
3) develop a two-dimensional numerical model of the embankment to estimate long-term thermal stability.

The remainder of this document is divided into six chapters that provide additional information about the project area and the methods used to achieve the research objectives. Chapter 2 contains details regarding project location, geology, geomorphology, permafrost, vegetation, and climate. Chapter 3 addresses the field work and instrumentation of the embankment, including embankment construction, instrument installation, and purpose and specifications of each instrument. Chapter 4 is a discussion of the results of the instrumentation, which includes evaluation of instrument performance, comparison of results from different instruments, and analysis of results. Chapter 5 provides details and results of laboratory testing conducted on soil samples from the site. Chapter 6 contains the methods used for numerical modeling of the embankment and analysis of the results of modeling. Finally, in Chapter 7 the results of this research are summarized, and conclusions and suggestions for future work are presented.

CHAPTER 2 PROJECT AREA

This chapter provides information about the project area, such as the location, typical geology, geomorphology, vegetation, and climate. Section 2.1 details the project location and geomorphology, namely the general location within the state of Alaska, the specific location with respect to local towns and roads, and the typical topography and drainage encountered. Section 2.2 provides information about the general bedrock and surficial geology, and vegetation. Finally, Section 2.3 details the climate of the area, such as the general climatic zone, seasonal temperature variations, historical normal temperatures, and typical precipitation.

2.1 LOCATION AND GEOMORPHOLOGY

Lost Chicken Slide is located in Interior Alaska, near MP 70 of the Taylor Highway, approximately 2.5 miles east of Chicken, Alaska (see Figure 1.1 and Figure 1.2). This area is within the Yukon-Tanana Upland physiographic region and is characterized by rounded ridges (Wahrhaftig 1965). There are few lakes in this region, and those that are present are primarily thaw lakes in valley bottoms and passes. There are no glaciers present; however, the area is underlain by discontinuous permafrost and ice wedges can be found in the frozen valley bottoms (Wahrhaftig 1965).

The project site is located along Lost Chicken Creek, just east of Lost Chicken Hill. A map derived from a United States Geological Survey (USGS) quadrangle depicting the project location is presented in Figure 2.1.

2.2 GEOLOGY, VEGETATION, AND PERMAFROST

The project area is underlain by the Taylor Mountain Batholith, which is composed primarily of biotite-hornblende-quartz monzodiorite, tonalite, granodiorite, and quartz diorite (Werdon et al. 2001). Other deposits include placer mine tailings that can be found in Lost Chicken Creek, which is adjacent to the site.

The majority of the hillsides in the Lost Chicken area are covered with fine-grained colluvium and silt. Surficial loess deposits have been re-transported by mudflows, frost action, gelifluction, and slopewash, and as a result can contain large amounts of angular clasts from local material (Werdon et al. 2001). Thickness of the silt varies; however, it is generally thickest

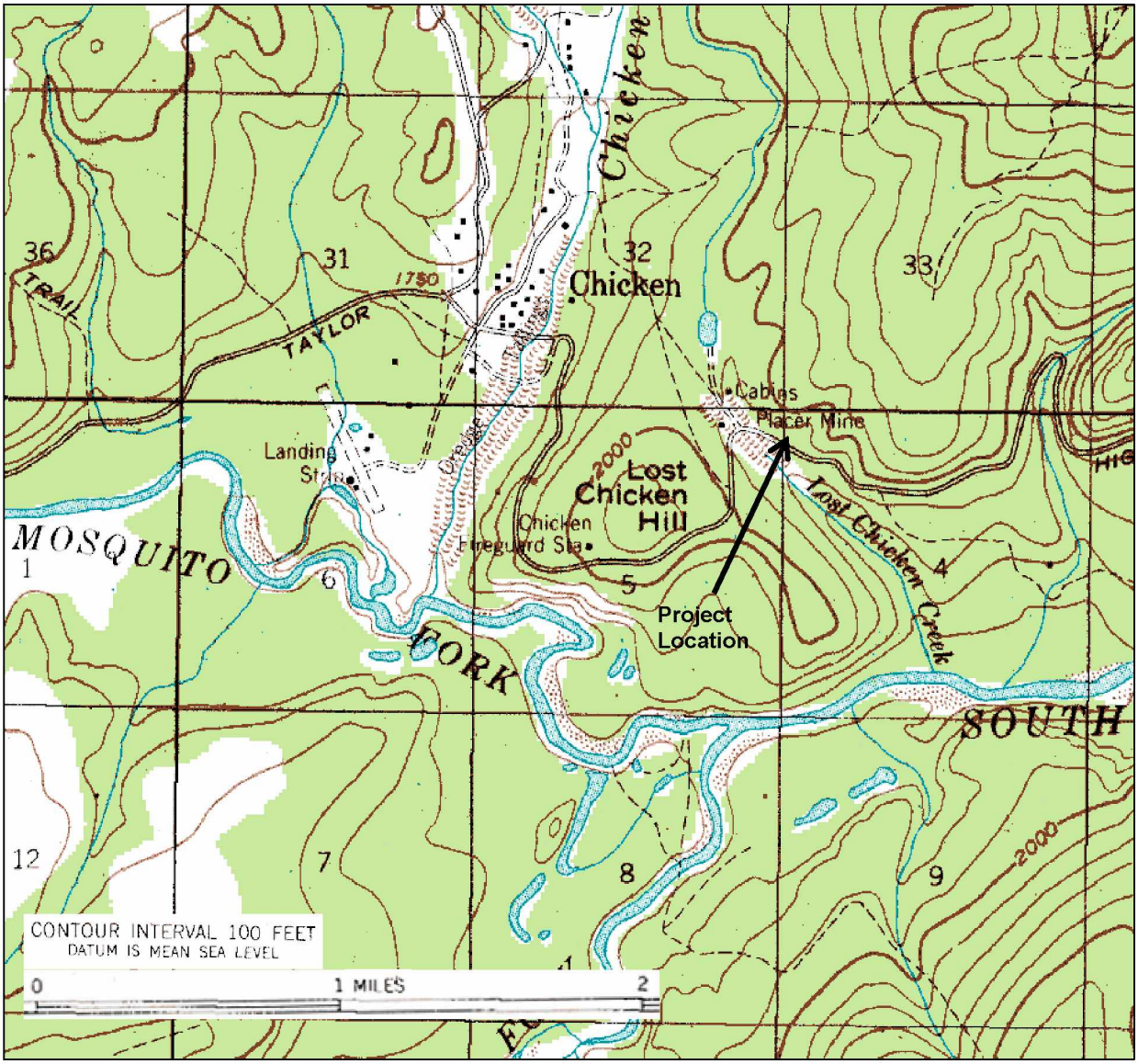

Figure 2.1 Project location, showing physiographic features (base map taken from Eagle A-2 Quadrangle (USGS 1956)).

near the base of slopes and decreases in thickness with elevation. Much of the silt is perennially frozen and ice-rich (Werdon et al. 2001).

The area lies within the Interior Highlands ecoregion, as defined by Gallant et al. (1995). This ecoregion consists primarily of rounded, low mountains. Vegetation is mostly dwarf scrub and spruce stands. The mountains in most of this area rise to approximately 3,900 ft, with several reaching higher than 4,900 ft (Gallant et al. 1995). Vegetation in the immediate project area consists primarily of black spruce, willow shrubs, sphagnum and feather mosses, Labrador tea, and grasses. Birch trees become prevalent in the drier soils along hill tops and slopes.

Typical black spruce and willow shrubs at the site are shown in Figure 2.2a, while the sphagnum and feather mosses, Labrador tea, and grasses are shown in Figure 2.2b.

The immediate project area is underlain by permafrost. The active layer depth was measured on Oct. 6, 2012 in several random locations in the undisturbed, vegetated area at the site using a steel probe. The depth of thaw was measured from the top of the moss downward. The average active layer depth was approximately 2 ft. Given that the typical thickness of moss (i.e., live organic material on the ground surface) is approximately 0.5 ft, the ground thaws approximately 1.5 ft into the near-surface decomposed organic matter (or peat) and ice-rich silt.

2.3 CLIMATE

The project site is located in the continental climate zone of Interior Alaska as depicted in Figure 2.3. This region is characterized by extreme seasonal temperature variations, with summer temperatures rising above 70°F while winter temperatures drop below -30°F. Spring and fall are generally short, resulting in primarily two seasons; winter and summer (Alaska History & Cultural Studies 2014).

The nearest weather station to the project site is located in Chicken. Historical weather data is available from 1953 to 2012; however, the earliest recorded data is largely incomplete. The average daily temperature recorded at the station from 1981 through 2010 was obtained from Golden Gate Weather Services (2011). A plot of the average daily air temperature from 1981 through 2010 is presented in Figure 2.4. Based on the historical average daily temperature data, the mean annual air temperature for the area is 20.0°F, the freezing index is -6,912.2 °F days, and the thawing index is 2,548.5 °F days. Table 2.1 provides a summary of the monthly freezing degree days, thawing degree days, mean air temperature, and precipitation.

Figure 2.2 Typical vegetation in project area. (a) Black spruce and willow shrubs, and (b) sphagnum and feather mosses, grasses, and Labrador tea.

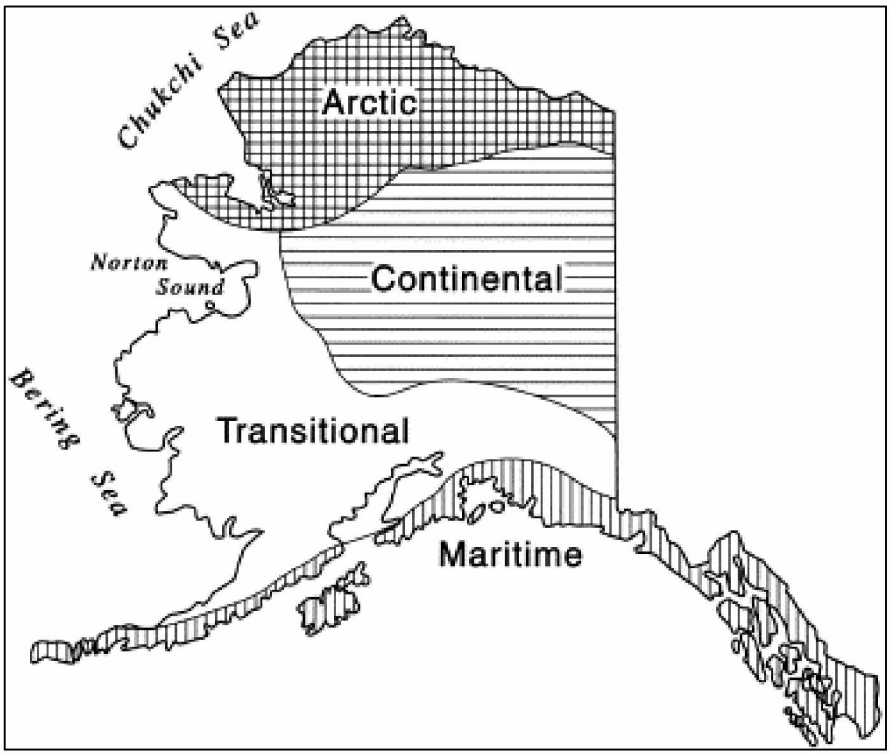

Figure 2.3 Modern climate zones of Alaska (Ager 2003).

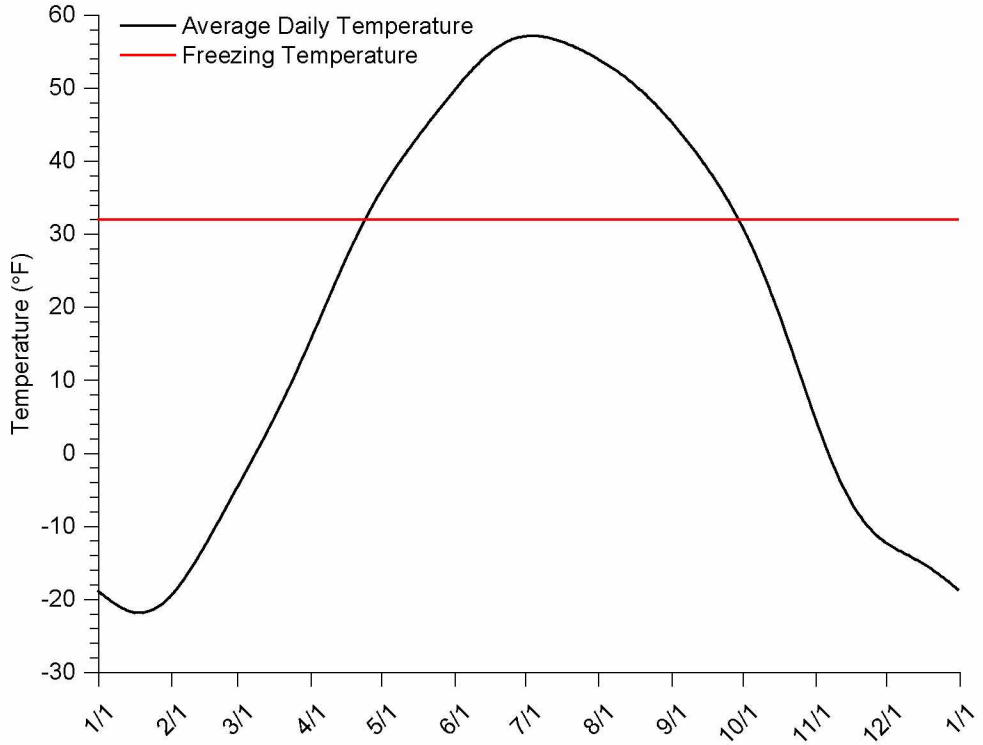

Figure 2.4 Average daily air temperature in Chicken from 1981 to 2010 (data from Golden Gate Weather Services 2011).

Table 2.1 Average monthly climate data from 1981 through 2010 (data from Golden Gate Weather Services 2011, and WRCC 2012).

Month	Freezing Degree Days (°F·days)	Thawing Degree Days (°F·days)	Mean Air Temperature (°F)	Precipitation (in.)
Jan.	1,638.2	0	-20.8	0.5
Feb.	1,250.2	0	-12.7	0.3
Mar.	841.6	0	4.9	0.2
Apr.	188.8	13.2	26.1	0.3
May	0	343.6	43.1	1.1
Jun.	0	668.9	54.3	2.2
Jul.	0	748.4	56.1	2.5
Aug.	0	565.5	50.2	2.2
Sep.	0.5	208.9	38.9	1.5
Oct.	406.0	0	18.9	0.7
Nov.	1,123.8	0	-5.5	0.5
Dec.	1,463.1	0	-15.2	0.6

CHAPTER 3 FIELD WORK AND INSTRUMENTATION

This chapter summarizes instrumentation installed at the site and data collection. Section 3.1 provides a detailed account of the field work performed, including instrument installation, and data collection procedures. Soil sampling and test hole logs are provided in Section 3.2. Descriptions of the instruments, including make, model, manufacturers' specifications, and installation details are included in Section 3.3.

3.1 FIELD WORK

Construction of the realignment at Lost Chicken began in the fall of 2011. The ground was cleared of trees and brush, while the surficial organic material and moss layer were left intact to help prevent thawing of ice-rich permafrost. Geofabric was placed over the organic layer and gravel fill was placed on top of it for construction of the thermal berm. Figure 3.1 is a photograph of the site conditions at the end of the 2011 construction period.

In spring 2012, construction of the new embankment resumed. The remaining geofabric was placed over the cleared ground and contractors began placing coarse rock for the ACE. A photograph of the site during the construction of the ACE is presented in Figure 3.2. In conjunction with placing ACE material, plastic pipe casings were installed across the base of the embankment perpendicular to centerline, for installation of geotechnical instrumentation. First, a layer of sand bedding was placed across the base of the embankment. Contractors had to trench through the existing portion of embankment from the 2011 construction (see Figure 3.3).

After spreading and compacting the sand bedding, three plastic pipe casings were placed on top of it and parallel to one another, extending beyond the width of the embankment. One casing was a PVC pipe used for housing a thermistor string and a digital temperature acquisition cable (TAC). The second was an inclinometer casing used to house a MEMS-based in-place inclinometer. The third was another inclinometer casing used for taking deformation measurements with a horizontal inclinometer probe. Special care was taken to ensure that the casing grooves, which provided wheel tracks for the probe, were aligned horizontally and vertically. The third casing also had a PVC casing attached to the top of it through which a return cable was run. A photograph of the casings in place prior to backfilling is shown in Figure 3.3a.

After the casings were placed, another layer of sand was placed over them to provide protection from the ACE material (see Figure 3.3b). The sand was compacted as shown in

Figure 3.1 Lost Chicken site, fall 2011 (photograph courtesy of ADOT&PF).

Figure 3.2 Construction of ACE, spring 2012 (photograph courtesy of M. Darrow).

Figure 3.3 Photographs of placement and backfill over instrument casings. (a) Instrument casings in place over sand bedding; (b) casings being covered with sand blanket (photograph courtesy of M. Darrow); (c) compacting sand blanket; (d) casing ends extending beyond embankment side slope.

Figure 3.3c, and embankment fill was placed over top of it leaving only the casing ends exposed (see Figure 3.3d). ACE rock was spread over the entire embankment area and built up to plan

grade, along with the thermal berm along the southern edge. Finally, geofabric was placed on the top of the ACE rock for separation, and then the gravel driving surface was constructed to finished grade.

The geotechnical instrumentation was installed at the site after completion of the instrument casing installation, but prior to completion of embankment construction. From Jul. 9 through Jul. 12, 2012, the instruments and automated data acquisition system (ADAS) were installed by UAF research personnel consisting of Dr. M. Darrow, and research assistants D. Jensen and J. Zottola. Along with the instruments and ADAS, a dead-end pulley was installed on one end of the inclinometer casing used for horizontal inclinometer probe measurements; the pulley allowed for measurements to be taken from one end of the casing by a single person.

Survey measurements of the embankment cross section and casing ends were taken at the beginning and end of construction and once more at the end of the summer; measurements were taken with a Leica total station. Instrument data was collected from the site by D. Jensen on a biweekly basis from Jul. 23, 2012 to Oct. 6, 2012, after which the highway was closed for the season. Data was collected once again by D. Jensen on May 11, 2013, after the highway was opened in the spring. The final data collection included in this thesis was conducted by Dr. M. Darrow on Jul. 16, 2013. The combined collected data results in a total of 371 days of data since instrument installation. Details and analysis of the data results are provided in Chapter 4.

3.2 SOIL SAMPLE COLLECTION AND TEST HOLE LOGS

Concurrent to the instrument installation, soil samples were collected from aggregate surface course, thermal berm material, organic mat, and *in situ* frozen soils, including ice-rich silt, peat, and coarse sand. Samples were transported to UAF where laboratory testing was done to determine moisture content, classification, dry unit weight, thermal conductivity, and thaw strain, among other properties, which are discussed in detail in Chapter 5.

Near-surface, unfrozen samples were obtained using a volumetric soil sampler to drive soil rings into the material; however, the thermal berm material consisted of aggregate too large to obtain an *in situ* sample with the soil sampler. Instead, samples were collected in tins for measurement of gravimetric moisture content, and one large bag of the material was collected for grain size analysis. Frozen core samples were obtained from undisturbed areas adjacent to the embankment using a Snow, Ice, and Permafrost Research Establishment (SIPRE) auger with power head. The frozen samples were extracted from the boreholes after each auger flight and immediately logged, wrapped in plastic, labeled, and placed in a freezer to prevent thawing.

Figure 3.4 consists of photographs of (a) the 3-in. diameter hollow-stem SIPRE auger flight, (b) the SIPRE boring into the ground, and (c) operation of the power head. Using this sampling method, five test holes were drilled in undisturbed areas adjacent to the ACE. Figure 3.5 is a map illustrating the test hole locations with respect to the new highway centerline, a portion of the embankment footprint, instrument casings, and the old alignment.

Figure 3.4 Photographs detailing the sampling of near-surface frozen soils; (a) hollow-stem SIPRE auger used for collection of frozen samples; (b) view of SIPRE auger during drilling; (c) drilling frozen core samples (photographs courtesy of M. Darrow).

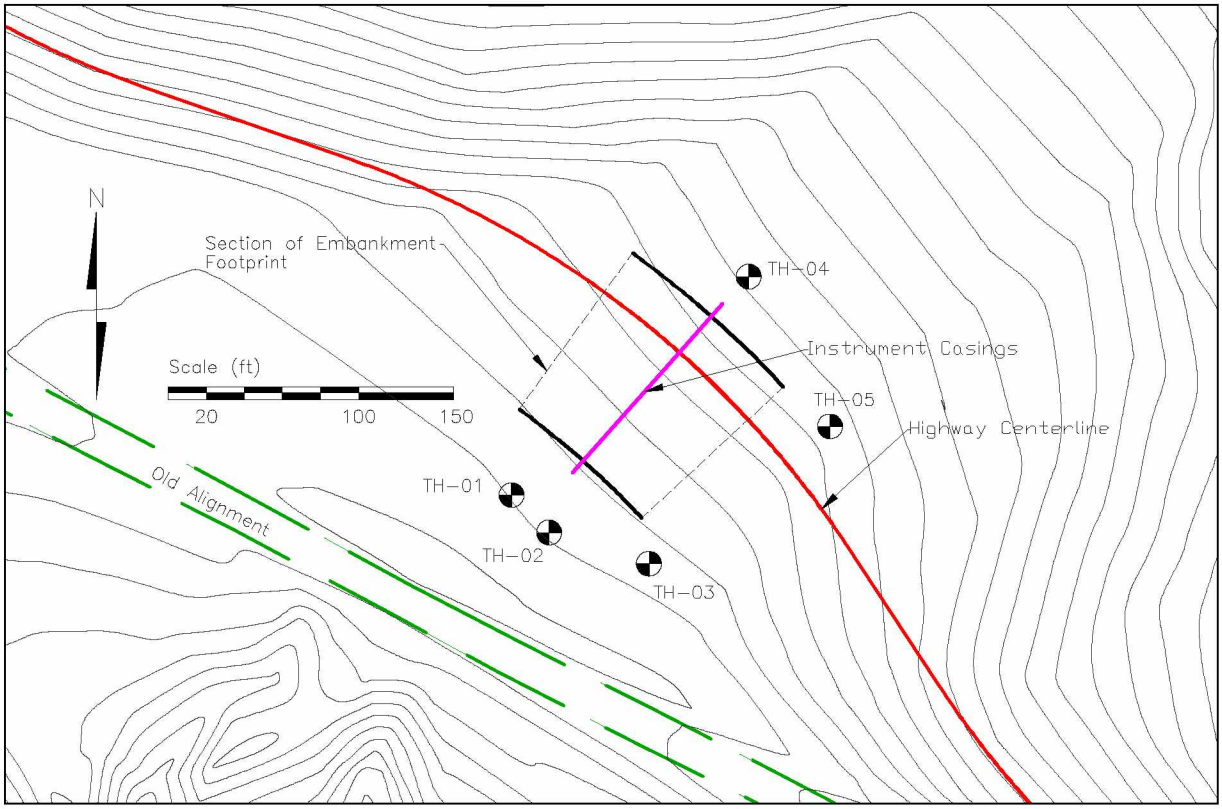

Figure 3.5 Test hole locations for 2012 drilling.

The soils encountered consisted primarily of ice-rich organic silt (see Figure 3.6 for photograph of typical sample) with sand, coarse angular sand (interpreted as colluvium), and ice-rich peat. The soils were frozen from within 1 ft of the ground surface to the bottom of each test hole and organics were present in all of the soils, including the colluvium. The unfrozen material near the surface consisted primarily of the organic mat, which transitioned into more decomposed, peat-like material with depth. Simplified test hole logs including laboratory test results are shown in Figures 3.7 through 3.9. Photographic logs of the frozen core samples recovered from test holes TH-01 through TH-05 are provided in Figures 3.10 through 3.14, respectively.

3.3 INSTRUMENTATION

3.3.1 Temperature Sensors

Several different instruments were used to monitor temperature at the site. A thermistor string and TAC were used to monitor temperature at the base of the embankment. Two

Figure 3.6 Photograph showing typical sample of ice-rich silt (photograph courtesy of M. Darrow).

Campbell Scientific Model 109 (CS109) sensors were used to measure air temperature, and three additional CS109 sensors were used to measure ground surface temperature.

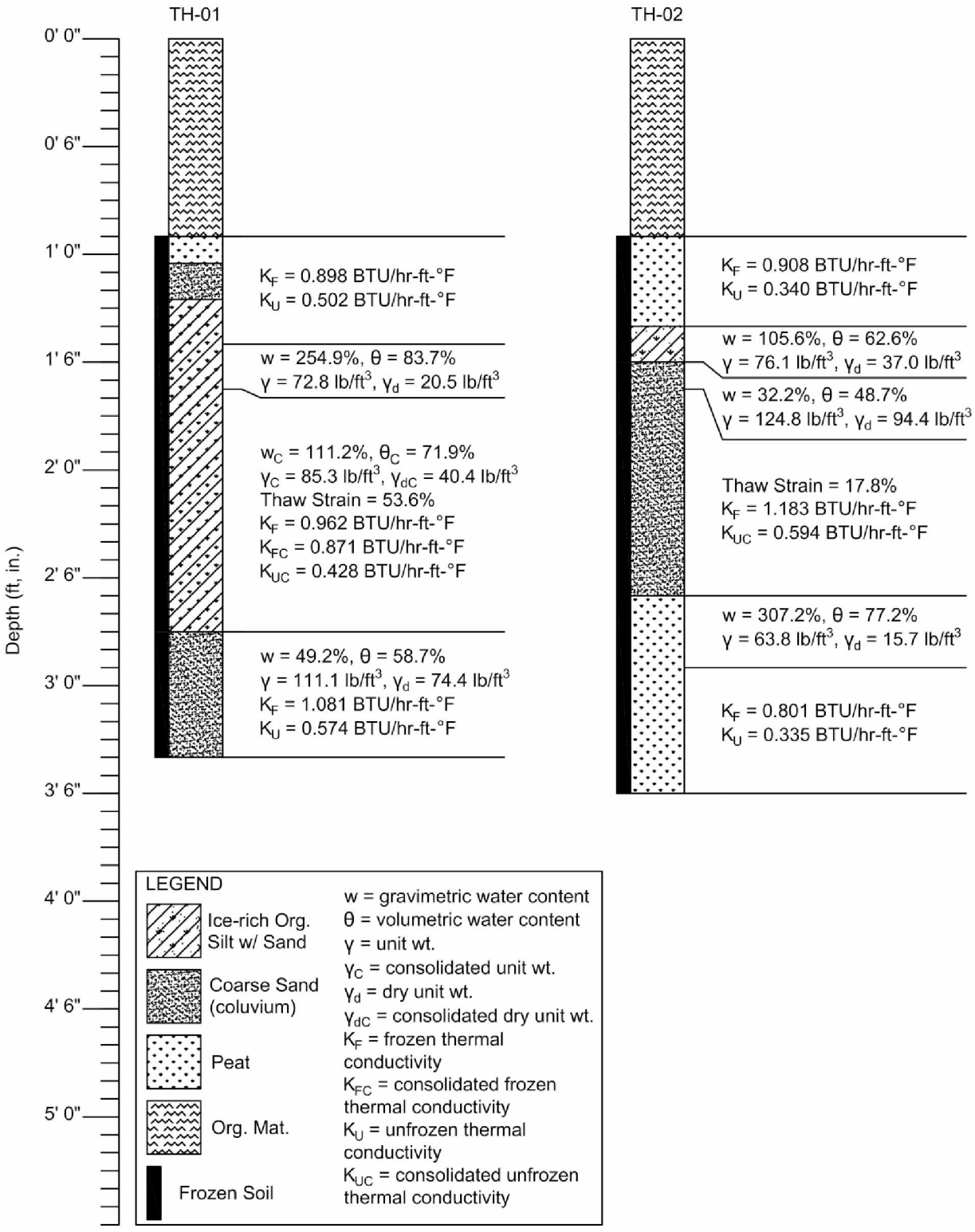

Figure 3.7 Test hole logs for TH-01 and TH-02 from the 2012 drilling. Depth from the ground surface is given in feet and inches.

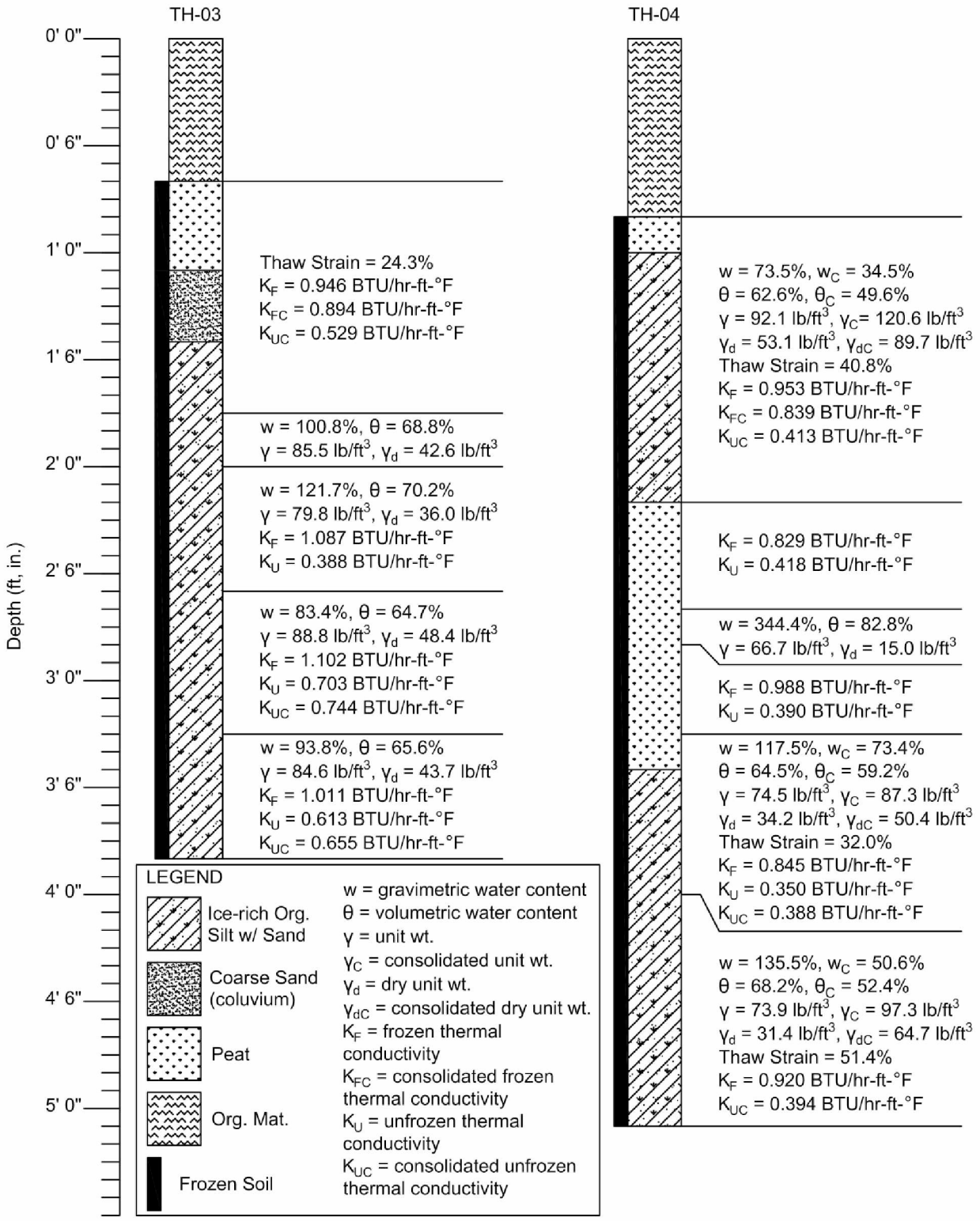

Figure 3.8 Test hole logs for TH-03 and TH-04 from the 2012 drilling. Depth from the ground surface is given in feet and inches.

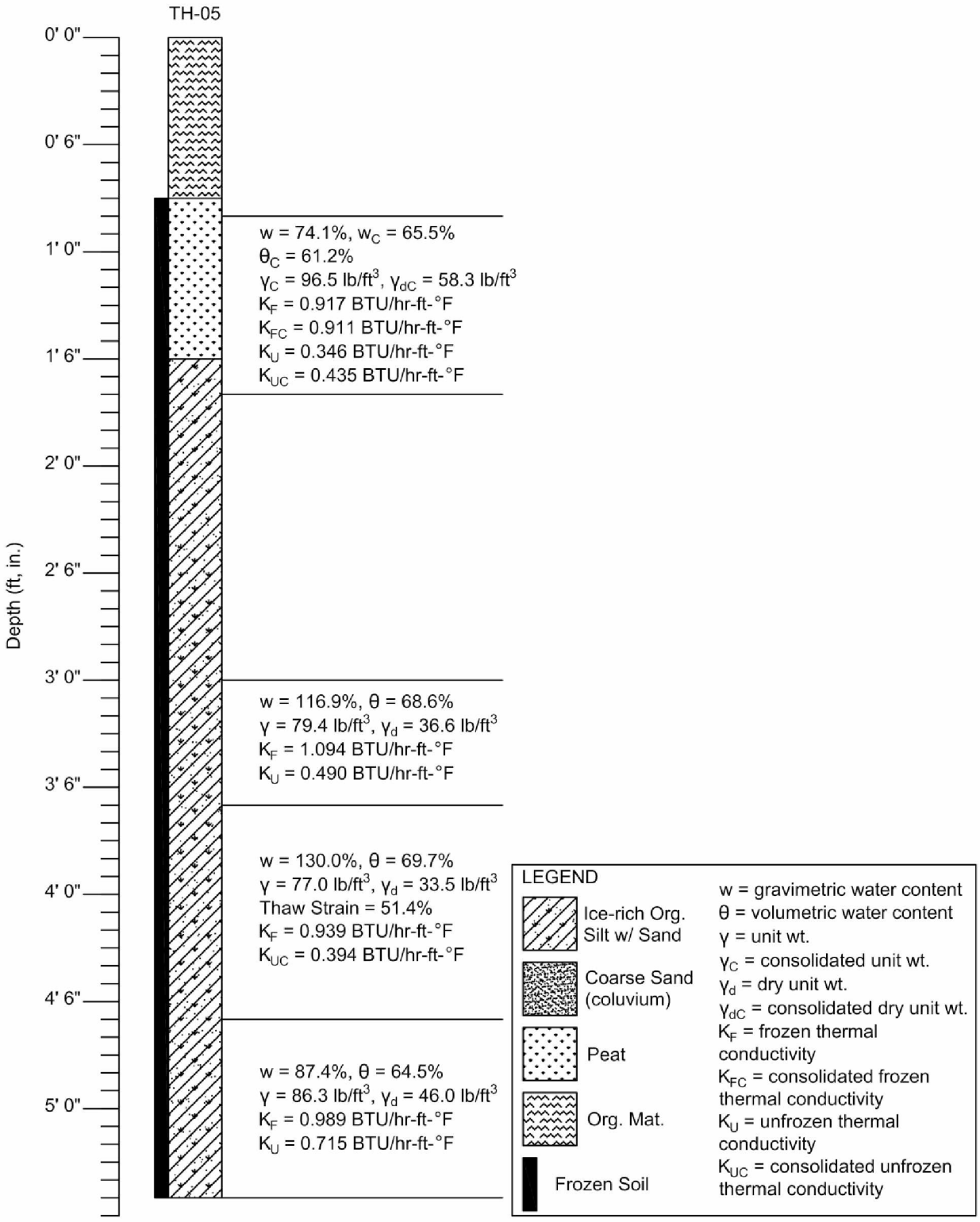

Figure 3.9 Test hole logs for TH-05 from the 2012 drilling. Depth from the ground surface is given in feet and inches.

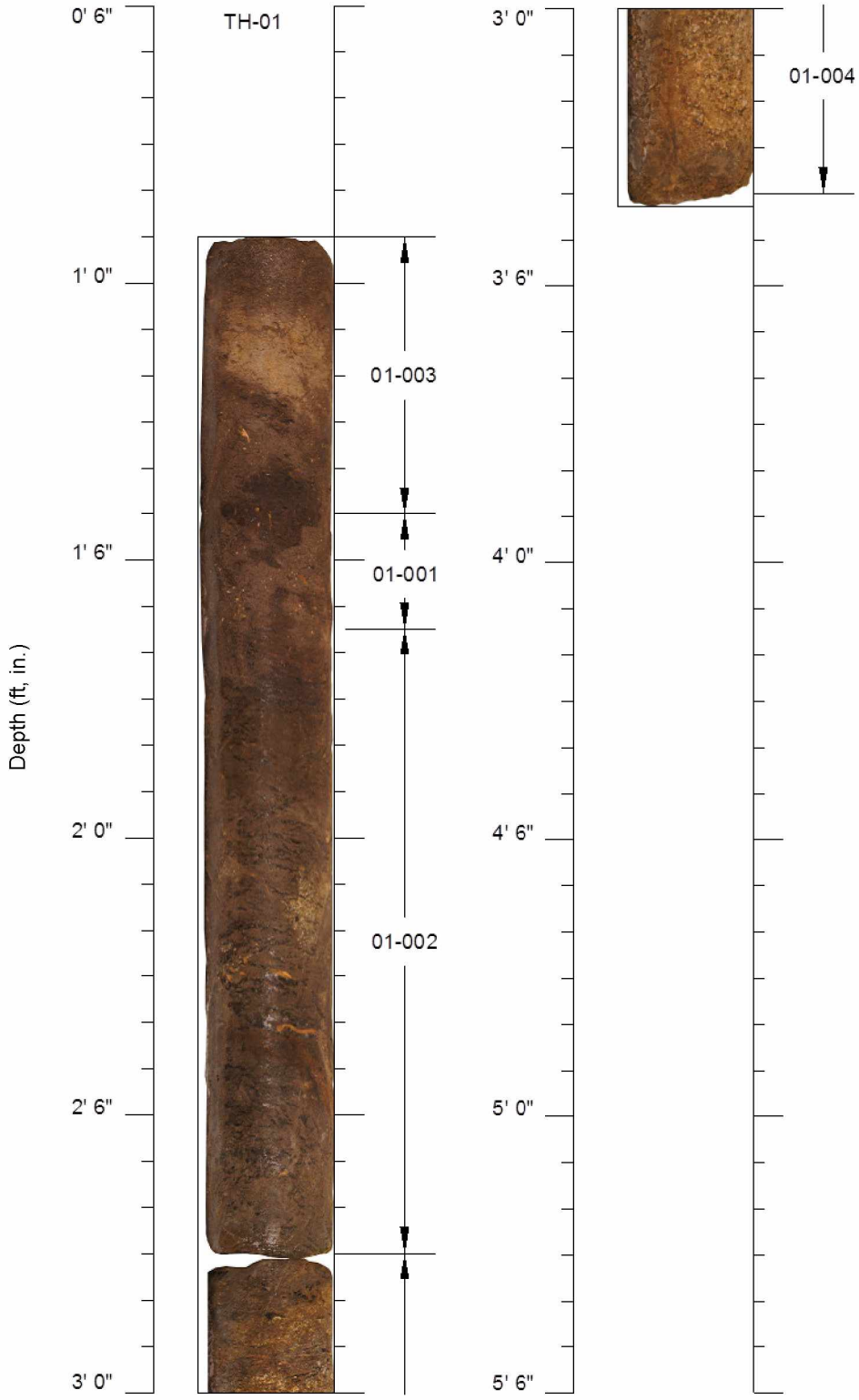

Figure 3.10 Photographic log of TH-01 core samples. The log is annotated with laboratory sample identifications (IDs), and the scale indicates *in situ* depth below ground surface.

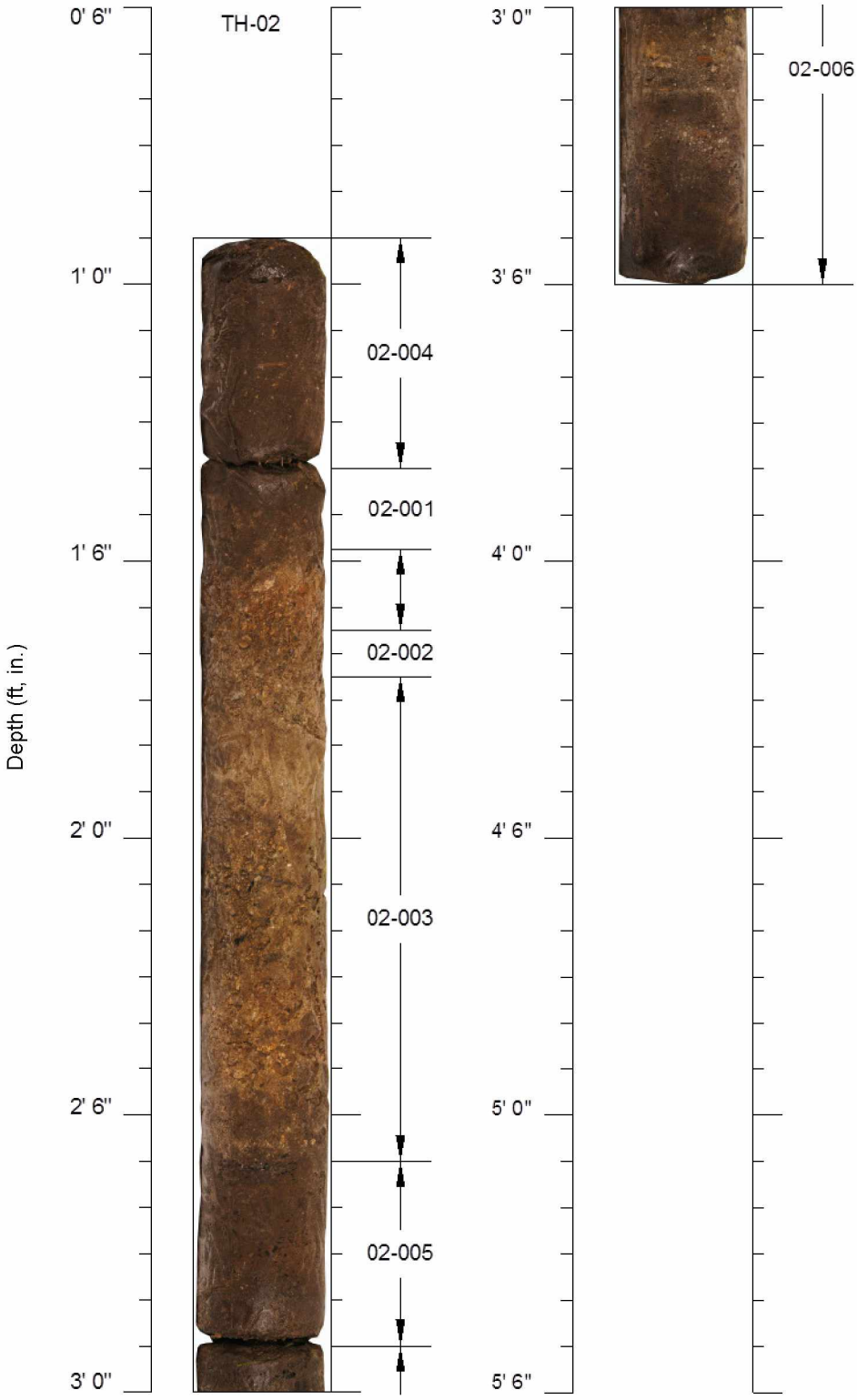

Figure 3.11 Photographic log of TH-02 core samples. The log is annotated with laboratory sample IDs, and the scale indicates *in situ* depth below ground surface.

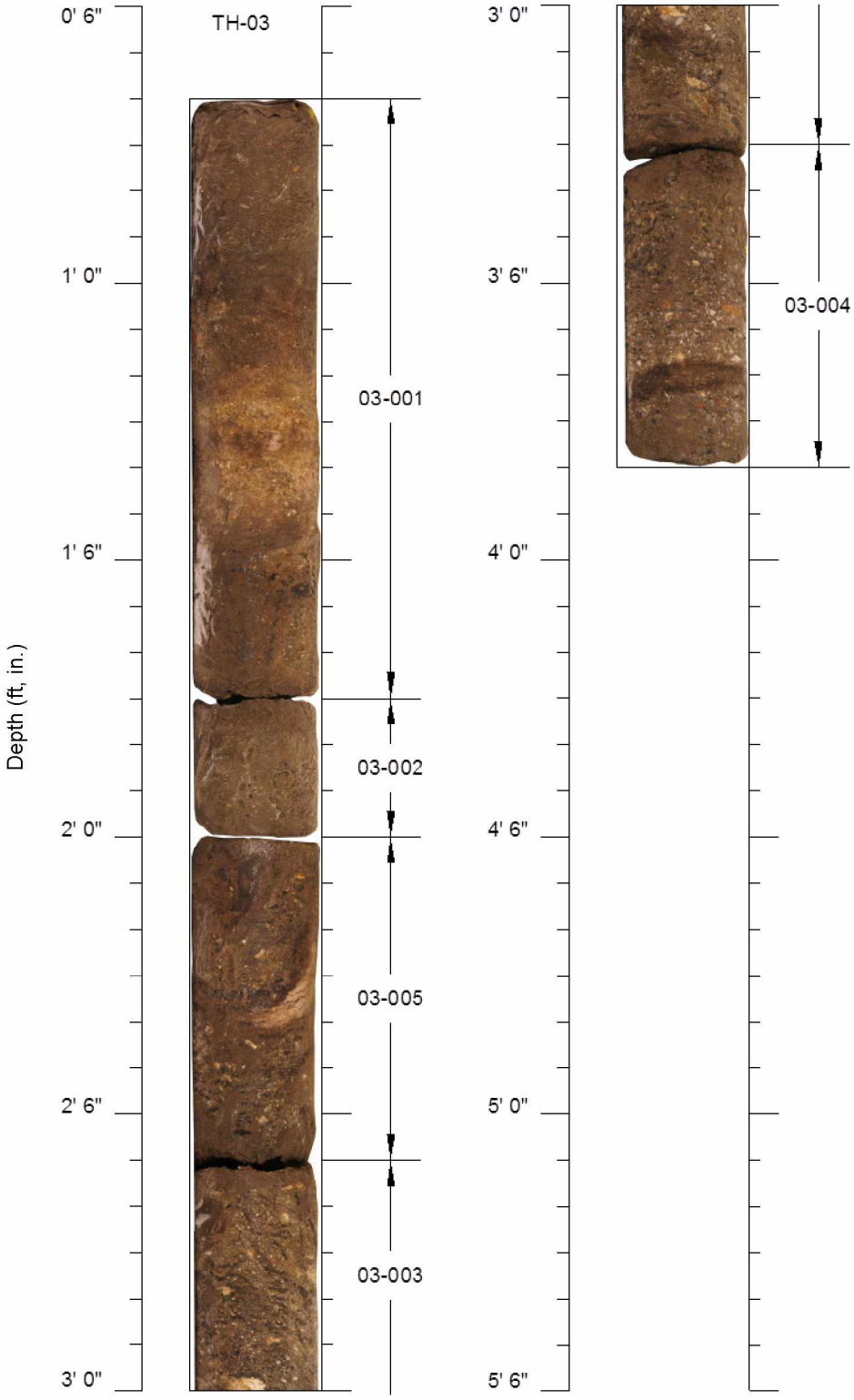

Figure 3.12 Photographic log of TH-03 core samples. The log is annotated with laboratory sample IDs, and the scale indicates *in situ* depth below ground surface.

Figure 3.13 Photographic log of TH-04 core samples. The log is annotated with laboratory sample IDs, and the scale indicates *in situ* depth below ground surface.

Figure 3.14 Photographic log of TH-05 core samples. The log is annotated with laboratory sample IDs, and the scale indicates *in situ* depth below ground surface.

The thermistor string was designed for use at a previous installation for a different phase of the overall research project. It was 70-ft long, with sensors located at 5.5, 13.5, 21.5, 29.5, 37.5, 45.5, 53.5, 61.5, and 70 ft along the string from a marked position. The thermistor sensors had a reported accuracy of ±0.2°F (YSI 1998). Prior to field installation, the thermistor string was checked for sensor function and calibration. The device was placed in an ice bath of deionized water and allowed to reach a stable temperature, after which several temperature measurements were recorded (see Figure 3.15). The temperature measurements indicated that the device was properly calibrated; however, two of the sensors located at 5.5 and 70 ft were not functioning properly. Results from those sensors were ignored when processing the collected data from the site.

In addition to the thermistor string, a TAC from BeadedStream LLC was used to monitor temperature beneath the embankment. The TAC consists of semiconductor-based board-mounted digital temperature sensors. Up to 100 temperature sensors can be placed within a single 0.28-in. diameter cable. Conversion from analog to digital temperature occurs in the sensors, which then output direct temperature readings. The TAC has an operating temperature range of -40°F to 158°F with a temperature sensor accuracy of ±0.18°F from 14°F to 185°F. Temperature measurements are logged on a data collector from which they can be collected in the field via computer (BeadedStream LLC. 2010).

The TAC and thermistor string were installed in the same white PVC casing (see Figure 3.3). Both cables were taped together so that sensors from the TAC would align with sensors from the thermistor string, thus allowing for a direct comparison of temperature measurements (see Figure 3.16). The thermistor string was connected to the ADAS via waterproof flexible conduit connected to the end of the casing (see casing on the left in Figure 3.17). The TAC was connected to its own proprietary DL235 datalogger which was housed in a section of ABS pipe attached to a “T” at the end of the casing as shown in Figure 3.17. Removable rubber end caps were used so the data logger could be easily accessed during field visits.

Five CS109 temperature probes were installed at the site to monitor air and ground surface temperatures. The CS109 sensors used BetaTherm 10K3A1 thermistors with a manufacturer-specified temperature range of -58°F to 158°F. Interchangeability error was specified as ±0.36°F from 32°F to 158°F (Campbell Scientific, Inc. 2011).

Two CS109 sensors were used to record air temperature and were housed in CS 41303-5A radiation shields (see Figure 3.18). The remaining three sensors were used to measure the ground surface temperature at the crest of the thermal berm, toe of the thermal berm, and in undisturbed vegetation. All CS109 sensors were connected to the ADAS via waterproof flexible

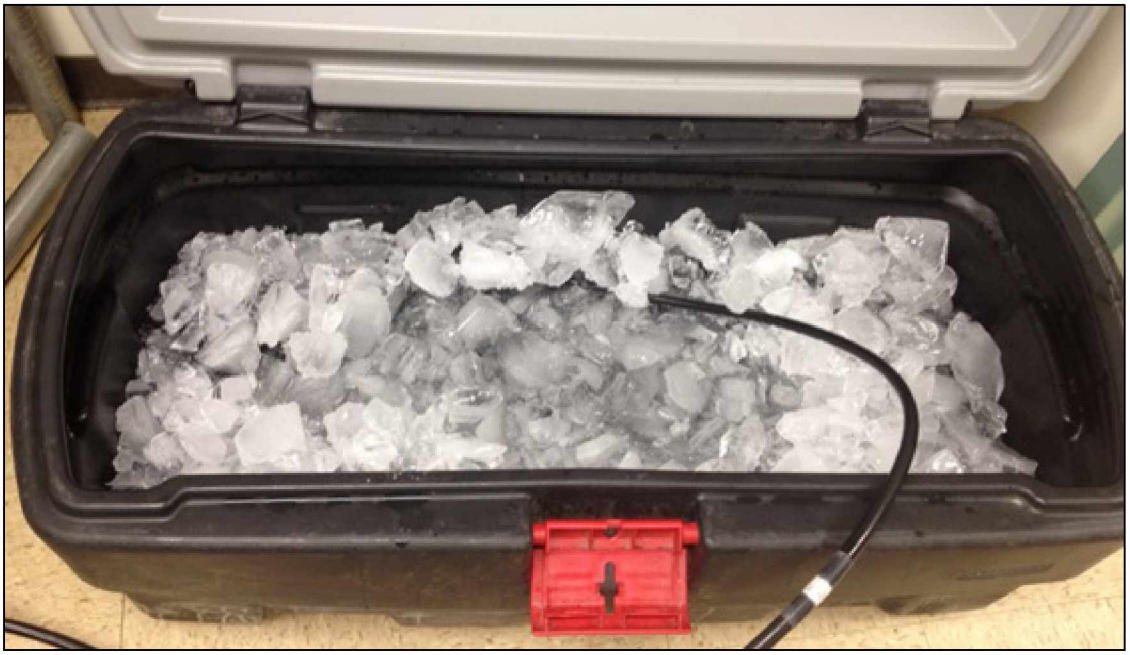

Figure 3.15 Ice bath used for calibration of thermistor string.

Figure 3.16 Photographs of thermistor string and TAC; (a) View of thermistor string (black) and TAC (yellow and blue) taped together prior to placement in casing; (b) close view of thermistor string and TAC sensors (photographs courtesy of M. Darrow).

Figure 3.17 Finished casing ends.

Figure 3.18 CS109 sensors installed in radiation shields (photograph courtesy of M. Darrow).

conduit. Where the sensor cable exited the conduit, plumbers putty was used to seal the end of the conduit against moisture.

Air temperature measurements were compared with historic data to determine if the short-term temperature changes followed the average temperature data, which was used in thermal modeling. The ground surface temperature measurements were compared to the air temperature measurements and used to estimate the *n*-factors (i.e., ratio of air thawing or freezing index to ground surface thawing or freezing index) for the embankment surface and the undisturbed ground.

3.3.2 Measurand ShapeAccelArray

A Measurand ShapeAccelArray (SAA) was used to measure vertical deformation beneath the embankment. The SAA is a relatively new in-place inclinometer which employs MEMS sensors. The SAA consists of 1.0-ft long rigid segments connected by flexible joints. Each segment contains three triaxial MEMS accelerometers. Each group of eight segments is called an octet, and each octet contains a microprocessor and digital temperature sensor (Measurand, Inc. 2013). The SAA is covered with a stainless steel braid that adds durability and abrasion resistance. The device is stored on an octagonal spool as shown in Figure 3.19, which prevents the segments from exceeding the maximum recommended bend angle of 45° at each joint.

In a vertical orientation the SAA can measure movement in three dimensions, while in a horizontal orientation the SAA measures only two-dimensional movement. The SAA MEMS accelerometers measure tilt in each segment over a 360° range. The tilt measurements are imported into the SAA software where deformation is automatically calculated relative to a chosen end of the device, which is assumed to be in stable ground. Accuracy of the SAA is reported as ±0.06 in. over a 105-ft long instrument (Measurand, Inc. 2013).

The SAA installed at Lost Chicken was 68-ft long and positioned so that the sensor at 0 ft was located at the toe of the embankment. The SAA was installed in a 2.75-in. diameter ABS casing (see Figure 3.20) by using a pull rope attached to the end of the device via a stainless steel braided sock. After pulling the SAA into the casing, PVC pipe fittings were used to connect waterproof flexible conduit to the end of the casing (see middle casing in Figure 3.17). The SAA communication cable was pulled through the conduit and connected to the datalogger.

Figure 3.19 SAA on wooden storage spool (photograph courtesy of M. Darrow).

Figure 3.20 SAA installation into casing at Lost Chicken (photograph courtesy of M. Darrow).

3.3.3 Horizontal Slope Inclinometer

A horizontal slope inclinometer (SI) probe from Durham Geo Slope Indicator (DGSI) also was used to measure vertical deformation beneath the embankment at Lost Chicken (see Figure 3.21). The SI probe had a 24-in. wheelbase and employed servo force-balanced accelerometers to measure the angle of tilt in the plane of the wheels. Multiplying the probe length and the sine of the tilt angle yields the deviation for each measurement interval. Changes in deviation are displacements that indicate movement from the original position. Summing the displacements over time yields the cumulative displacement of the casing (Slope Indicator 2006). The SI has an operating temperature range of -4°F to 122°F and a tilt measurement range of ±35°. The SI manufacturer stated accuracy is ±0.01 in. per reading and ±0.3 in. per 50 readings (Slope Indicator 2010).

The SI system included a 3.34-in. diameter inclinometer casing, dead-end pulley assembly, pull-cable return pipe, probe, control cable, pull cable, and readout unit. The inclinometer casing was installed sub-horizontally across the base of the embankment, perpendicular to centerline, with one set of grooves aligned vertically. The pull-cable return pipe was secured parallel to the top of the SI casing. The dead-end pulley assembly was attached to the upslope end of the SI casing and the pull cable was drawn through the SI casing and the pull-cable return pipe. Figure 3.22 is an illustration of a typical horizontal SI installation with dead-end pulley.

SI measurements are typically taken at 2-ft intervals; however, at Lost Chicken measurements were taken at 1-ft intervals to allow for direct comparison to the SAA which had sensors located every 1 ft. Measurements were taken beginning at the far (upslope) end of the casing and ending at the near (downslope) end of the casing, after which the probe was reversed and another set of readings was taken at the same intervals to eliminate error due to sensor bias. The initial measurements were used to establish a baseline profile while subsequent measurements showed changes in the profile. All measurements were referenced to the near end of the casing. Figure 3.23 illustrates measurement collection with the SI instrument.

3.3.4 Automated Data Acquisition System (ADAS)

The ADAS was used to collect temperature data from the CS109 sensors and thermistor string, and deformation data from the SAA. The CS109 sensors were wired directly to a CR1000

Figure 3.21 SI probe, cable, and DataMate readout unit (Slope Indicator 2010).

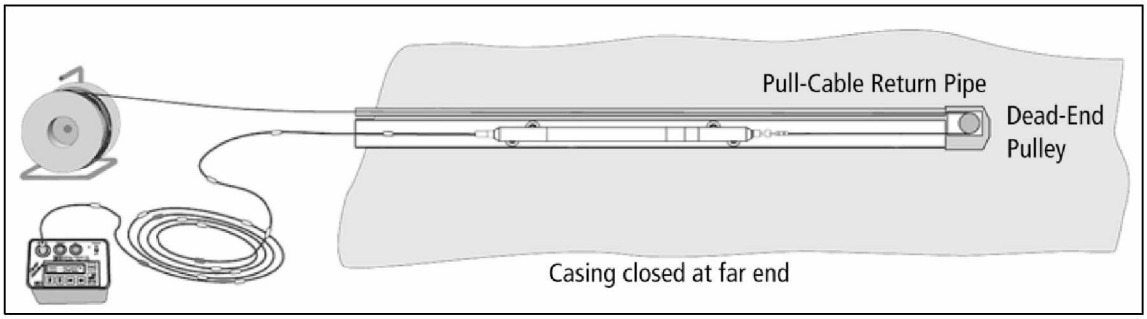

Figure 3.22 Typical horizontal SI installation with dead-end pulley (Slope Indicator 2010).

datalogger, while the thermistor string sensors were wired to the AM16/32B multiplexer. The multiplexer allowed for data to be collected from all the thermistor string sensors and stored on the data logger through a single communication port.

An SAA232 interface device enabled communication and data collection between the SAA and CR1000 datalogger, as well as provided power connectivity. Power to the ADAS was provided by a bank of four 12V deep-cycle batteries, which were maintained via a 70W solar panel, and a solar charge controller was used to prevent over charging of the batteries.

Instrument cables, as well as the solar panel and battery bank cables, were fed into the weather-proof enclosure through waterproof flexible conduit and then sealed using plumber's

Figure 3.23 Photograph of SI measurement collection (photograph courtesy of M. Darrow).

putty. Silicon desiccant packs were placed inside the weather-proof enclosure to prevent moisture build up and condensation. The desiccant packs were exchanged for fresh packs during each site visit.

The weather-proof enclosure was secured to a 4 in. by 4 in. wooden post. The post was installed by contractors who reported using a propane torch and post hole digger to thaw and dig a hole in the permafrost soil. A metal pipe was secured to the back of the post, onto which was mounted the solar panel and two CS109 sensors with radiation shields. The weather-proof enclosure was used to house the CR1000 datalogger, AM16/32B multiplexer, SAA232 interface device, solar charge controller, and excess cable from the SAA and CS109s (see Figure 3.24). The completed installation, including the battery bank enclosure, wooden post, weather-proof enclosure, solar panel, and CS109 radiation shields is presented in Figure 3.25.

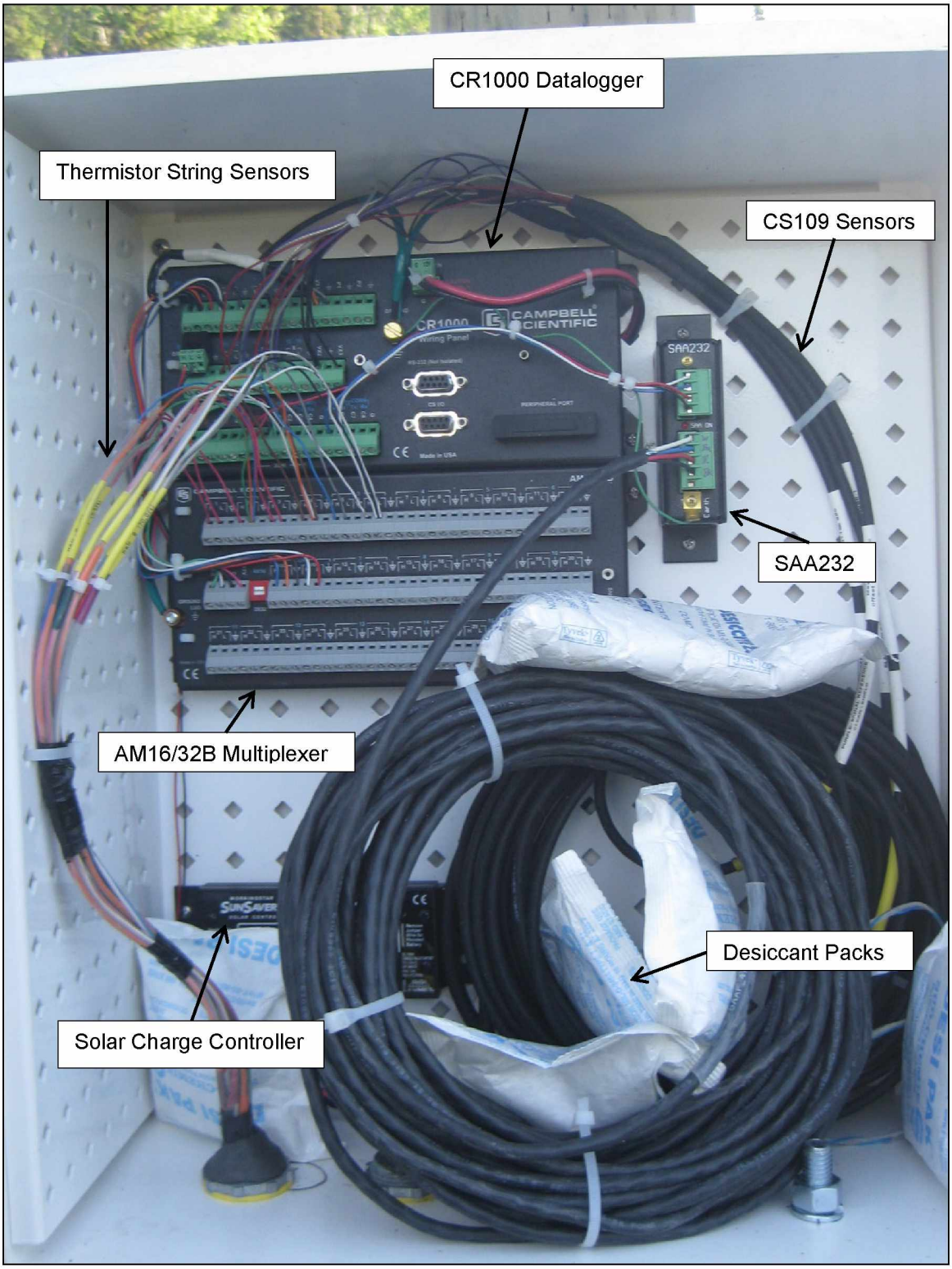

Figure 3.24 ADAS wiring with descriptions (photograph courtesy M. Darrow).

Figure 3.25 Completed ADAS installation (photograph courtesy M. Darrow).

CHAPTER 4 INSTRUMENTATION RESULTS AND ANALYSIS

Data from the geotechnical instrumentation were analyzed to assess temperature change at the base of the embankment and embankment deformation, as well as to compare performance of instruments. Results from the horizontal inclinometer probe and SAA were plotted and compared to check for consistency and instrument drift. Temperature results from the TAC, thermistor string, and SAA also were plotted and compared to check for consistency of measurements, accuracy, and sensor performance. The results from the temperature and deformation monitoring instruments were used to determine: 1) if any embankment settlement had occurred, and if so, 2) if it was the result of thawing permafrost or post-construction settlement.

Data from the CS109 sensors were used to compare ground surface temperatures to air temperatures. The results were used to estimate freezing and thawing *n*-factors, which are critical input parameters for thermal modeling. The results from the air temperature measurements also were compared to historical and concurrent air temperature measurements from a weather station in Chicken to evaluate if temperatures from the station were similar to those at the project site and thus useful for thermal modeling.

4.1 TEMPERATURE SENSORS RESULTS AND ANALYSIS

4.1.1 TAC, Thermistor String, and SAA Performance

Figure 4.1 contains a comparison of the temperature measurements from the TAC, thermistor string, and SAA for Aug. 1, Sep. 1, and Oct. 1, 2012. The data points include whiskers showing each range of accuracy, which are ±0.18°F, ±0.2°F, and ±2.2°F for the TAC, thermistors, and SAA, respectively. For analysis of temperature sensor performance, the thermistor string, widely used in industry, was the standard used to evaluate performance of the relatively new SAA and TAC. The results of the TAC compare favorably with the results of the thermistor string and are generally within the accuracy range of the thermistors, indicating good performance. The SAA also appears to compare favorably to the thermistor string despite its wider range of accuracy; however, it is difficult to make a direct comparison due to the offset of the thermistors and SAA sensor locations.

The measured temperatures from both TAC and thermistor string sensors located at 22, 30, 38, 46, 54, and 70 ft from the casing near end were used for comparison, and are

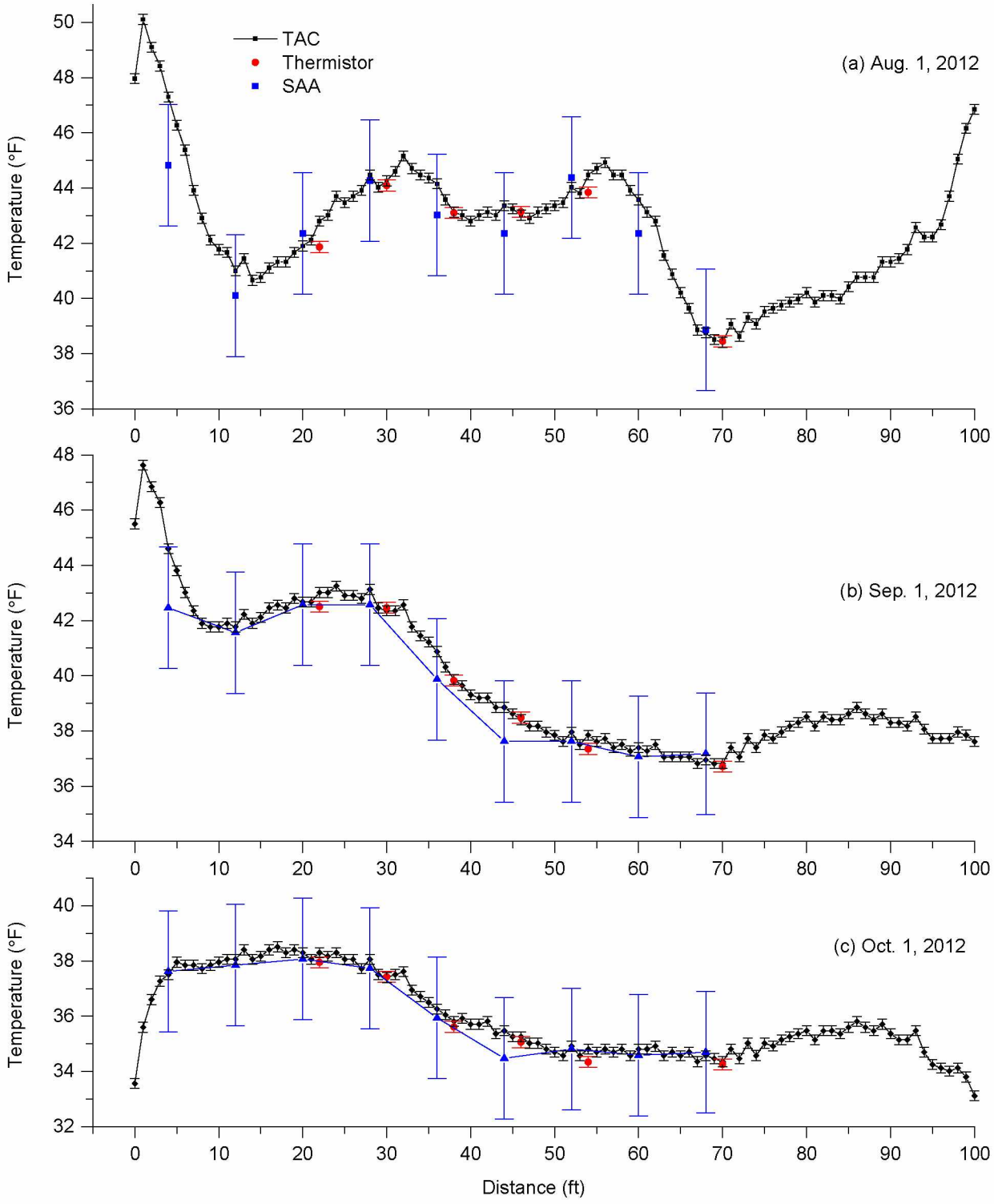

Figure 4.1 Comparison of TAC, thermistor string, and SAA measurements. Whiskers indicate the manufacturers' stated accuracies for the TAC AC (±0.18°F), thermistors beads (±0.2°F), and SAA (±2.2°F). Temperature measurements are given for (a) Aug. 1, 2012, (b) Sep. 1, 2012 and (c) Oct. 1, 2012.

summarized in Table 4.1. The temperatures from the SAA used for comparison are given in Table 4.2. Due to SAA sensor spacing and location from the end of the instrument, the sensors were located at 20, 28, 36, 44, 52, and 68 ft from the casing near end, an offset of approximately 2 ft from the nearest thermistor string sensors.

In order to quantify the performance of the TAC and SAA as compared to the thermistor string, the absolute differences in temperature measurements were calculated for Aug. 1, Sep. 1, and Oct. 1, 2012. Table 4.3 contains the absolute differences between SAA and thermistor string temperature measurements as well as the mean difference and standard deviation for each sensor location. The average difference between measurements from the SAA and thermistor string was 0.36°F with a standard deviation of 0.24°F, which is well within the stated accuracy of ±2.2°F for the SAA temperature sensors.

The differences between TAC and thermistor string temperature measurements as well as mean difference and standard deviation for each selected sensor location is provided in Table 4.4. The mean difference between measurements from the TAC and thermistor string was 0.26°F with a standard deviation of 0.25°F, which is greater than the manufacturer-stated accuracy of ±0.2°F for the thermistor string. Although the mean TAC measurements exceed the manufacturer-stated accuracy of the thermistor string by 0.06°F, the difference is small enough that either device would be suitable for monitoring temperature change depending on the specific needs of a given project.

4.1.2 Analysis of Results from Temperature Sensors

Hourly air temperature measurements from two CS109 sensors were combined and averaged to generate the daily average air temperature at the site. Figure 4.2 is a comparison of

Table 4.1 Thermistor string and TAC temperatures for Aug. 1, Sep. 1, and Oct 1, 2012.

Distance	Thermistor String (°F)			TAC (°F)		
(ft)	Aug. 1	Sep. 1	Oct. 1	Aug. 1	Sep. 1	Oct. 1
22	41.87	42.50	37.95	42.80	43.02	38.30
30	44.09	42.47	37.43	44.26	42.35	37.40
38	43.10	39.83	35.61	43.12	39.87	35.82
46	43.14	38.49	35.07	43.02	38.41	35.26
54	43.84	37.35	34.34	44.47	37.85	34.81
70	38.45	36.71	34.26	38.41	36.82	34.36

Table 4.2 SAA temperatures for Aug. 1, Sep. 1, and Oct. 1, 2012.

Distance (ft)	SAA (°F) Aug. 1	Sep. 1	Oct. 1
20	42.35	42.58	38.08
28	44.26	42.58	37.74
36	43.03	39.88	35.94
44	42.35	37.63	34.48
52	44.38	37.63	34.81
68	38.86	37.18	34.70

Table 4.3 Absolute difference between SAA and thermistor string temperatures for Aug. 1, Sep. 1, and Oct. 1, 2012.

Distance (ft)	SAA Difference (°F) Aug. 1	Sep. 1	Oct. 1	Mean (°F)	Standard Deviation (°F)
20	0.48	0.07	0.12	0.23	0.23
28	0.17	0.11	0.31	0.20	0.10
36	0.08	0.05	0.33	0.15	0.15
44	0.79	0.86	0.59	0.75	0.14
52	0.53	0.27	0.47	0.43	0.14
68	0.41	0.47	0.44	0.44	0.03

Table 4.4 Absolute difference between TAC and thermistor string temperatures for Aug. 1, Sep. 1, and Oct. 1, 2012.

Distance (ft)	TAC Difference (°F) Aug. 1	Sep. 1	Oct. 1	Mean (°F)	Standard Deviation (°F)
22	0.93	0.51	0.35	0.60	0.30
30	0.17	0.12	0.03	0.10	0.07
38	0.02	0.04	0.20	0.09	0.10
46	0.12	0.08	0.19	0.13	0.06
54	0.63	0.50	0.47	0.53	0.09
70	0.04	0.12	0.10	0.09	0.04

the measured daily average air temperature from Jul. 11, 2012 to Jul. 11, 2013 and the historical daily average air temperature from 1981 to 2010. The temperatures measured at the

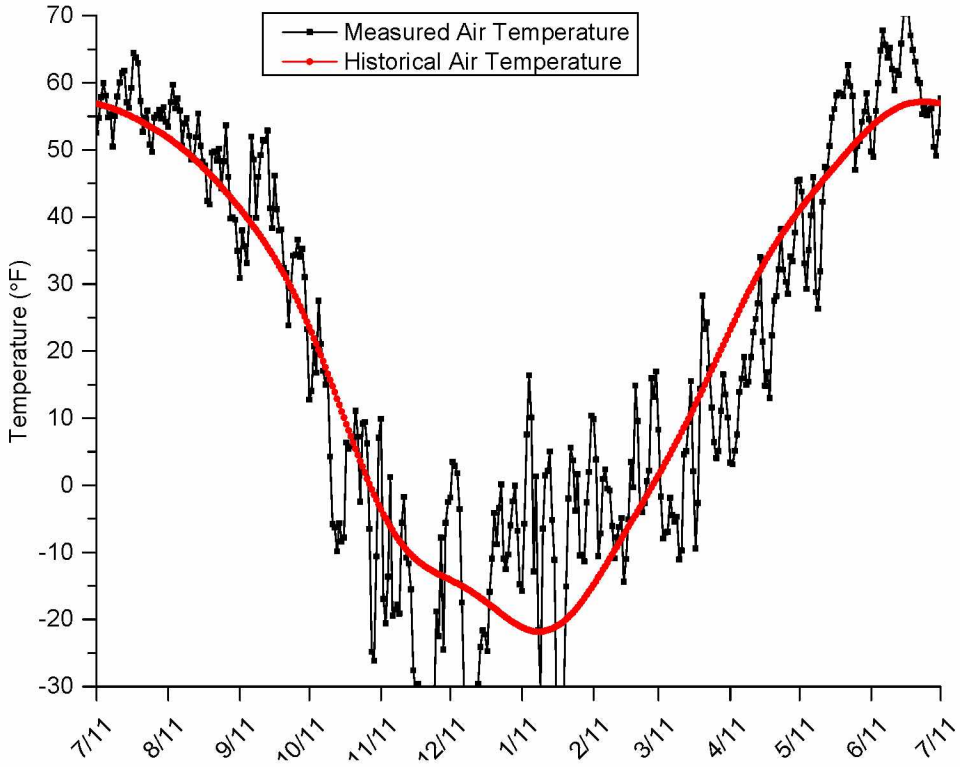

Figure 4.2 Comparison of measured and historical air temperature. Measured temperatures are from Jul. 11, 2012 to Jul. 11, 2013 and historical daily average air temperatures are from 1981 to 2010.

site follow the same general trend as the historical temperatures measured at Chicken; however, it appears that the measured temperatures for January and February 2013 were generally warmer than the historical average.

The measured monthly average ground surface and air temperatures are presented in Figure 4.3. Ground surface temperatures were measured in an undisturbed area, and at the toe and the top of the thermal berm, the latter located near the toe of the ACE. The measured surface temperatures and air temperatures are similar throughout the summer; however, after the first snowfall (approximately Sep. 30), there is a distinct difference between the ground surface temperatures and the air temperature. Figure 4.4 is a two-dimensional contour plot of thermistor string temperatures versus time, and includes data from Jul. 11, 2012 to Jul. 15, 2013. The sensors were located beneath the embankment at 22, 30, 38, 46, 54, 70, and 79 ft as measured from the downhill toe. The temperature measurements were taken hourly and then averaged to calculate the daily average. It is evident from the data that there is a distinct difference in temperatures beneath the thermal berm and the ACE. At the end of data collection period, the temperature profile beneath the ACE was cooler than beneath the thermal berm.

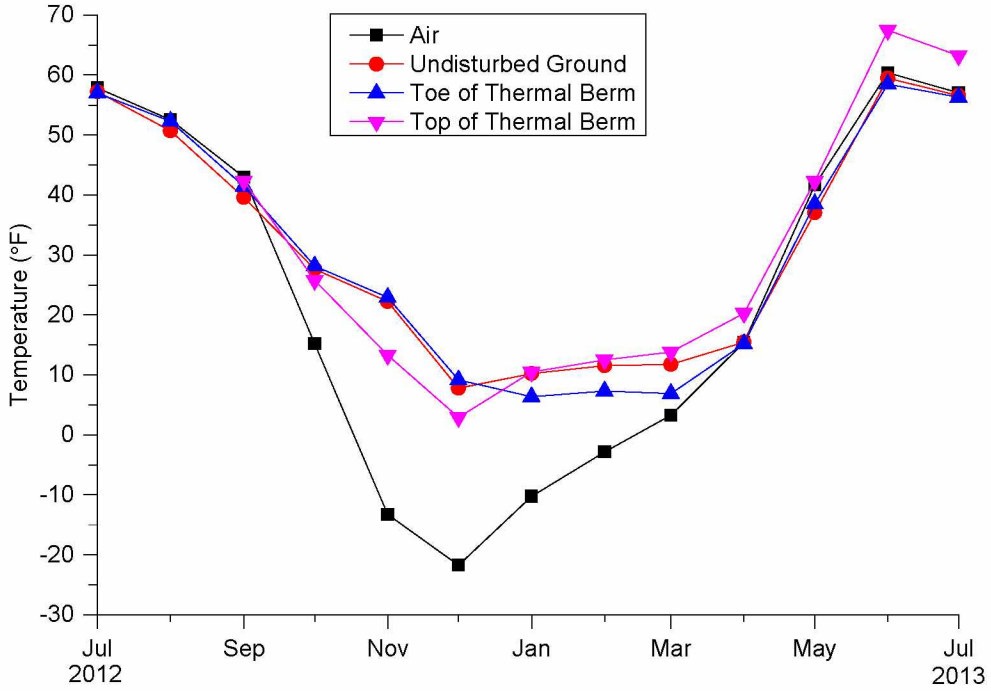

Figure 4.3 Monthly average air and ground surface temperatures.

The temperatures beneath the thermal berm on July 15, 2013 ranged between 36 to 42°F, whereas beneath the ACE the temperature remained between 30 to 32°F.

Figure 4.5, another two-dimensional plot, illustrates the SAA measured temperatures beneath the embankment versus time for the same period. There was a temperature sensor located approximately every 8 ft, from 4 to 68 ft from the downhill embankment toe, which provided greater resolution of temperature measurements than the thermistor string. Temperature was recorded once every 24 hours. The temperature profile is similar to that shown in Figure 4.4; there is a general cooling trend beneath both the thermal berm and the ACE going into winter. During winter, temperatures were coldest beneath the ACE and the toe of the thermal berm, while temperatures remained warmer beneath the center of the thermal berm.

Since the SAA temperature measurements were taken closer to the embankment toe than those recorded by the thermistor string, there was noticeable temperature fluctuation present at the first sensor, located 4 ft from the embankment toe. This sensor likely experienced greater impact from short-term variations in air temperature due to less material covering the casing at this location.

Finally, Figure 4.6 is a two-dimensional plot of the TAC measured temperatures beneath the embankment versus time. The TAC had a temperature sensor located every 1 ft from 0 to

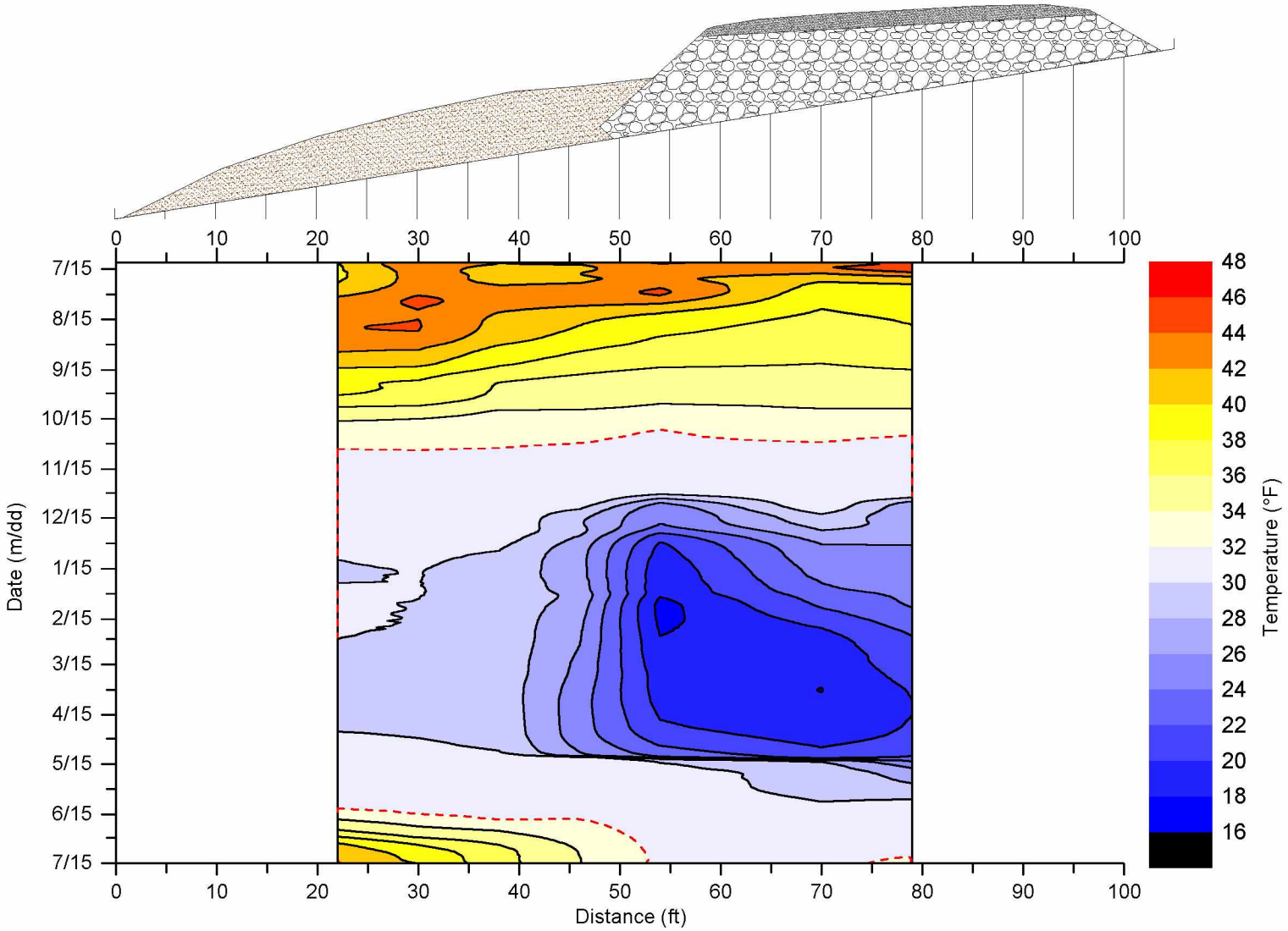

Figure 4.4 Two-dimensional contour plot of thermistor string measured temperatures versus time. Data included is from Jul. 11, 2012 to Jul. 15, 2013.

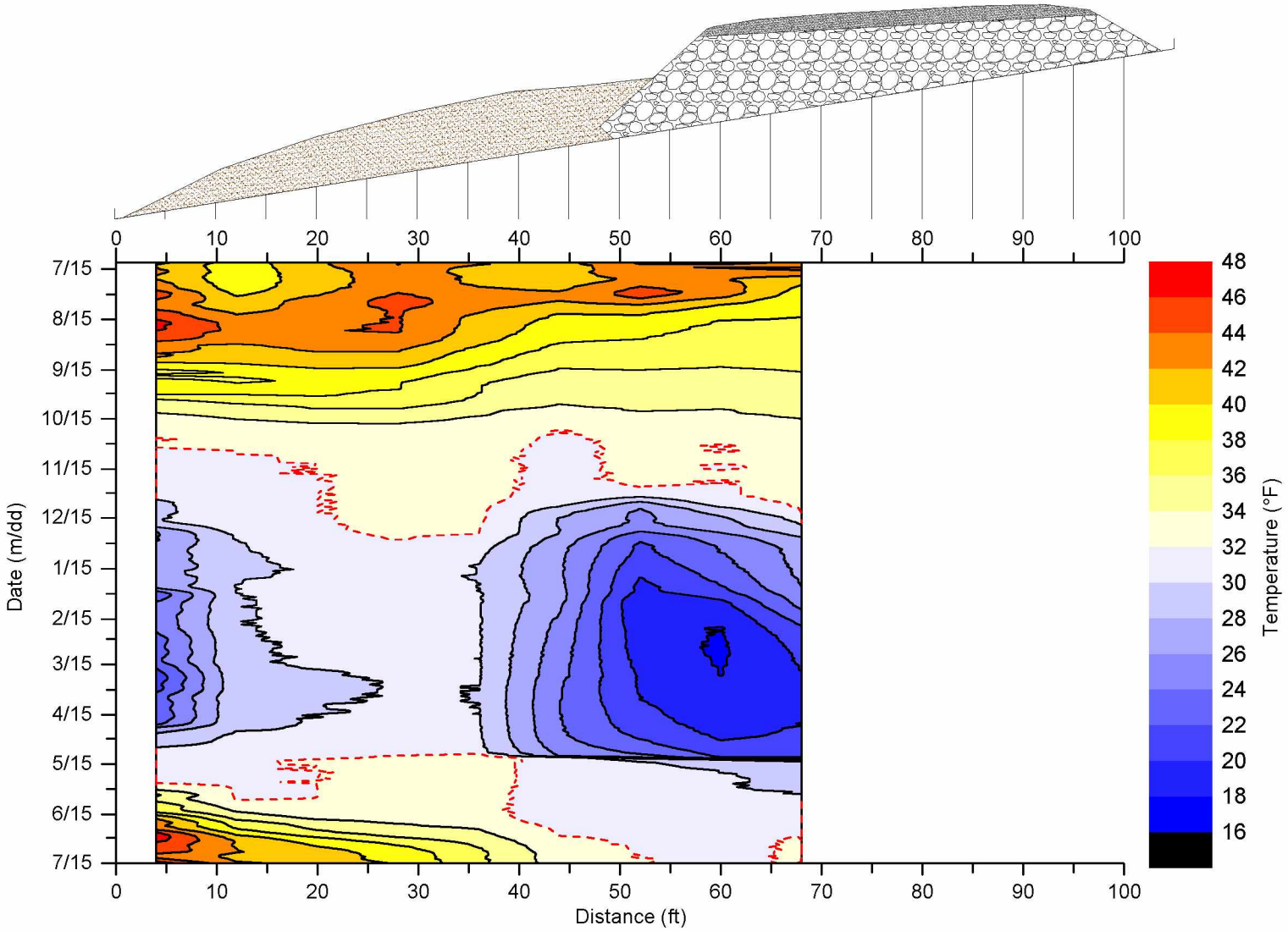

Figure 4.5 Two-dimensional contour plot of SAA measured temperatures versus time. Data included is from Jul. 11, 2012 to Jul. 15, 2013.

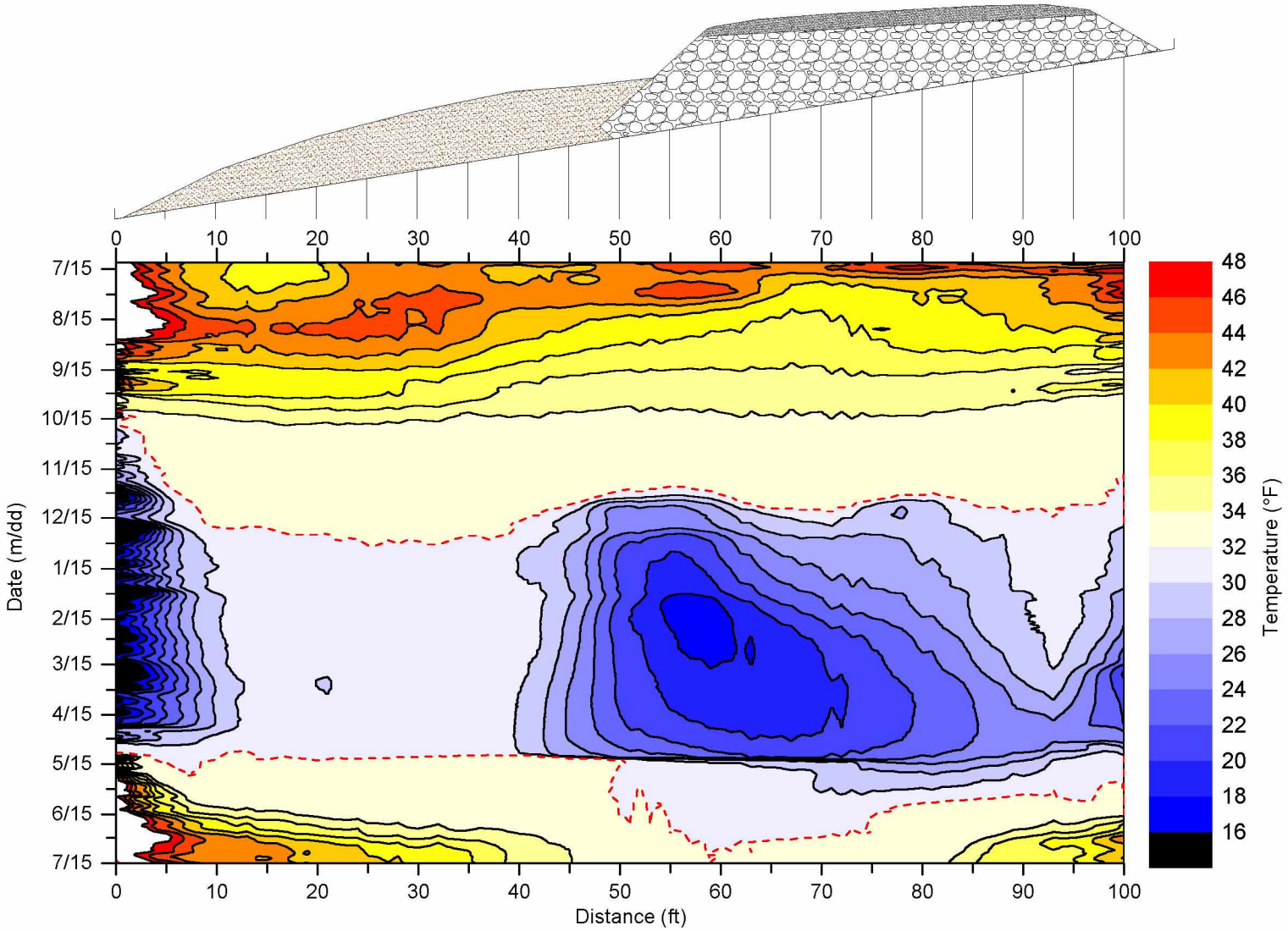

Figure 4.6 Two-dimensional contour plot of TAC measured temperatures versus time. Data included is from Jul. 11, 2012 to Jul. 15, 2013.

100 ft, which provided exceptional temperature resolution. Temperature measurements were recorded every 12 hours. The data demonstrated the same trends shown in Figure 4.4 and Figure 4.5. Over the same period of analysis, there was a greater decrease in temperature beneath the ACE than beneath the thermal berm. Also evident in Figure 4.6 is the large fluctuation in temperature within 5 ft of both embankment toes; again, this is likely due to less material covering the casing near the toe. Thus changes in air temperature have a greater immediate impact on the measured temperature.

The average monthly temperatures beneath the embankment were calculated using the TAC data to show the changes in temperature from month to month. From Oct. 2012 to Mar. 2013, the temperature at the base of the embankment decreased (see Figure 4.7). From Mar. to Jun. 2013 the temperature at the base of the embankment increased (see Figure 4.8) with temperatures above freezing beneath the thermal berm and the uphill toe of the ACE; however, the temperature beneath the center of the ACE remained just below freezing in Jun. 2013.

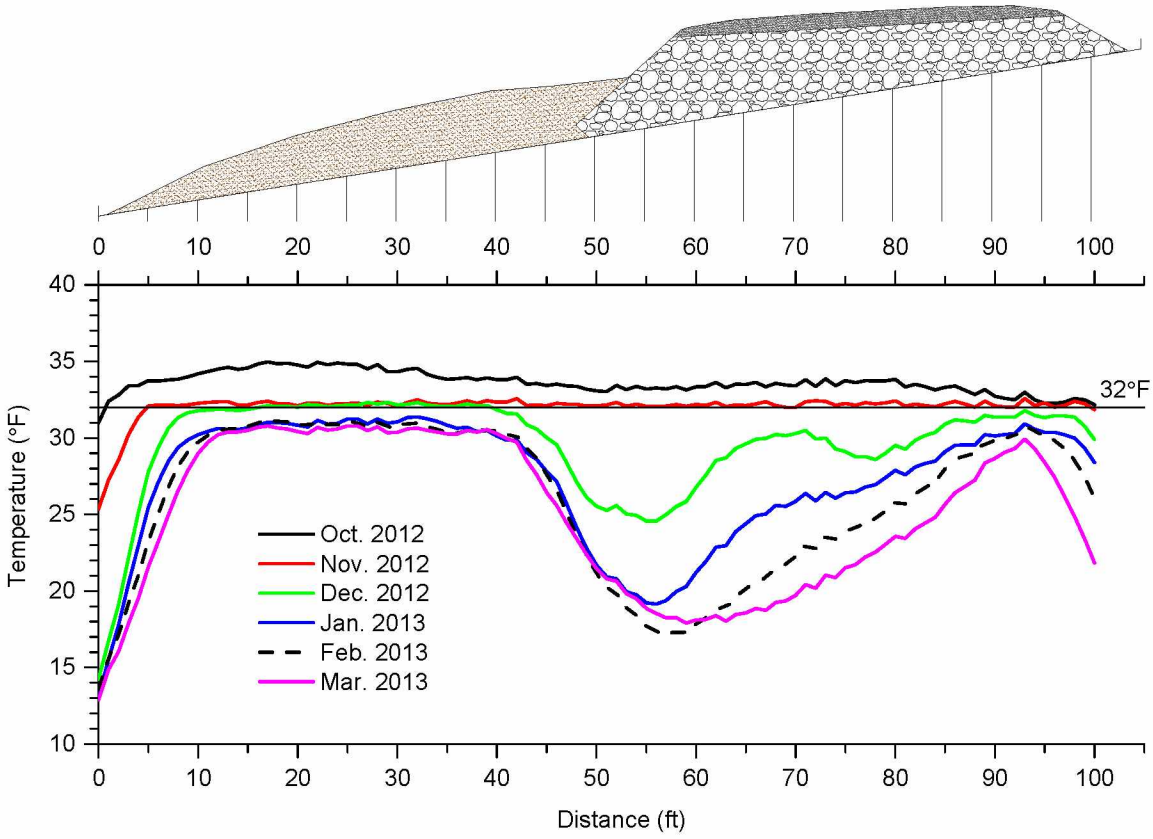

Figure 4.7 Average monthly temperatures at base of embankment from TAC measurements for Oct. 2012 through Mar. 2013.

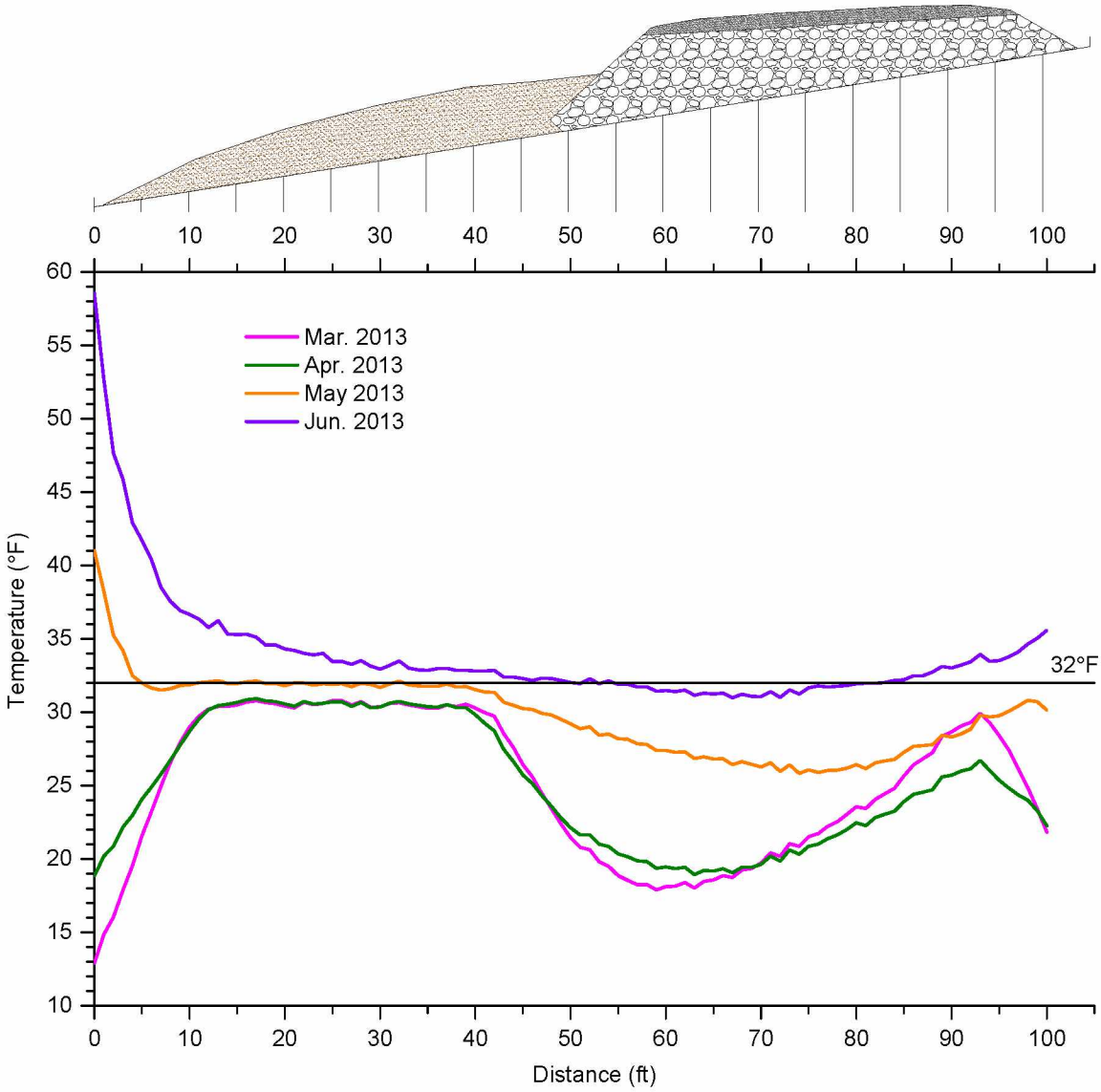

Figure 4.8 Average monthly temperatures at base of embankment from TAC measurements for Mar. 2013 through Jun. 2013.

4.2 DEFORMATION MONITORING

4.2.1 Instrument Performance

The data recorded by the SAA were compared to SI data, with the latter serving at the industry standard. Measurements with the SI were taken biweekly, beginning with the initial measurement on Jul. 10, 2012. A total of six trips were made to the site after the initial reading, with measurements on Jul. 23, Aug. 6, Aug. 20, Sep. 1, Sep. 14, and Oct. 6, 2012. The SAA

data were logged daily from Jul. 10, 2012 to Jul. 15, 2013. The data for both the SI and SAA were analyzed using the near end of the casing (downslope end) as the reference point from which displacement was calculated.

The raw data obtained from each instrument were imported into the relevant software program where the cumulative displacement was automatically calculated. The results were exported in a tabular format and imported into Origin Pro spreadsheet software. The cumulative displacement for the SI and SAA recorded on the same days was plotted; the results are presented in Figure 4.9. Since the SAA did not extend across the entire embankment, data was only available from 0 to 68 ft from the casing end. Regardless, both instruments revealed nearly identical changes in deformation over time for the overlapping measurements.

For comparison of instrument performance, plots of the cumulative displacement measured by each instrument on the same day were created. As presented in Figure 4.10, both instruments demonstrate the same trend in displacement over time; however, it appears that the difference between cumulative displacement recorded by each instrument increases slightly over time.

The differences between the SAA and SI readings were calculated for each day and the maximum, mean, and minimum difference, as well as standard deviation, were determined; the results are provided in Table 4.5. The maximum, mean, minimum, and standard deviation of the differences between SAA and SI readings increase from Jul. 23, to Oct. 6, 2012, confirming the trend illustrated in Figure 4.10.

Field observations of the near end of the casings revealed that there was a slight difference (approximately 0.3 in.) in the amount of settlement between the SAA and SI casings. To correct for this difference, the data from Aug. 6, 2012 to Oct. 10, 2012 were adjusted by manually adding the estimated amount of differential settlement to all the SAA data points. Values of 0.05, 0.10, 0.20, 0.25, and 0.30 in. were added to SAA measurements from Aug. 6, Aug. 20, Sep. 1, Sep. 14, and Oct. 6, respectively. Figure 4.11 shows the SI and SAA comparison with adjustments applied to the SAA measurements. The adjusted SAA data corresponds better to the SI data, although differences still exist.

The differences between the adjusted SAA and SI readings were calculated for each day and the maximum, mean, and minimum differences, as well as standard deviation were determined; the results are provided in Table 4.6. The maximum and minimum of the differences between adjusted SAA and SI readings still increase from Jul. 23, to Oct. 6, 2012; however, the mean differences between readings are less than the uncorrected values in

Table 4.5. The standard deviation of the differences between measurements remains the same since a constant value was added to all the SAA readings on each day.

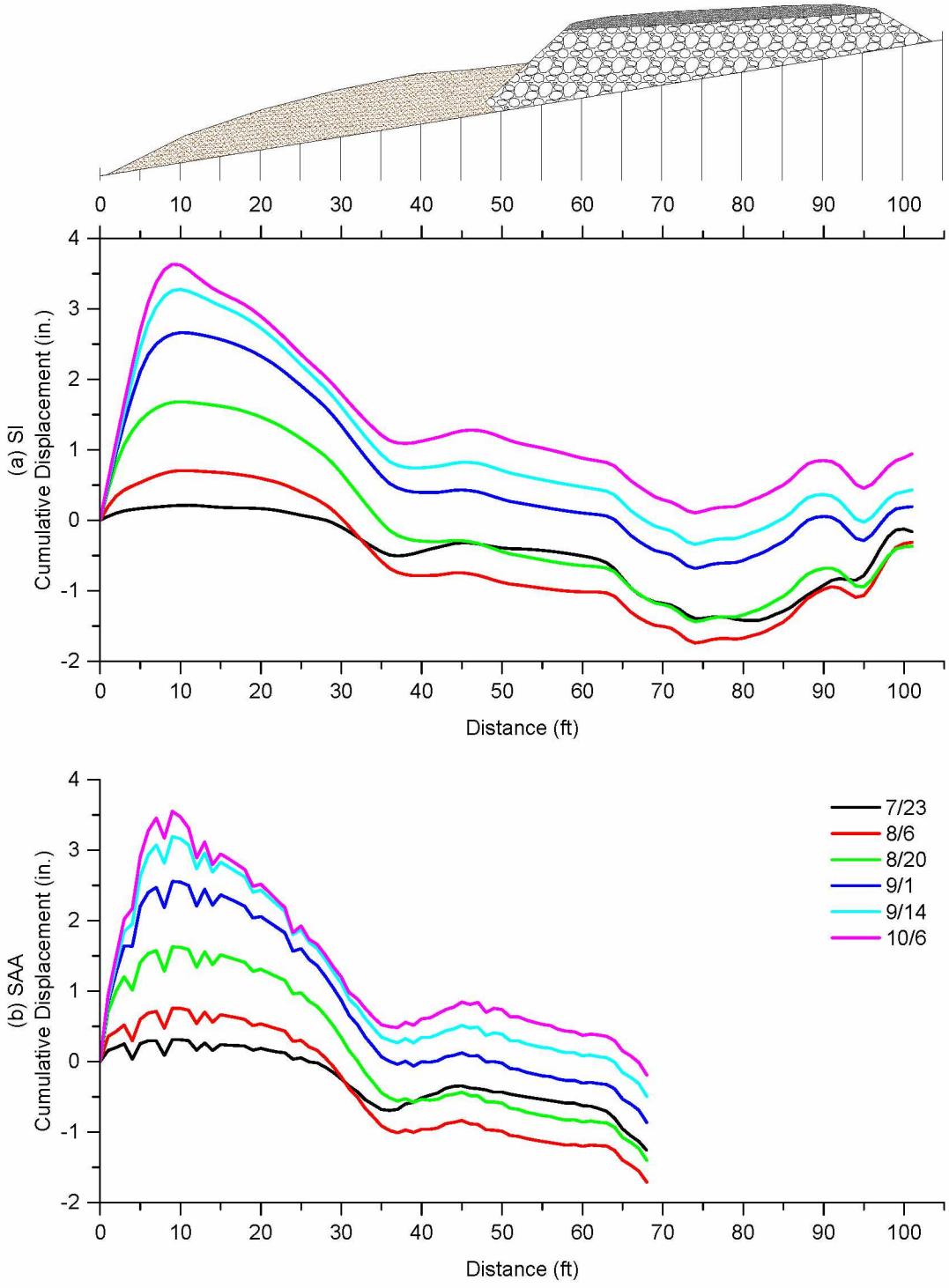

Figure 4.9 SI and SAA cumulative displacement over time, using raw data from 2012 referenced to the near end of the casing for (a) SI and (b) SAA.

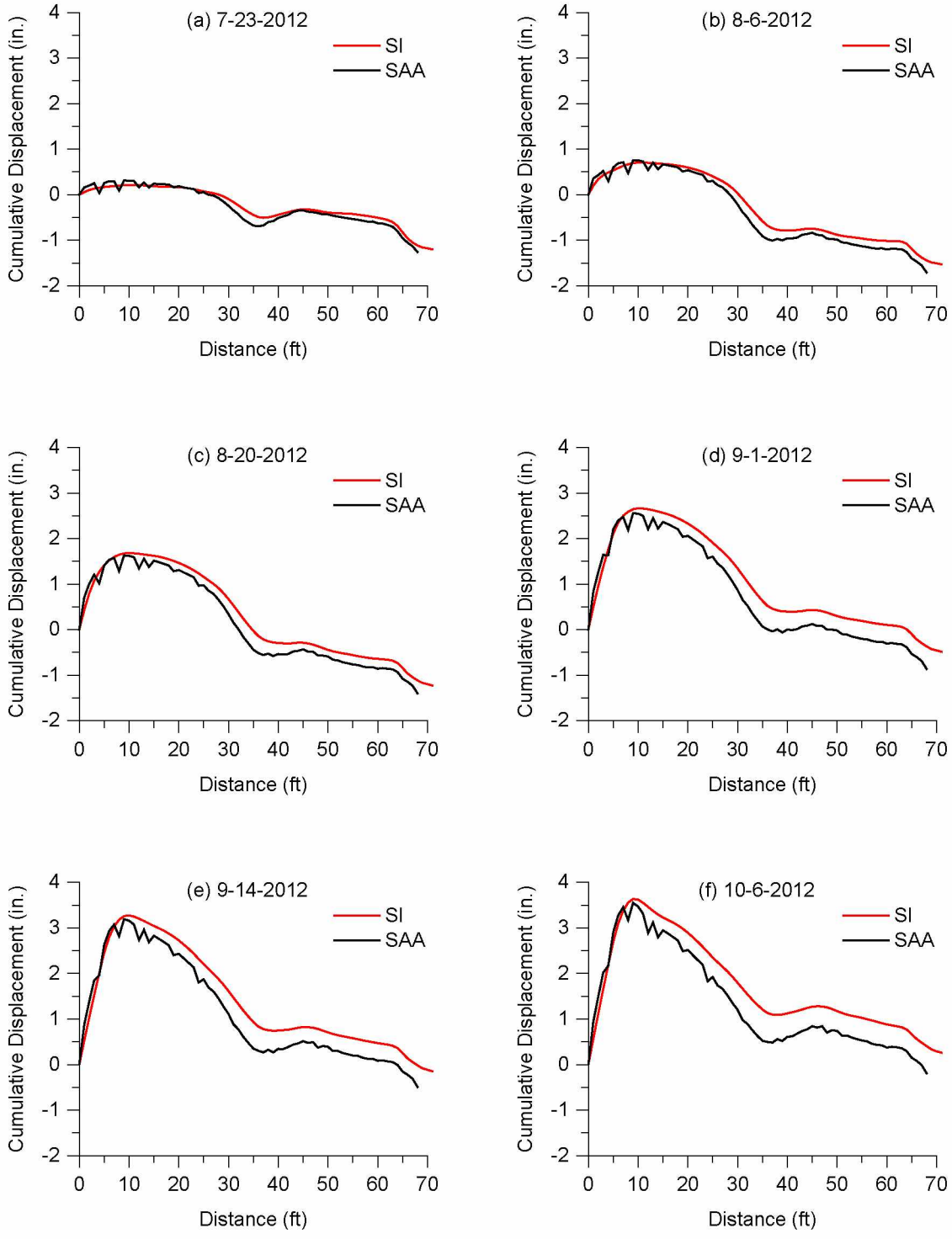

Figure 4.10 Comparison of SI and SAA results using raw data; for (a) Jul. 23, 2012, (b) Aug. 6, 2012, (c) Aug. 20, 2012, (d) Sep. 1, 2012, (e) Sep. 14, 2012, and (f) Oct. 6, 2012.

Table 4.5 Comparison of SAA and SI readings.

Date	Jul. 23, 2012	Aug. 6, 2012	Aug. 20, 2012	Sep. 1, 2012	Sep. 14, 2012	Oct. 6, 2012
Maximum (in.)	0.12	0.16	0.28	0.34	0.35	0.38
Mean (in.)	-0.05	-0.13	-0.19	-0.31	-0.31	-0.40
Minimum (in.)	-0.23	-0.33	-0.41	-0.56	-0.58	-0.69
Standard Deviation (in.)	0.09	0.11	0.13	0.19	0.21	0.25

4.2.2 Analysis of Results

For analysis of embankment settlement, all measurements from the SAA and SI were referenced to the casing near end of the embankment. During data processing, it was assumed that the casing end was fixed and no movement occurred at that point; however, field observations indicated that settlement had occurred at the casing ends. Analysis of the cumulative displacement measured by the instruments (see Figure 4.9) confirmed that settlement of the casing near end was occurring, because relative to the casing end, the entire embankment appeared to be moving upward over time, which was not possible. To properly correct for this error, a survey of the near end elevation should have been conducted each time deformation was measured. Then the amount of casing end settlement would have been added to the entire data set.

Since no survey data were available to correct for daily movement of the casing ends, the data were corrected mathematically using logical assumptions, deformation trends, and temperature trends in order to ascertain a best estimate of the actual settlement. The SAA data were used for the analysis since there was a full year of daily-recorded data. Temperature data was taken from the TAC since it provided the highest temperature resolution across the base of the embankment. For the analysis the following two assumptions were made:

1) No part of the embankment experienced downward movement (i.e., thaw settlement or consolidation) if the foundation soil was frozen.
2) No part of the embankment experienced upward movement (i.e., frost heave) if the foundation soil was unfrozen.

First, the raw data for the first day of each month were examined to predict the types of movement that occurred based on the deformation and temperature trends. From Aug. 1 to Oct. 1, 2012 the embankment appeared to be moving upward relative to the casing end while the

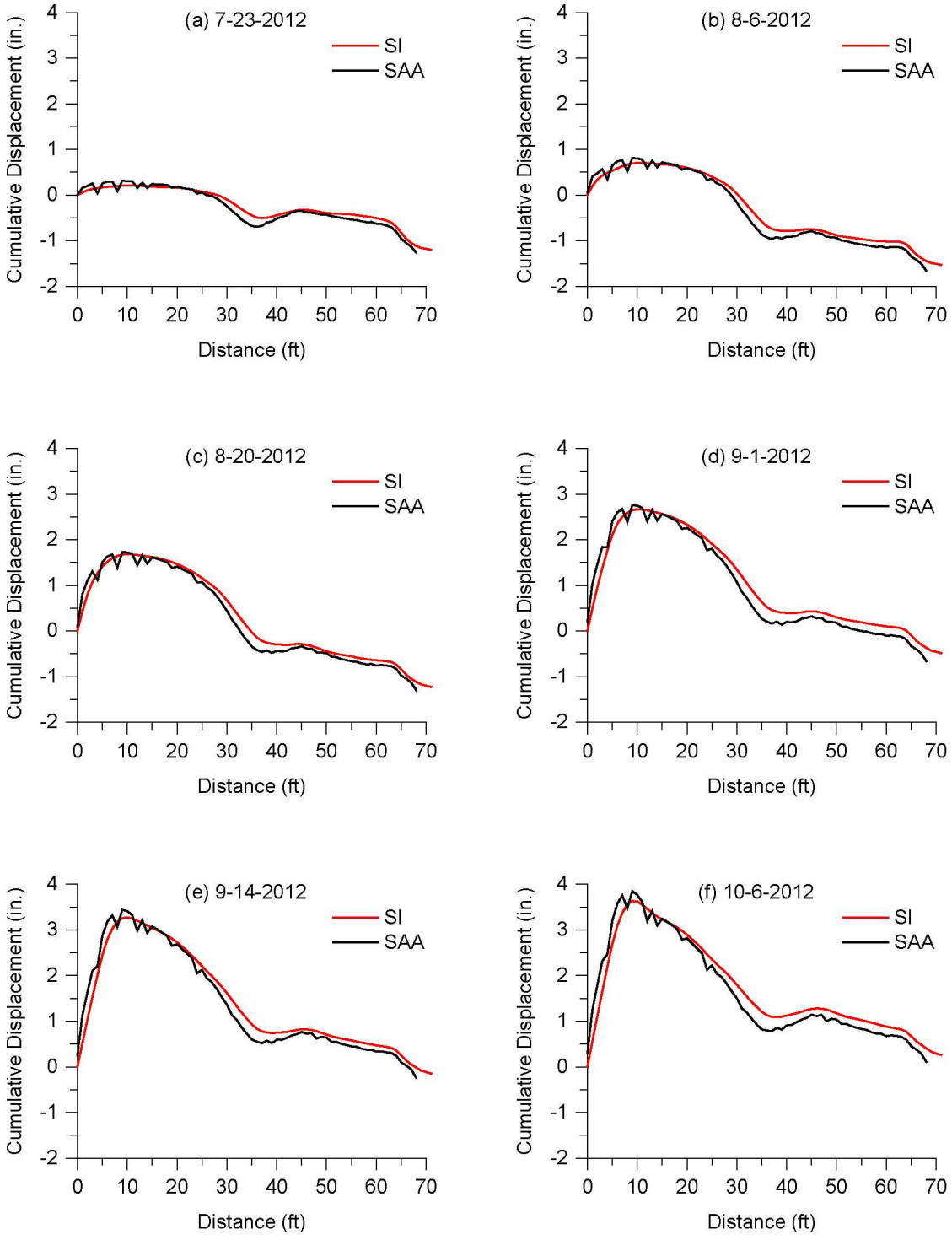

Figure 4.11 Comparison of adjusted SI and SAA results; for (a) Jul. 23, 2012, (b) Aug. 6, 2012, (c) Aug. 20, 2012, (d) Sep. 1, 2012, (e) Sep. 14, 2012, (f) and Oct. 6, 2012.

Table 4.6 Comparison of adjusted SAA and SI readings.

Date	Jul. 23, 2012	Aug. 6, 2012	Aug. 20, 2012	Sep. 1, 2012	Sep. 14, 2012	Oct. 6, 2012
Maximum (in.)	0.12	0.21	0.38	0.54	0.60	0.68
Mean (in.)	-0.05	-0.08	-0.09	-0.11	-0.06	-0.10
Minimum (in.)	-0.23	-0.28	-0.31	-0.36	-0.33	-0.39
Standard Deviation (in.)	0.09	0.11	0.13	0.19	0.21	0.25

temperatures at the base of the embankment were above freezing (see Figure 4.12). This movement trend is not possible given the established assumptions; therefore, the casing end must have moved downward relative to the rest of the embankment, making it appear as though the embankment were moving upward. Most likely, thaw settlement occurred at the embankment toe due to relatively high temperatures between Aug. 1 and Sep. 1, 2012.

From Oct. 1, 2012 to Jan. 1, 2013 the embankment deformation trend changed; the embankment appeared to move downward relative to the casing end (see Figure 4.13). Settlement at this time of year is counterintuitive since the temperatures across the base of the embankment were at or below freezing by Nov. 1. If settlement did not actually occur, then the casing end must have experienced upward movement. It is hypothesized that frost heaving occurred at the embankment toe from Oct. 1, 2012 to Jan. 1, 2013, moving the casing end upward and creating the appearance of embankment settlement. Temperature data supports this hypothesis and the change in embankment deformation trend coincides exactly with the appearance of freezing temperatures at the embankment toe.

From Jan. 1 to May 1, 2013 temperatures across the base of the embankment were all below freezing and embankment deformation appeared to cease (see Figure 4.14). This suggests that during this time period frost heave no longer occurred at the embankment toe and the foundation soil beneath the embankment was frozen, resulting in little to no embankment movement.

Finally, from May 1 to Jul. 1, 2013 the embankment appeared to move upward again (see Figure 4.15), which coincided exactly with the recurrence of above-freezing temperatures at the toe of the embankment. Since temperatures across much of the base of the embankment were at or below freezing from May 1 to Jun. 1, 2013, and the embankment had been stable from Jan. 1 to May 1, 2013, there is no logical reason why it would begin to move upward.

Instead, thaw settlement most likely occurred again at the toe of the embankment beneath the casing end, thus generating the appearance of upward movement relative to the casing end.

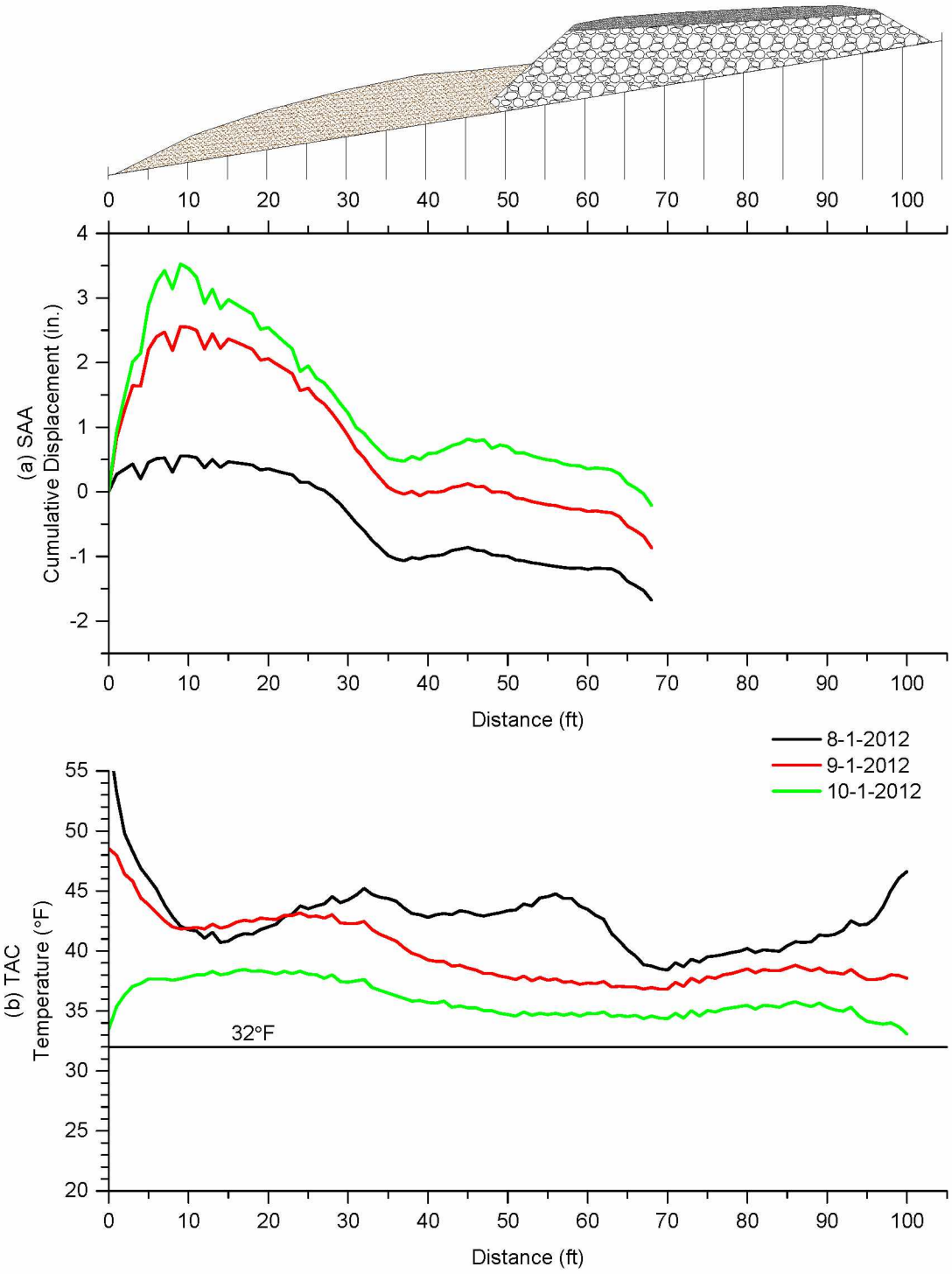

Figure 4.12 Monthly (a) SAA and (b) TAC measurements from Aug. 1 to Oct. 1, 2012.

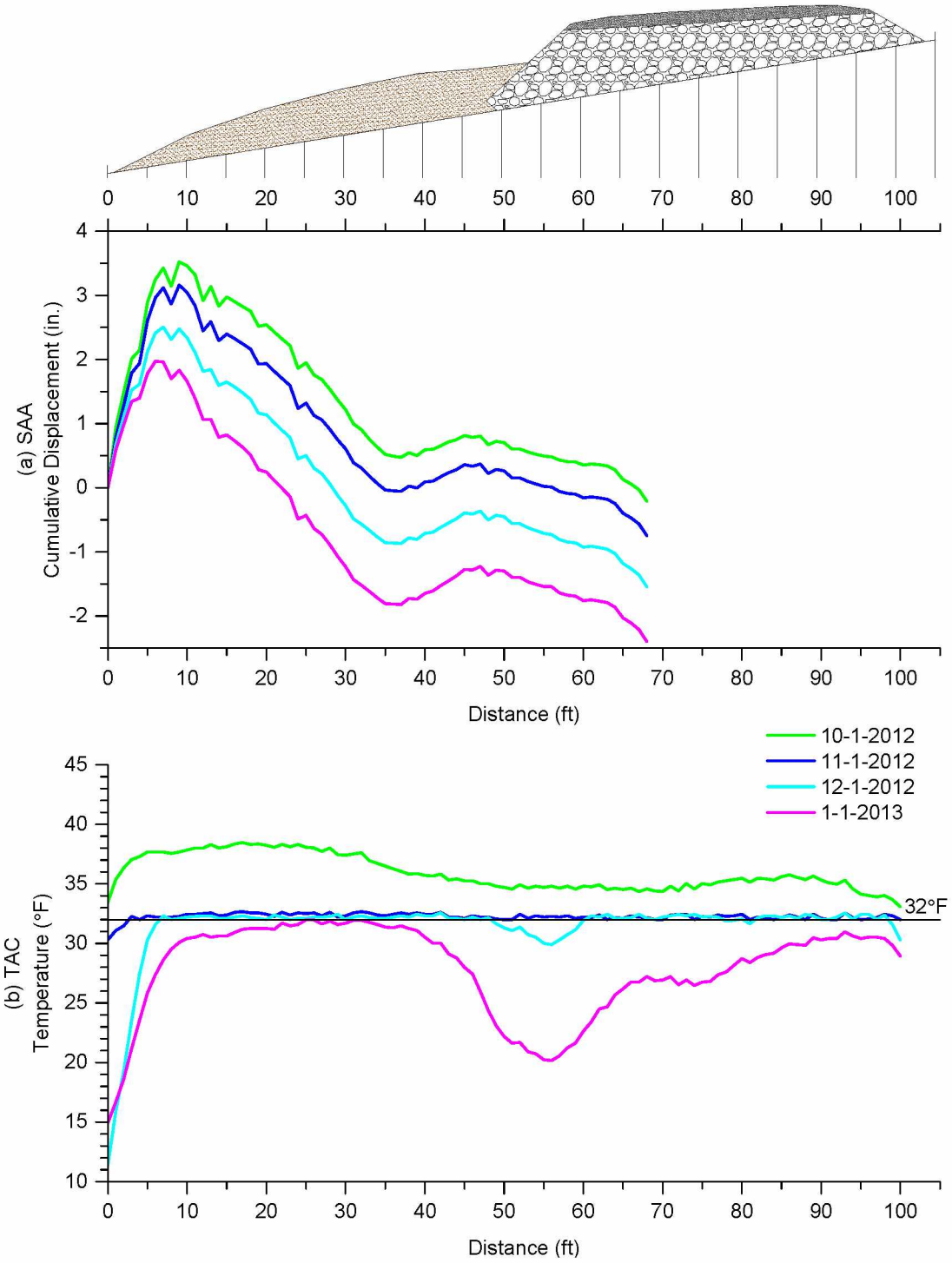

Figure 4.13 Monthly (a) SAA and (b) TAC measurements from Oct. 1, 2012 to Jan. 1, 2013.

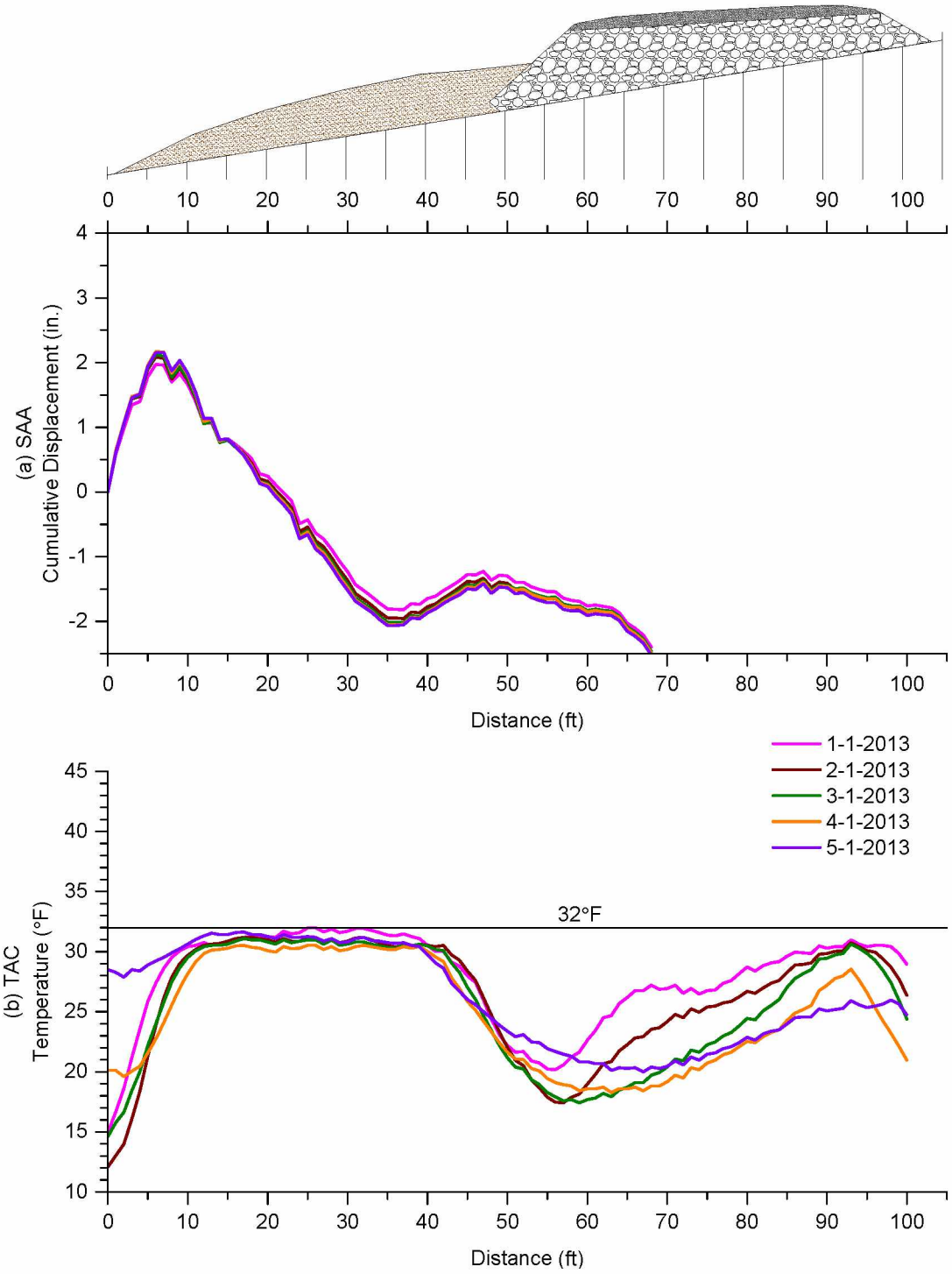

Figure 4.14 Monthly (a) SAA and (b) TAC measurements from Jan. 1 to May 1, 2013.

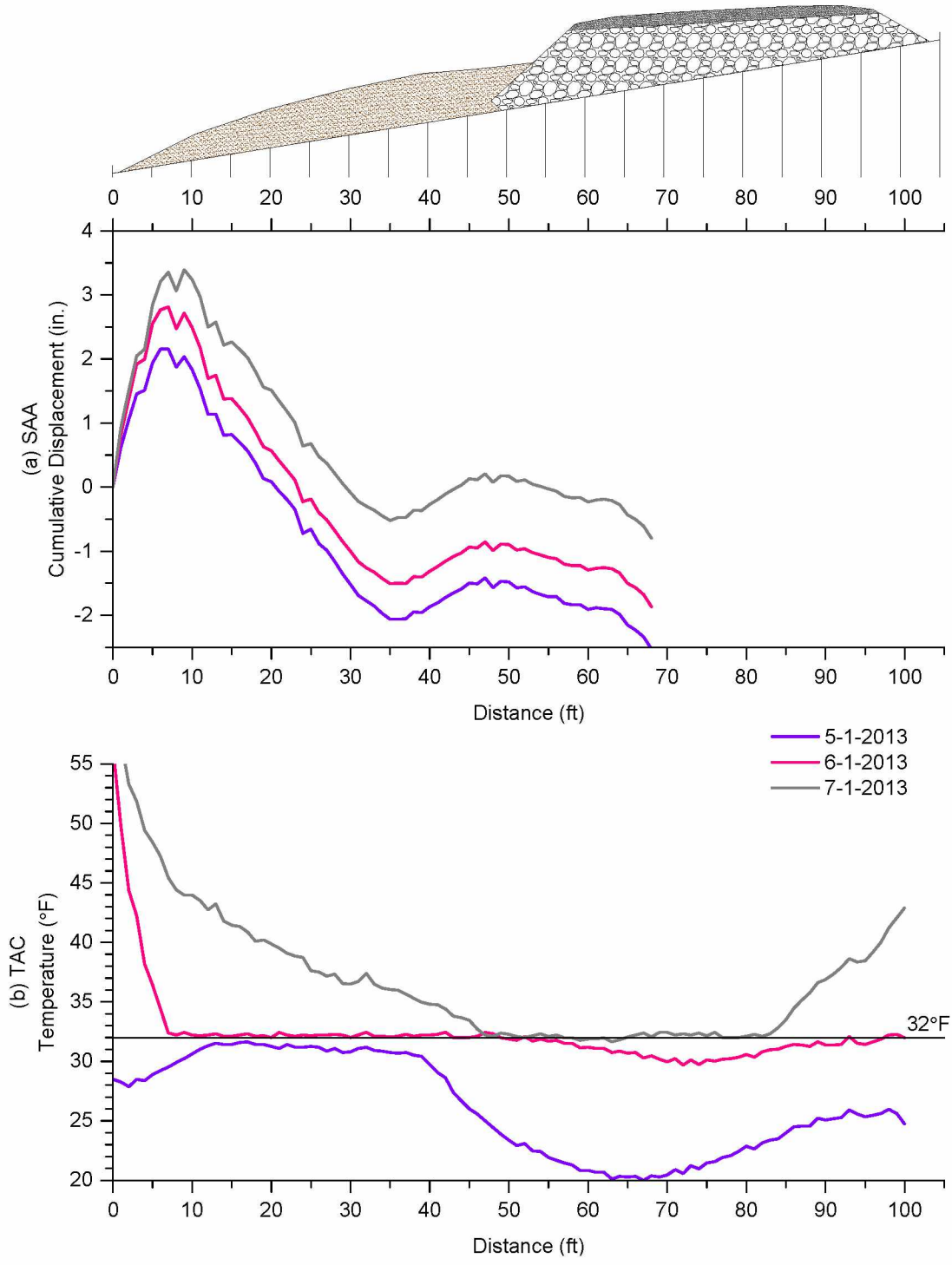

Figure 4.15 Monthly (a) SAA and (b) TAC measurements from May 1 to Jul. 1, 2013.

A plot of SAA cumulative displacement versus time for select distances from the casing end is provided in Figure 4.16. At the casing end (0 ft) there is no movement shown since it is the reference end and is assumed by the SAA software to be fixed. At 10, 15, 20, and 25 ft from the casing end, nearly identical deformation trends are exhibited. From July 10 to approximately Oct. 1, 2012 the cumulative displacement increases, indicative of thaw settlement at the embankment toe. From approximately Oct. 1, 2012 to Jan. 1, 2013 the cumulative displacement decreases, indicative of heave at the embankment toe; however, at 50 ft the cumulative displacement decreases before increasing, which is likely due to the placement of embankment fill during this time. From approximately Jan. 1 to May 8, 2013 there is little change in cumulative displacement, indicative of frozen foundation soil. Finally, from approximately May 8 to Jul. 1, 2013 the cumulative displacement again increases, indicative of continued thaw settlement at the embankment toe.

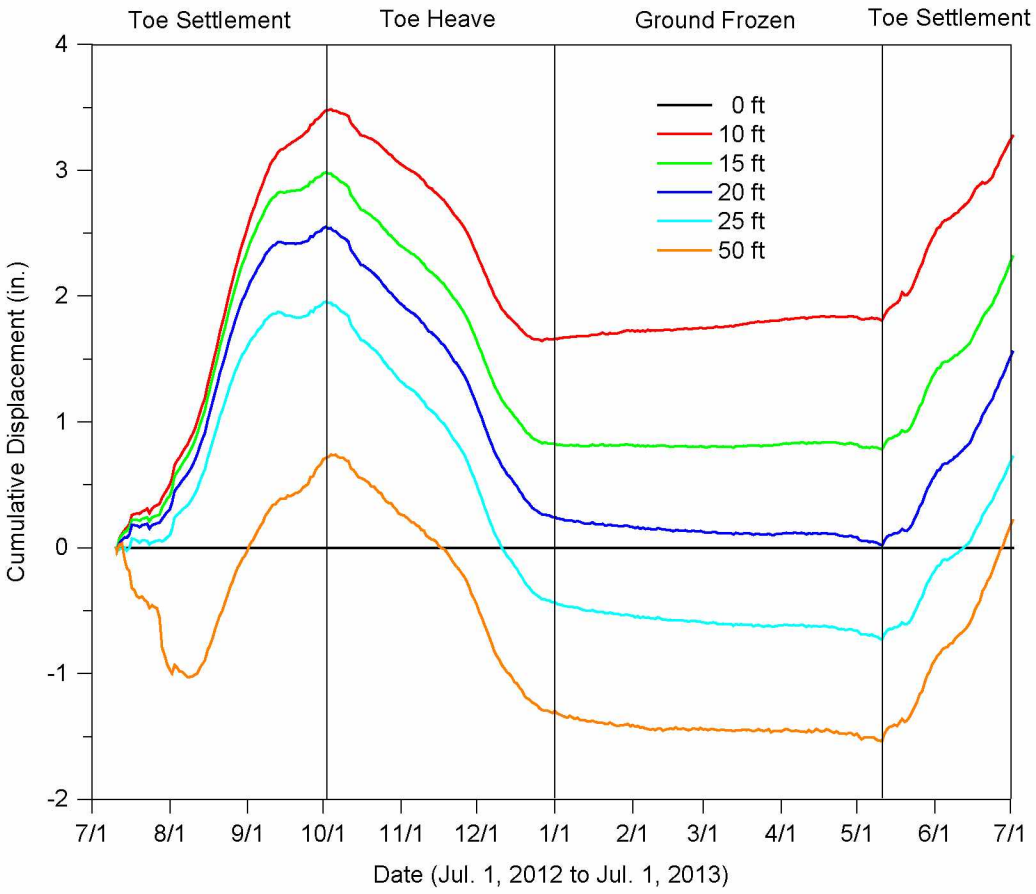

Figure 4.16 SAA cumulative displacement versus time for select distances from thermal berm toe.

To correct the data, it was first necessary to calculate the daily incremental displacement along the casing for all measurements. The daily incremental displacement was calculated from the difference in daily cumulative displacements using:

$$dY_{X(t)} = Y_{X(t)} - Y_{X(t-1)} \quad (4.1)$$

where $dY_{X(t)}$ is incremental displacement for distance X from the casing end at time t, Y is cumulative displacement (in.), X is distance from the casing end (ft), and t is time (days).

Since it is hypothesized that the casing end was moving downward relative to the rest of the embankment from Jul. 10 to Oct. 1, 2012, any positive incremental displacements during this time represented downward movement. The maximum positive incremental displacement for each day represents the point along the casing that moved downward the least relative to the casing end.

To correct for thaw settlement at the casing end from Jul. 10 to Oct. 10, 2012, the daily incremental displacement was added to the corrected cumulative displacement from the previous day and the maximum positive daily incremental displacement was subtracted as follows:

$$Y'_{X(t)} = Y'_{X(t-1)} + dY_{X(t)} - MAX\left(dY_{(t)}\right) \quad (4.2)$$

where $Y'_{X(t)}$ is the corrected cumulative displacement (in.) for X distance from the casing end at time t, and $MAX\left(dY_{(t)}\right)$ is the maximum positive incremental displacement along the casing at time t. Subtracting the maximum positive daily incremental displacement effectively results in the daily incremental displacements being referenced to the point that moved downward the least on each day. The corrected cumulative displacement for thaw settlement from Aug. 1 to Oct. 1, 2012 is presented in Figure 4.17. The results suggest that the entire embankment experienced settlement, with the least amount of settlement at approximately 10 ft from the casing near end. The minimum settlement at 10 ft is likely due to the fact that this portion of the thermal berm was constructed in the fall of the previous year (see Figure 3.1) and already experienced post-construction settlement prior to instrument installation and completion of embankment construction.

To correct for the assumed frost heaving from Oct. 10 to Dec. 22, 2012, the daily incremental displacement at 68 ft was subtracted from the daily cumulative displacement:

$$Y'_{X(t)} = Y'_{X(t-1)} + dY_{X(t)} - dY_{68(t)} \quad (4.3)$$

thus referencing the daily incremental displacements to the end of the instruments at 68 ft. It was assumed that the settlement at this location was complete by Oct. 10, 2012 and the

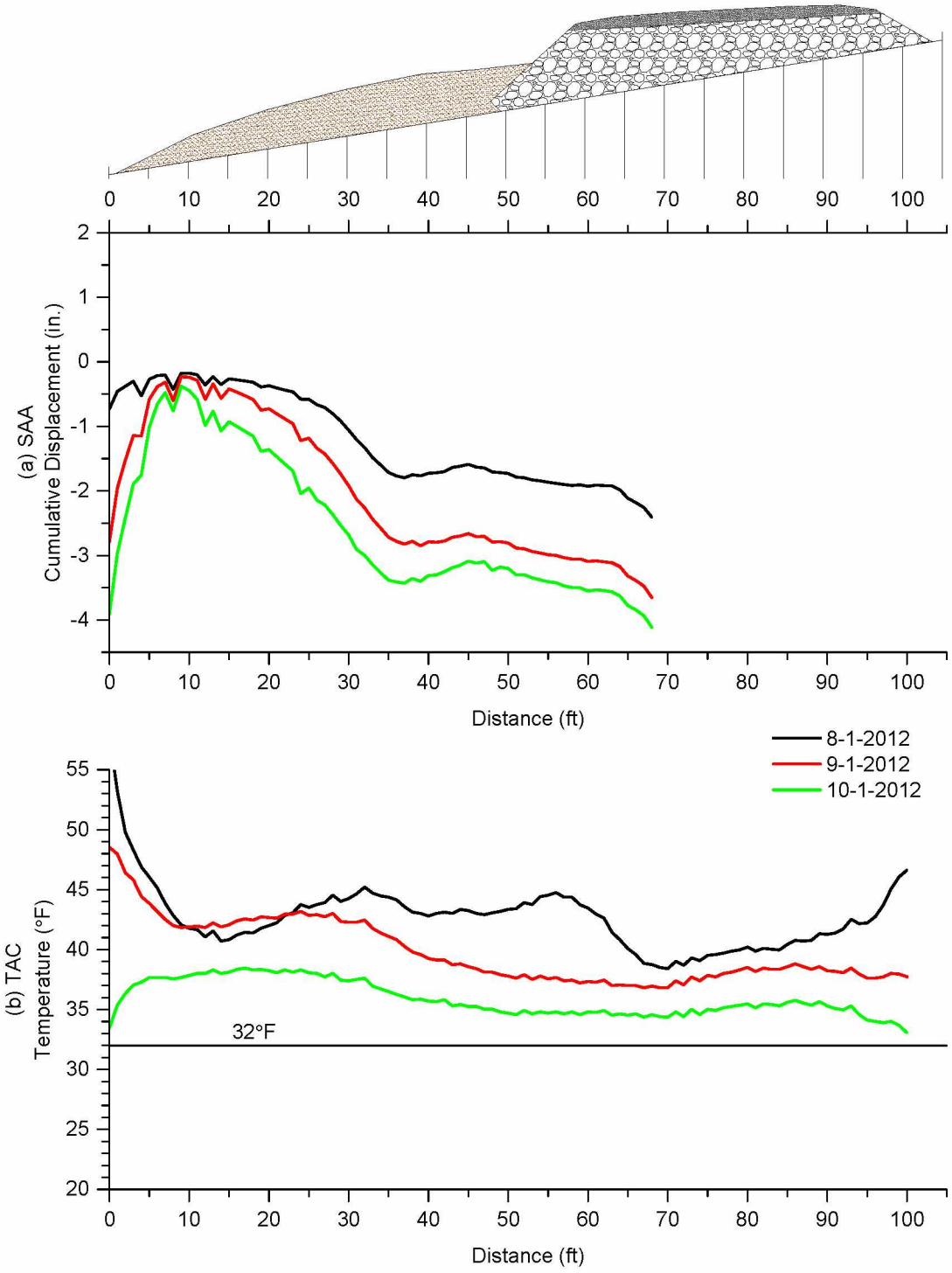

Figure 4.17 Corrected monthly (a) SAA and (b) TAC measurements from Aug. 1 to Oct. 1, 2012.

underlying soil was frozen by Dec. 23, 2012. The corrected cumulative displacement from Oct. 1, 2012 to Jan. 1, 2013 is presented in Figure 4.18.

Since temperatures beneath the embankment at 68 ft did not rise above freezing from Dec. 23, 2012 to Jul. 15, 2013, it is assumed that no movement occurred at this location; hence Equation 4.2 was used to correct the cumulative displacement for this time period. The corrected cumulative displacement for Jan. 1 to May 1, 2013 is presented in Figure 4.19; during this time little to no deformation occurred since the foundation soil was frozen. Finally, the corrected cumulative displacement for May 1 to Jul. 1, 2013 is presented in Figure 4.20. During this time settlement again occurred at the embankment toe, coinciding with the rise in temperature at this location.

A plot of corrected SAA cumulative displacement versus time for select distances from the casing near end is provided in Figure 4.21. At the casing end (0 ft) there is settlement from July to October 2012, after which there is heave from October to the end of December 2012. From January to May 2013, the toe remains relatively stable, while the embankment at 10 ft appears to continue heaving at a steady rate until approximately mid-April, 2013. The prolonged heaving at 10 ft may be the result of a greater depth of thawed foundation soil due to placement of fill in 2011 (see Figure 3.1). The insulating effect of the thermal berm during winter also could slow the rate of heave, prolonging it into spring.

From May to July 2013 the embankment toe again experiences settlement. Beneath the ACE at 50 ft there is settlement from July to October 2012, likely due to post-construction settlement after placement of fill. After October 2012 the ACE at 50 ft appears to remain relatively stable, even into July 2013. It should be noted that these settlement and heave values are only approximate due to the assumptions made and lack of survey data.

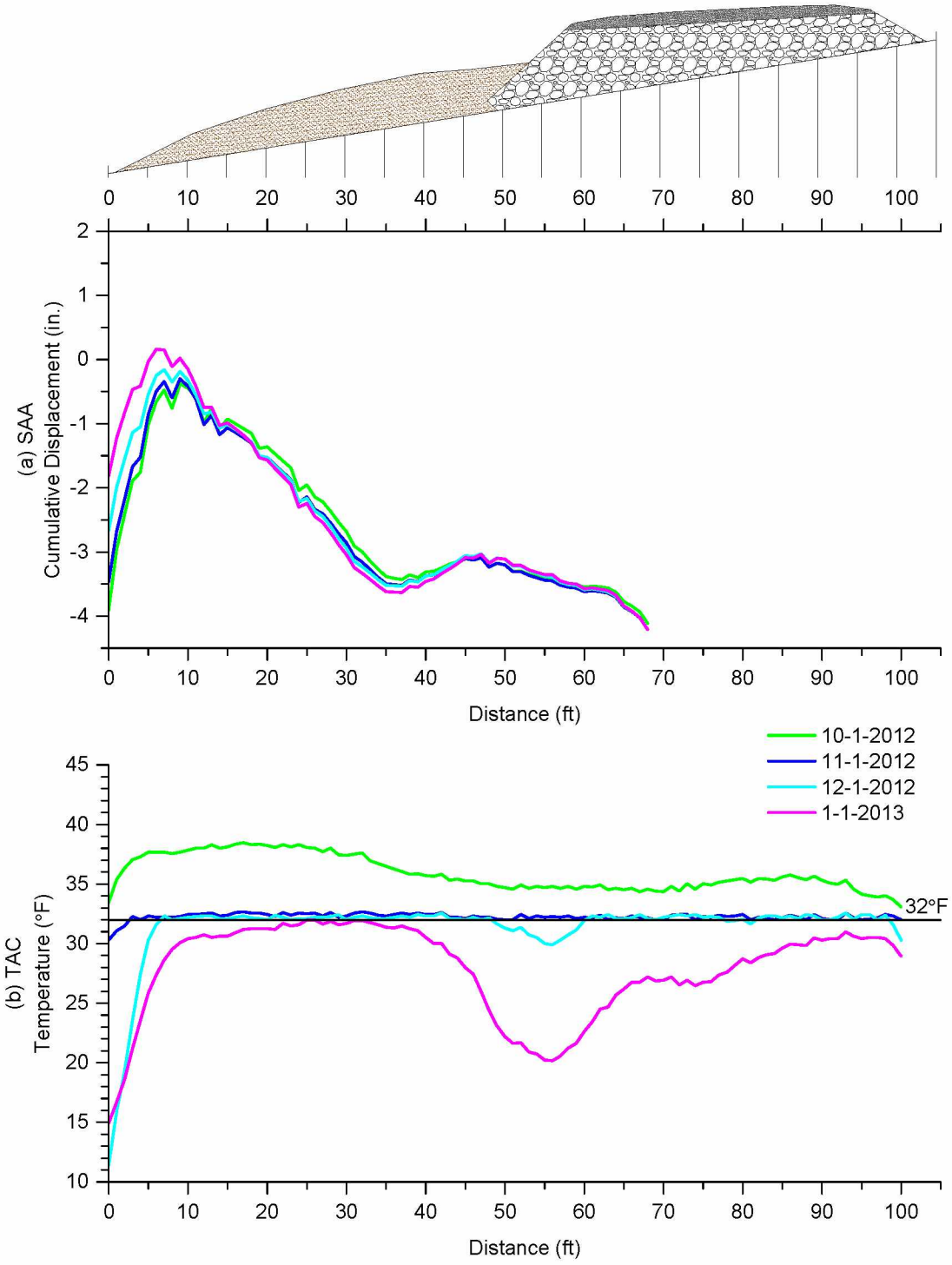

Figure 4.18 Corrected monthly (a) SAA and (b) TAC measurements from Oct. 1 to Jan. 1, 2013.

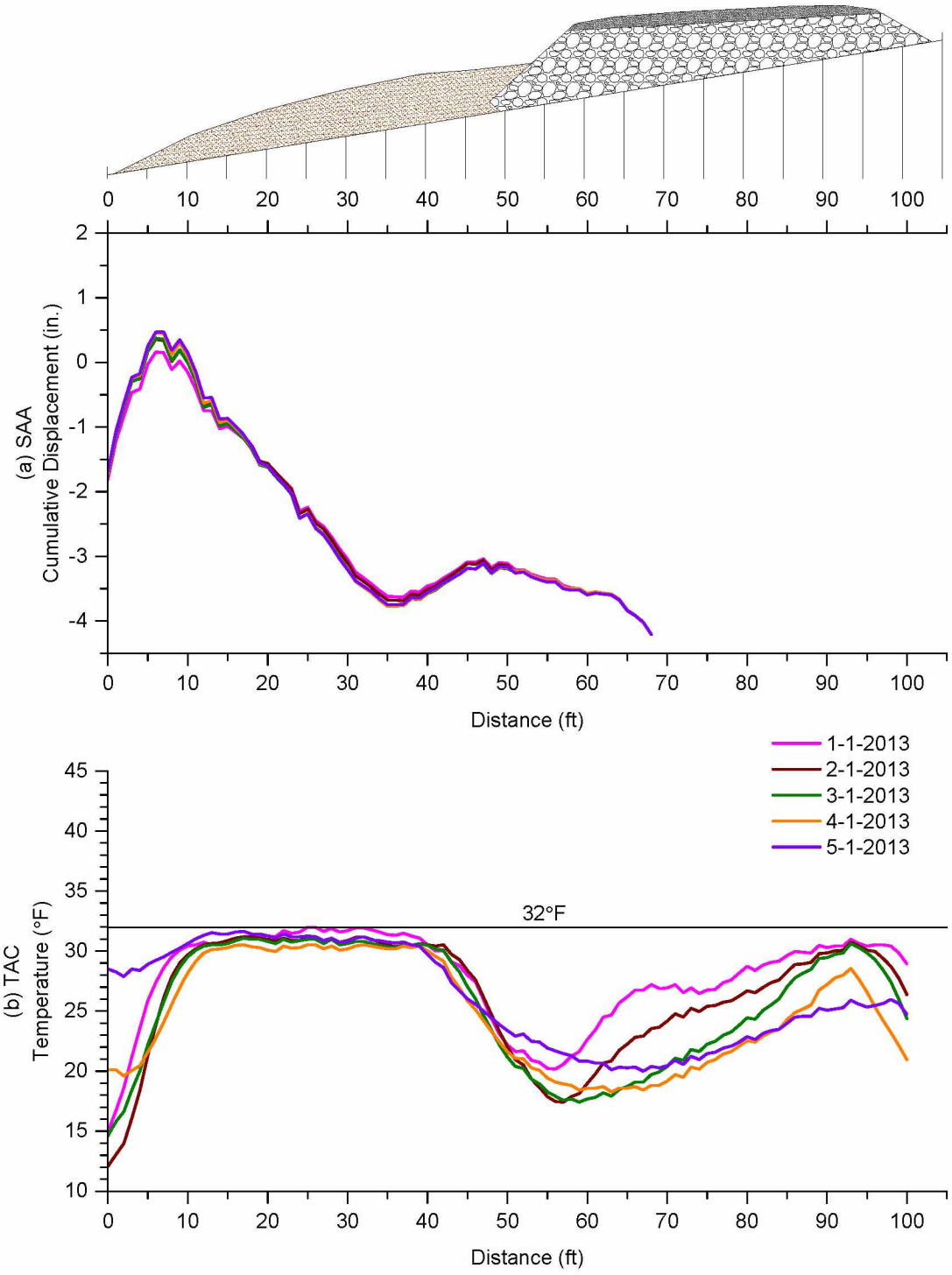

Figure 4.19 Corrected monthly (a) SAA and (b) TAC measurements from Jan. 1 to May 1, 2013.

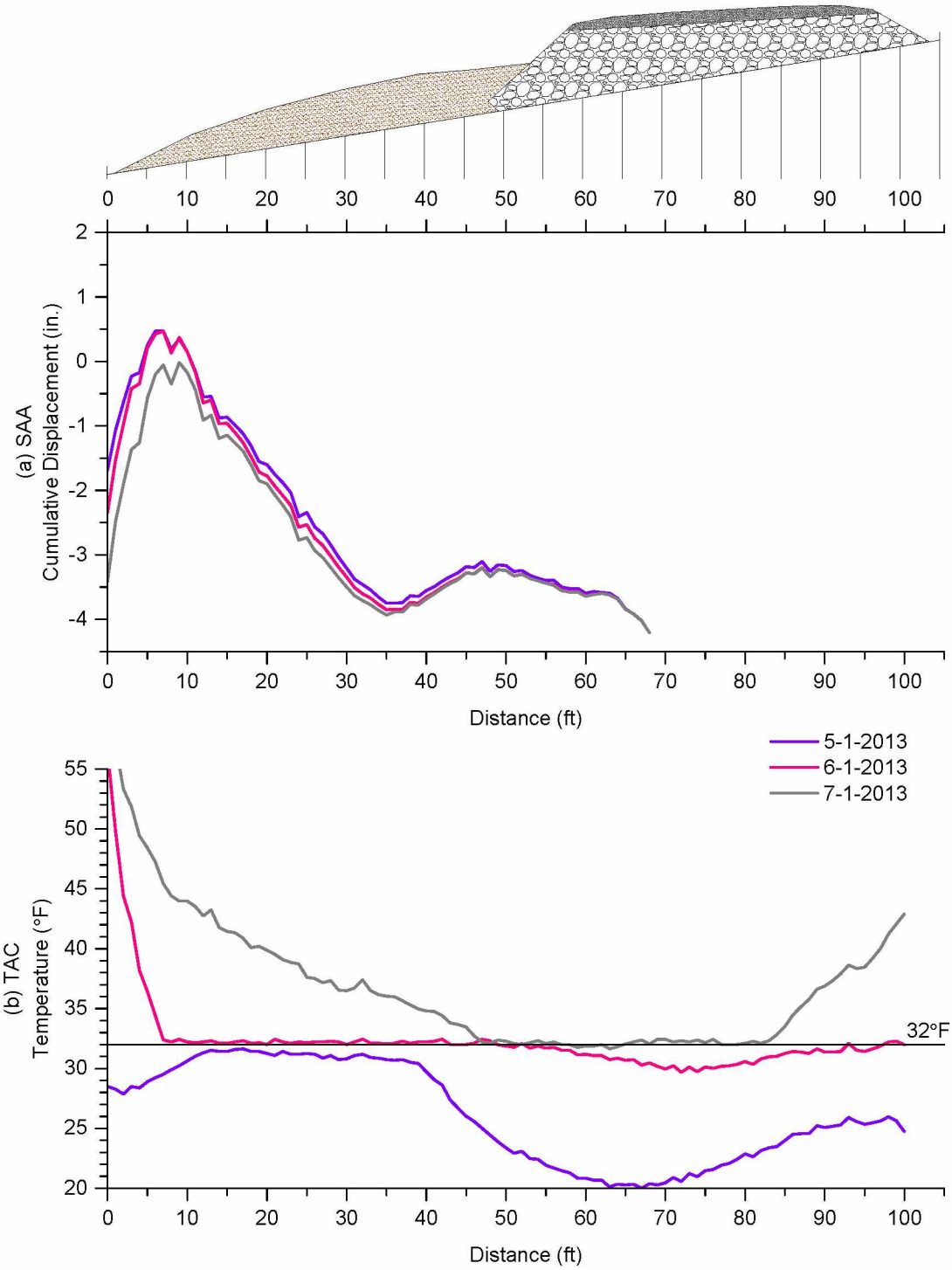

Figure 4.20 Corrected monthly (a) SAA and (b) TAC measurements from May 1 to Jul. 1, 2013.

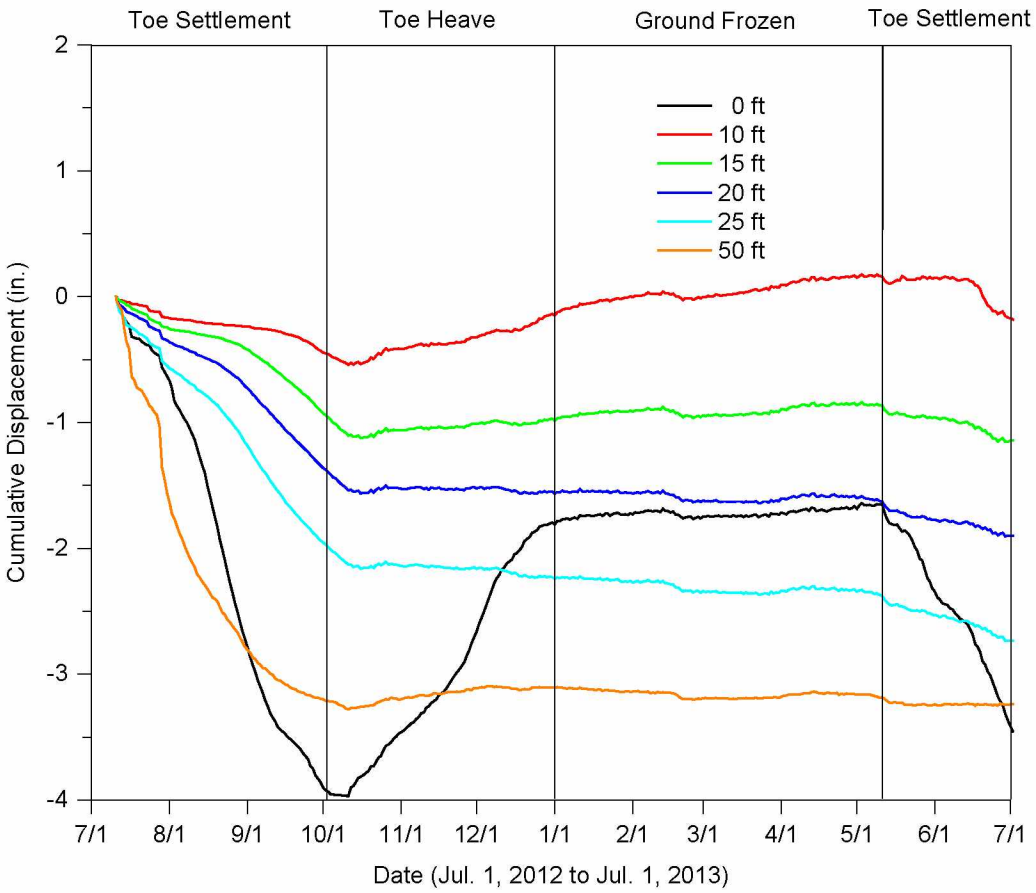

Figure 4.21 Corrected monthly SAA movement versus time for select distances from thermal berm toe.

CHAPTER 5 LABORATORY TESTING

Soil samples were collected from the Lost Chicken site for laboratory testing to determine physical and thermal properties for use in thermal modeling. This chapter includes testing procedures, laboratory equipment, and test results. Thermal conductivity and thaw strain testing procedures and test results are discussed in Section 5.1. Gravimetric and volumetric water content and dry unit weight testing procedures and test results are discussed in Section 5.2. Finally, the results of a grain size analysis performed on thermal berm material for classification purposes are provided in Section 5.3.

5.1 THERMAL CONDUCTIVITY AND THAW STRAIN TESTING

Testing was conducted to estimate the frozen and unfrozen thermal conductivity of the *in situ* soil for use in thermal modeling. Samples for testing were taken from the 3-in. diameter frozen core samples shown in Figures 3.9 through 3.13. The samples were cut to between 5 and 6 in. in length using an electric saber saw. Several samples from each of the main soil types identified were tested.

A KD2 Pro Thermal Properties Analyzer, from Decagon Devices Inc., was used to measure thermal conductivity of the frozen and unfrozen soil samples. This device is capable of manual or automated readings and can store up to 4,095 readings (Decagon Devices, Inc. 2012). The KD2 Pro operates based on the principles of transient line heat source methods that have been in use for more than 50 years. A steel needle probe with a heater element and temperature sensor inside is inserted into a soil sample. Electric current then is applied to the heating element and the probe temperature is monitored over time. The temperature change over time is used to estimate the thermal conductivity.

Unfortunately, the theoretically ideal probe and environmental conditions for this application are impractical. The ideal probe would be too long and thin, making it too fragile for insertion into many materials. It is also difficult to maintain a constant sample temperature outdoors in field conditions, due to fluctuations in ambient temperature. Drilling a hole for insertion of the probe also can induce contact resistance which leads to errors. Finally, in the case of frozen soil samples, the application of heat from the probe may thaw the sample, changing its properties.

Some of these problems have been minimized with the KD2 Pro (see Figure 5.1). The sensors are robust, making them easier to insert into materials without fear of damaging them.

The sensors also use a very low amount of heat applied over a short time to estimate thermal conductivity (Decagon Devices, Inc. 2012), which helps to prevent water movement or thawing within the sample; however, such minor temperature changes require that temperature be measured at a very high resolution. According to Decagon Devices, Inc. (2012) the KD2 Pro is capable of 0.001°C resolution. Special algorithms also are employed to account for fluctuation in ambient temperature.

The KS-1 needle probe was used for thermal conductivity measurements (see Figure 5.1b). The KS-1 is a small, single needle (see Table 5.1 for specifications). According to Decagon Devices, Inc. (2012), the KS-1 is well-suited for measuring the thermal conductivity of liquid and insulating materials; however, it is a poor choice for measuring dry granular materials. Since all of the samples were saturated and most were fine-grained with high water contents, the KS-1 was considered the most appropriate probe.

Before beginning thermal conductivity testing, the KS-1 probe was checked to verify measurement accuracy using a glycerin verification standard. According to a certificate of quality assurance provided from the manufacturer, the KD2 Pro device using the KS-1 needle probe should read approximately 0.165 BTU/(hr·ft·°F) ±5% at room temperature in glycerin. The probe was inserted into the glycerin vial and six measurements were taken. The average thermal conductivity measured was 0.168 BTU/(hr·ft·°F), which was within the 5% error quoted by the manufacturer.

After checking instrument calibration, prepared frozen samples were placed inside plastic ABS pipe containers that were capped on one end and open on the other (see Figure 5.1c). A small hole, approximately equal in length to the KS-1 needle probe, was drilled vertically in the center of the end of each sample using a 1/16-in. diameter drill bit. Before inserting the probe into the samples, contact resistance was reduced by coating the needle with Arctic Silver 5 thermal paste (see Figure 5.1d).

After inserting the needle probe into the frozen sample, the sample and probe were placed in a freezer at an average temperature of -2°F. The KD2 Pro was set to take automatic measurements every 30 min. until at least five measurements were obtained with the sample at a relatively stable temperature; the thermal conductivity was measured every 60 min. for samples left in the freezer overnight. The exposed ends of the plastic containers were sealed during testing to prevent sublimation of the samples. Figure 5.2 illustrates a sample prepared for thermal conductivity measurements.

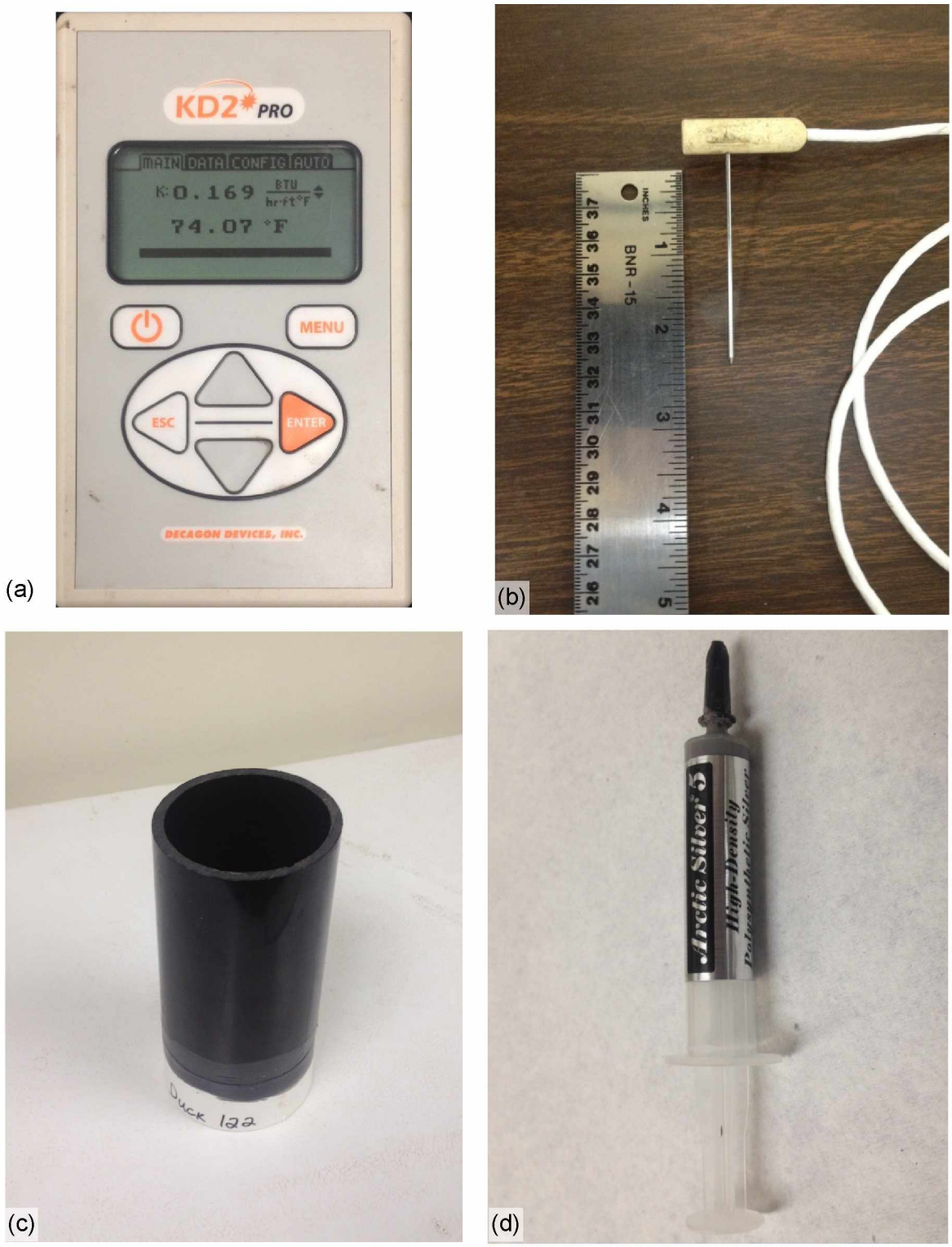

Figure 5.1 Equipment for thermal conductivity testing; (a) KD2 Pro Thermal Properties Analyzer. (b) KS-1 needle probe; (c) sample container; (d) Arctic Silver 5 thermal paste.

Table 5.1 KS-1 single needle probe specifications (Decagon Devices, Inc. 2012).

Size	0.051 in. diameter by 2.36 in. length
Range	0.012 to 1.16 BTU/(hr·ft·°F)
Accuracy	+/- 5% from 0.12 to 1.16 BTU/(hr·ft·°F)
	+/- 0.006 BTU/(hr·ft·°F) from 0.012 to 0.12 BTU/(hr·ft·°F)
Cable Length	31.5 in.

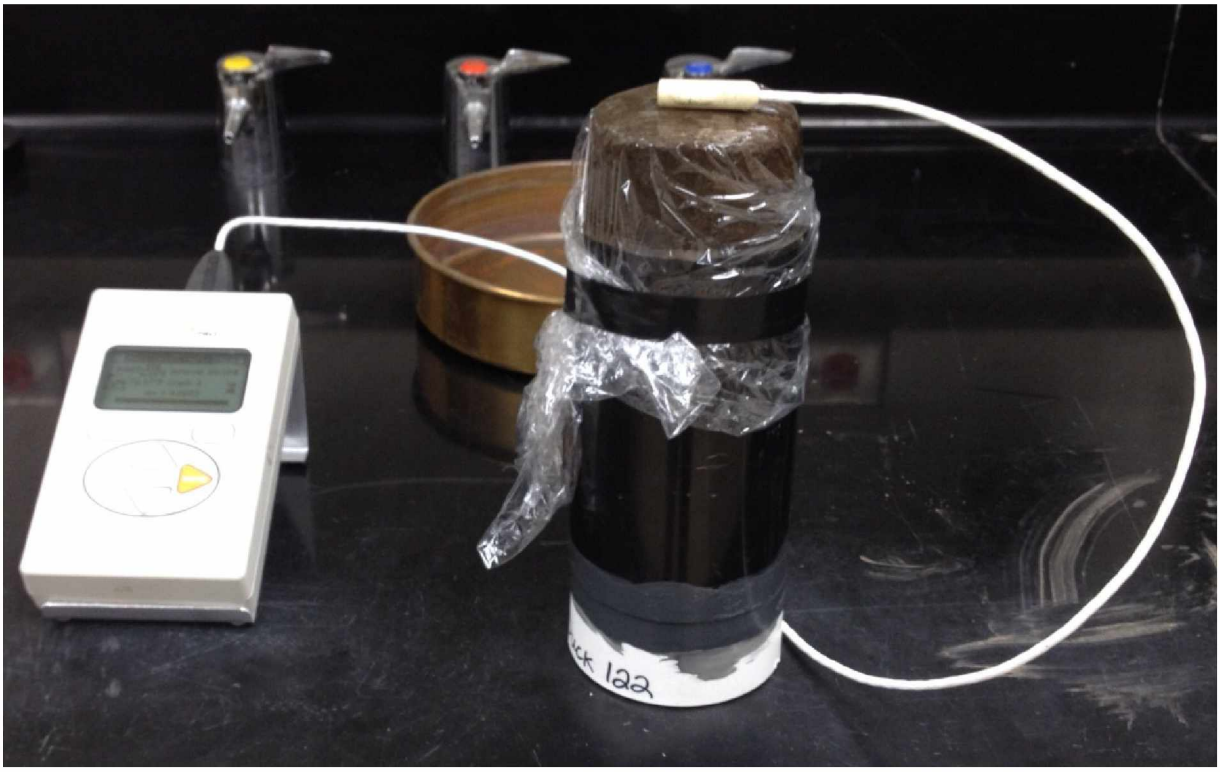

Figure 5.2 Frozen soil sample ready for thermal conductivity measurements.

After measurements were collected with the sample at thermal equilibrium, the sample was removed from the freezer and allowed to thaw at room temperature with the probe still in place. After thawing, it was usually necessary to press the needle farther into the sample, since the soil had settled. At least five thermal conductivity measurements were collected with the sample at thermal equilibrium and at least five minutes were allowed between measurements.

Soil samples that were allowed to thaw under no external loading provided reasonable unfrozen thermal conductivity estimates for soils within the active layer and under undisturbed conditions; however, any soil that thawed beneath the highway embankment would consolidate under an external load. Therefore, some samples were thawed and consolidated to identify any

significant changes in thermal properties between the unconsolidated and consolidated states. In the course of thawing and consolidating samples, the thaw strain of the ice-rich soil also was measured to estimate potential settlement risk to the roadway embankment.

In order to consolidate samples, a makeshift load cell that could accommodate core samples approximately 3 in. in diameter and with lengths in excess of 12 in. was constructed using standard 2 in. by 4 in. lumber, and the load piston consisted of metal pipe and fittings (see Figure 5.3). Finally, the cell was built using a standard 3 in. ABS pipe and a rubber end cap and coupler.

The weight, length, diameter, and frozen thermal conductivity of each soil sample were measured prior to placement into the load cell. Then the load piston was lowered onto the sample and weight was placed on top of the piston. Two 10-lb and one 5-lb weights were used; one 10-lb weight was applied immediately after placing the sample in the cell, and the following day the other weights were added for a total pressure of approximately 3.5 psi, representative of a 4 to 5-ft thick gravel embankment. A photograph of the load cell with a sample loaded for testing is presented in Figure 5.4.

The initial piston height was measured as well as the final height after thawing and consolidation, a process that usually took about two days. The change in piston height combined with the initial sample measurements were used to calculate the thawed consolidated volume. Then the cell was removed from the apparatus and the end cap removed, allowing the consolidated sample to be pushed out into a container for thawed-consolidated thermal conductivity measurements. Some samples were placed in the freezer, with the needle probe still in place, and allowed to refreeze for measurement of frozen-consolidated thermal conductivity.

Table 5.2 is a summary of the average thaw strain, frozen thermal conductivity, and unfrozen thermal conductivity for each soil type, both in the unconsolidated and consolidated states. The laboratory test results for individual soil samples are provided in Appendix B. Based on the results, the peat with silt and silt with sand and organics had the highest thaw strain values of 53.6% and 40.0%, respectively. They also had very similar frozen thermal conductivities, most likely due to their high water contents. The coarse sand with silt had the lowest thaw strain of 17.8%, and also had the highest thermal conductivities for both the frozen and unfrozen states. No frozen-consolidated thermal conductivities were measured for the coarse sand; however, little change from the unconsolidated frozen thermal conductivity was expected due to the relatively low moisture content and thaw strain.

Figure 5.3 Photograph of load cell constructed for thaw strain analysis.

The average unfrozen-consolidated thermal conductivities of the peat and coarse sand increased compared to their unfrozen-unconsolidated thermal conductivities. The average unfrozen-consolidated thermal conductivity of the silt decreased slightly compared to the unconsolidated value; this may be attributed to the disproportionate number of unfrozen-consolidated and unconsolidated samples. Examination of individual unfrozen samples tested for both unconsolidated and consolidated thermal conductivity revealed that the consolidated thermal conductivity of the silt tended to increase similarly to the other soils tested.

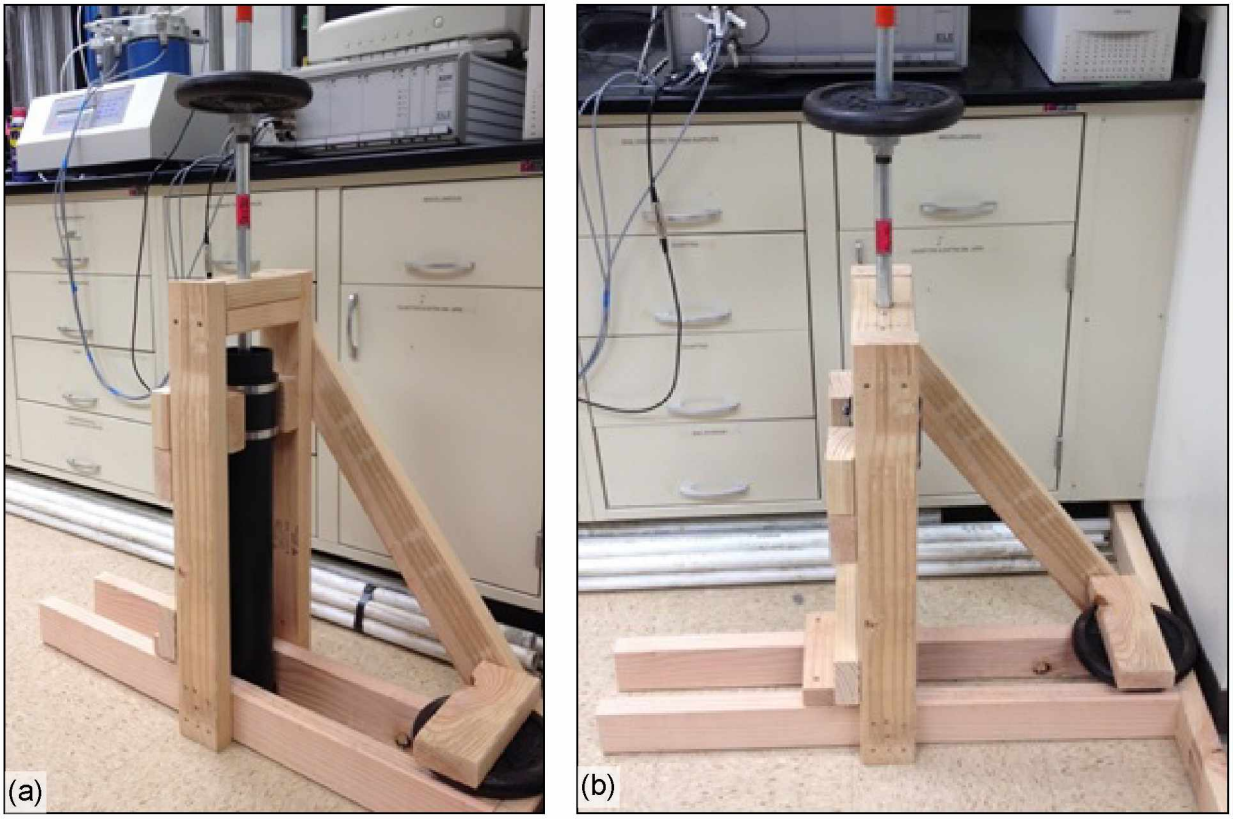

Figure 5.4 Photographs of sample loaded for thaw strain analysis; (a) front view, (b) side view.

Table 5.2 Average soil thaw strain, and frozen and unfrozen thermal conductivity. Consolidated samples are indicated by "(cons)", "–" indicates no data, ε_v is thaw strain, K_f is frozen thermal conductivity, and K_u is unfrozen thermal conductivity.

Soil Type	ε_v (%)	K_f BTU/(hr·ft·°F)	K_u BTU/(hr·ft·°F)
Peat w/ silt	53.6	0.901	0.366
Peat w/ silt (cons)	–	0.891	0.432
Silt w/ sand & org.	40.0	0.980	0.537
Silt w/ sand & org. (cons)	–	0.867	0.502
Coarse sand w/ silt	17.8	1.132	0.574
Coarse sand w/ silt (cons)	–	–	0.594

5.2 WATER CONTENT AND DRY UNIT WEIGHT TESTING

Laboratory testing was conducted to determine gravimetric and volumetric water contents, as well as wet and dry unit weights of soils at the site for use in thermal modeling. Soil

samples were taken from ice-rich permafrost, thermal berm material, the organic mat, and road surface course.

Three samples were collected from the road surface course and two were collected from the organic mat. Because the thermal berm material was too coarse for the volumetric soil sampler, three grab samples were taken from the upper 12 in. of this material for water content testing only. Samples of ice-rich soil were cut from the frozen core samples, and each sample's diameter and height were measured to determine the sample volume. Water content tests were conducted following the ASTM D2216 standard (ASTM International 1999). Table 5.3 is a summary of gravimetric water content, volumetric water content, and wet and dry unit weight for the tested samples. The laboratory test results for all of the tested samples are included in Appendix B.

The data indicated strong correlations between the soils' dry unit weights and gravimetric and volumetric water contents. The plot of gravimetric water content versus dry unit weight shown in Figure 5.5 reveals this strong correlation, indicating an exponential increase in gravimetric water content with decrease in dry unit weight. A similar trend between the volumetric water content and dry unit weight is shown in Figure 5.6.

Table 5.3 Average soil water contents and unit weights. Consolidated samples are indicated by "(cons)", "–" indicates no data, w is gravimetric water content, θ is volumetric water content, γ is unit weight, and γ_d is dry unit weight.

Material Type	w (%)	θ (%)	γ (lb/ft^3)	γ_d (lb/ft^3)
Road Surface Course	5.2	9.4	120.0	114.1
Organic Mat	223.0	75.8	76.10	57.6
Thermal Berm	9.9	–	–	–
Peat w/ silt	245.2	81.2	67.8	17.1
Peat w/ silt (cons)	88.4	66.6	90.9	49.3
Silt w/ sand & organics	106.0	66.3	81.6	40.2
Silt w/ sand & organics (cons)	52.8	53.8	101.8	68.2
Coarse sand w/ silt	40.7	53.7	117.9	84.4
Coarse sand w/ silt (cons)	–	–	–	–

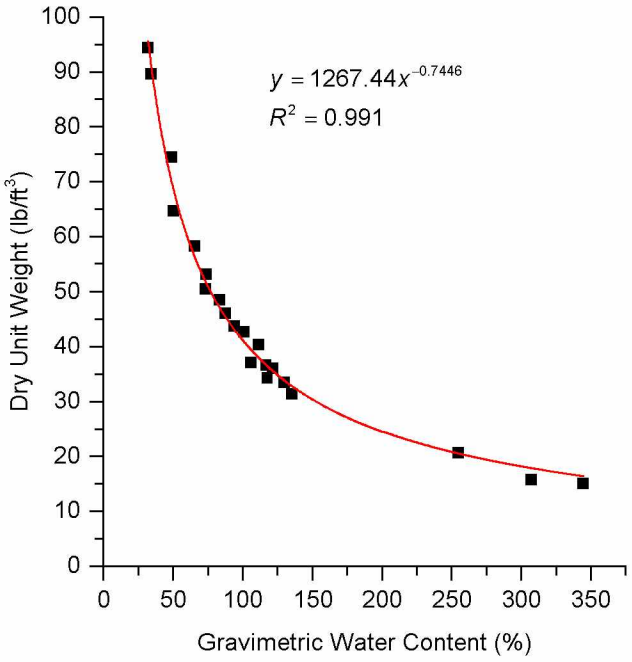

Figure 5.5 Relationship between gravimetric water content and dry unit weight.

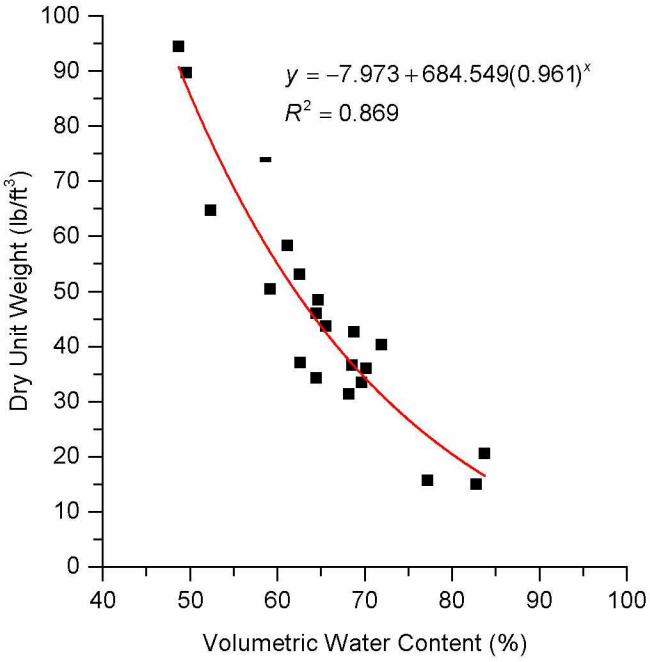

Figure 5.6 Relationship between volumetric water content and dry unit weight.

5.3 GRAIN SIZE ANALYSIS OF THERMAL BERM MATERIAL

A grain size analysis was conducted on a grab sample of material collected from the upper 12 in. of the thermal berm, and Figure 5.7 is a plot of the results. SI units were used to remain consistent with the conventional way of presenting grain size distribution. Using the Unified Soil Classification System (USCS), the soil was classified as well-graded gravel (GW).

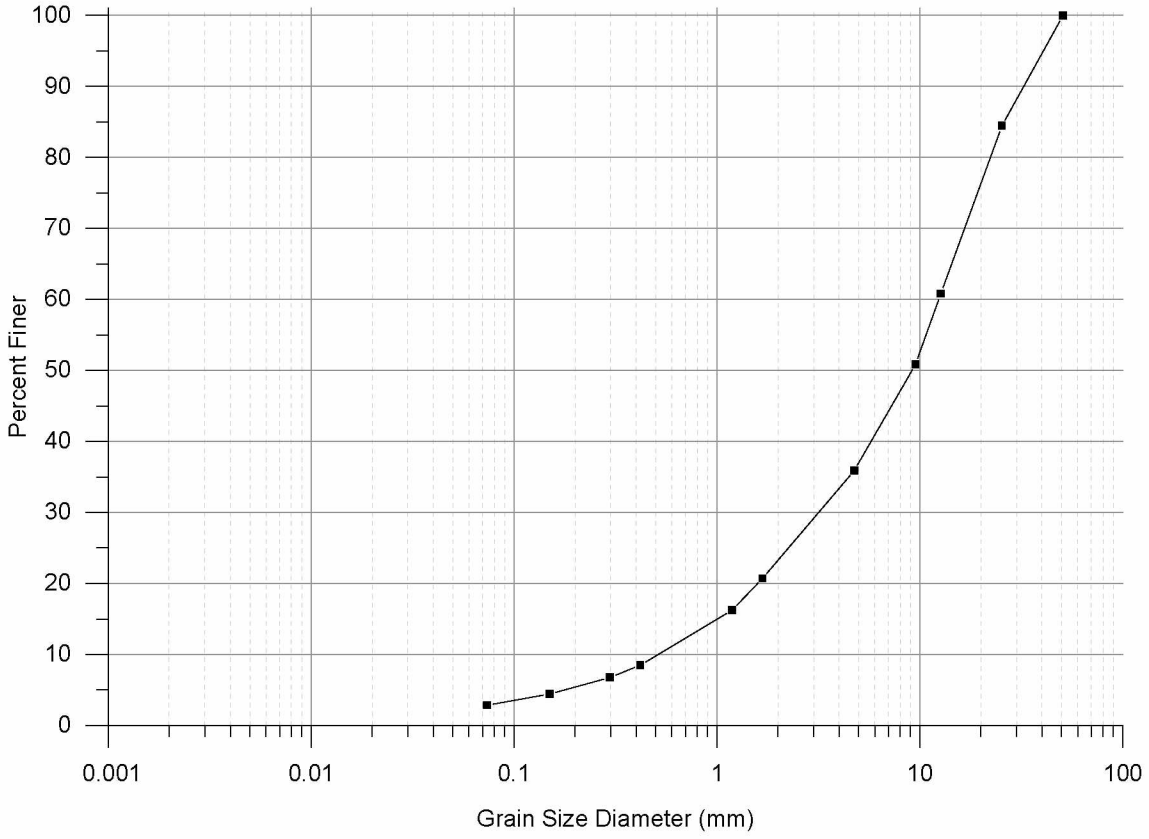

Figure 5.7 Grain size distribution for thermal berm material. Note: gravel > 4.75 mm, sand 4.75 to 0.075 mm, and silt < 0.075 mm.

CHAPTER 6 NUMERICAL MODELING

Over the course of the Lost Chicken Slide research, a thermal model of the ACE and thermal berm was developed to compare predicted embankment temperatures to temperatures collected from the site and to estimate long-term temperature changes beneath the embankment. A two-dimensional finite element model was created using three modules from the GeoStudio 2012 software suite: TEMP/W for evaluation of conductive heat transfer, and SEEP/W and AIR/W for density-driven air convection. The three modules were run together to model heat transfer due to temperature dependent, density-driven air convection within the ACE and the conductive heat flow within the thermal berm and foundation soil. Different models were run to simulate plowed and unplowed driving surfaces. The models were run to estimate long-term temperature changes beneath the embankment.

This chapter provides a detailed explanation of the numerical modeling conducted on the ACE and thermal berm. Section 6.1 provides an overview of the software in which the basic limitations, assumptions, and governing differential equations are presented. Subsection 6.1.1 summarizes a case study analysis in which GeoStudio 2012 was used to reproduce modeling results for an ACE modeled by researchers Goering and Kumar in 1996. The modeling parameters are presented in Section 6.2 and include the model geometry and mesh, material properties, boundary conditions, and modeling stages and time stepping. Finally, Section 6.3 is a summary and analysis of the modeling results.

6.1 SOFTWARE OVERVIEW

GeoStudio 2012, version 8.0.10, by GEO-SLOPE International Ltd. was used for the numerical analysis. GeoStudio is a finite element, geotechnical engineering software suite containing several different programs, each of which can be used independently for different analyses, or may be combined with others to perform complex analyses. In order to model temperature change beneath the embankment due to conductive and convective heat transfer, the TEMP/W, SEEP/W, and AIR/W programs were utilized.

TEMP/W is used to model heat transfer through both porous and solid materials, wherein it is assumed that the moisture content does not change over time. For the analysis of conductive heat flow, TEMP/W operates on the assumption that conduction is the flow of heat due to energy transfer between soil particles and pore fluids. This process is governed by the following equation:

$$q = -k\frac{\partial T}{\partial x} \tag{6.1}$$

where q is heat flux, k is thermal conductivity, T is temperature, and x is distance. Heat flow is dependent primarily on temperature difference and thermal conductivity. The negative sign in Equation 6.1 indicates that heat flows from high to low temperature across the distance x.

The governing differential equation used in TEMP/W is as follows:

$$\frac{\partial}{\partial x}\left(k_x\frac{\partial T}{\partial x}\right)+\frac{\partial}{\partial y}\left(k_y\frac{\partial T}{\partial y}\right)+Q=\lambda\frac{\partial T}{\partial t} \tag{6.2}$$

where k_x and k_y are the thermal conductivities in the x- and y-directions, respectively, T is the temperature, Q is the applied boundary flux, λ is the capacity for heat storage, and t is time (GEO-SLOPE International Ltd. 2012d). According to Equation 6.2, any change in stored energy in a soil element at a given time is equal to the difference between the amount of energy entering and leaving that element. The capacity for heat storage in Equation 6.2 consists of two parts, the volumetric heat capacity and latent heat of fusion. Therefore, the capacity for heat storage can be expressed as Equation 6.3:

$$\lambda = c + L\frac{w_u}{T} \tag{6.3}$$

where c is the volumetric heat capacity, L is the latent heat of water, and w_u is the volumetric unfrozen water content. Substituting Equation 6.3 into Equation 6.2, the complete governing differential equation for two dimensional heat flow is expressed as:

$$\frac{\partial}{\partial x}\left(k_x\frac{\partial T}{\partial x}\right)+\frac{\partial}{\partial y}\left(k_y\frac{\partial T}{\partial y}\right)+Q=\left(c+L\frac{\partial w_u}{\partial T}\right)\frac{\partial T}{\partial t} \tag{6.4}$$

During steady-state conditions, the amount of heat entering and leaving a soil element is equal at all times. Therefore, Equation 6.4 reduces to Equation 6.5:

$$\frac{\partial}{\partial x}\left(k_x\frac{\partial T}{\partial x}\right)+\frac{\partial}{\partial y}\left(k_y\frac{\partial T}{\partial y}\right)+Q=0 \tag{6.5}$$

SEEP/W is used to model fluid flow through porous media; it can be used to model both steady-state saturated flow and transient saturated/unsaturated flow conditions. The SEEP/W program operates on the assumption that water flow through saturated and unsaturated soil follows Darcy's Law as presented in Equation 6.6:

$$q = ki \tag{6.6}$$

where q is specific discharge, k is the hydraulic conductivity of the soil, and i is the total hydraulic head gradient (GEO-SLOPE International Ltd., 2012c). Although derived for saturated

soils, it is assumed that Darcy's Law can be applied to unsaturated soils by varying the hydraulic conductivity with changes in pore water pressure.

For two-dimensional flow, the general governing differential equation used in the SEEP/W program is:

$$\frac{\partial}{\partial x}\left(k_x \frac{\partial H}{\partial x}\right)+\frac{\partial}{\partial y}\left(k_y \frac{\partial H}{\partial y}\right)+Q=\frac{\partial \theta}{\partial t} \tag{6.7}$$

where k_x and k_y are the hydraulic conductivities in the *x*- and *y*-directions, respectively, H is the total head, Q is the applied boundary flux, θ is the volumetric water content, and t is time. Equation 6.7 indicates that for a given soil element, the sum of the change in flow rate in the x and y directions together with the applied boundary flux, equals the change in volumetric water content over time.

Since SEEP/W is based on constant total stress conditions and constant atmospheric pressure, the changes in volumetric water content can be expressed by changes in pore water pressure:

$$\partial \theta = m_w \partial u_w \tag{6.8}$$

where m_w is the slope of the water storage curve, and u_w is the pore water pressure. If pore water pressure is described in terms of total head, elevation, and unit weight of water, then Equation 6.8 can be expressed as:

$$\partial \theta = m_w \gamma_w \partial (H - y) \tag{6.9}$$

where γ_w is the unit weight of water, and y is elevation. Equation 6.9 is then substituted into Equation 6.7 and, given that the elevation is a constant, the derivative of y with respect to time is zero. The resulting Equation 6.10 is the complete governing differential equation used in SEEP/W for two dimensional flow conditions:

$$\frac{\partial}{\partial x}\left(k_x \frac{\partial H}{\partial x}\right)+\frac{\partial}{\partial y}\left(k_y \frac{\partial H}{\partial y}\right)+Q=m_w \gamma_w \frac{\partial H}{\partial t} \tag{6.10}$$

AIR/W is used to model air pressure and flow due to changes in pressure boundary or water pressure. AIR/W is not a standalone program; instead it must be run as part of SEEP/W. When coupled with TEMP/W, AIR/W can be used to solve for thermally induced, density-driven air flow and pressure changes (GEO-SLOPE International Ltd. 2012a). By default, the SEEP/W program operates under the assumption that pore air pressure is atmospheric and constant; however, for the analysis of compressible air flow, it is necessary to solve the coupled conservation of mass equations for pore-air and pore-water flow. The water conservation of mass equation for a one-dimensional analysis is:

$$m_w \gamma_w \frac{\partial H_w}{\partial t} = \frac{\partial}{\partial y}\left(k_w \frac{\partial H_w}{\partial y} \right) + m_w \frac{\partial P_a}{\partial t} + Q_w \qquad (6.11)$$

where H_w is total water head, k_w is hydraulic conductivity, P_a is air pressure, and Q_w is water flux.

The air conservation of mass equation for a one-dimensional analysis is:

$$\left(\frac{\theta_a}{RT} + \rho_a m_w \right) \frac{\partial P_a}{\partial t} = \frac{\partial}{\partial y}\left(\frac{\rho_a k_a}{\gamma_{oa}} \frac{\partial P_a}{\partial y} + \frac{\rho_a{}^2 k_a}{\rho_{oa}} \right) - \frac{\theta_a P_a}{R} \frac{\partial T^{-1}}{\partial t} + \rho_a \gamma_w m_w \frac{\partial H_w}{\partial t} \qquad (6.12)$$

where θ_a is volumetric air content, R is the universal gas constant (287 J/kg·K for dry air), ρ_a is density of air, k_a is air conductivity, γ_{oa} is initial unit weight of air, and ρ_{oa} is initial density of air. Here we have two equations and two unknowns: water head and air pressure. When the air density is dependent on temperature, as is the case with thermally dependent density-driven air convection, the following energy balance equation must also be solved:

$$\left(\rho_s c_{ps} + L\theta_w \frac{\partial \theta_u}{\partial T} \right) \frac{\partial T}{\partial t} = \frac{\partial}{\partial y}\left(K_t \frac{\partial T}{\partial y} \right) + c_{pa} \frac{\partial (\dot{m}_a T)}{\partial y} + \rho_w c_{pw} \frac{\partial (q_w T)}{\partial y} + Q \qquad (6.13)$$

where ρ_s is density of soil, c_{ps}, c_{pa}, c_{pw} are mass specific heats of soil, air, and water, respectively, L is latent heat of water, $\dot{m}_a$ is mass flow rate of air, θ_u is volumetric unfrozen water content, and q_w is specific discharge of water.

6.1.1 Case Study Analysis

In preparation for numerical modeling of the Lost Chicken embankment, a case study analysis was conducted. The goal of the analysis was to validate the GeoStudio software recreating results from a numerical model created by Goering and Kumar (1996). The case study analysis also established procedures for creating and running the coupled TEMP/W and SEEP/W analysis necessary for modeling thermally dependent, density-driven air convection. Since the original modeling was conducted using SI units, the same units were used for the GeoStudio analysis; however, US customary units also are provided in this text for the material properties.

In the model created by Goering and Kumar (1996), a high permeability embankment constructed of poorly-graded rock and gravel was modeled over permafrost soil consisting of ice-rich silt with high moisture content. The model geometry is depicted in Figure 6.1. Due to the

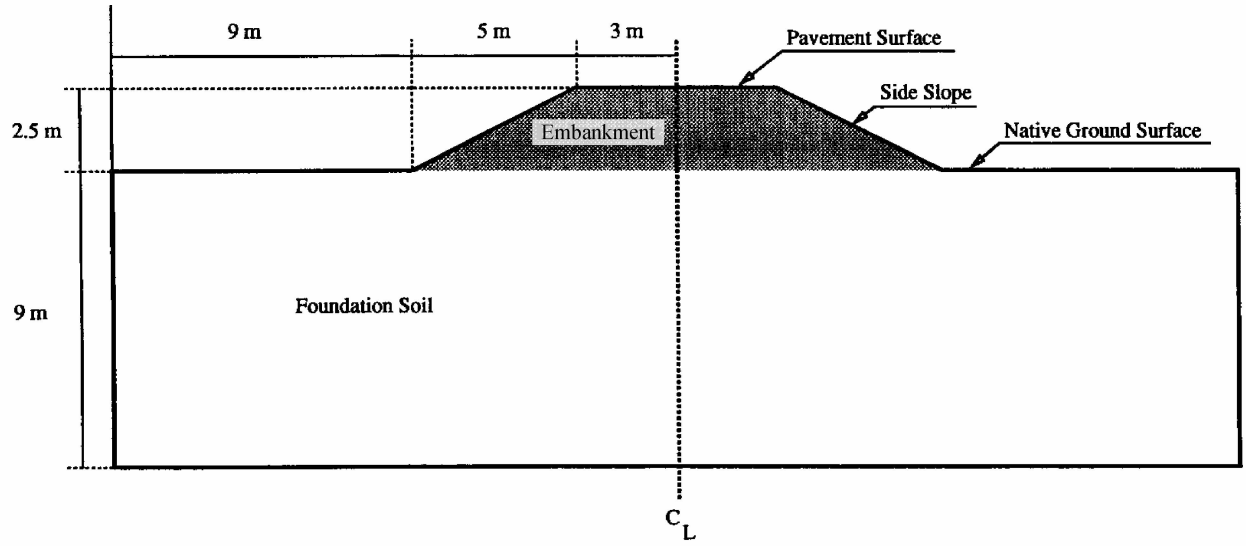

Figure 6.1 Model embankment geometry (Goering and Kumar 1996).

symmetry of the embankment geometry, Goering and Kumar (1996) chose to model only half of the embankment.

The material properties assigned to the high permeability embankment were chosen to correspond with poorly-graded rock having an average diameter of 3 cm (1.2 in.) and porosity of 40%. The foundation soil properties were chosen to correspond with ice-rich silt having a dry density of 1442 kg/m^3 (90 lb/ft^3) and a moisture content of 45%. The material properties for the embankment and foundation soil are summarized in Table 6.1 and Table 6.2, respectively.

The GeoStudio analysis was established using the same model geometry, boundary conditions, and material properties given by Goering and Kumar. Finer mesh spacing was used for the GeoStudio analysis; 0.05 m (0.16 ft) mesh spacing was applied to the upper portion of

Table 6.1 Thermal and hydraulic properties for ACE material (modified from Goering and Kumar (1996)).

Property	Value (SI)	Value (US Customary)
Thawed thermal conductivity	0.346 W/m·°C	4.80 BTU/day·ft·°F
Frozen thermal conductivity	0.346 W/m·°C	4.80 BTU/day·ft·°F
Thawed specific heat	1006 kJ/m^3·°C	15 BTU/ft^3·°F
Frozen specific heat	1006 kJ/m^3·°C	15 BTU/ft^3·°F
Latent heat	≈ 0 kJ/m^3	≈ 0 BTU/ft^3
Permeability	6.32×10^{-7} m^2	6.80×10^{-6} ft^2

Table 6.2 Thermal and hydraulic properties for foundation soil (modified from Goering and Kumar (1996)).

Property	Value (SI)	Value (US Customary)
Thawed thermal conductivity	1.49 W/m·°C	20.66 BTU/day·ft·°F
Frozen thermal conductivity	2.32 W/m·°C	32.17 BTU/day·ft·°F
Thawed specific heat	3740 kJ/m^3·°C	55.77 BTU/ft^3·°F
Frozen specific heat	2380 kJ/m^3·°C	35.49 BTU/ft^3·°F
Latent heat	2.17×10^5 kJ/m^3	5824 BTU/ft^3
Permeability	≈ 0	≈ 0

the ACE, 0.10 m (0.33 ft) spacing was applied to the lower ACE and the upper portion of the silt, and 0.25 m (0.82 ft) spacing was applied to the silt at greater depth. The model geometry and mesh for the GeoStudio analysis are shown in Figure 6.2.

First, a steady-state analysis was run to establish the initial conditions for the transient model. A constant temperature of -1.9°C (28.6°F) was applied to the upper boundary, and a geothermal flux of 5.18 kJ/day/m^2 (0.456 BTU/day·ft^2) was applied to the lower boundary. All thermal properties for the ice-rich silt were taken directly from Goering and Kumar (1996) and converted to the appropriate units for the GeoStudio analysis. The TEMP/W program, however, required the soil volumetric water content for the full thermal material model. Although Goering and Kumar (1996) did not specify whether the reported moisture content for the ice-rich silt (45%) was gravimetric or volumetric, it was possible to back-calculate the water content from those values from the given latent heat and dry density to confirm that it was gravimetric. Given the gravimetric water content and dry density, and assuming soil particles had a specific gravity of 2.7, the volumetric water content was calculated as 46.6%. The material properties assigned to the ice-rich silt are summarized in Table 6.3.

For SEEP/W, zero-flow air pressure boundary conditions were applied to each edge of the domain. This represents the impermeable road surface, impermeable native ground surface, and impermeable embankment slopes, assuming they were covered with geo-fabric and topsoil (Goering and Kumar 1996). Finally, a constant, total hydraulic head of zero meters was applied to the entire domain in SEEP/W to eliminate water flow.

The steady-state analysis was run for one day. Then a transient thermal analysis was run for ten years so the ground temperatures could reach equilibrium. For the transient analysis, the upper temperature boundary conditions were assigned to each surface according to Table 6.4. Analysis of the results indicated that the ground temperatures had reached equilibrium.

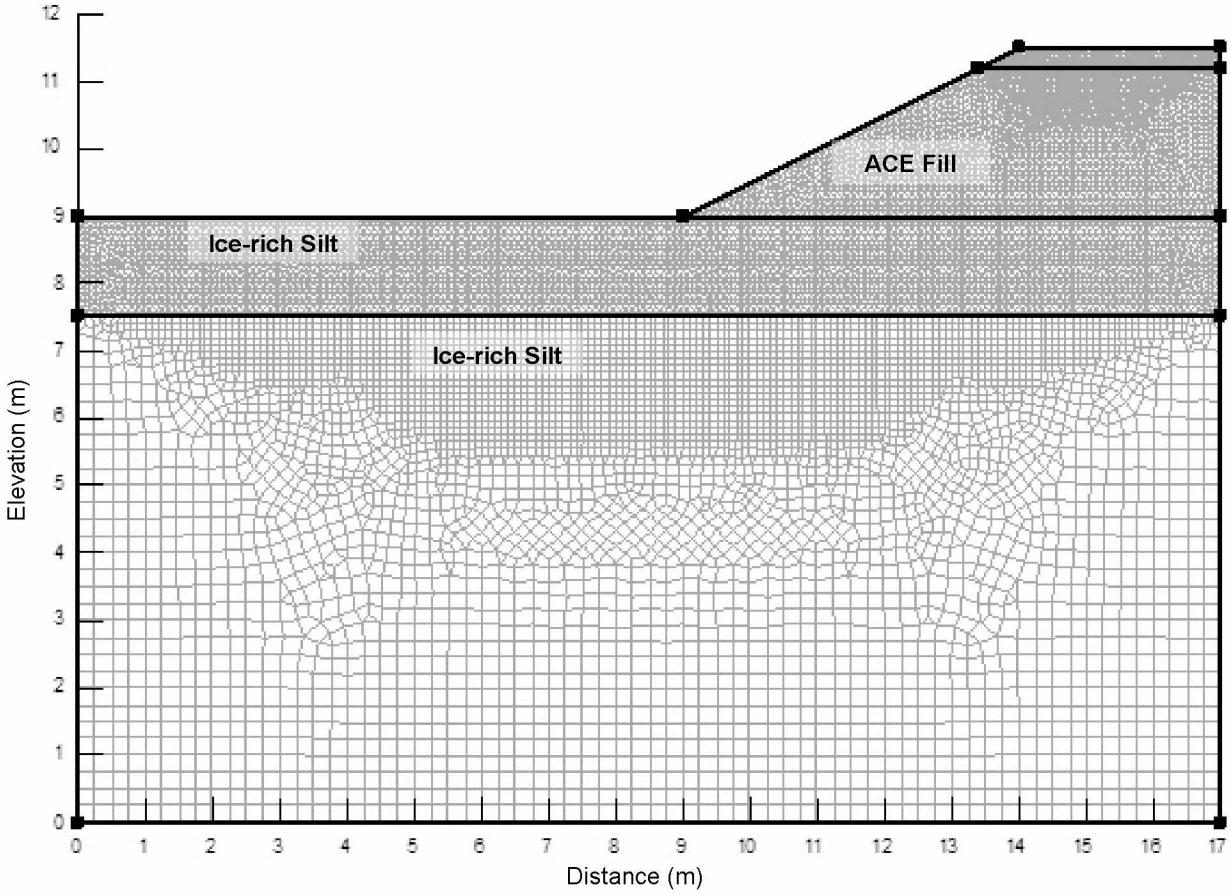

Figure 6.2 Model geometry and mesh for GeoStudio analysis.

Table 6.3 Properties of foundation soil for TEMP/W and SEEP/W analysis.

Property	Value (SI)	Value (US Customary)
Thawed thermal conductivity	128.7 kJ/day·m·°C	20.66 BTU/day·ft·°F
Frozen thermal conductivity	200.4 kJ/ day·m·°C	32.17 BTU/day·ft·°F
Thawed specific heat	3,740 kJ/m^3·°C	55.77 BTU/ft^3·°F
Frozen specific heat	2,380 kJ/m^3·°C	35.49 BTU/ft^3·°F
Volumetric water content	0.466 m^3/m^3	0.466 ft^3/ft^3
Hydraulic Conductivity	1×10^{-5} m/day	3.28×10^{-5} ft/day
Air Conductivity	0.001 m/day	0.00328 ft/day

The next part of the GeoStudio analysis was to run the coupled TEMP/W and SEEP/W analysis to model the heat transfer due to density-driven air convection within the ACE material. A case history by GEO-SLOPE International Ltd. (2012b) was used as a guide for establishing

Table 6.4 Temperature boundary conditions at upper surface (Goering and Kumar 1996).

Surface	Thaw *n*-factor	Freeze *n*-factor	Temperature function (°C)
Pavement surface	1.9	0.9	$1.1-26.1\cos\left(\frac{2\pi}{365}(t-9)\right)$
Gravel side slope	1.7	0.6	$2.7-20.9\cos\left(\frac{2\pi}{365}(t-9)\right)$
Native surface	0.5	0.5	$-1.9-10.0\cos\left(\frac{2\pi}{365}(t-9)\right)$

the coupled TEMP/W and SEEP/W analysis, and for assigning some of the boundary conditions and material properties to the SEEP/W model.

The ACE material was modeled using the full thermal material model in TEMP/W. The material properties were taken directly from Goering and Kumar (1996) and are summarized in Table 6.5. The volumetric moisture content of the ACE was essentially zero; however, a value of 0.01 m^3/m^3 was assigned in order for the TEMP/W software to solve the governing equations. The surface temperature boundary conditions were established using harmonic temperature functions and freezing and thawing *n*-factors as presented in Table 6.4. At the lower boundary, a geothermal heat flux of 0.06 W/m^2 (0.456 BTU/day·ft^2) was used (Goering and Kumar 1996).

For SEEP/W, both the ACE material and foundation soil were modeled using the saturated/unsaturated material model, which requires the hydraulic conductivity versus matric suction function, volumetric water content versus matric suction function, and air conductivity versus degree of saturation function. Since it was assumed no water flow was occurring, the hydraulic conductivity was set to an arbitrarily low, constant value of 1e-5 m/day for both the ACE and foundation soil. The volumetric water content function was estimated for both materials using the "Estimate volumetric water content function" feature in SEEP/W, which estimates the function based on the selected material type and porosity. Finally, the air conductivity function was set to an arbitrarily low, constant value of 0.001 m/day for the foundation soil since it was assumed no airflow occurred in the material.

One of the most important input parameters for the model was the air conductivity function for the ACE material. Goering and Kumar (1996) provided only the intrinsic permeability of the ACE. According to GEO-SLOPE International Ltd. (2012b), estimation of the air conductivity from the relationship between conductivity and intrinsic permeability results in an

Table 6.5 Properties of ACE material for TEMP/W and SEEP/W analysis.

Property	Value (SI)	Value (US Customary)
Thermal conductivity	29.89 kJ/day·m·°C	4.80 BTU/day·ft·°F
Specific heat	1,006 kJ/m^3·°C	15 BTU/ft^3·°F
Volumetric water content	0.01 m^3/m^3	0.01 ft^3/ft^3
Hydraulic Conductivity	1e-5 m/day	3.28×10^{-5} ft/day
Air Conductivity	20,000 m/day	65,617 ft/day

equivalent air conductivity of approximately 36,000 m/day. Such an extremely high air conductivity value can lead to termination of the solver due to ill-conditioned global finite element matrices (GEO-SLOPE International Ltd. 2012b). In their case history analysis, GEO-SLOPE International Ltd. (2012b) used an air conductivity value of 10,000 m/day and were able to achieve results comparable to those reported by Goering and Kumar (1996).

In 1999, Goering and Kumar reported on modeling the same embankment using the same geometry and material properties; however, they investigated the impact of changing the intrinsic permeability of the embankment (Goering and Kumar 1999). The model was run using intrinsic permeabilities of 1.86×10^{-6}, 6.32×10^{-7}, and 6.32×10^{-8} for the embankment, representing high, base, and low permeability conditions, respectively. The mean annual temperature at the embankment/foundation soil interface is presented in Figure 6.3.

Although the high permeability material had an intrinsic permeability an order of magnitude greater than the base permeability material, there was little difference in the mean annual temperature beneath the embankment. These results indicated that there was a limit to how high the permeability of the material could be increased before there was no significant change in cooling beneath the embankment. Therefore, it was decided to run the analysis using several different air conductivity values to determine what value would yield results most similar to those obtained by Goering and Kumar (1999), and to determine how changes in air conductivity impacted the mean annual temperature at the embankment/foundation soil interface.

The GeoStudio analysis was run using air conductivity values of 5,000, 10,000, 15,000, 20,000, and 25,000 m/day. The mean annual temperature at the embankment/foundation soil interface was calculated at the end of each analysis and the results are presented in Figure 6.4. The results show that increasing the air conductivity value decreases the mean annual temperature beneath the embankment due to increased convective heat transfer; however, it is evident that there is a limiting effect to increasing the air conductivity and beyond 20,000 m/day

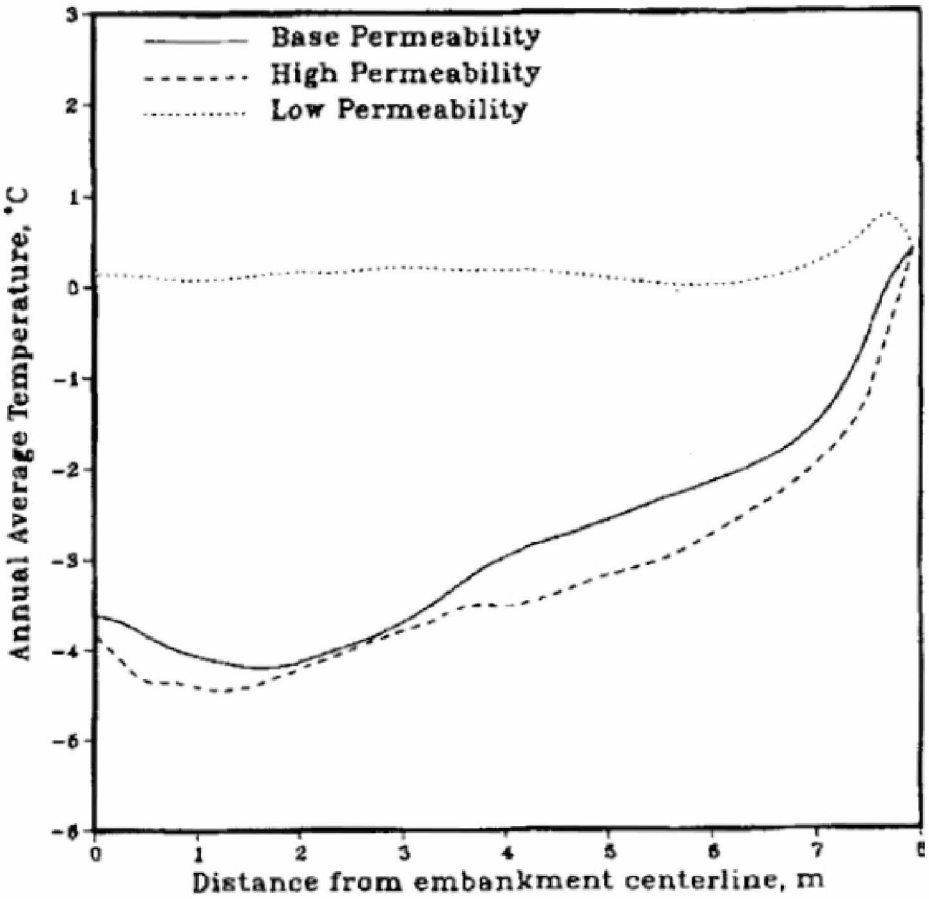

Figure 6.3 Mean annual temperature at base of embankment (Goering and Kumar 1999).

there is little decrease in mean annual temperature beneath the embankment. Comparison of the GeoStudio model results with those of Goering and Kumar revealed that an air conductivity value of 20,000 m/day produced results most similar to those of Goering and Kumar (1999).

The GeoStudio model results were plotted and compared to the results from Goering and Kumar (1999) for the exact same days of the year. The model results for Jan. 1, Mar. 3, Apr. 2, Jun. 2, Oct. 2, Nov. 2, and Dec. 2 are presented in Figures 6.5 through 6.11, respectively. The results were plotted using the same dimensions and temperature contour spacing as those of Goering and Kumar (1999). Analysis revealed that the results of the GeoStudio analysis were nearly identical to those of Goering and Kumar (1999); however, the ground temperatures shown in the GeoStudio results, especially below the active layer, were slightly warmer than the previous model. The reason for the slight difference in temperatures could be due to how each thermal model handles unfrozen water content in the soil. Another slight difference was noted between the two model results for Dec. 2, shown in Figure 6.11. The

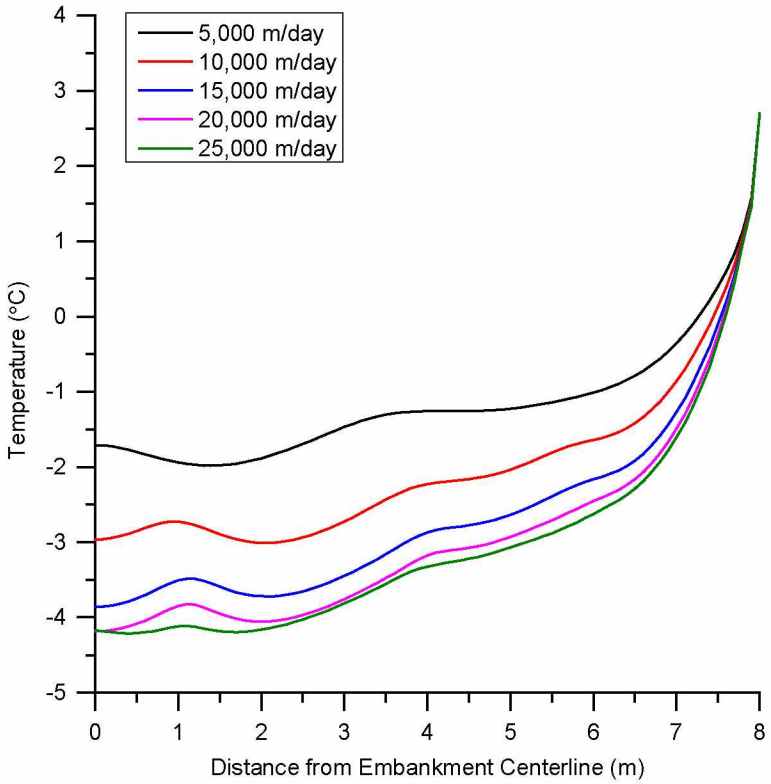

Figure 6.4 Air conductivity sensitivity analysis, showing mean annual temperature at embankment/foundation soil interface for different air conductivity values.

GeoStudio temperature contours within the embankment indicate the presence of an additional convective eddy near the center of the embankment. This could be due to slight differences in the mesh spacing for each model.

6.2 MODELING PARAMETERS

6.2.1 Model Geometry and Mesh

In order to establish the model geometry, it was first necessary to analyze the available subsurface data, surficial topography, and location and dimensions of the embankment. The subsurface test hole logs, surficial topography, and location of the embankment centerline were all provided by ADOT&PF. The ground slope beneath the embankment was estimated based on the topographic map of the project area. The GPS coordinates of the test hole locations were used to plot the test holes on the topographic map in AutoCAD. Three test holes (TH08-02, TH08-01, and TH07-1655) were used to estimate the soil stratigraphy beneath the

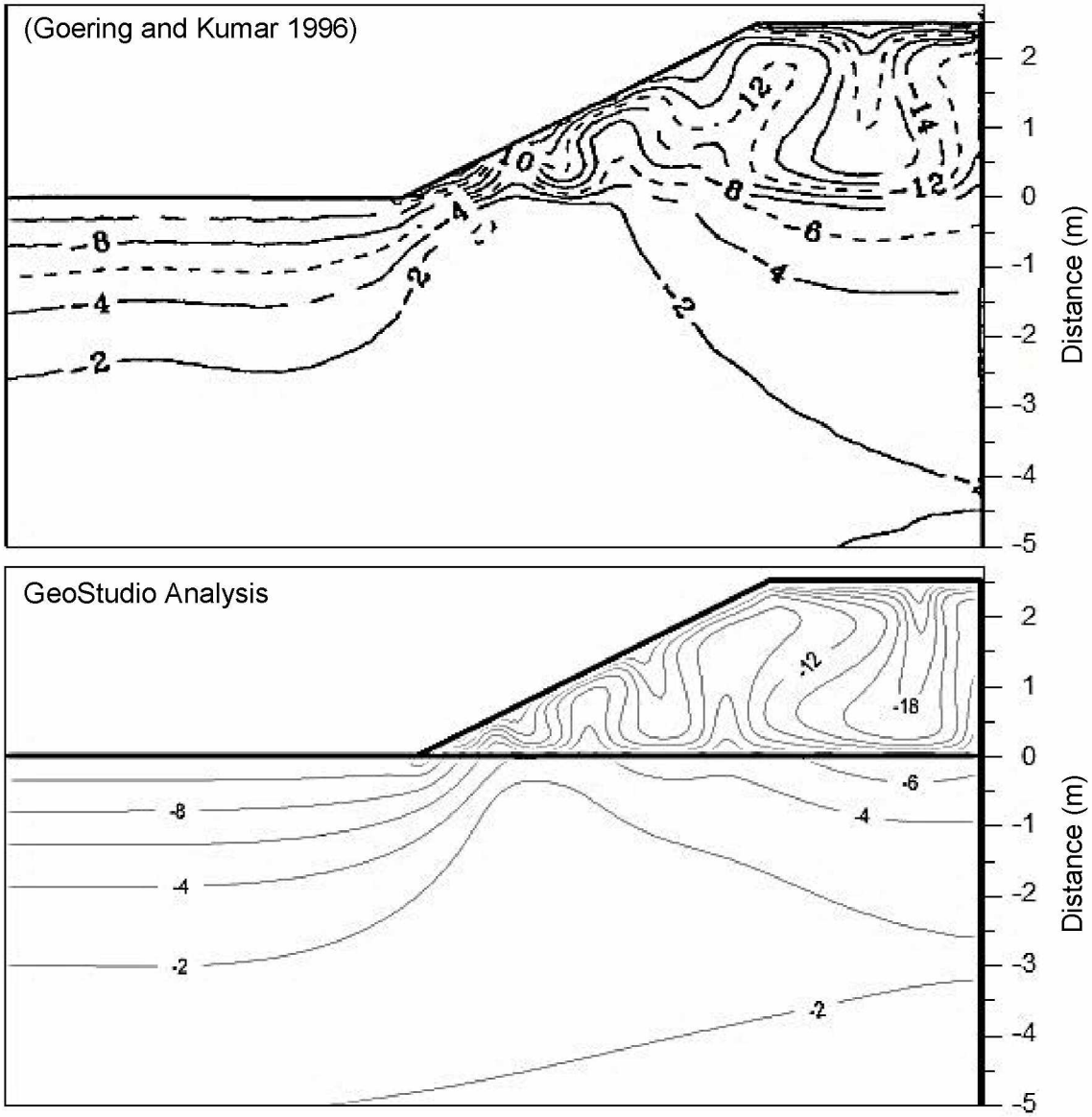

Figure 6.5 Modeling results for Jan. 1. Temperature contours are in 2°C increments.

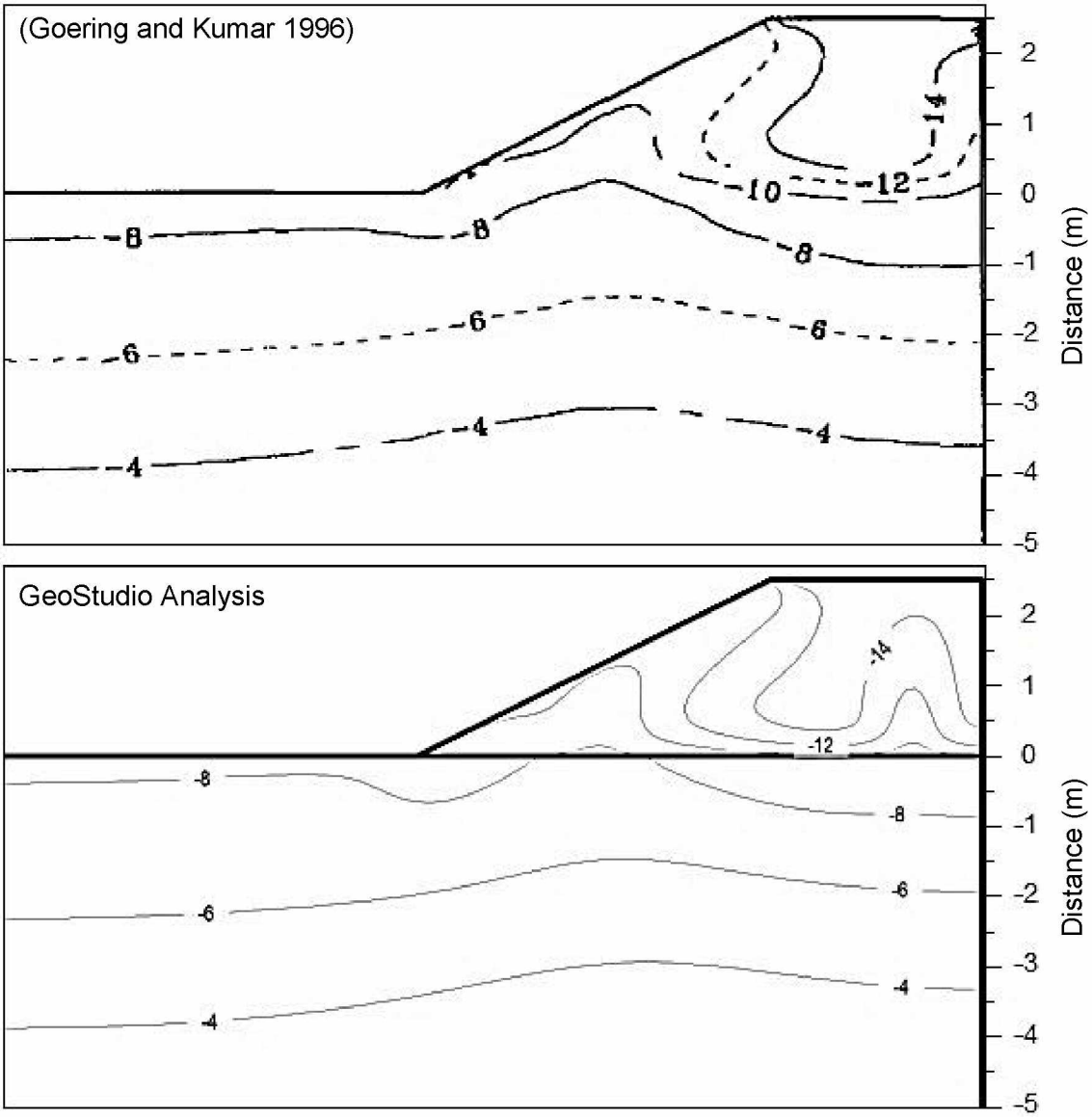

Figure 6.6 Modeling results for Mar. 3. Temperature contours are in 2°C increments.

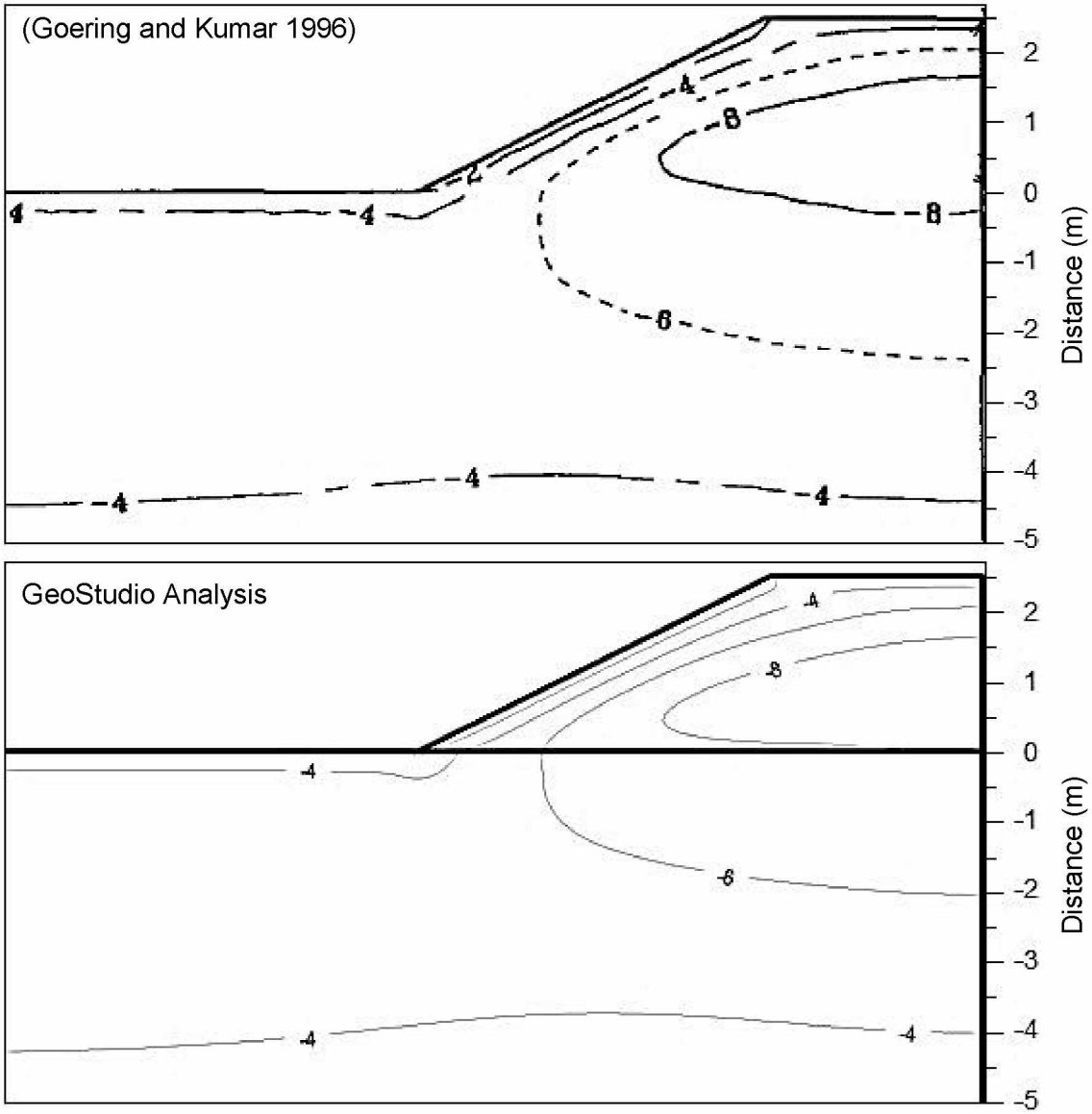

Figure 6.7 Modeling results for Apr. 2. Temperature contours are in 2°C increments.

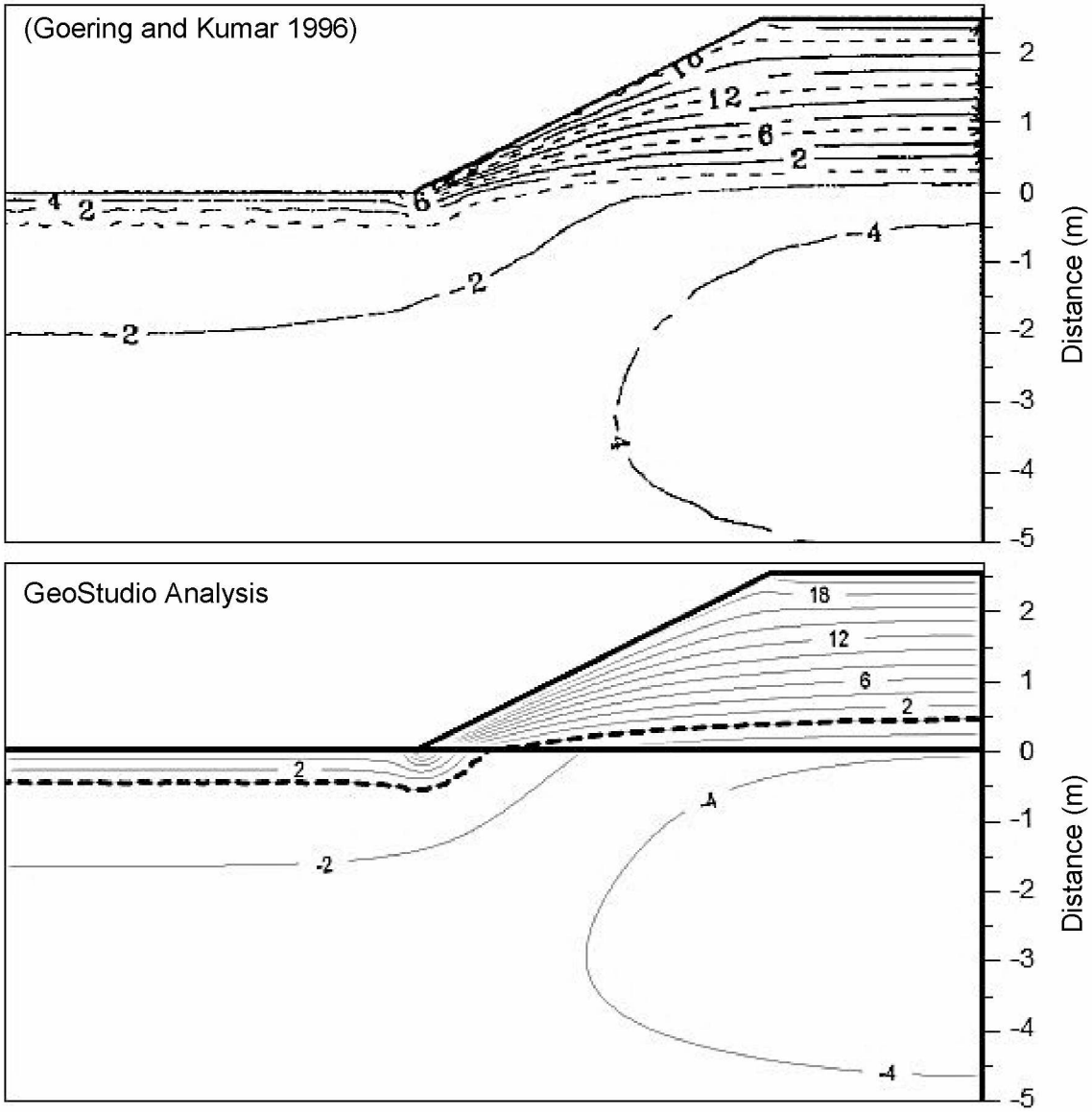

Figure 6.8 Modeling results for Jun. 2. Temperature contours are in 2°C increments.

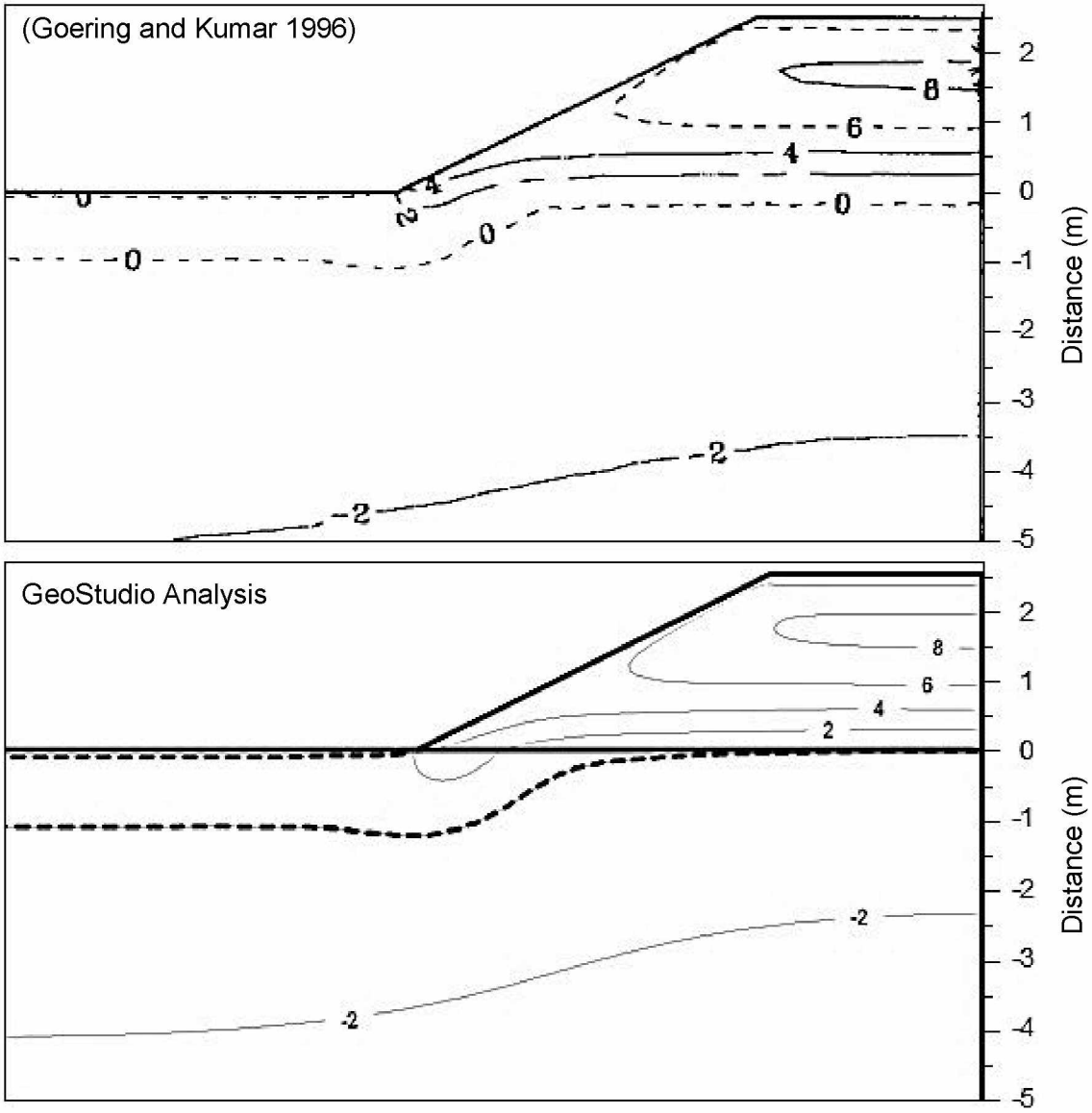

Figure 6.9 Modeling results for Oct. 2. Temperature contours are in 2°C increments.

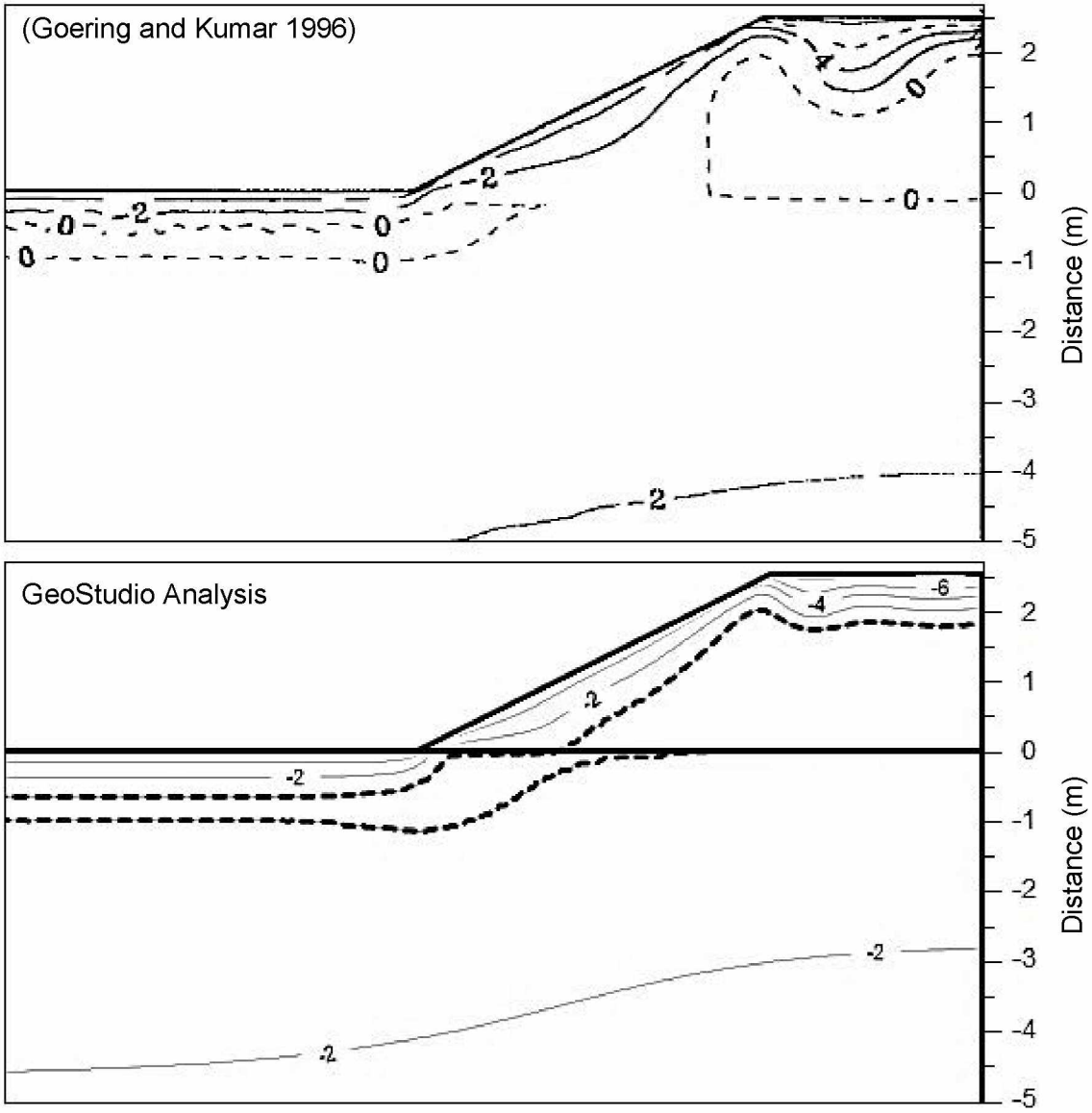

Figure 6.10 Modeling results for Nov. 2. Temperature contours are in 2°C increments.

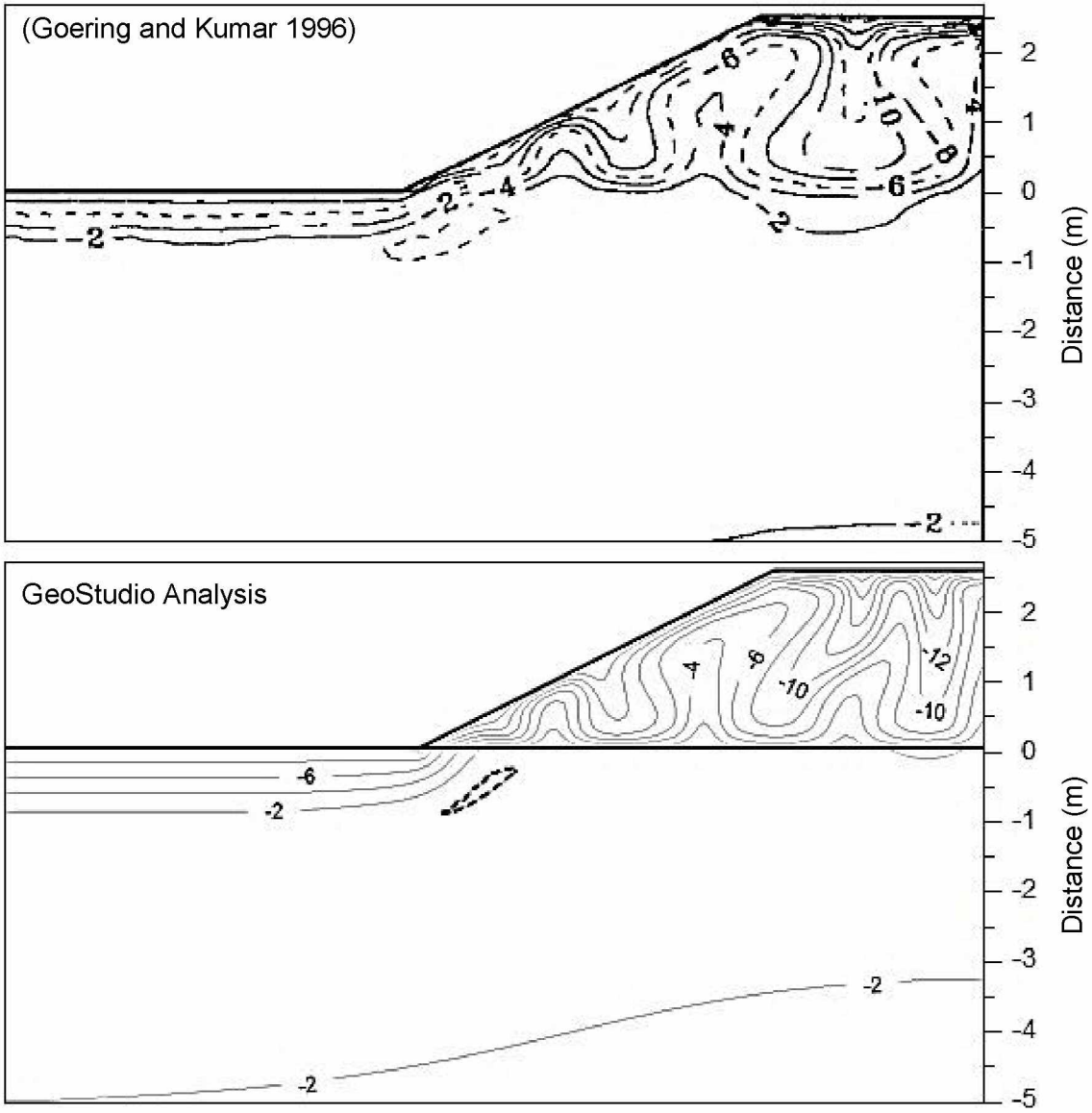

Figure 6.11 Modeling results for Dec. 2. Temperature contours are in 2°C increments.

embankment. The test holes indicated the subsurface typically consisted of 1 ft of organic material, 30.6 ft of ice-rich silt, and 4.9 ft of clay (weathered bedrock) overlying granodiorite bedrock. The slope of the ground surface was approximately 9° or 6H:1V. The embankment cross section was developed using survey data collected during and after embankment construction along the length of the instrument casings described in Chapter 3.

Given the available information, the model geometry was drafted in AutoCAD and then imported into GeoStudio where it was used to create the model regions. Since heat flow through the upper and lower boundaries was perpendicular to the boundary surface, it was necessary to create the regions so that the ground surface, soil layers, and base of the model were parallel. The entire model domain, showing the individual regions, is provided in Figure 6.12. The subsurface of the model was made 252.8-ft wide and 275-ft deep to prevent the edges of the model domain from impacting the results. A close-up view of the embankment geometry, with region labels, is shown in Figure 6.13.

A specific mesh element type and edge length were assigned to each region in the model. For the road surface course, a mesh of triangles with element edge length of 0.20 ft was used. The thermal berm and the ACE were assigned a mesh of triangles with element edge length of 0.26 ft. The organic mat was assigned a mesh of triangles with element edge length of 0.39 ft. The silt was assigned a mesh quads and triangles with an element edge length of 1.31 ft. The clay was assigned a mesh of triangles with an edge length of 5.25 ft. Finally, the bedrock was assigned a rectangular grid of quads mesh with an element length of 6.56 ft. A close-up view of the model mesh is presented in Figure 6.14.

6.2.2 Material Properties for SEEP/W

For the SEEP/W analysis it was necessary to use the saturated/unsaturated material model for all materials, requiring the following input parameters: hydraulic conductivity function, hydraulic conductivity ratio and rotation angle, volumetric water content function, and air conductivity function. It was assumed that the materials were isotropic; therefore, the hydraulic conductivity ratio was equal to 1 and the rotation angle equal to 0 for all materials.

Since the ACE was a very porous and well-drained material, and the foundation soils were fine-grained with a potentially low hydraulic conductivity, it was assumed that no water flow occurred in either material. Also, it was assumed that only the ACE experienced significant density-driven air convection; all other materials, such as the permafrost foundation soil, active layer, thermal berm, and road surface course, were assumed to experience no airflow. Based

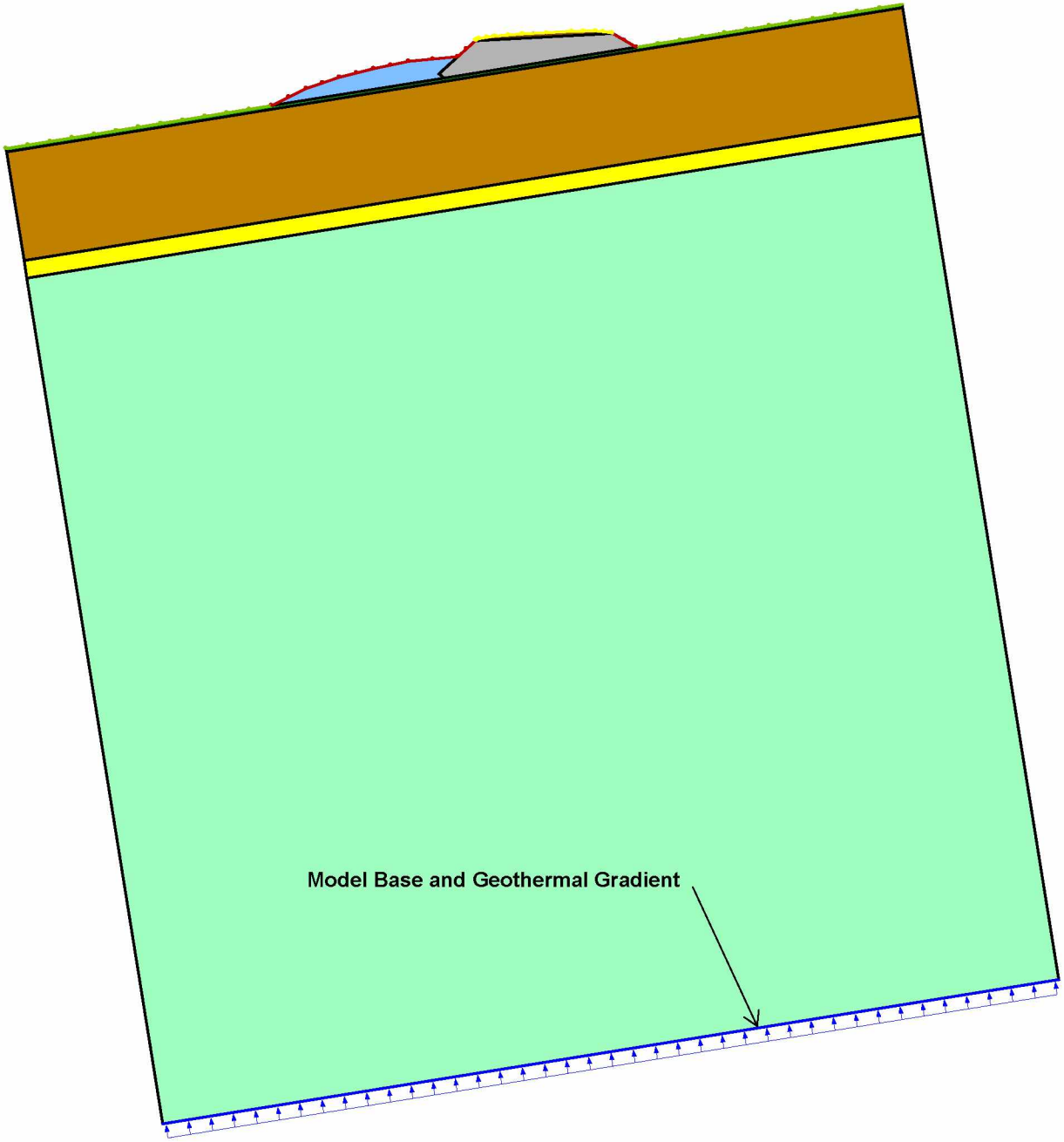

Figure 6.12 Model geometry and domain. Material types are provided in Figure 6.13.

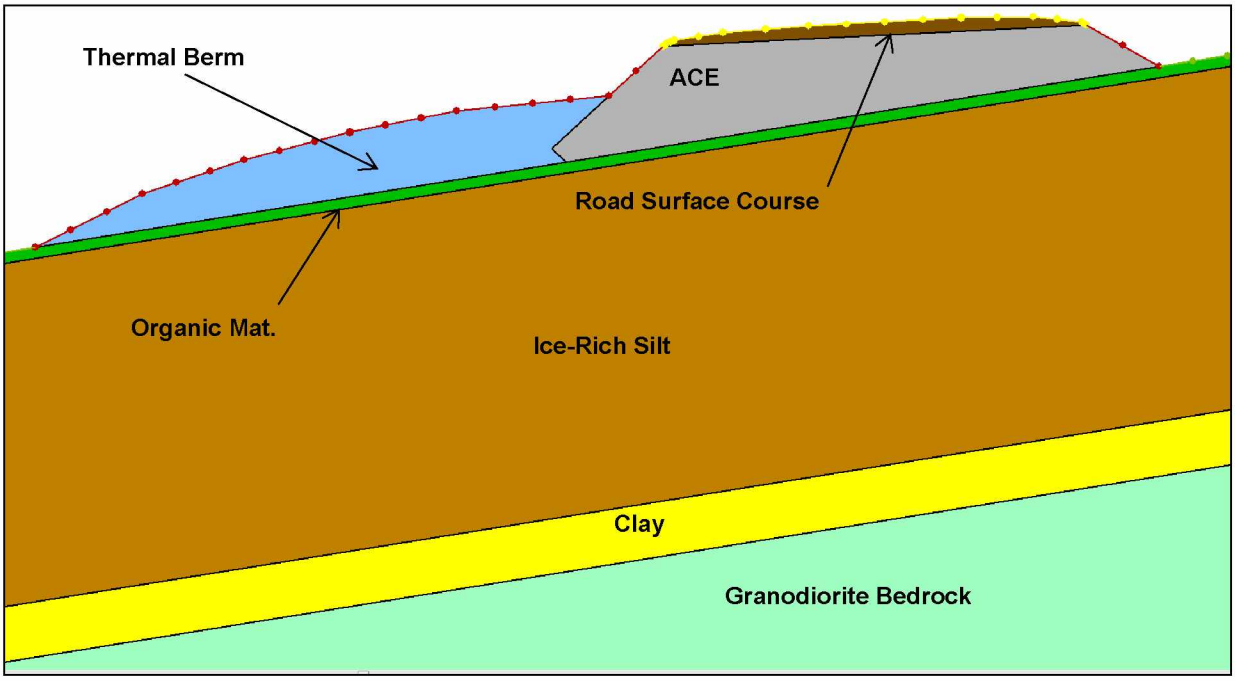

Figure 6.13 Close-up view of model geometry showing embankment materials and foundation soils.

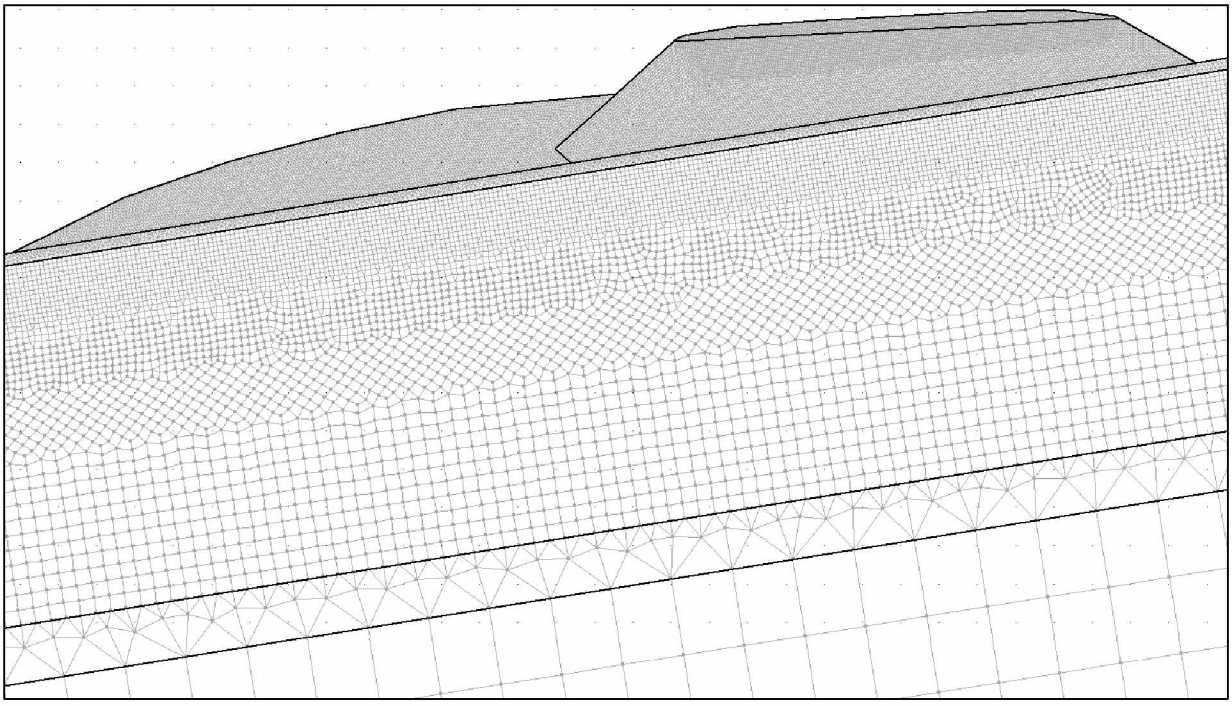

Figure 6.14 Model mesh for embankment and foundation soils.

on these assumptions, only two materials were necessary for this modeling: ACE material and non-ACE material.

For the ACE material, the hydraulic conductivity versus matric suction function was set to a constant, arbitrarily low value of 1×10^{-5} ft/day for matric suctions between 1 and 100 lb/ft^2. This essentially eliminated water movement from the numerical analysis. The volumetric water content versus matric suction function was calculated using the "Estimate Volumetric Water Content Function" for a gravel material with a saturated water content of 0.40 ft^3/ft^3. Finally, the air conductivity versus degree of saturation function was set to a constant value of 65,617 ft/day, for saturation ranging between 0 and 1, based on the results of the case study analysis presented in Subsection 6.1.1.

The non-ACE material was modeled based on arbitrary values presented by GEO-SLOPE International Ltd. (2012b). In order to restrict water flow within the non-ACE material, the hydraulic conductivity versus matric suction function was set to a constant, arbitrarily low value of 1×10^{-5} ft/day, for matric suctions between 1 and 100 lb/ft^2. To restrict airflow within the non-ACE material, the air conductivity versus degree of saturation function was set to a constant value of 0.001 ft/day, for saturation ranging between 0 and 1. Finally, the volumetric water content versus matric suction function was calculated using the "Estimate Volumetric Water Content Function" of SEEP/W for a silt material with a saturated water content of 0.36 ft^3/ft^3. A summary of the material properties necessary for the SEEP/W analysis for the ACE and non-ACE material is provided in Table 6.6.

Table 6.6 Material properties for SEEP/W.

Material	Property	Value
ACE Material	Hydraulic conductivity	1×10^{-5} ft/day
	Porosity	0.40
	Air conductivity	65,617 ft/day
Non-ACE Material	Hydraulic conductivity	1×10^{-5} ft/day
	Porosity	0.36
	Air conductivity	0.001 ft/day

6.2.3 Material Properties for TEMP/W

Two different material models were used for the TEMP/W analysis: the simplified thermal material model and the full thermal material model. The simplified thermal material model only required the frozen and unfrozen thermal conductivities, frozen and unfrozen volumetric heat capacities, and volumetric moisture content of the material. It was assumed that phase change occurred at the phase change temperature and no energy was absorbed or released during phase change. This model was only applicable to soils with low to no moisture contents, in which latent heat of phase change was negligible or nonexistent.

The full thermal model required the thermal conductivity versus temperature function, unfrozen water content versus temperature function, frozen and unfrozen volumetric heat capacities, and volumetric water content. The "Estimate Thermal Conductivity Function" feature of TEMP/W was used to approximate the thermal conductivity versus temperature curve for each material. The function required selecting the appropriate material, such as clay, silt, sand, or gravel, from the material drop down menu, and then entering the frozen and unfrozen thermal conductivities, which were obtained via lab testing or literature review. The curve was generated based on the default unfrozen water content functions used in TEMP/W for each material type. Since no lab testing was conducted to determine the unfrozen water content for each material, it was decided to use the default functions included with the TEMP/W software, in which case the material was simply selected from a dropdown menu and the function automatically generated. The volumetric moisture content and volumetric heat capacities were estimated based on lab testing data or values obtained from literature.

The ACE material was modeled using the simplified thermal material model. This model was chosen due to the ACE being exceptionally well-drained, thus having a negligible volumetric moisture content (Figure 6.15). Although the moisture content within the ACE was assumed to be zero, a volumetric water content of 0.01 ft^3/ft^3 was used in order for the model to solve the equations. Since the ACE was assumed to have a negligible moisture content, there was no change in thermal conductivity or volumetric heat capacity for the frozen and unfrozen states. According to Johansen (1977), a good estimation of thermal conductivity for dry crushed rock can be made using the following empirical equation:

$$\lambda = 0.039 \cdot n^{-2.2} \pm 25\% \qquad (6.14)$$

where λ is thermal conductivity in W/m·°C and n is porosity (0 to 1). In order to utilize Equation 6.14, the porosity of the ACE material had to be estimated.

Figure 6.15 Photograph of ACE material showing an approximately 3 ft by 2 ft area.

According to Latham et al. (2002), the average void porosity of coastal armor stone is approximately 34%. A tech sheet from StormTech International (2012) advised that a porosity of 40% be used for clean, open-graded, crushed stone. Based on these sources, the higher porosity of 40% was assumed for the ACE material. Using this value in Equation 6.14 and converting the result to English units yielded a frozen/unfrozen thermal conductivity of approximately 4.1 BTU/day·ft·°F for the ACE material.

The volumetric heat capacity of the material was estimated by multiplying the specific heat capacity of each soil constituent by its respective mass fraction as a percent of dry soil weight, and then summing the results and multiplying by the dry unit weight of the soil:

$$c = \gamma_d \left[c_s + c_w w_u + c_i w_f \right] \tag{6.15}$$

where c is volumetric heat capacity in BTU/ft^3·°F, γ_d is dry unit weight in lb/ft^3, c_s, c_w, and c_i are specific heat capacities of soil particles (approximately 0.17 for most soils), water, and ice, respectively, in BTU/lb·°F, and w_u and w_f are the unfrozen and frozen water contents, respectively, as percent of dry weight of soil. Using porosity of 40%, and assuming the solid rock particles had a specific weight of 173.9 lb/ft^3 (Waples and Waples 2004), the dry unit weight was estimated to be 104.3 lb/ft^3. Assuming a frozen and unfrozen water content of

approximately zero, and a specific heat capacity of 0.19 BTU/lb·°F for solid granodiorite (Adl-Zarrabi 2006), yielded a frozen/unfrozen volumetric heat capacity of 19.7 BTU/ft^3·°F. Table 6.7 is a summary of the material properties used for the ACE and other materials in TEMP/W. The properties estimated were similar to those used by Goering (2003) (see Table 6.8) for numerical modeling of an ACE, which was composed of crushed rock material with diameters ranging from 2 to 3 in., porosity of 35%, and dry density of 101.4 lb/ft^3.

As with the ACE material, the granodiorite bedrock was modeled using the simplified thermal material model. This model was chosen due to the expected low moisture content in the bedrock material and the expectation that the bedrock would not undergo significant phase change within the chosen modeling time period.

Since it was not possible to obtain samples for testing during 2012, the thermal conductivity, volumetric heat capacity, and volumetric water content of the bedrock had to be estimated. According to ADOT&PF test hole data, two samples of bedrock material were collected from test holes TH08-9 and TH08-10 in 2008. The samples were taken from approximately 5 ft into the bedrock, and laboratory testing revealed gravimetric water contents of 16.0% and 7.1%. The high water content was likely due to the bedrock being highly fractured and weathered near the surface; however, it was assumed that the bedrock would be less fractured and have much lower water content with depth. Therefore, the results from the ADOT&PF samples were not used; instead, the model was simplified and it was assumed that the bedrock material was solid from its surface downward.

A negligible volumetric moisture content was assumed for the solid bedrock; however, in order to solve the equations in TEMP/W, a value of 0.01 ft^3/ft^3 was used. The frozen/unfrozen thermal conductivity of the bedrock was estimated as 37.4 BTU/day·ft·°F based on the thermal conductivity of solid granodiorite (Muhll and Haeberli 1990). The frozen/unfrozen volumetric heat capacity was estimated using Equation 6.15, with the assumption that solid granodiorite rock had a dry unit weight of 173.9 lb/ft^3 (Waples and Waples 2004), a specific heat capacity of 0.19 BTU/lb·°F (Adl-Zarrabi 2006), and moisture content of zero. The resulting frozen/unfrozen volumetric heat capacity was approximately 32.8 BTU/ft^3·°F.

The road surface course material was modeled using the full thermal material model. Proctor tests conducted by ADOT&PF indicated a typical optimum gravimetric moisture content and maximum dry unit weight of 6.7% and 133.8 lb/ft^3, respectively. Although the material had low moisture content, it was decided that the effect of latent heat should be accounted for since there was enough moisture to result in slightly different frozen and unfrozen thermal conductivities and volumetric heat capacities.

Table 6.7 Material properties for TEMP/W. The symbol "–" indicates no data, γ_d is dry unit weight, K_u and K_f are unfrozen and frozen thermal conductivity, respectively, C_u and C_f are unfrozen and frozen volumetric heat capacity, respectively, and θ is volumetric water content.

Material Type	Porosity (%)	γ_d (lb/ft^3)	K_u $\left(\frac{BTU}{day \cdot ft \cdot ^\circ F}\right)$	K_f $\left(\frac{BTU}{day \cdot ft \cdot ^\circ F}\right)$	C_u $\left(\frac{BTU}{ft^3 \cdot ^\circ F}\right)$	C_f $\left(\frac{BTU}{ft^3 \cdot ^\circ F}\right)$	θ (%)
ACE	40	104.3	4.1	4.1	19.7	19.7	1.0
Granodiorite Bedrock	–	173.9	37.4	37.4	32.8	32.8	1.0
Road Surface Course	–	133.8	42.6	46.7	31.7	27.2	14.0
Ice-Rich Silt	–	40.2	12.9	23.5	51.6	30.3	66.3
Thermal Berm	–	125.0	39.0	48.7	33.6	27.4	20.6
Clay	–	–	24.0	28.8	41.8	30.3	37.0
Peat	–	17.1	8.8	21.6	57.5	32.2	81.2

Table 6.8 Thermal and hydraulic properties for embankment aggregate (Goering 2003).

Property	Value
Thermal Conductivity	4.80 BTU/day·ft·°F
Specific heat	15.21 BTU/ft^3·°F
Latent heat	≈ 0
Permeability	6.78×10^{-6} ft^2

Since the material was coarse-grained and compacted, it was too difficult to use the needle probe to measure the thermal conductivity in the field; therefore empirical methods were used to obtain an estimate. The unfrozen and frozen thermal conductivity of coarse-grained soils, with a moisture content of at least 1%, can be calculated with an estimated accuracy of approximately ±25% using the following empirical equations set forth by Kersten:

$$K_u = 0.1442\left(0.7\times\log(w\%)+0.4\right)10^{0.6243\gamma_d} \quad (6.16)$$

$$K_f = 0.01096\times10^{0.8116\gamma_d} + 0.00461\times10^{0.9115\gamma_d}(w\%) \quad (6.17)$$

where K_u and K_f are the unfrozen and frozen thermal conductivity, respectively, in W/m·K, w is the gravimetric water content, and γ_d is the dry unit weight in g/cm^3 (Farouki 1981). Using Equations 6.16 and 6.17 with the data obtained from ADOT&PF, and converting the results to

English units, yielded frozen and unfrozen thermal conductivities of approximately 46.7 and 42.6 BTU/day·ft·°F, respectively.

Equation 6.15 was used to estimate the frozen and unfrozen volumetric heat capacities. The dry unit weight and gravimetric water content obtained from ADOT&PF were used in the calculations. Since the bedrock in the area was primarily granodiorite, and the material used for the road surface course was obtained locally, the specific heat capacity of granodiorite was used in Equation 6.15 for the specific heat capacity of the soil particles. Based on the dry unit weight and gravimetric water content, the volumetric water content was estimated to be 14.0%.

The ice-rich silt was modeled using the full thermal material model, which was considered appropriate due to the high water content. Several frozen samples were collected from the site to determine gravimetric moisture content, volumetric moisture content, dry unit weight, and frozen/unfrozen thermal conductivity; the average values obtained from laboratory testing, for undisturbed and consolidated samples, are summarized in Table 6.9.

Although samples were only obtained down to 5 ft below the ground surface, there was evidence to support that the material properties likely remained consistent with depth. Several samples obtained by ADOT&PF in 2008 indicated an average gravimetric water content of 109.3% from various depths down to bedrock; the average gravimetric water content obtained from lab testing was 106.0%.

Equation 6.15 was used to estimate the frozen and unfrozen volumetric heat capacities of the ice-rich silt. Drill data from 2008 revealed an average organic content of approximately 11.7%. The specific heat capacity of the organic material was assumed to be 0.46 BTU/lb·°F (Williams and Smith 1989). Using the dry unit weight and gravimetric water content values from Table 6.9, and an assumed specific heat capacity of soil solids of 0.17 BTU/lb·°F, the frozen and unfrozen volumetric heat capacities were calculated as 30.3 and 51.6 BTU/ft^3·°F, respectively, for the unconsolidated silt. For the consolidated sit, the frozen and unfrozen volumetric heat capacities were calculated as 33.3 and 51.3 BTU/ft^3·°F, respectively. Only minor differences exist between the volumetric heat capacities of the unconsolidated and consolidated samples. This is likely due to the fact that the water content, although less for the consolidated samples, was still quite high and was accompanied by an increase in dry unit weight after consolidation, which resulted in little change in volumetric heat capacity. Based on these results, the unconsolidated physical and thermal properties for ice-rich silt were used for modeling.

The thermal berm material was modeled using the full thermal material model. Based on laboratory results of three samples, the thermal berm material was well-graded gravel with an

Table 6.9 Average physical and thermal properties of ice-rich silt from laboratory testing. Consolidated samples are indicated by "(cons)", "–" indicates no data, w is gravimetric water content, θ is volumetric water content, γ is unit weight, γ_d is dry unit weight, ε_v is thaw strain, and K_f and K_u are frozen and unfrozen thermal conductivity, respectively.

Soil Type	w (%)	θ (%)	γ (lb/ft^3)	γ_d (lb/ft^3)	ε_v (%)	K_f $\left(\frac{BTU}{day \cdot ft \cdot °F}\right)$	K_u $\left(\frac{BTU}{day \cdot ft \cdot °F}\right)$
Silt w/ sand & org.	106.0	66.3	81.6	40.2	40.0	23.5	12.9
Silt w/ sand & org. (cons)	52.8	53.8	101.8	68.2	–	20.8	12.1

average gravimetric water content of 9.9%. The typical ranges for maximum dry unit weight and optimum moisture content for well-graded gravel are 125-135 lb/ft^3 and 8-11%, respectively (Lindeburg 2012). Assuming a dry unit weight of 125 lb/ft^3, and given a gravimetric water content of 9.9%, the volumetric water content was approximately 19.8%; however, a slightly higher value of 20.6% was used for modeling to account for potentially higher water content due to precipitation over time and poor drainage beneath the embankment. Using Equation 6.15, the frozen and unfrozen volumetric heat capacities were calculated as 27.4 and 33.6 BTU/ft^3·°F, respectively. Equations 6.16 and 6.17 were used to estimate the unfrozen and frozen thermal conductivities of the thermal berm material. Using the gravimetric water content from laboratory testing and the estimated dry unit weight, the unfrozen and frozen thermal conductivities were calculated as 39.0 and 48.7 BTU/day·ft·°F, respectively.

The clay was modeled using the full thermal material model. No samples of the clay material were collected for laboratory testing; therefore, the thermal properties and water content were estimated entirely from typical values from literature. The frozen and unfrozen thermal conductivities used for clay, with a volumetric water content of 37%, were assumed to be 28.8 and 24.0 BTU/day·ft·°F, respectively (Darrow 2011). The assumed frozen and unfrozen volumetric heat capacities were 30.3 and 41.8 BTU/ft^3·°F, respectively (Darrow 2011).

The organic material or peat was modeled using the full thermal material model due to the extremely high water content. Several samples were collected from the frozen peat within the active layer. Laboratory testing was conducted to determine the physical and thermal properties for both unconsolidated and consolidated peat; the results are summarized in Table 6.10. As with the ice-rich silt, volumetric water content decreased substantially after

Table 6.10 Average physical and thermal properties of peat from laboratory testing. Consolidated samples are indicated by "(cons)", "– " indicates no data, w and θ are gravimetric and volumetric water content, respectively, γ is unit weight, γ_d is dry unit weight, ε_v is thaw strain, and K_f and K_u are frozen and unfrozen thermal conductivity, respectively.

Soil Type	w (%)	θ (%)	γ (lb/ft^3)	γ_d (lb/ft^3)	ε_v (%)	K_f $\left(\frac{BTU}{day \cdot ft \cdot °F}\right)$	K_u $\left(\frac{BTU}{day \cdot ft \cdot °F}\right)$
Peat w/ silt	245.2	81.2	67.8	17.1	53.6	21.6	8.8
Peat w/ silt (cons)	88.4	66.6	90.9	49.3	–	21.4	10.4

consolidation; however, there was little change between the unconsolidated and consolidated thermal conductivities.

To estimate volumetric heat capacity, it was assumed that the material solids were composed entirely of organic matter. Using a specific heat capacity of organics of 0.46 BTU/lb·°F (Williams and Smith 1989), and the gravimetric water content and dry unit weight from Table 6.10, the volumetric heat capacity was calculated using Equation 6.15. The unfrozen and frozen volumetric heat capacities for unconsolidated peat were 49.7 BTU/ft^3·°F and 28.7 BTU/ft^3·°F, respectively, while the unfrozen and frozen values for consolidated peat were 67.6 BTU/ft^3·°F and 37.3 BTU/ft^3·°F, respectively.

Given the dry unit weight, volumetric water content, and bulk unit weight of the peat, it was possible to estimate the volume of silt and organics using soil weight-volume relationships. Using published values of unit weights for water, organics, and silt (Williams and Smith 1989), the solver function in Excel was used to find the volume of silt and organics for which the unit weight, dry unit weight, and water content of the soil, obtained through laboratory testing, would be satisfied. The results indicated that the unconsolidated soil was composed of 81.24% water, 2.15% silt, and 16.61% organics by volume. The dry unit weight of the soil as a percent of silt then was calculated, as was the gravimetric water content and organic content. Using Equation 6.15 yielded unfrozen and frozen volumetric heat capacities of 57.5 BTU/ft^3·°F and 32.2 BTU/ft^3·°F, respectively, for the unconsolidated peat. These results are slightly higher than those obtained using the assumption that the soil is composed entirely of organics and water. The calculations were repeated using laboratory data for the consolidated soil. The results indicated that the consolidated soil was composed of 66.55% water, 26.11% silt, and 7.34% organics. The solver function was unable to find a solution for which the volume of organics was greater than the volume of silt; therefore, it was decided to use the values for the

unconsolidated soil. The final physical and thermal properties of the peat used in TEMP/W are summarized in Table 6.7.

6.2.4 Boundary Conditions

Four different ACE scenarios were modeled to simulate a plowed and unplowed gravel driving surface and a closed and open air flow boundary along the ACE side slopes. The closed air flow boundary prevented any outside air from flowing into or out of the ACE, while the open air flow boundary allowed air to infiltrate and exit the embankment. The first scenario was an ACE with a plowed gravel driving surface and a closed air flow boundary (plowed-closed). The second scenario was an ACE with a snow-covered gravel driving surface and closed air flow boundary (snow-closed). The third model was an ACE with a plowed gravel driving surface and an open air flow boundary (plowed-open). Finally, the fourth model was an ACE with a snow-covered gravel driving surface and an open air flow boundary (snow-open).

The SEEP/W boundary conditions for the models consisted of a hydraulic boundary and an air boundary. For all the model scenarios, a constant hydraulic head of 0 ft was assigned to all regions to eliminate water movement. For the plowed-closed and snow-closed models, a zero air flow boundary was applied to the undisturbed ground and embankment surfaces to prevent atmospheric air from flowing into or out of the embankment.

For the plowed-open and snow-open models, a zero air flow boundary was applied to the undisturbed ground and embankment driving surface. An air pressure boundary was applied to the side slopes of the ACE to allow air to flow into and out of the embankment. Since the elevation along the side slopes of the ACE changed from one node to the next, a constant air pressure of 0 psi could not be applied to all the nodes. Instead, the node at the highest elevation was assigned constant air pressure of 0 psi while the nodes at lower elevations were assigned slightly greater pressures using the unit weight of air at 68°F as follows:

$$P = \left(0.07516 \text{ lb/ft}^3\right)(y)\left(0.006944 \text{ ft}^2/\text{in}^2\right) \quad (6.18)$$

where P is pressure (psi) and y is the absolute change in elevation (ft) from the highest node.

The TEMP/W boundary conditions consisted of temperature boundary functions applied to the ground surfaces and a heat flux boundary applied to the bottom surface (see Figure 6.12). For all of the models, a constant heat flux of 0.670 BTU/day·ft^2 was applied to the lower boundary to simulate the average geothermal heat flux in Interior Alaska (Williams et al. 2006).

Three surface temperature boundary functions were used to simulate natural ground, a gravel surface snow-covered in winter, and a gravel surface plowed in winter. To create the surface temperature boundary functions, *n*-factors (i.e., ratios of the air thawing or freezing indices to the surface thawing or freezing indices) were applied to the model air temperature function. The model air temperatures were taken from the historical mean daily air temperatures from 1981 to 2010 (see Figure 2.4) recorded at Chicken.

For the natural ground, a freezing *n*-factor (n_f) of 0.30 and a thawing *n*-factor (n_t) of 0.38 were used. The values were derived by slightly adjusting the *n*-factors for spruce trees, brush, and moss over peat (n_f = 0.29 and n_t = 0.37) until the typical active layer thickness and ground temperatures were achieved in the model (GEO-SLOPE Ltd. 2012d). For snow-covered gravel, an n_f of 0.50 and an n_t of 1.50 were used modified from values from Darrow and Xu (2011). Finally, for the plowed road surface an n_f of 0.90 and an n_t of 1.50 were used (Darrow and Xu 2011). The model freezing and thawing *n*-factors are summarized in Table 6.11.

The natural ground boundary condition was applied to the undisturbed ground in all the modeling scenarios. The plowed-closed and plowed-open models had the snow-covered gravel boundary condition applied to the surface of the thermal berm and side slopes of the ACE, while the plowed road surface boundary was applied to the road driving surface. Finally, the snow-closed and snow-open models had the snow-covered gravel boundary condition applied to the thermal berm, ACE side slopes, and road driving surface.

6.2.5 Modeling Stages and Time Stepping

The first step of the thermal modeling was to develop the initial ground temperatures for the two-dimensional model. It was necessary to run a transient model for an extended period of time until the model reached thermal equilibrium using the assigned natural ground surface and geothermal heat flux boundary conditions. To reduce the modeling time required, a "one-dimensional" model was developed, which was a two-dimensional model of the subsurface soils

Table 6.11 Model freezing and thawing *n*-factors.

Surface Type	Freezing *n*-factor	Thawing *n*-factor
Natural Ground	0.30	0.38
Snow-Covered Gravel	0.50	1.50
Plowed Road Surface	0.90	1.50

with a top width of 10 ft and a depth of 275 ft. It used the same soil profile and material properties as the full-width model (see Figure 6.12).

The "one-dimensional" model was run for 820 years to achieve thermal equilibrium. The process was repeated several times, slightly adjusting the natural ground *n*-factors until a reasonable active layer thickness (i.e., 1.5 ft measured at the site) and ground temperature profile were achieved. The final adjusted natural ground *n*-factors are presented in Table 6.11. The final temperature distribution from the "one-dimensional" model was exported and used as the spatial temperature profile for the initial ground temperatures in the full-width two-dimensional model.

All the two-dimensional model scenarios used the same modeling stages and time stepping. First, a transient model of the existing ground with no embankment was run for a period of 5 years beginning on Jan. 1 of year 1 and ending on Jan. 1 of year 5 (day 1,825). The transient model used the spatial temperature profile from the "one-dimensional" model for the initial temperatures, and 1 day time steps with results saved once at the end of the time period.

A transient model of the natural ground then was run from Jan. 1 to Aug. 1 of the same year using the results of the first transient model for the initial temperatures. In all subsequent models, the final results of the previous model were used for initial temperatures. The transient model used 1 day time steps with results saved once at the end of the time period. At this stage (day 2,038), the embankment was introduced into the model to simulate the approximate time of year it was finished being constructed. The model was run from Aug. 1 to Jan. 1, using 1 day time steps with results saved every 5 days.

Next, the model was run for a period of 20 years (days 2,038 to 9,490) to reach thermal equilibrium. The model was run using 0.25 day time steps with results saved every 30 days. Unfortunately, due to the size and complexity of the model, it was necessary to run 20 separate transient analyses (one for each modeled year) in series to prevent the software from crashing. The results from each analysis were used for the initial temperatures of the next analysis.

After the 20 year period, the model was run for a period of one year, using 0.25 day time steps, with results saved every day. The model was ended on Jan. 1, day 9,855, for a total modeling period of 27 years. The TEMP/W and SEEP/W results for the final year for each modeling scenario were exported for further analysis. The results included screen captures of the TEMP/W temperature contours and SEEP/W air velocity vectors for the first day of each month, and temperatures at the embankment/foundation soil interface for each day.

6.3 RESULTS AND ANALYSIS

6.3.1 Numerical Modeling Results

After the "one-dimensional" model of the undisturbed ground reached thermal equilibrium, the ground temperatures with depth were plotted for Jan., Mar., May, Jul., Sep., and Nov. as shown in Figure 6.16. The results indicated the bottom of permafrost was approximately 255 ft below the ground surface with a depth of zero annual amplitude at approximately 30 ft. The typical depth to bottom of permafrost in the Chicken area ranges from 240 to 361 ft (Jorgenson et al. 2008); thus the model results are reasonable. A close-up view of the ground temperature results (0 to 30 ft depth) is presented in Figure 6.17 and indicates an active layer thickness of approximately 1.5 ft, which is similar to what was observed from field measurements at the site. The temperature at the depth of zero annual amplitude is approximately 28°F, which is reasonable, although approximately 2°F colder than temperatures measured in the region (Jorgenson et al. 2008).

The modeling results for Jan. 1, Mar. 1, May 1, Jul. 1, Sep. 1, and Nov. 1 in the 27th year for each model scenario are presented in this subsection. The modeling results consist of two-dimensional temperature contours from the TEMP/W analyses and air velocity vectors from the SEEP/W analyses. The temperature contours show the changes in temperature within the embankment and foundation soils over time, while the air velocity vectors shows the changes in air flow intensity within the ACE.

The plowed-closed model results for Jan. 1, Mar. 1, May 1, Jul. 1, Sep. 1, and Nov. 1 are presented in Figures 6.18 through 6.23, respectively. The temperature results for Jan. 1 show the ACE experiencing significant convective heat transfer and the air velocity vectors show the formation of convection eddies within the ACE. By Mar. 1, the temperatures at the surface of the ACE are warmer and the convective heat transfer is less pronounced as well as the air velocity vectors in the ACE. On May 1, the temperature contours and air velocity vectors show that air convection within the ACE has essentially stopped and conductive heat transfer is dominating. On Jul. 1, conductive heat transfer is still controlling, and thawing deeper than the typical active layer depth is evident beneath the toe of the thermal berm and under the uphill embankment toe, while the bottom of the ACE remains frozen. Results for Sep. 1 show the maximum seasonal thawing, with the deepest and most extensive thawing occurring beneath the thermal berm while thawing beneath the ACE does not penetrate the original ground surface. Finally, by

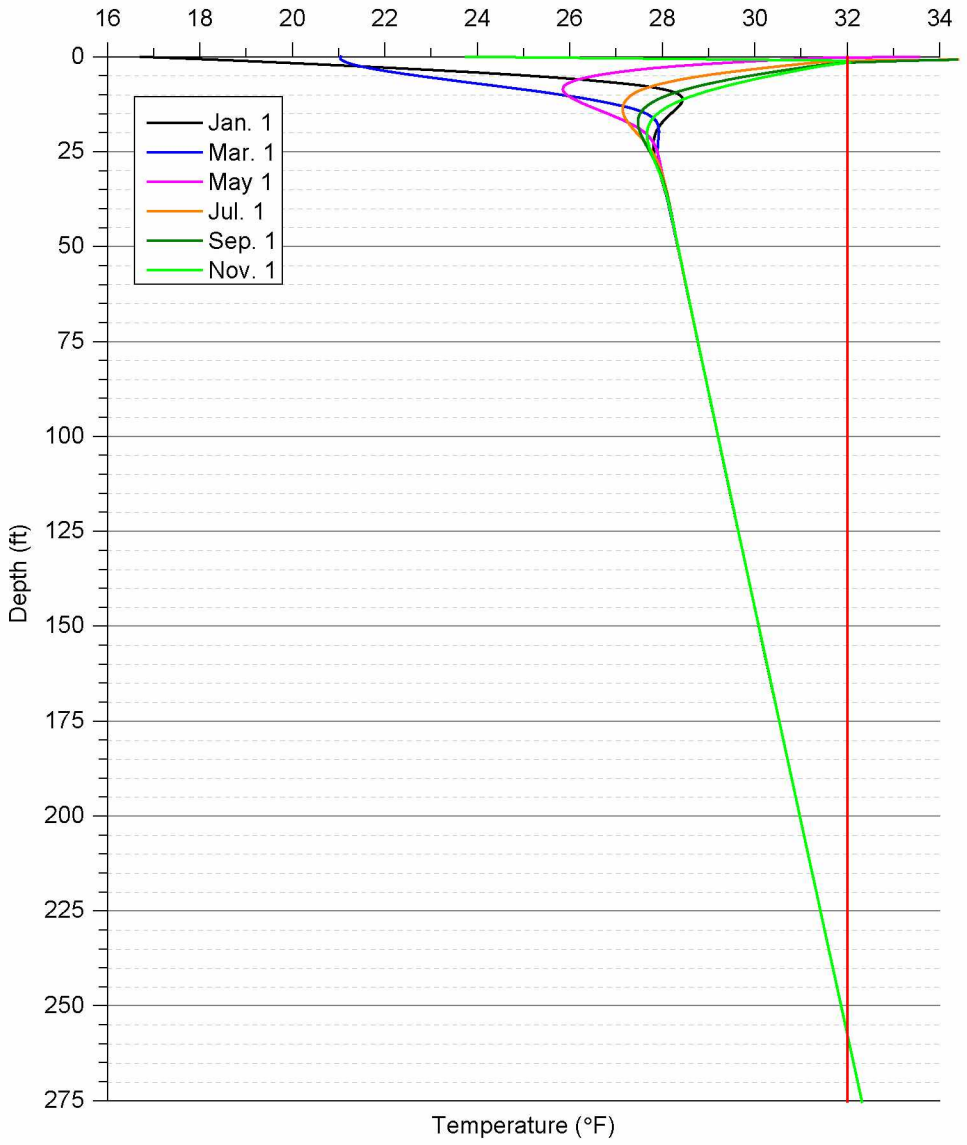

Figure 6.16 Ground temperature versus depth (0 to 275 ft).

Nov. 1, the embankment surface temperatures have cooled enough to begin causing air convection to occur within the ACE.

The plowed-open model results for Jan. 1, Mar. 1, May 1, Jul. 1, Sep. 1, and Nov. 1 are presented in Figures 6.24 through 6.29, respectively. The temperature results throughout the year are very similar to those of the plowed-closed model. The air velocity vectors show that air flows in and out of the ACE along the side slopes where the air pressure boundary conditions were applied. The air flows into the ACE at the top of each side slope and flows out at the bottom. Although circular air convection eddies form similar to the plowed-closed model, the air generally flows into the right side slope of the embankment and out the left side slope.

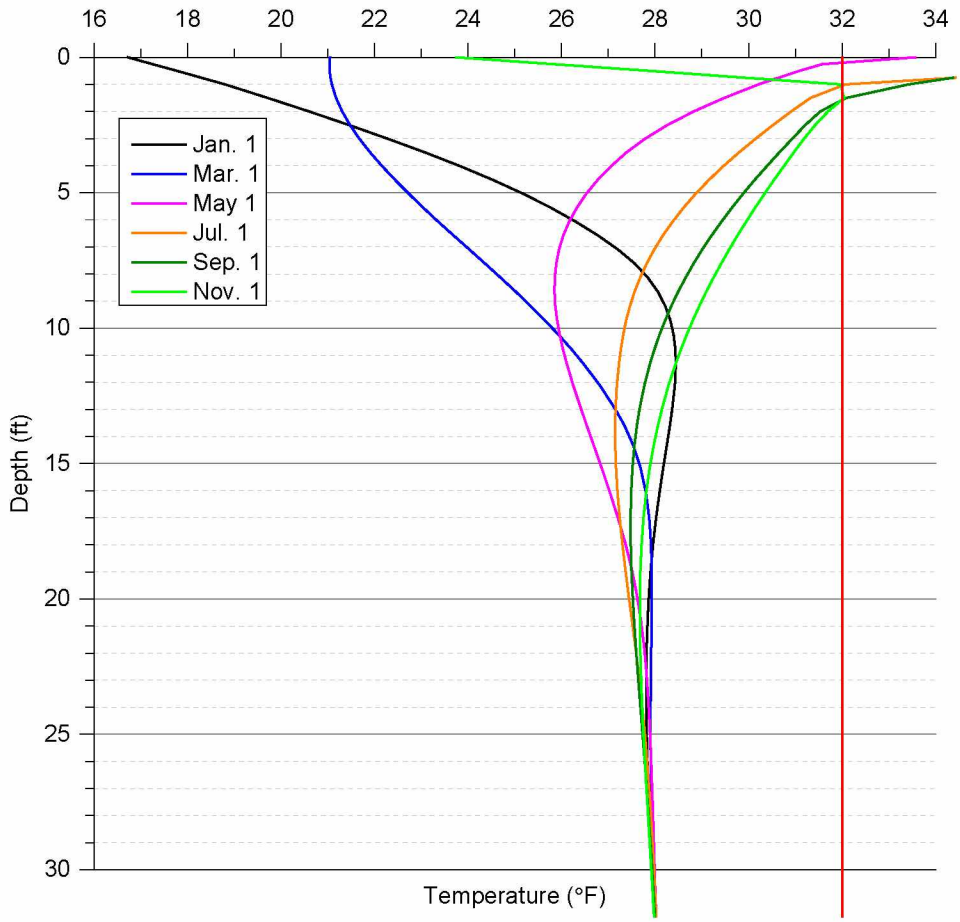

Figure 6.17 Ground temperature versus depth (0 to 30 ft).

It was expected that allowing air to flow in and out of the ACE side slopes would significantly improve convective heat transfer within the embankment; however, it appears that the snow-covered gravel boundary condition applied to the side slopes of the ACE was controlling the temperature of the air flowing into the embankment. The air flowing into the ACE was warmer than the model air temperature function. Thus, the plowed-open embankment temperatures do not significantly differ from the plowed-closed results.

The snow-closed model results for Jan. 1, Mar. 1, May 1, Jul. 1, Sep. 1, and Nov. 1 are presented in Figures 6.30 through 6.35, respectively. The results for Jan. 1 show that the ACE temperatures in the snow-closed model are significantly warmer than in the plowed-closed model; for example, the temperature at the surface of the ACE is 8°F in the snow-closed model compared to -12°F in the plowed-closed model. The snow-closed model's warmer surface temperatures and lower air convection intensity results in warmer temperatures in the

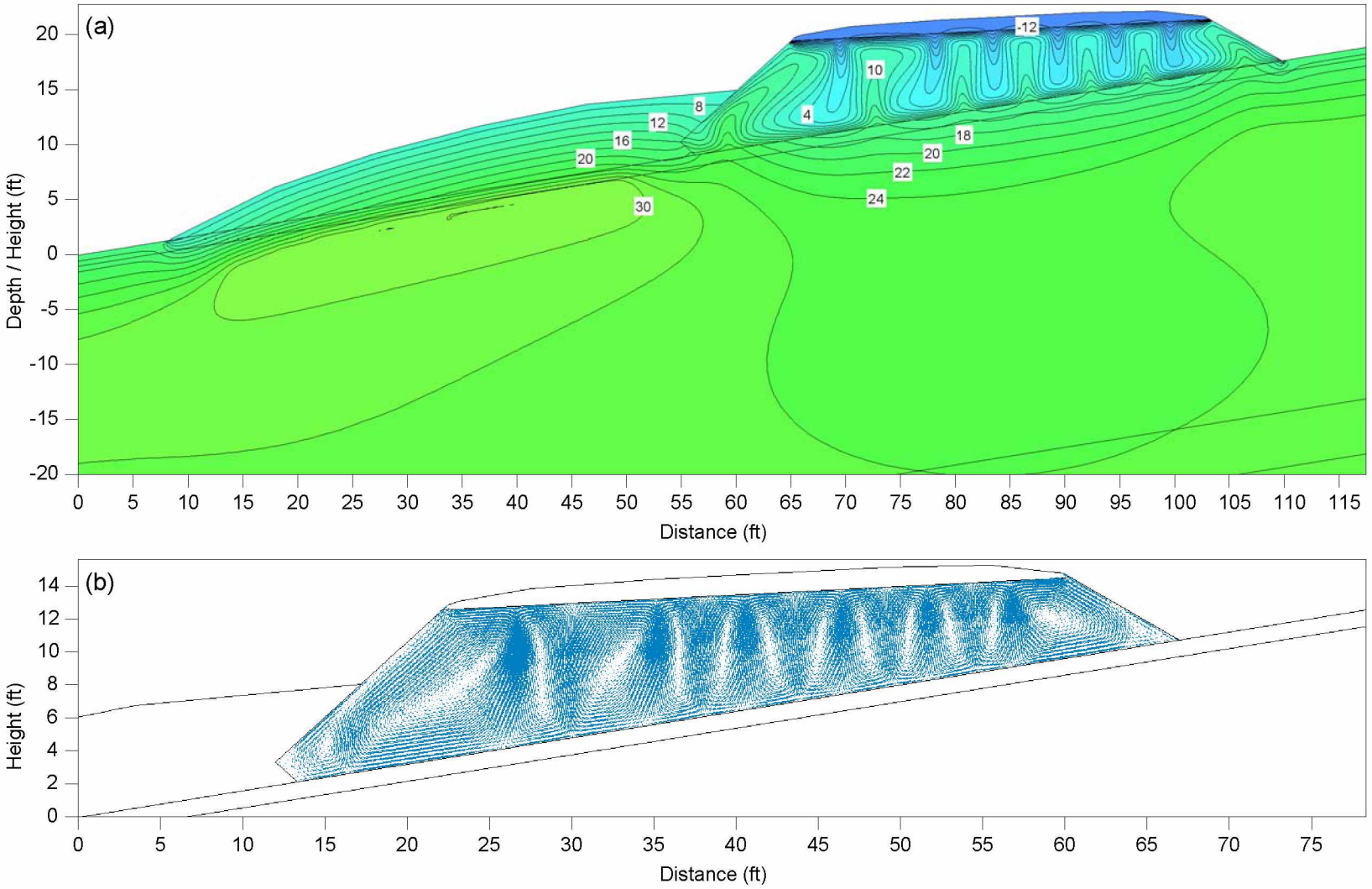

Figure 6.18 Plowed-closed model results for Jan. 1 with (a) temperature and (b) air velocity vectors. Temperature contours are spaced every 2°F.

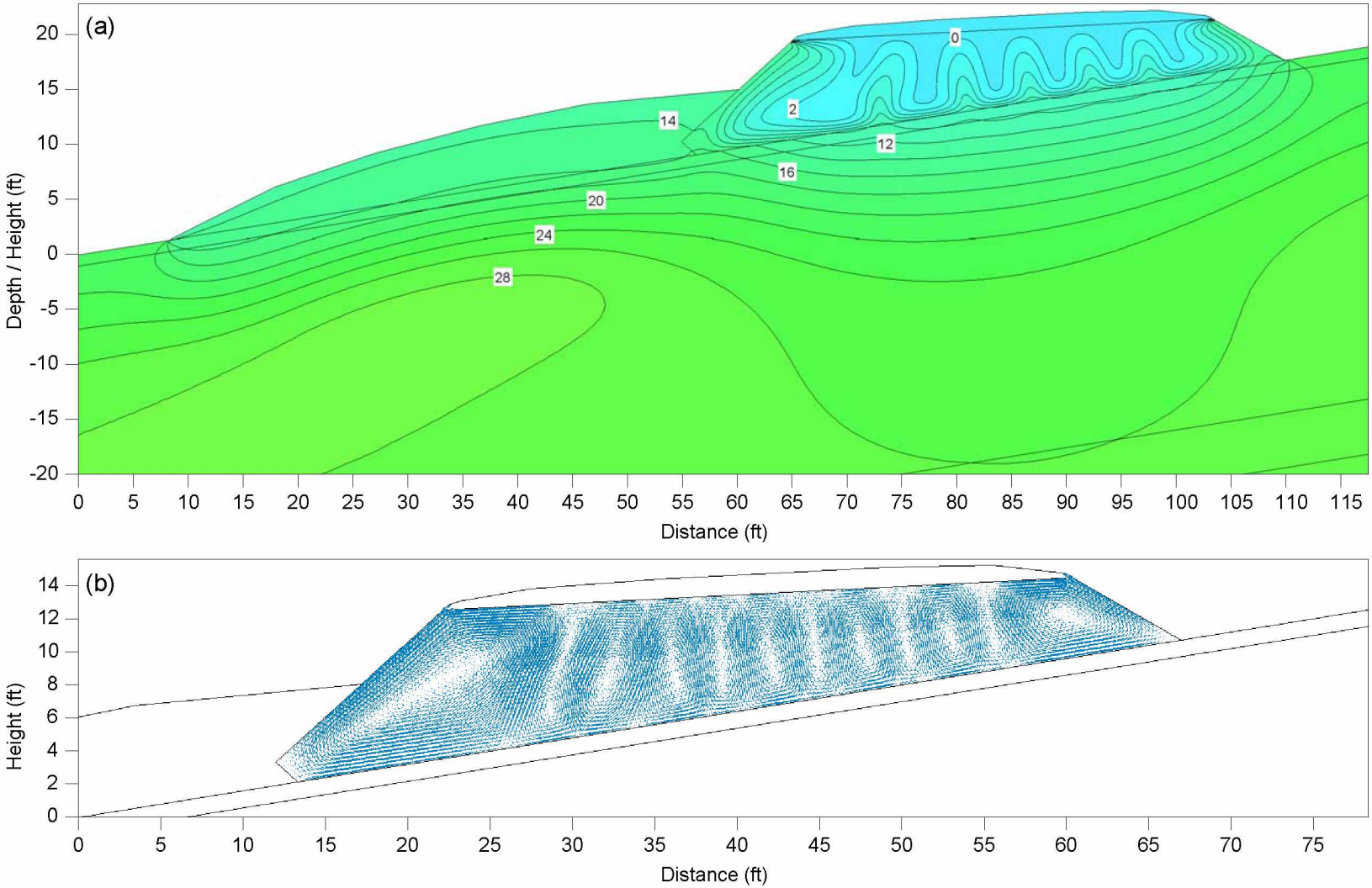

Figure 6.19 Plowed-closed model results for Mar. 1 with (a) temperature and (b) air velocity vectors. Temperature contours are spaced every 2°F.

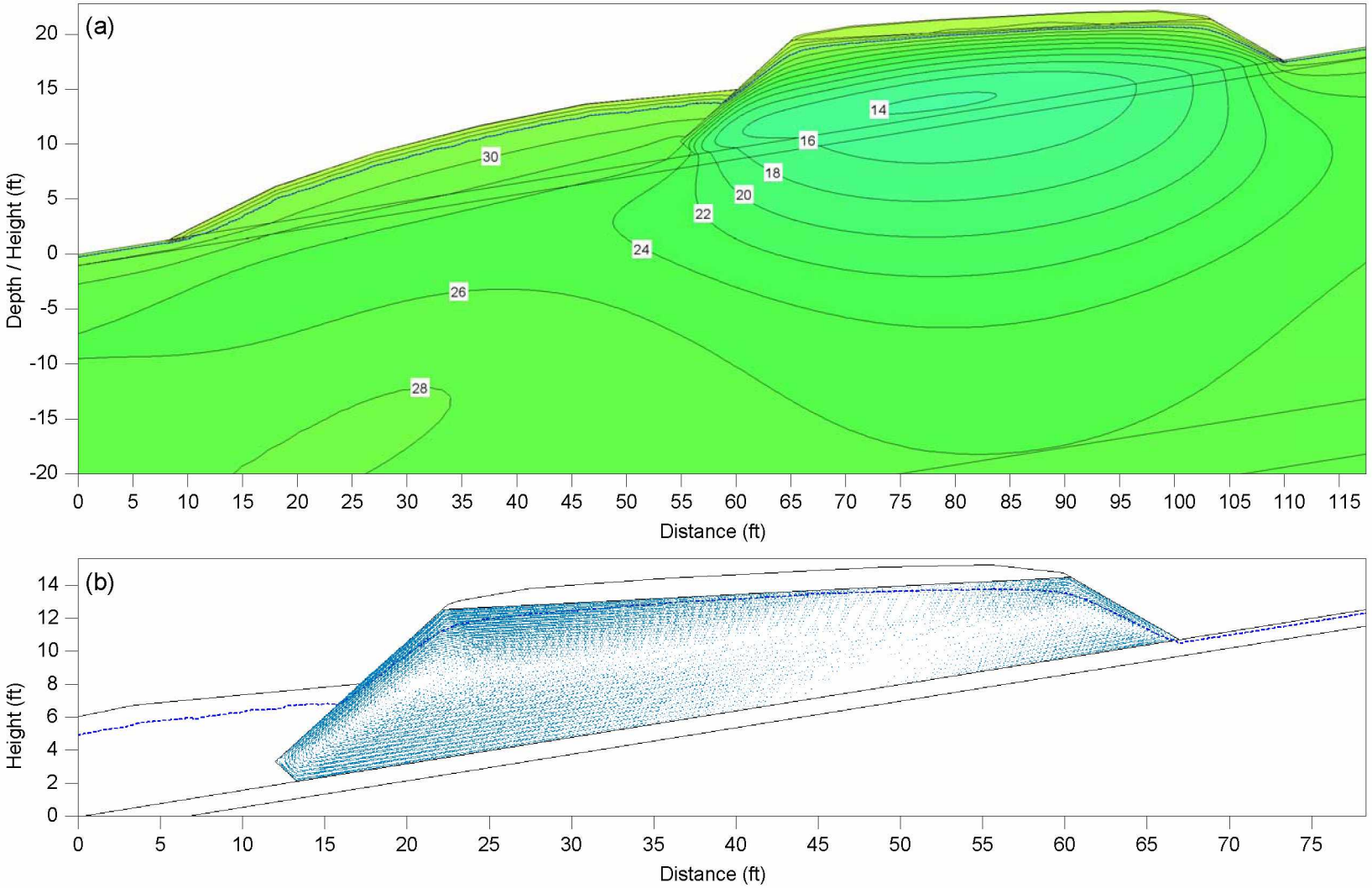

Figure 6.20 Plowed-closed model results for May 1 with (a) temperature and (b) air velocity vectors. Temperature contours are spaced every 2°F and the dashed blue line represents the 32°F isotherm.

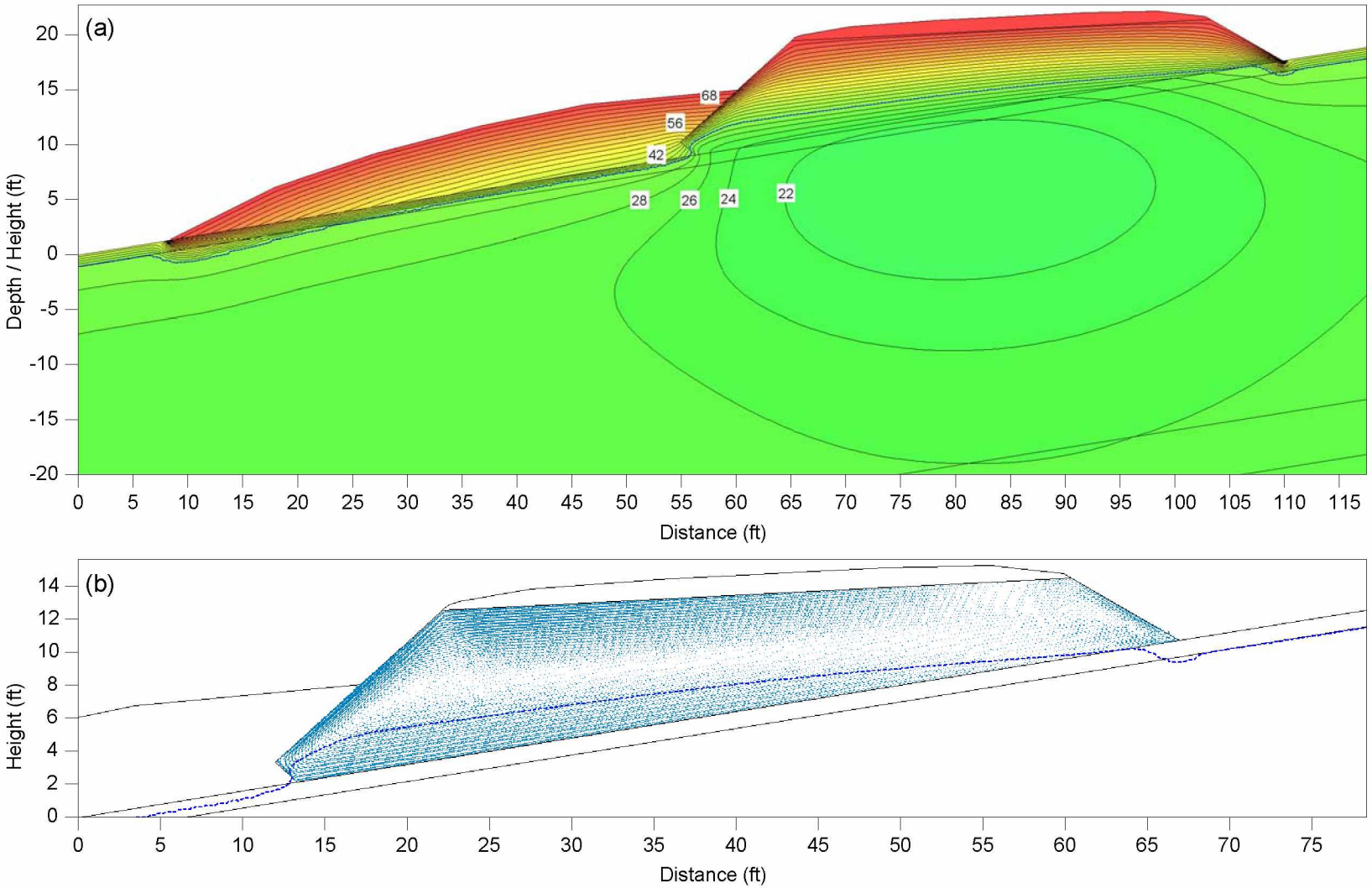

Figure 6.21 Plowed-closed model results for Jul. 1 with (a) temperature and (b) air velocity vectors. Temperature contours are spaced every 2°F and the dashed blue line represents the 32°F isotherm.

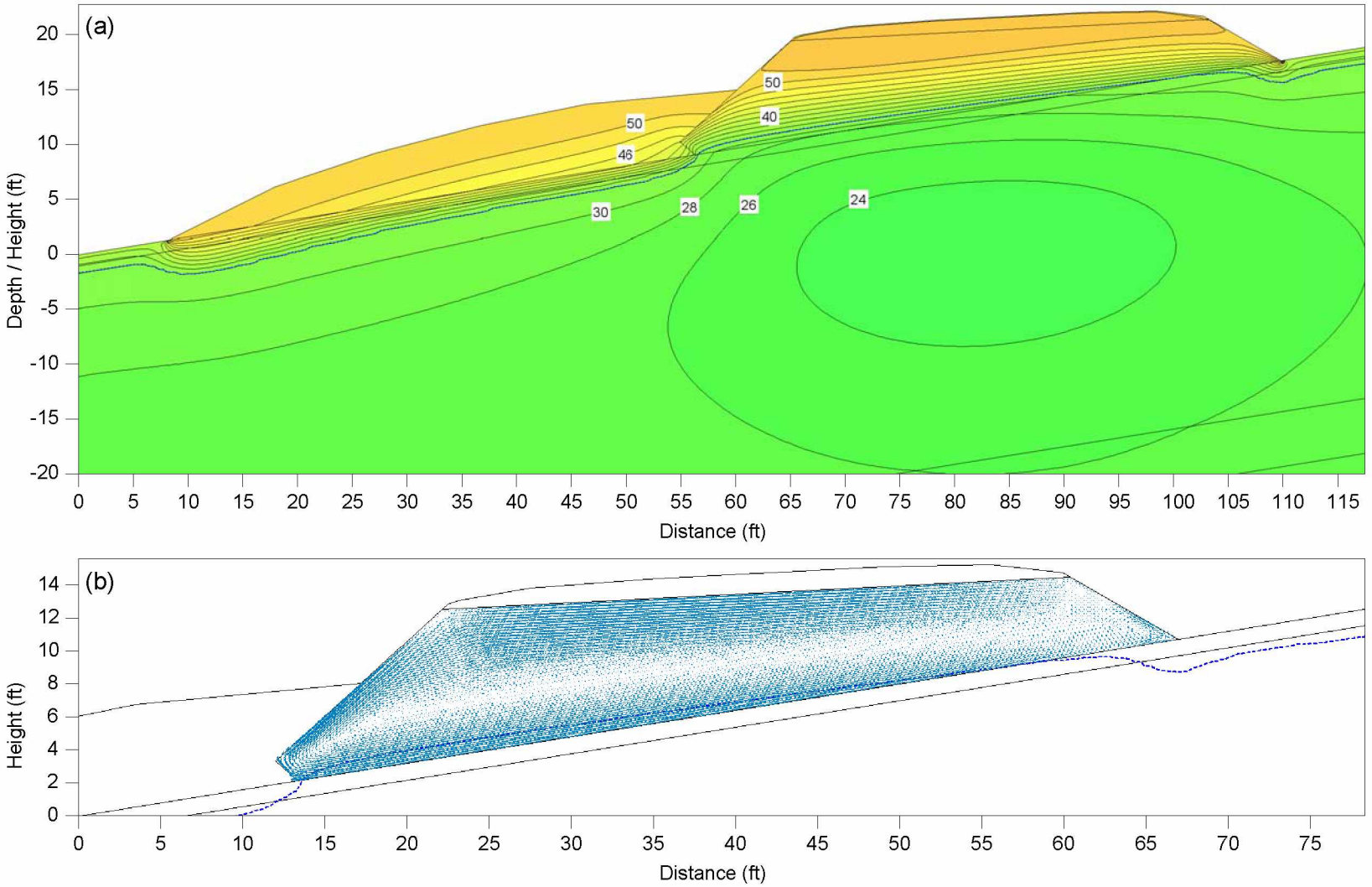

Figure 6.22 Plowed-closed model results for Sep. 1 with (a) temperature and (b) air velocity vectors. Temperature contours are spaced every 2°F and the dashed blue line represents the 32°F isotherm.

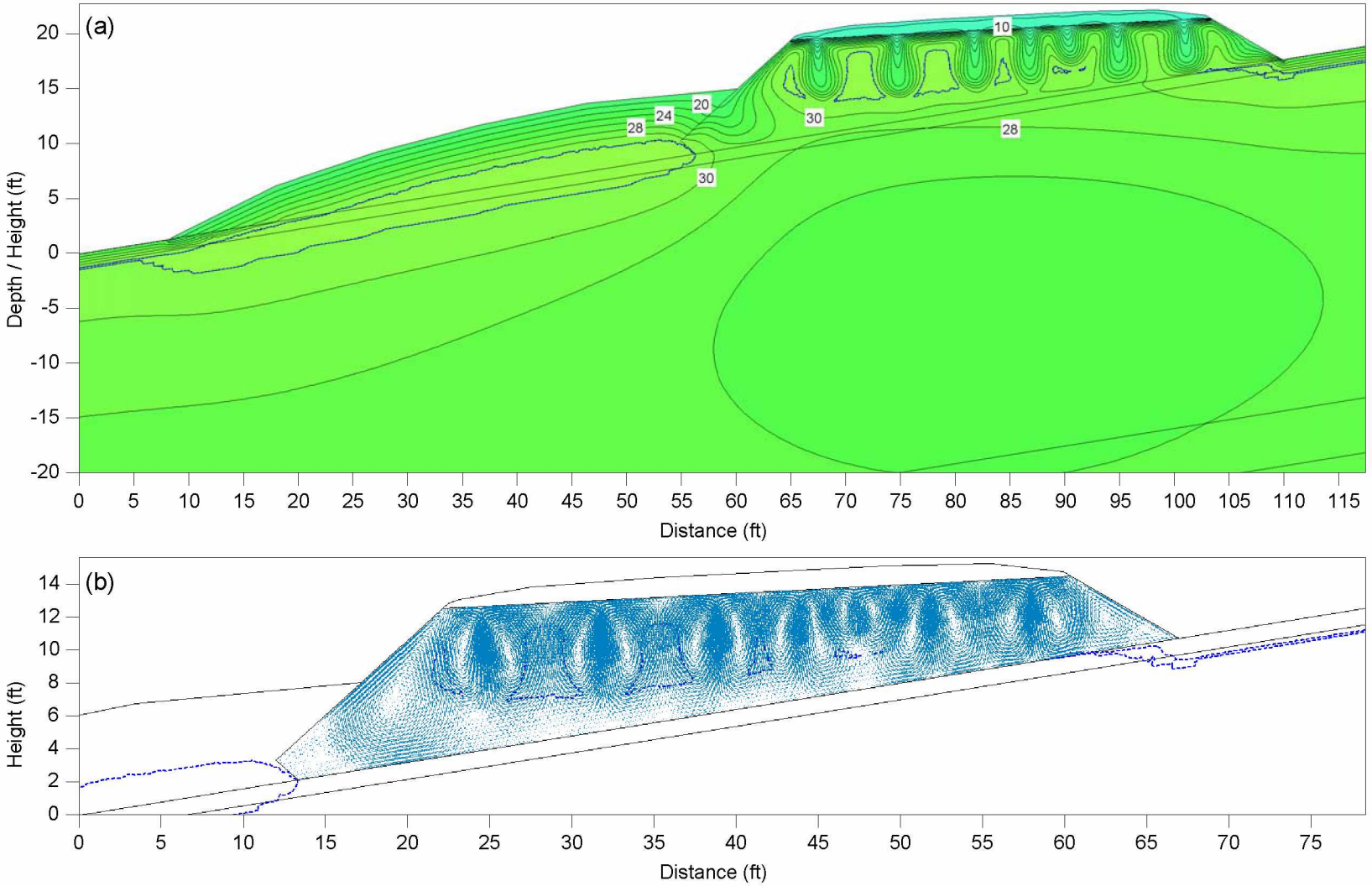

Figure 6.23 Plowed-closed model results for Nov. 1 with (a) temperature and (b) air velocity vectors. Temperature contours are spaced every 2°F and the dashed blue line represents the 32°F isotherm.

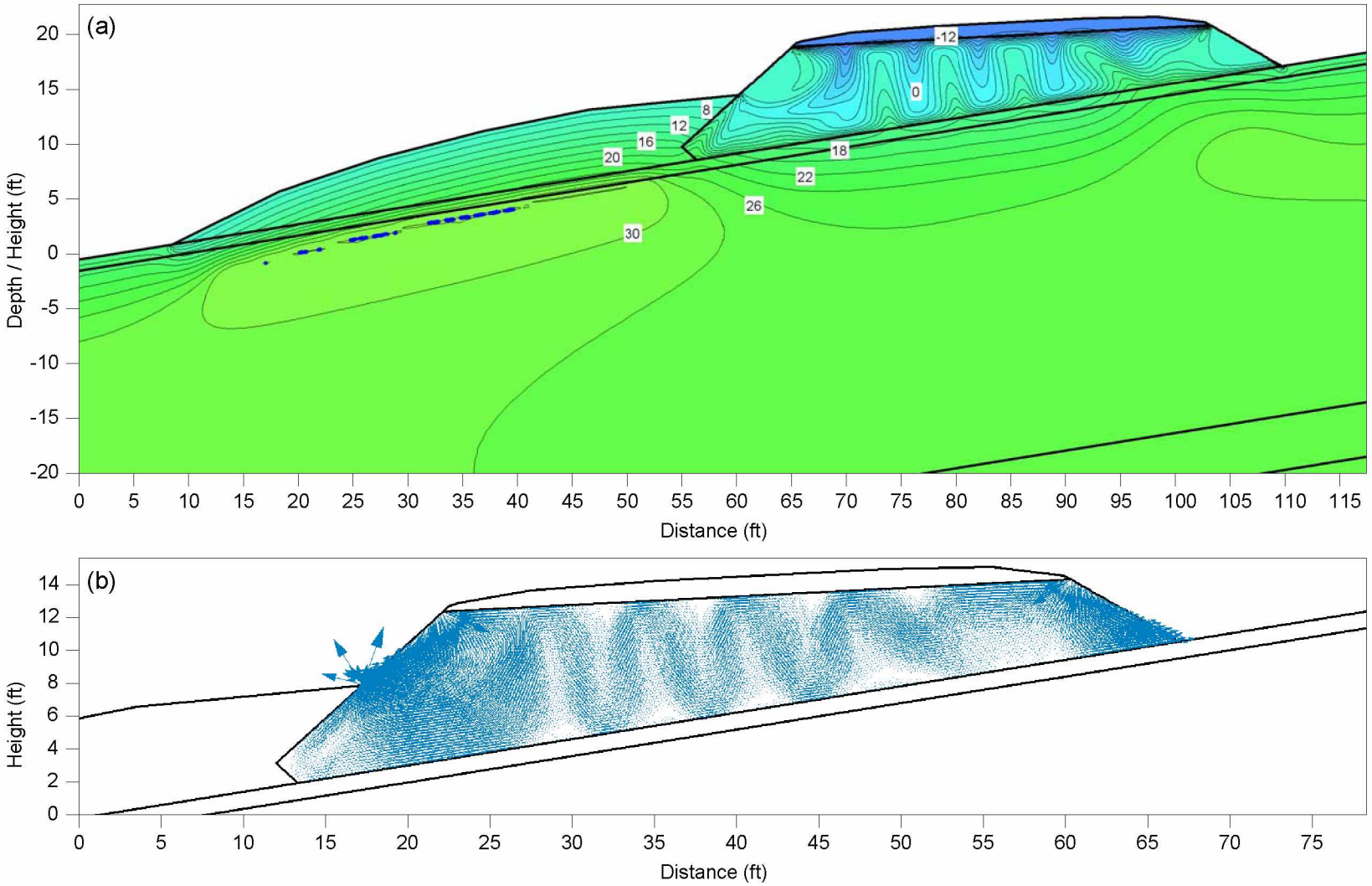

Figure 6.24 Plowed-open model results for Jan. 1 with (a) temperature and (b) air velocity vectors. Temperature contours are spaced every 2°F and the dashed blue line represents the 32°F isotherm.

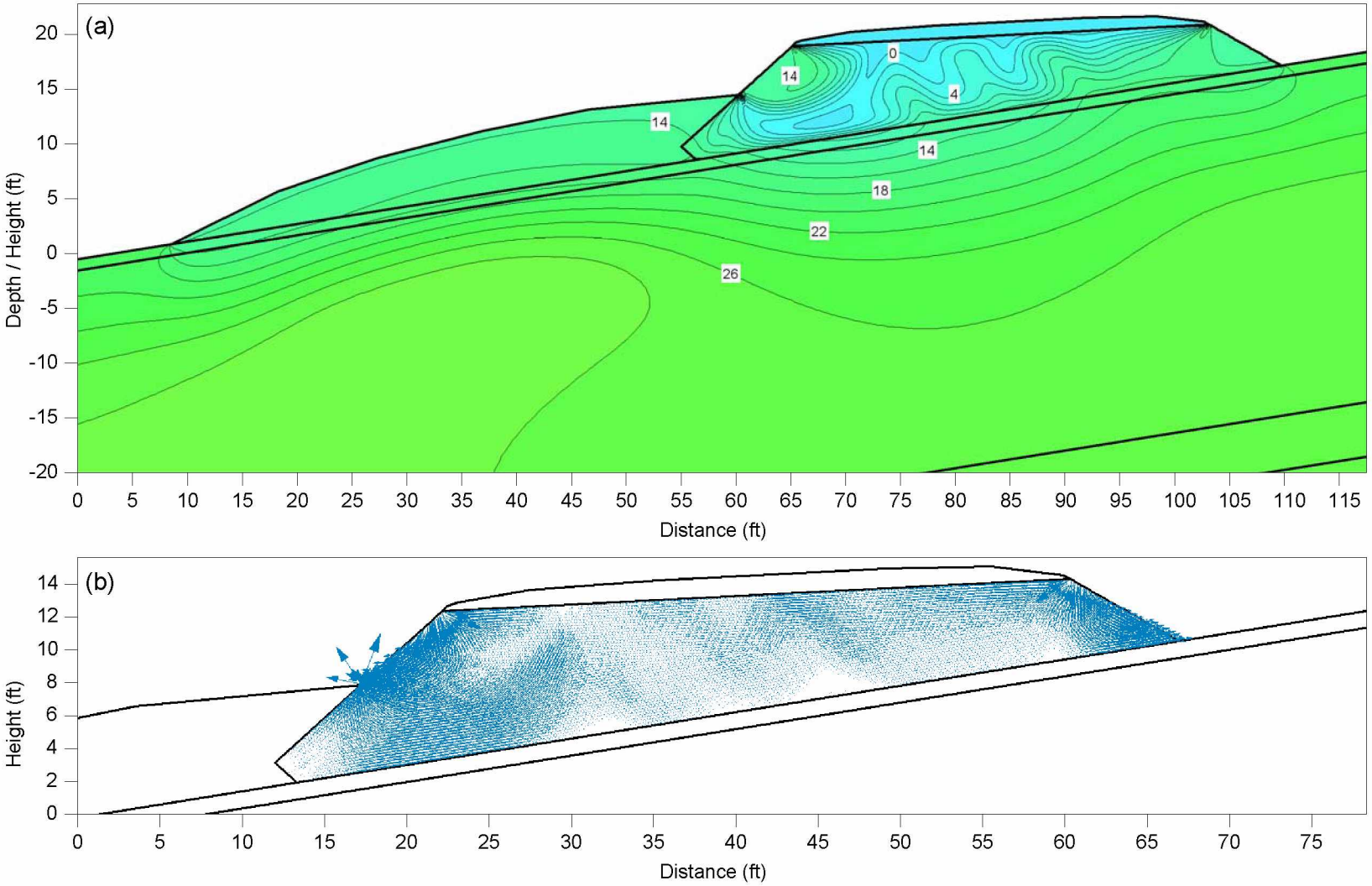

Figure 6.25 Plowed-open model results for Mar. 1 with (a) temperature and (b) air velocity vectors. Temperature contours are spaced every 2°F.

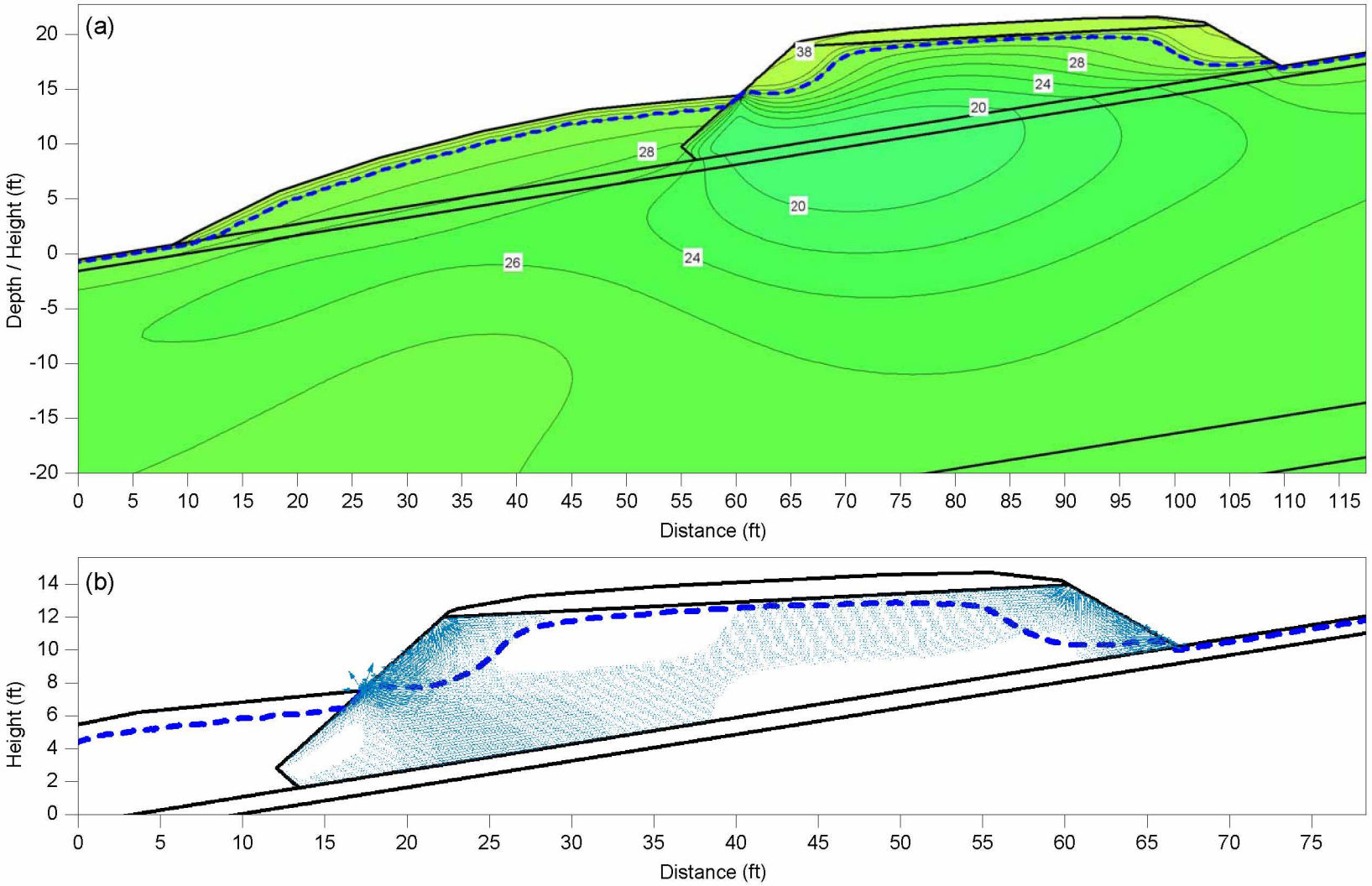

Figure 6.26 Plowed-open model results for May 1 with (a) temperature and (b) air velocity vectors. Temperature contours are spaced every 2°F and the dashed blue line represents the 32°F isotherm.

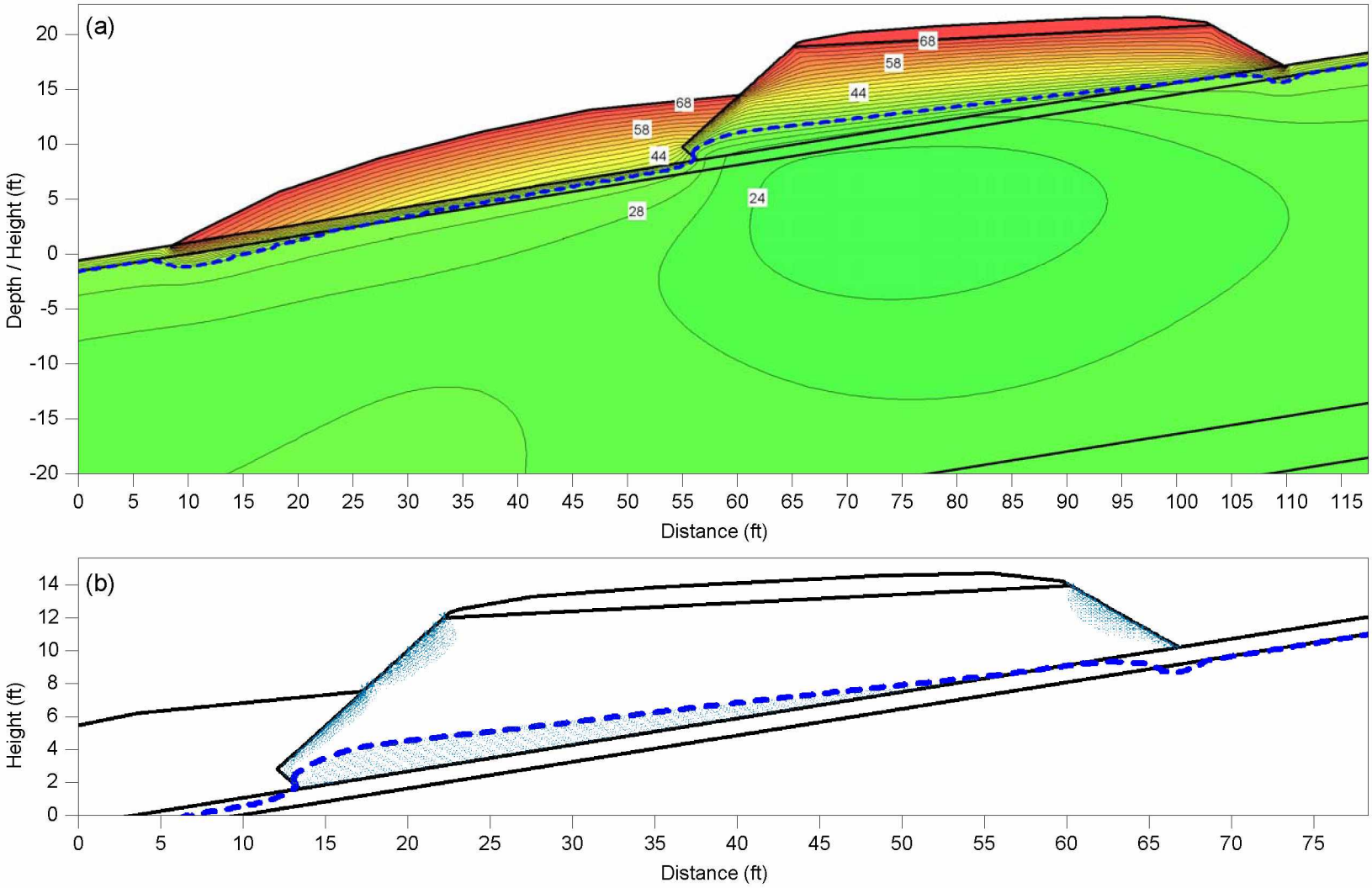

Figure 6.27 Plowed-open model results for Jul. 1 with (a) temperature and (b) air velocity vectors. Temperature contours are spaced every 2°F and the dashed blue line represents the 32°F isotherm.

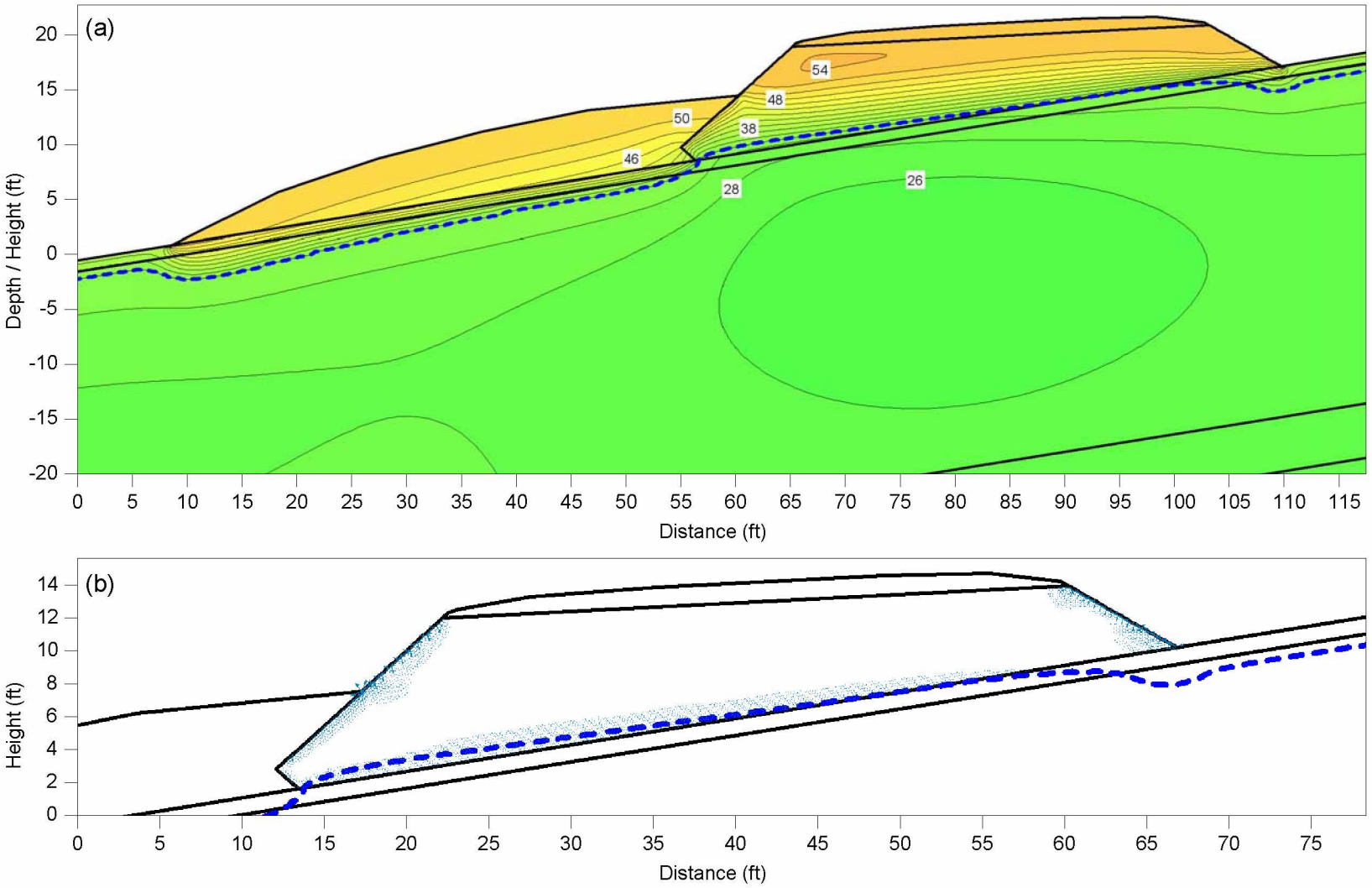

Figure 6.28 Plowed-open model results for Sep. 1 with (a) temperature and (b) air velocity vectors. Temperature contours are spaced every 2°F and the dashed blue line represents the 32°F isotherm.

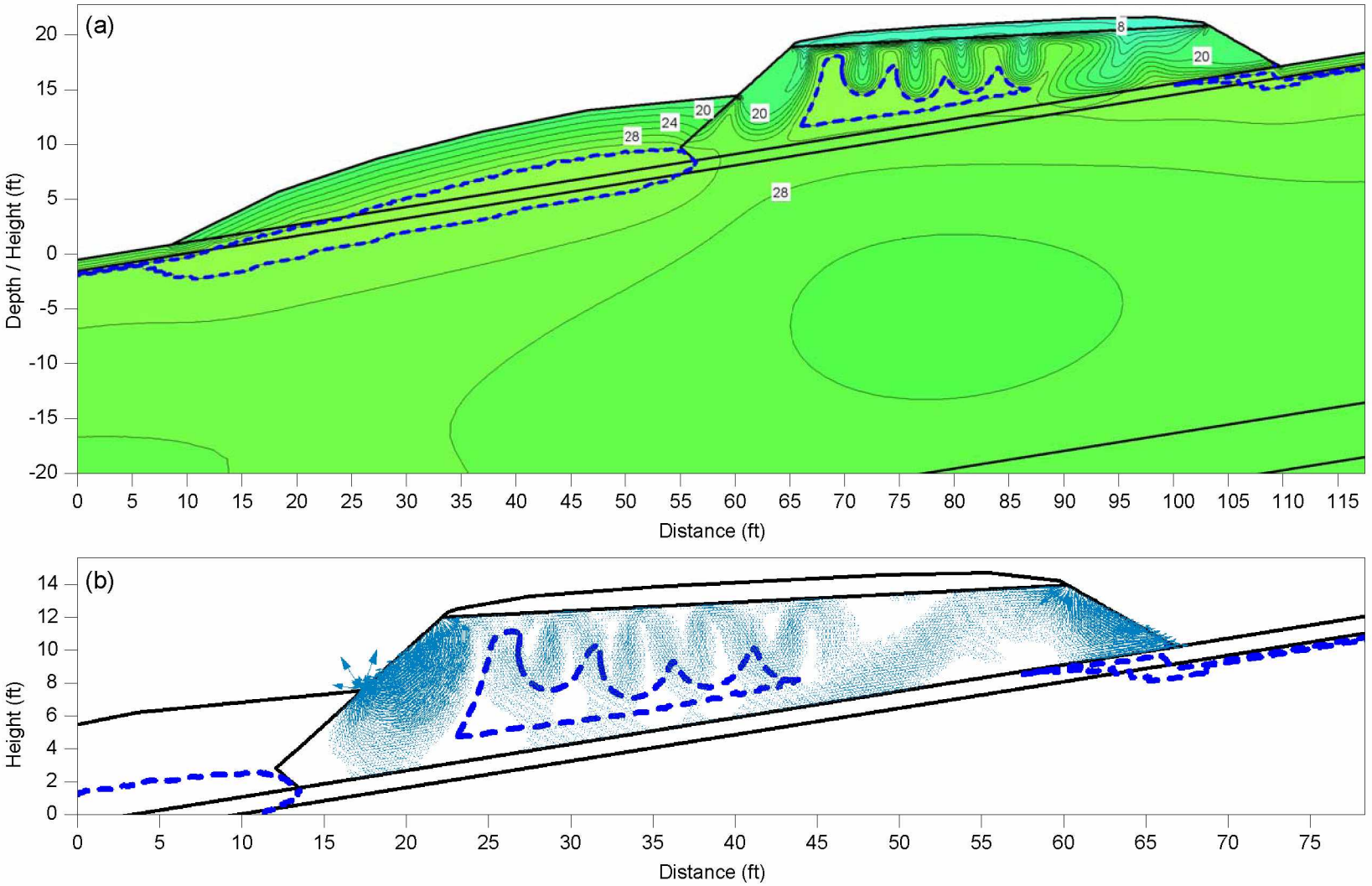

Figure 6.29 Plowed-open model results for Nov. 1 with (a) temperature and (b) air velocity vectors. Temperature contours are spaced every 2°F and the dashed blue line represents the 32°F isotherm.

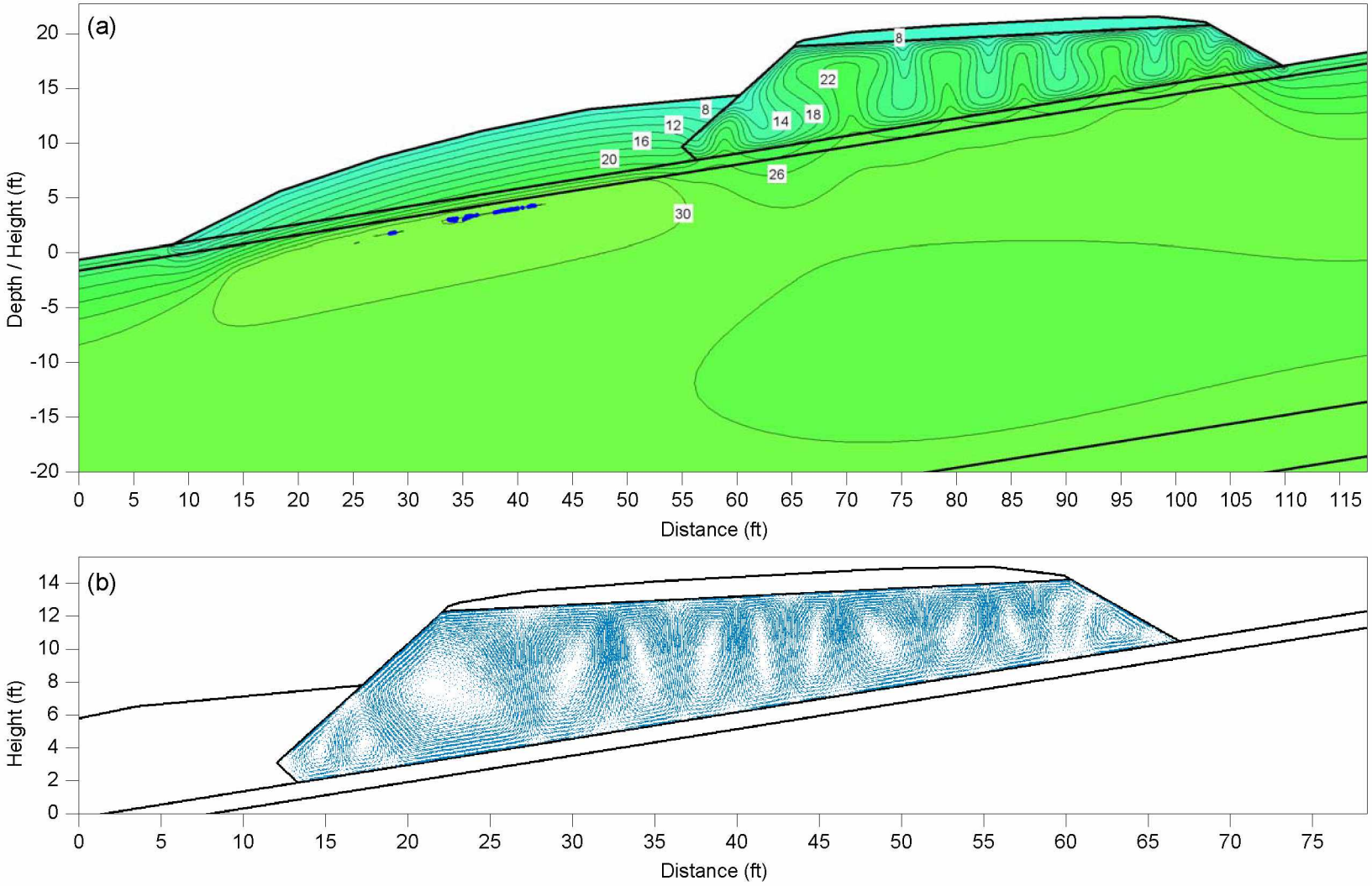

Figure 6.30 Snow-closed model results for Jan. 1 with (a) temperature and (b) air velocity vectors. Temperature contours are spaced every 2°F and the dashed blue line represents the 32°F isotherm.

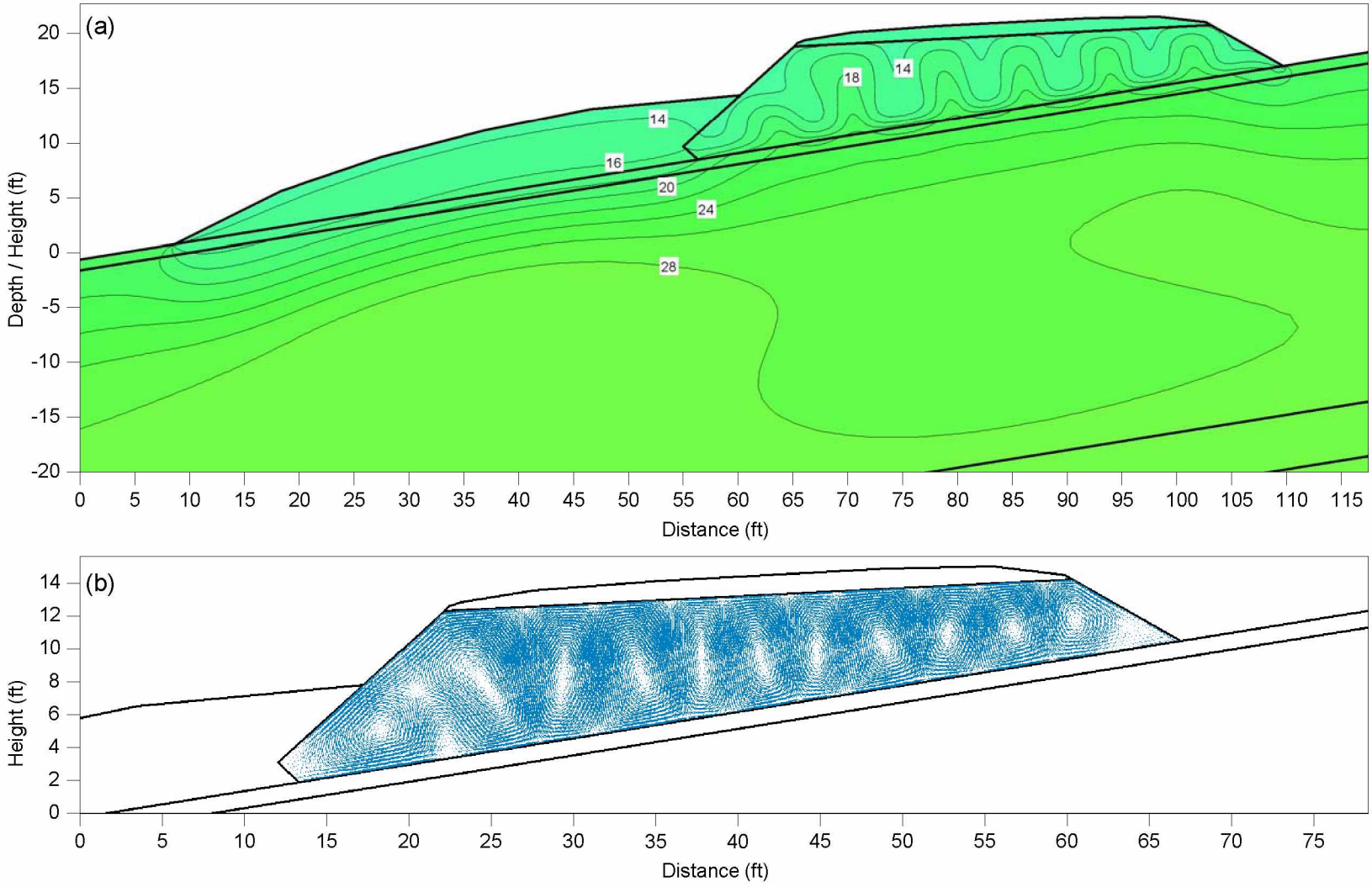

Figure 6.31 Snow-closed model results for Mar. 1 with (a) temperature and (b) air velocity vectors. Temperature contours are spaced every 2°F.

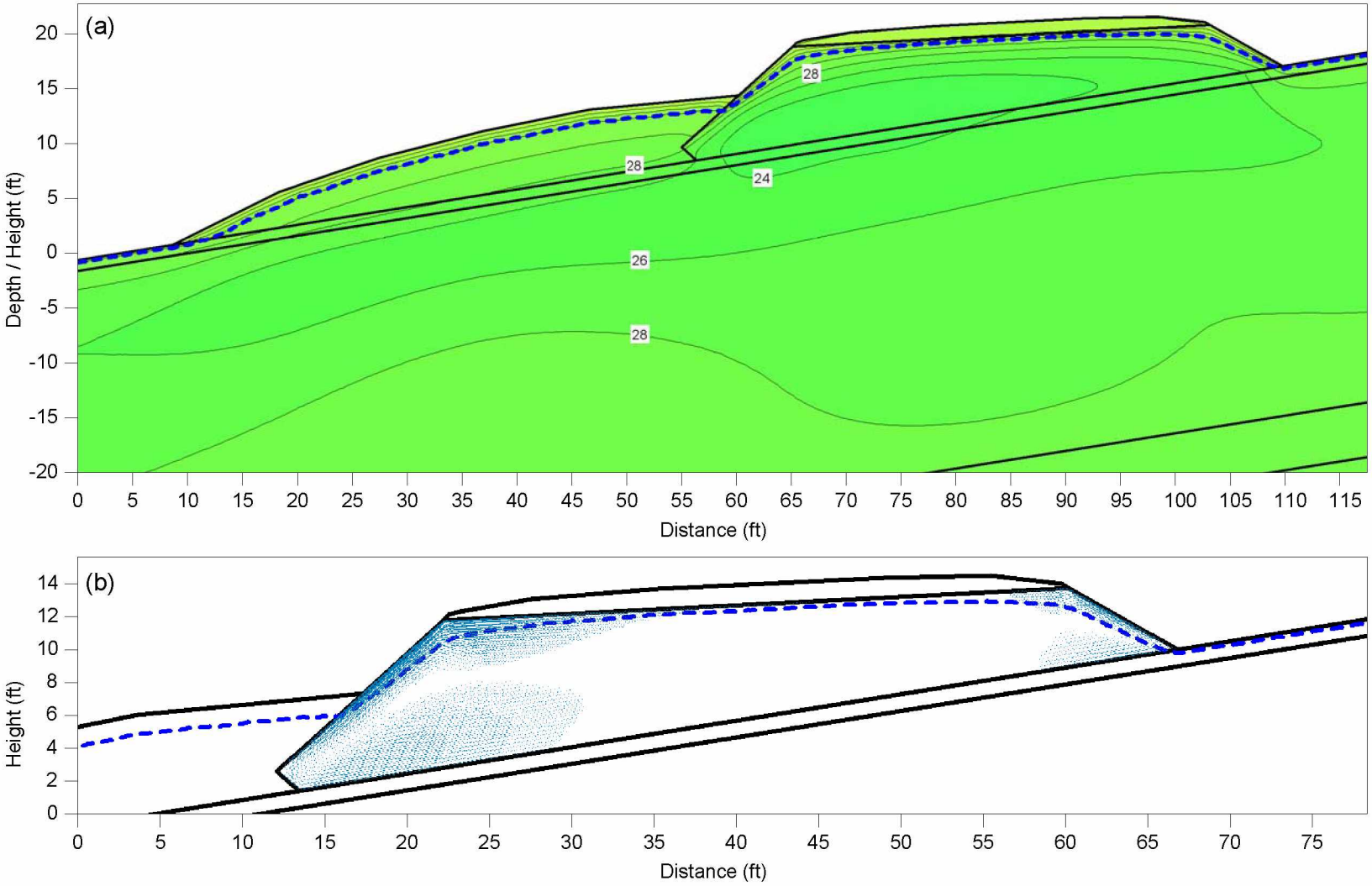

Figure 6.32 Snow-closed model results for May 1 with (a) temperature and (b) air velocity vectors. Temperature contours are spaced every 2°F and the dashed blue line represents the 32°F isotherm.

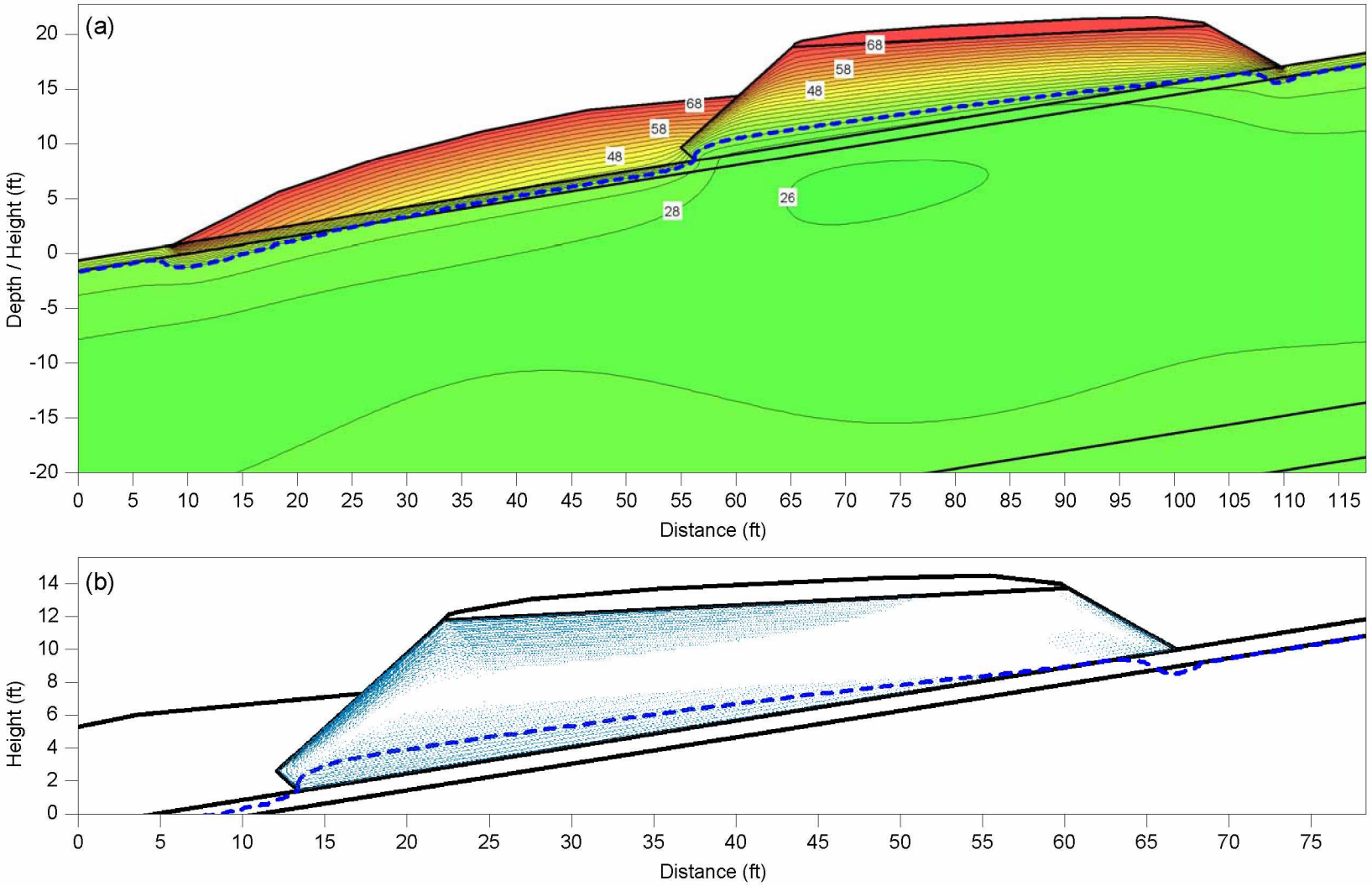

Figure 6.33 Snow-closed model results for Jul. 1 with (a) temperature and (b) air velocity vectors. Temperature contours are spaced every 2°F and the dashed blue line represents the 32°F isotherm.

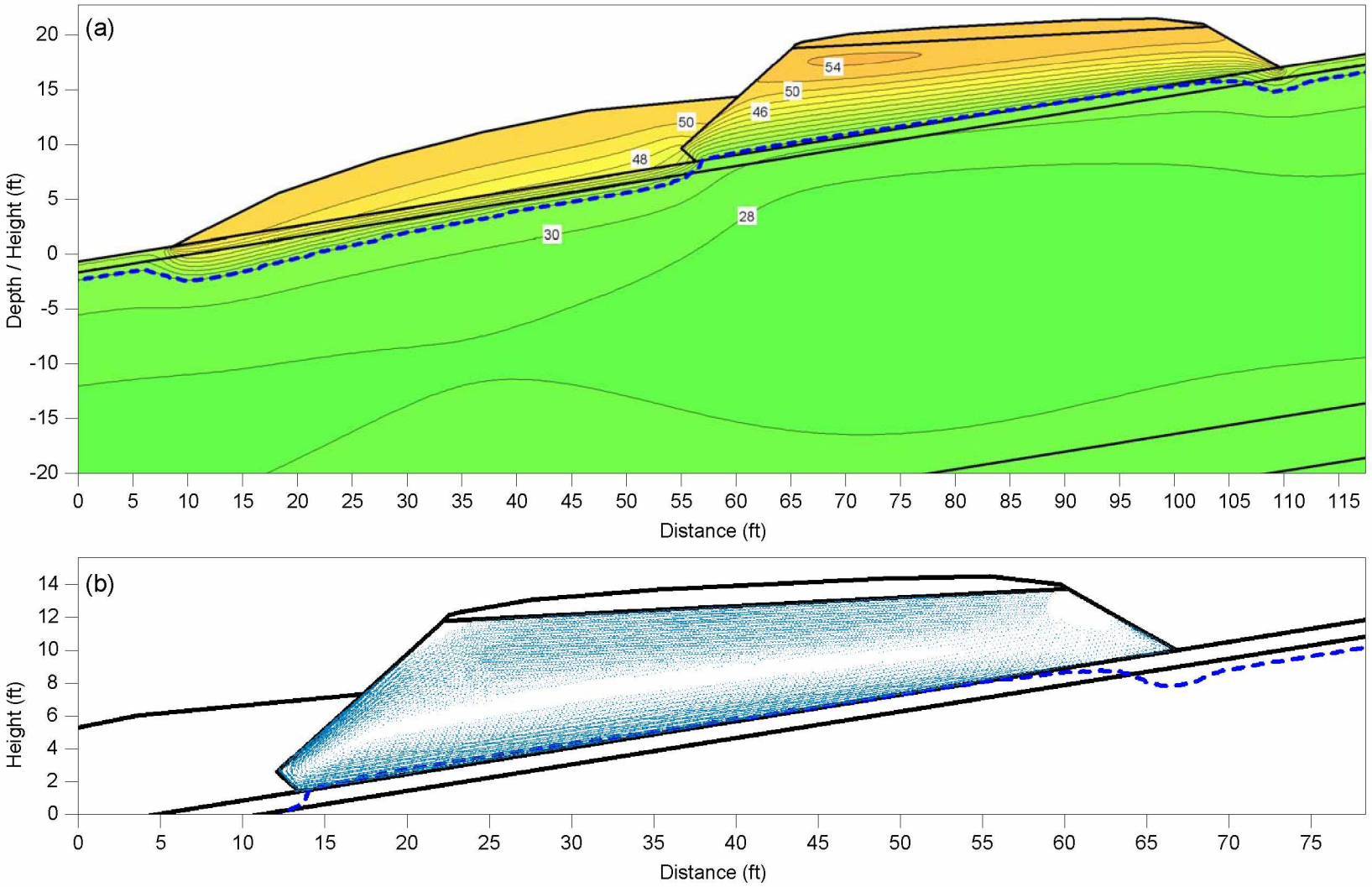

Figure 6.34 Snow-closed model results for Sep. 1 with (a) temperature and (b) air velocity vectors. Temperature contours are spaced every 2°F and the dashed blue line represents the 32°F isotherm.

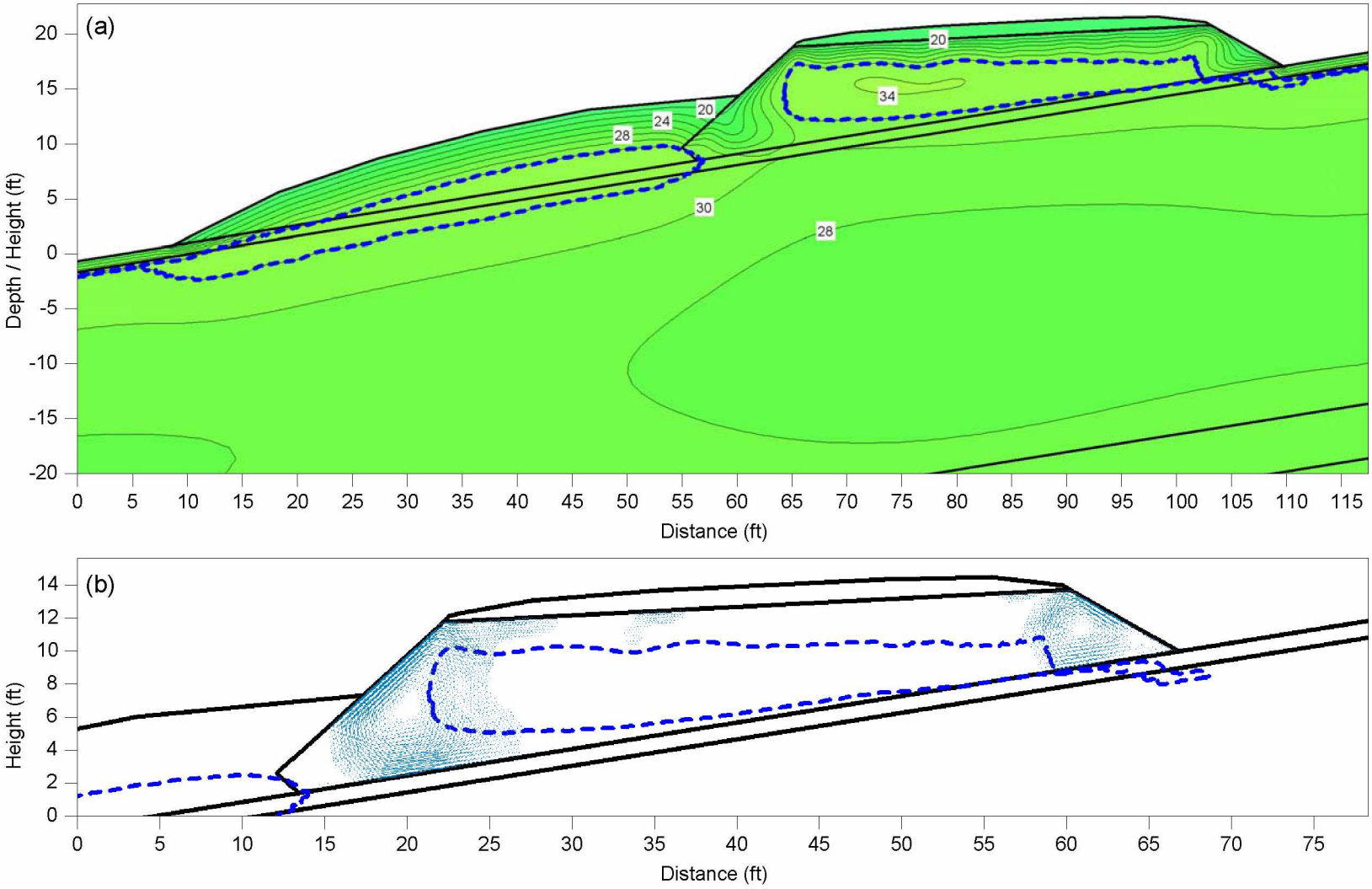

Figure 6.35 Snow-closed model results for Nov. 1 with (a) temperature and (b) air velocity vectors. Temperature contours are spaced every 2°F and the dashed blue line represents the 32°F isotherm.

foundation soil as well. By Mar. 1, the temperature at the surface of the ACE is increased and the convective heat transfer is less evident than in the plowed-closed model.

On May 1, the temperature contours and air velocity vectors for the snow-closed model show that air convection within the ACE has stopped and the depth of thaw is similar to the plowed-closed model, despite the latter having colder temperatures within the ACE. This is likely due to the lack of latent heat within the ACE material on account of the extremely low moisture content. On Jul. 1, conductive heat transfer is still controlling, and thawing is evident beneath the toe of the thermal berm, and uphill embankment toe, while the bottom of the ACE remains frozen. Again the depth of thaw within the ACE is only slightly greater than for the plowed-closed model. Results for Sep. 1 show maximum seasonal thawing, with the greatest thawing occurring beneath the thermal berm and the least thawing occurring beneath the ACE. The depth of thaw within the snow-closed model reaches bottom of the ACE while it remains slightly above the bottom in the plowed-closed model. Finally, by Nov. 1, air convection again begins within the snow-closed model, although the eddies are not yet well-defined as within the plowed-closed model.

The last set of model results for snow-open conditions, for Jan. 1, Mar. 1, May 1, Jul. 1, Sep. 1, and Nov. 1, are shown in Figures 6.36 through 6.41, respectively. As with the plowed-closed versus plowed-open model results, the snow-open temperature results do not differ greatly from the snow-closed results. Again, the reason for the similarity in temperature between the snow-closed and snow-open models is due to the surface temperature boundary condition applied to the side slopes of the ACE. The snow-covered gravel surface boundary condition controls the temperature of the air flowing in and out of the ACE through the side slopes. Therefore, even though outside air flows through the ACE, the results do not show the expected increased cooling.

On Jan. 1, the snow-open model exhibits warmer temperatures within the ACE than the plowed-open model, and it has fewer convection eddies; however, temperatures along the side slopes of the ACE are the same for both models due to them having the same surface temperature boundary functions along the side slopes. On Mar. 1 the convection cells within the snow-open model are much less pronounced than within the plowed-open model, and temperatures within the foundation soil are also warmer in the plowed-open model. For May 1 though Sep. 1, the temperatures within the ACE and depth of thaw for the snow-open and plowed-open models is nearly identical; this is likely due to the same surface thawing *n*-factors being used for both models and the low latent heat of the ACE. Finally, on Nov. 1, air convection begins in both plowed-open and snow-open models, although less evident in the latter.

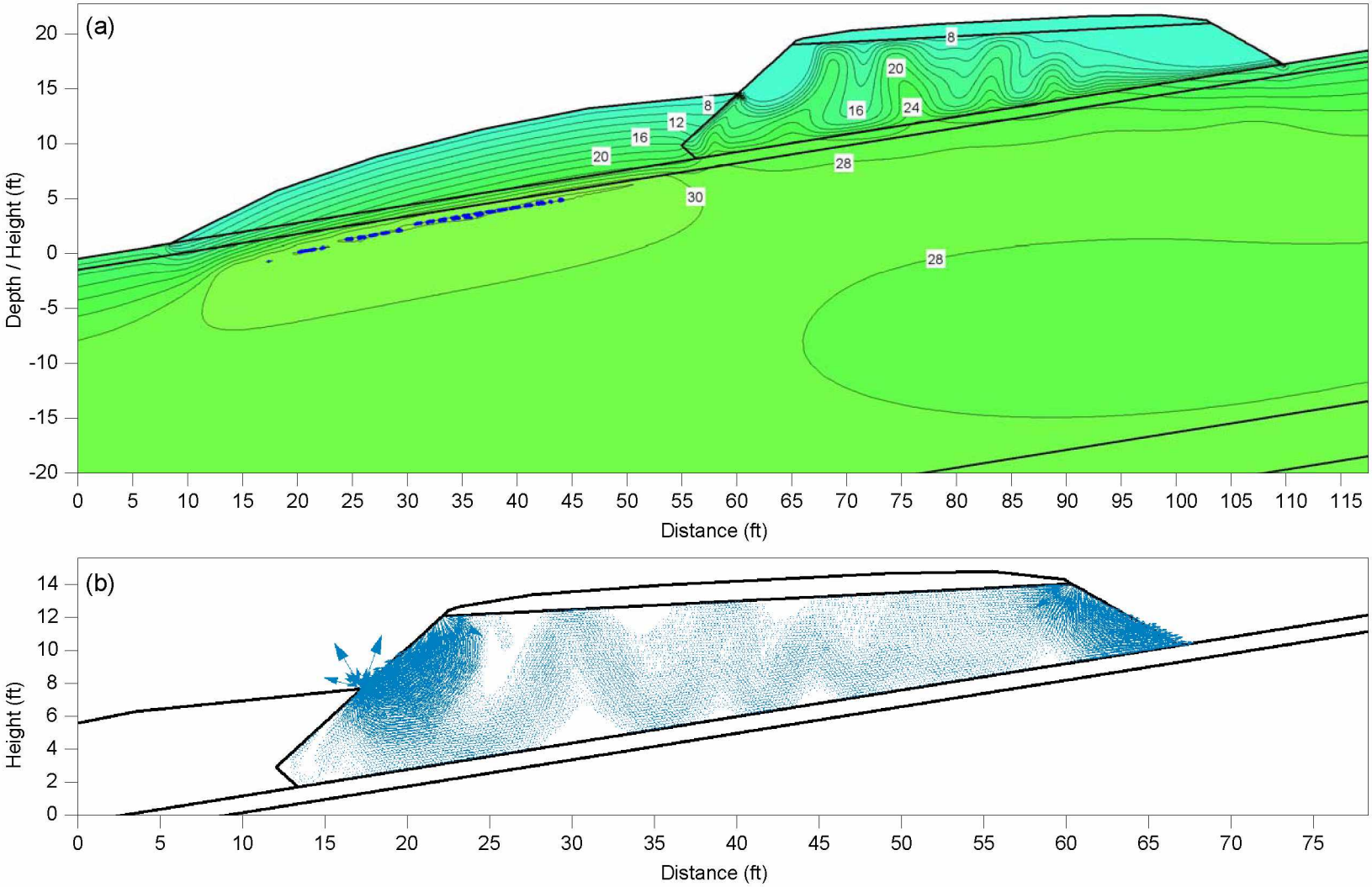

Figure 6.36 Snow-open model results for Jan. 1 with (a) temperature and (b) air velocity vectors. Temperature contours are spaced every 2°F and the dashed blue line represents the 32°F isotherm.

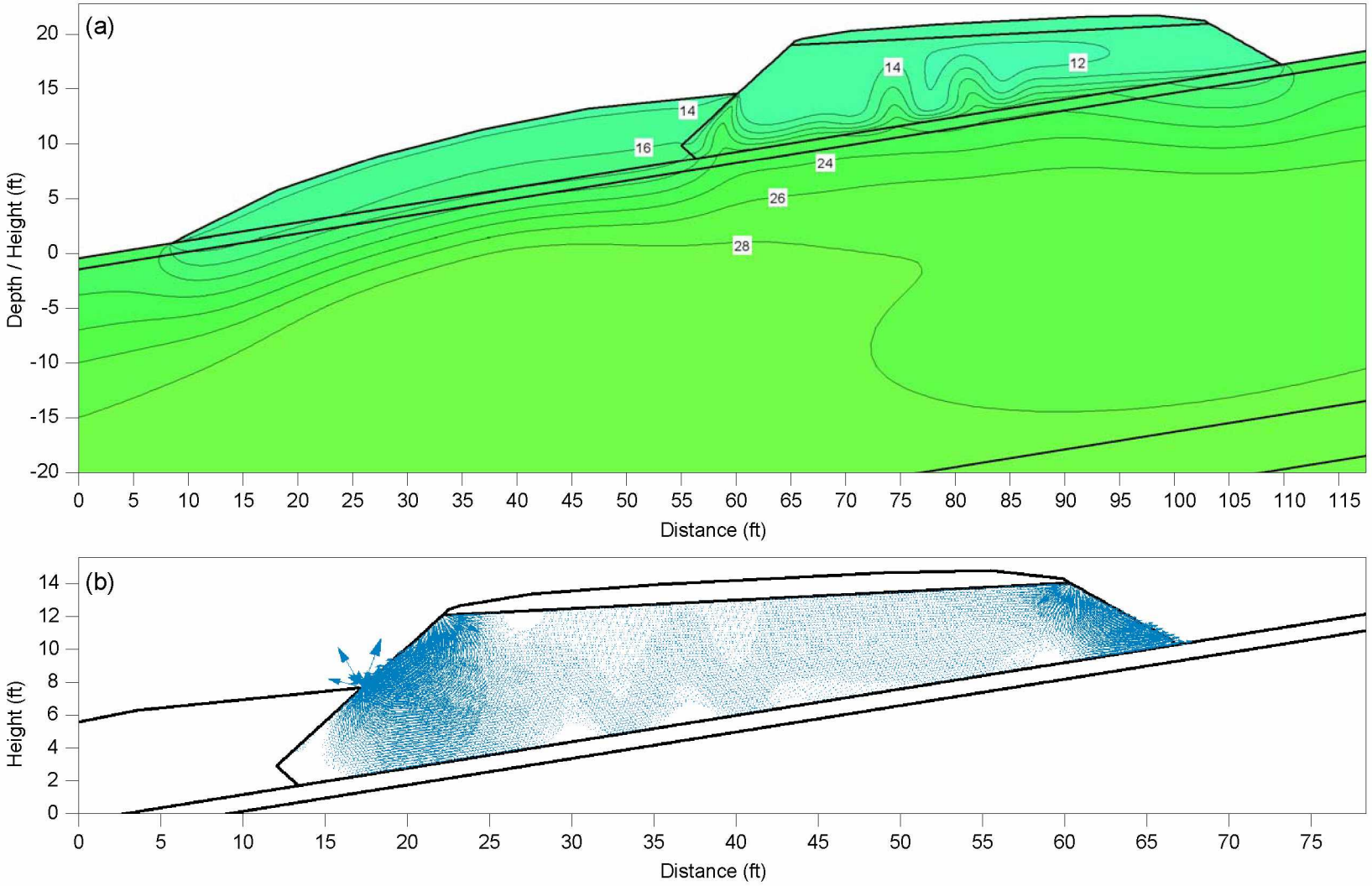

Figure 6.37 Snow-open model results for Mar. 1 with (a) temperature and (b) air velocity vectors. Temperature contours are spaced every 2°F.

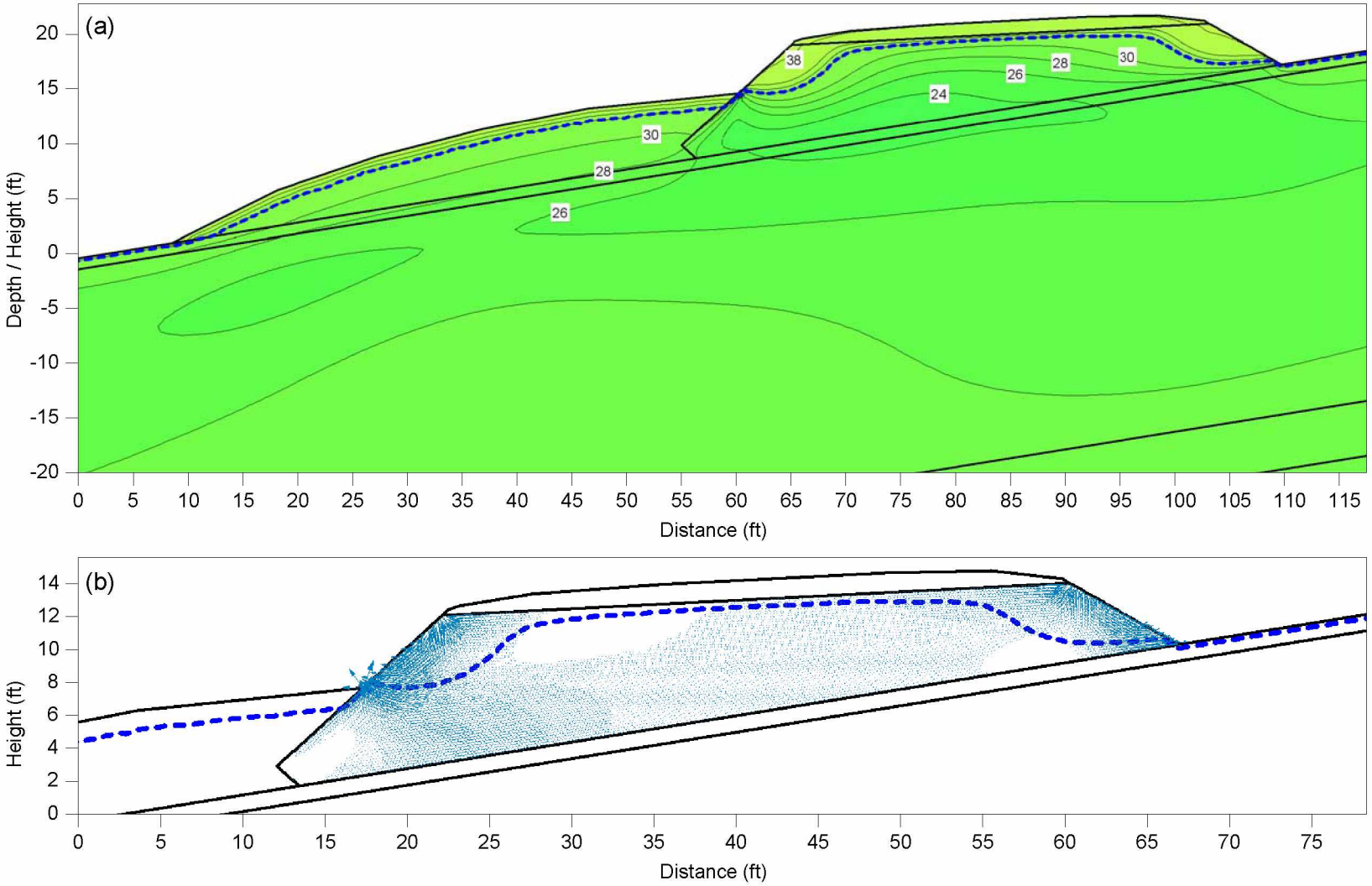

Figure 6.38 Snow-open model results for May 1 with (a) temperature and (b) air velocity vectors. Temperature contours are spaced every 2°F and the dashed blue line represents the 32°F isotherm.

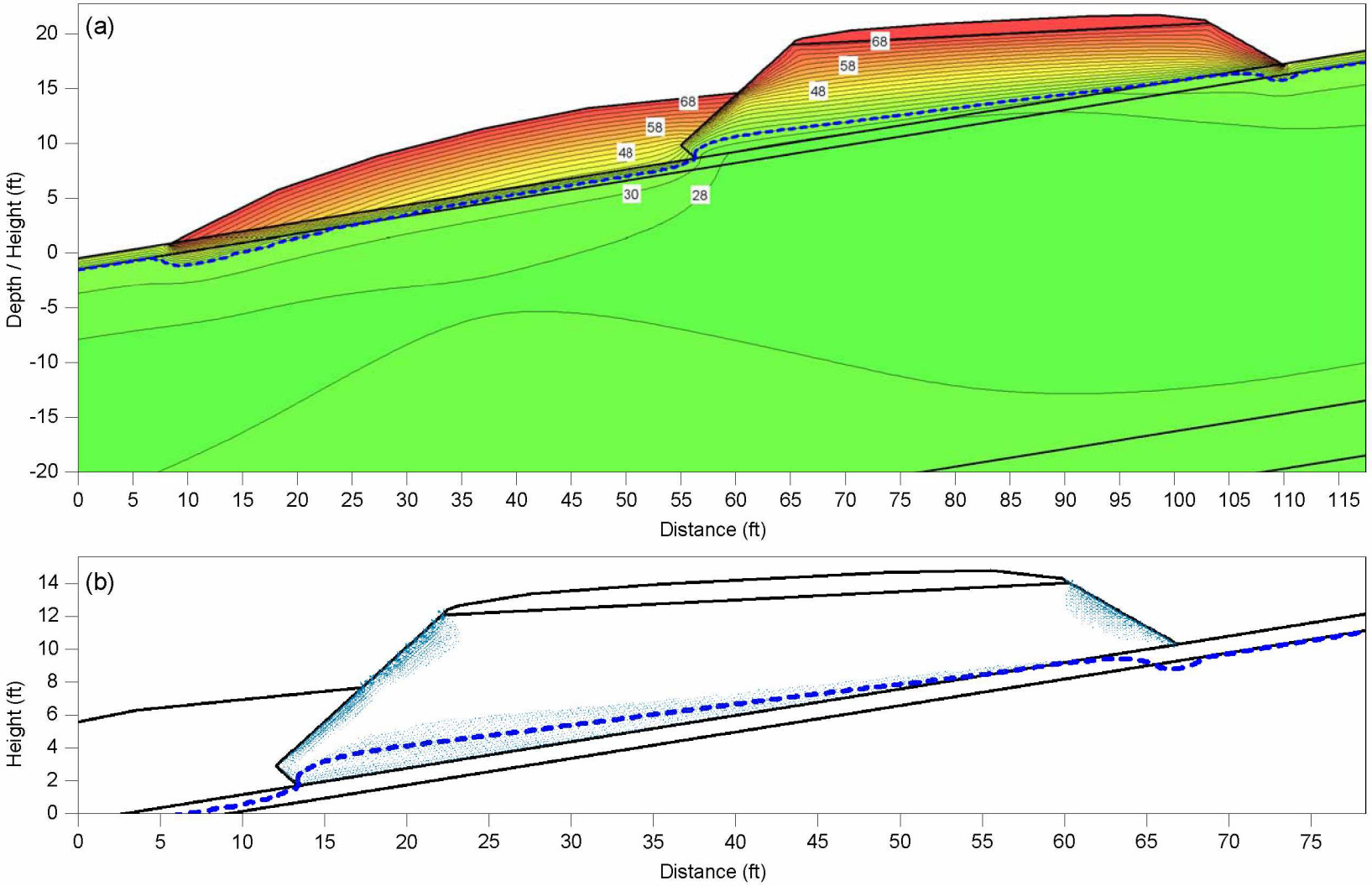

Figure 6.39 Snow-open model results for Jul. 1 with (a) temperature and (b) air velocity vectors. Temperature contours are spaced every 2°F and the dashed blue line represents the 32°F isotherm.

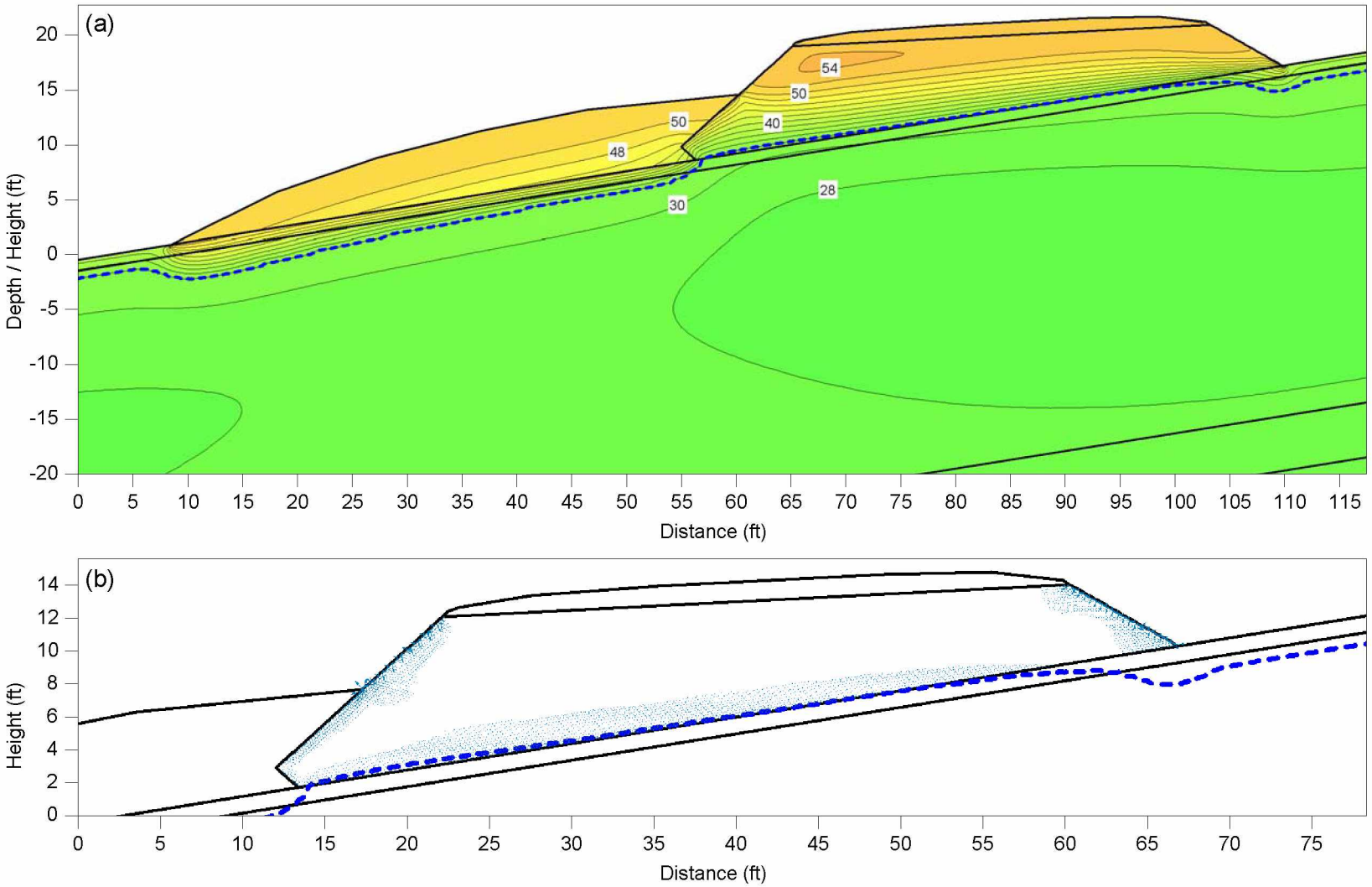

Figure 6.40 Snow-open model results for Sep. 1 with (a) temperature and (b) air velocity vectors. Temperature contours are spaced every 2°F and the dashed blue line represents the 32°F isotherm.

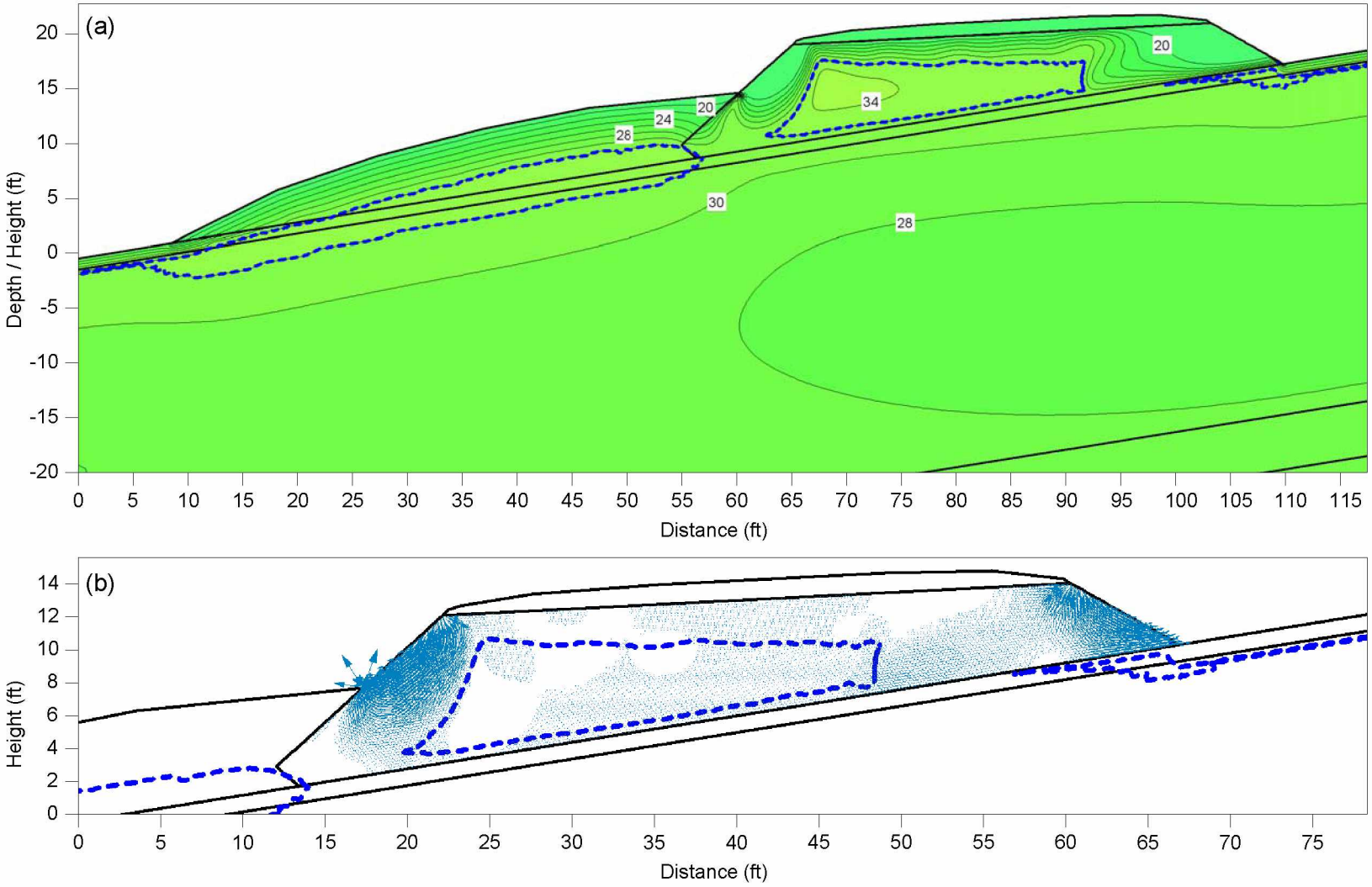

Figure 6.41 Snow-open model results for Nov. 1 with (a) temperature and (b) air velocity vectors. Temperature contours are spaced every 2°F and the dashed blue line represents the 32°F isotherm.

6.3.2 Analysis of Modeling Results

The modeling results were analyzed to compare temperatures at the base of the embankment for the plowed-closed, snow-closed, plowed-open, and snow-open models. The mean monthly temperatures at the base of the embankment for each model were plotted, and the results for Jan., Mar., May, Jul., Sep., and Nov. are presented in Figures 6.42 through 6.47, respectively.

The snow-closed and snow-open models had warmer temperatures beneath the ACE (horizontal distance 48 to 103 ft) during Jan. and Mar. than beneath the thermal berm (horizontal distance 0 to 48 ft); this is likely due to the lower thermal conductivity of the ACE and the decreased effectiveness of the air convection due to a snow-covered road surface. Temperatures beneath the ACE for the plowed-closed and plowed-open models were colder than beneath the thermal berm for almost the entire year; this is due to colder temperatures at the driving surface of the ACE, thus leading to a more unstable air density gradient and increased air convection.

The snow-open model results indicate warmer temperatures beneath the ACE than the snow-closed model. Likewise, the plowed-open model shows warmer temperatures beneath the ACE than the plowed-closed model. It is also evident that from approximately 95 to 103 ft, the snow-open and plowed-open models exhibit almost the same temperatures for all months. The warmer temperature results from the open air boundary models were not expected, and are the result of the snow-covered gravel temperature boundary condition applied to the side slopes of the ACE, which decreased the cooling effect by 0.50. In reality, an ACE with open side slopes would be expected to have increased convective heat transfer due to cold outside air being permitted to flow more easily into the embankment while warm air flows out.

The modeling results also reveal large temperature variations at both ends of the embankment for each modeling scenario. The reason for the extreme temperatures is due to the embankment fill becoming thinner at the embankment toes. As the thickness of the fill decreases toward the toes, there is less material to insulate the base of the embankment from changes in model air temperature. Since model temperature results were taken from the embankment/foundation soil interface, the first node and last node at each end of the embankment represent the point of intersection between the embankment slope and the foundation soil, thus the temperature displayed at each end of the embankment is actually the surface boundary temperature.

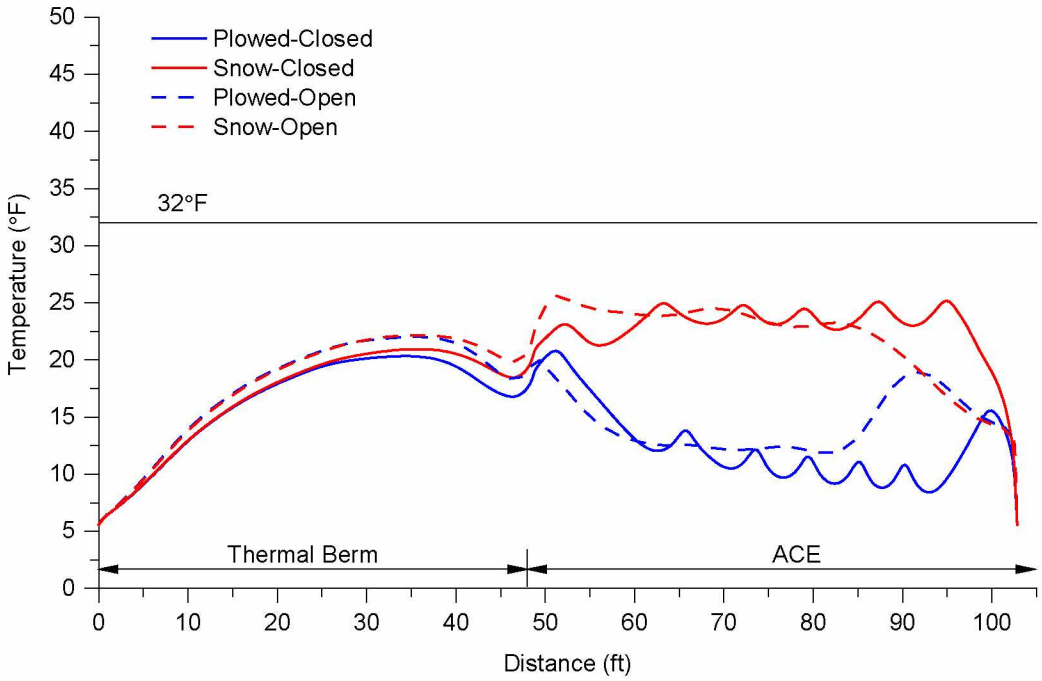

Figure 6.42 Mean monthly Jan. model temperatures at base of embankment.

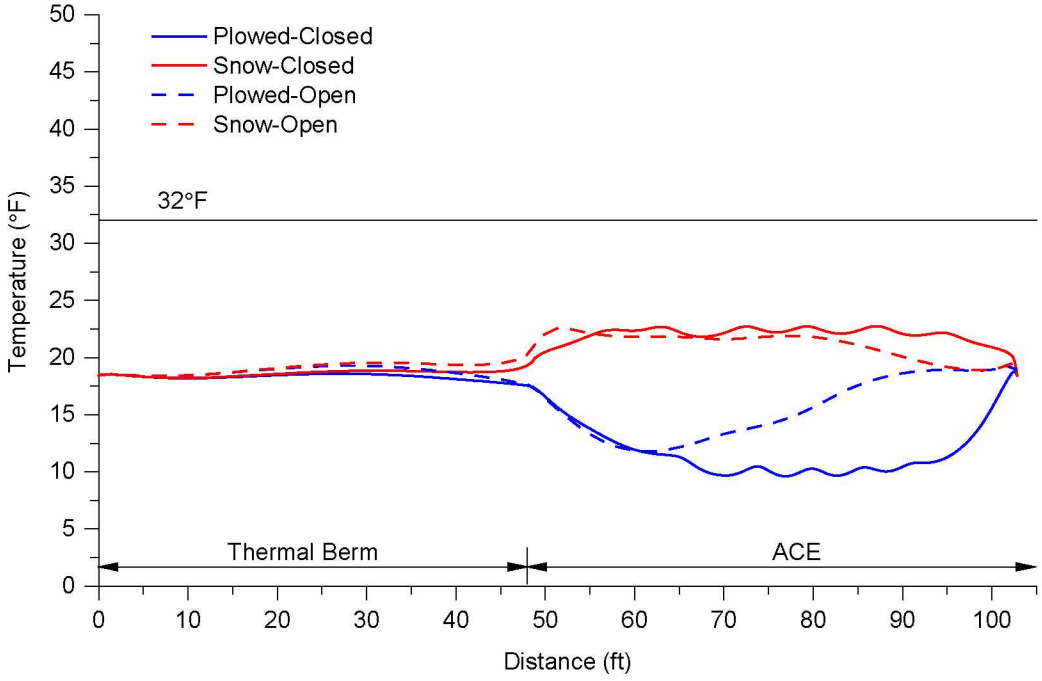

Figure 6.43 Mean monthly Mar. model temperatures at base of embankment.

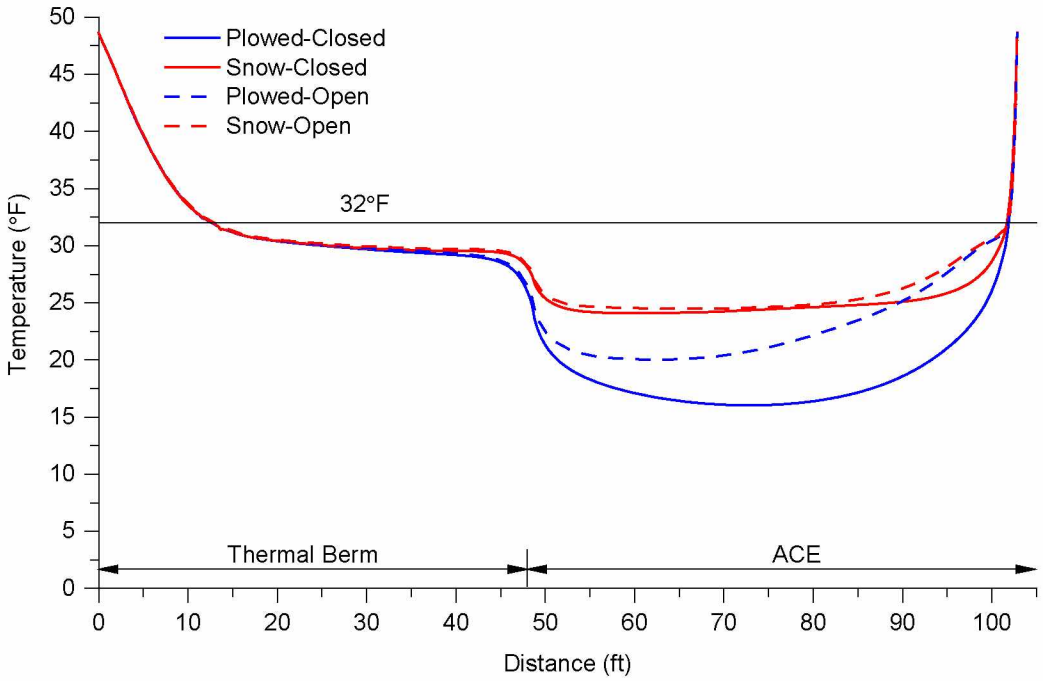

Figure 6.44 Mean monthly May model temperatures at base of embankment.

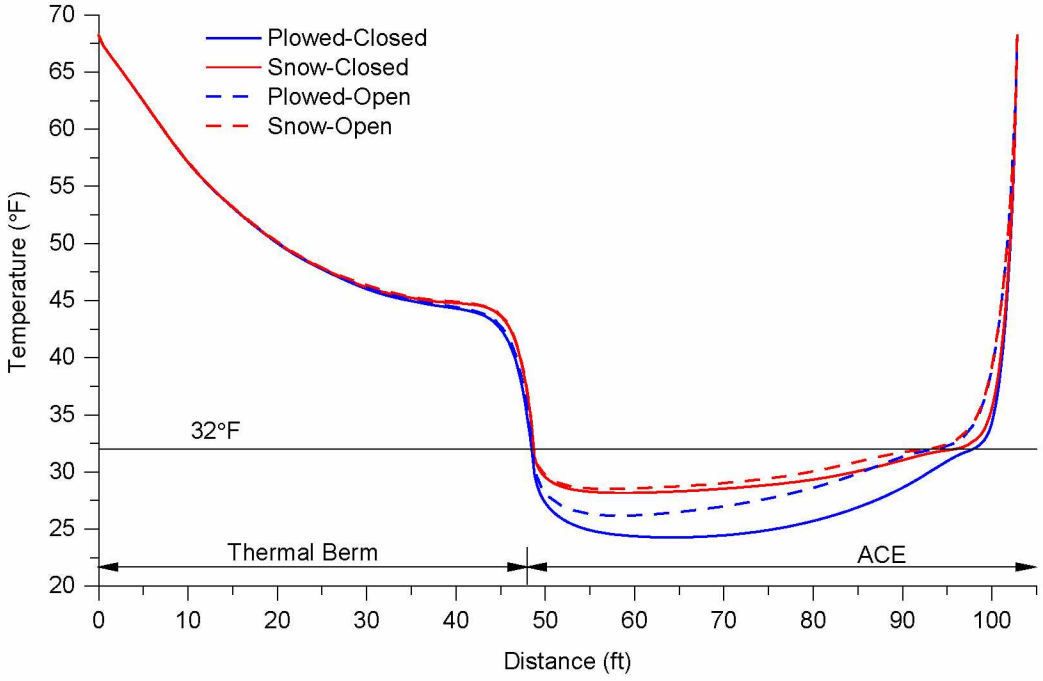

Figure 6.45 Mean monthly Jul. model temperatures at base of embankment.

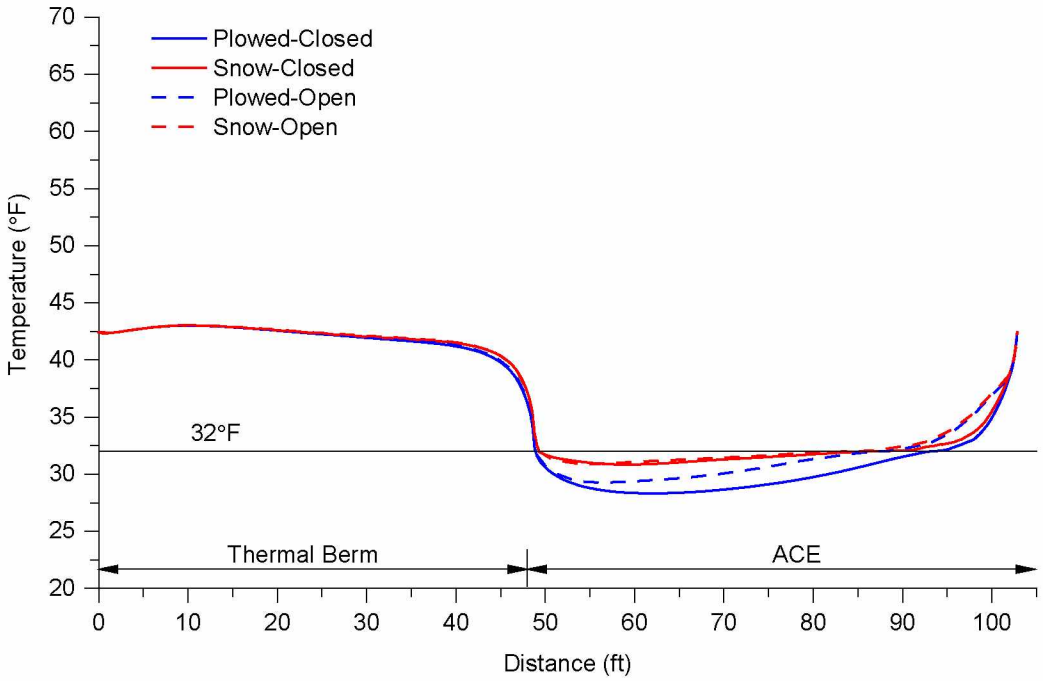

Figure 6.46 Mean monthly Sep. model temperatures at base of embankment.

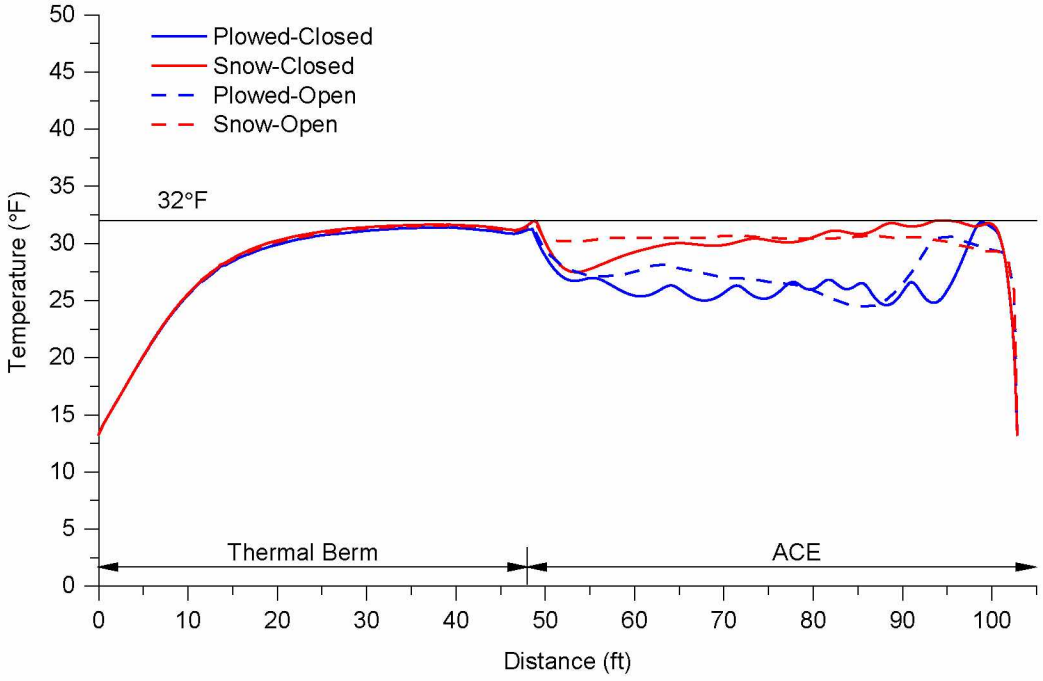

Figure 6.47 Mean monthly Nov. model temperatures at base of embankment.

The mean annual model temperatures at the base of the embankment are shown in Figure 6.48. The average temperatures at the base of the thermal berm were similar for all the models, with the mean annual temperatures ranging from 31.1°F for the plowed-closed model, to 31.6°F for the snow-open model. Given the ice-rich and thaw unstable nature of the silt beneath the embankment, it is likely that any above freezing temperatures at the base of the embankment could translate to thaw settlement, especially at the toes of the thermal berm and ACE where the mean annual temperatures are above freezing. Although the mean annual temperature across most of the base of the thermal berm is just below freezing, thaw settlement is still expected due to the high mean monthly temperatures that occur at the base of the thermal berm from May through Sep. (see Figures 6.44 through 6.46).

At the base of the ACE, the warmest mean annual temperatures of 27.1°F were from the snow-closed and snow-open models. The coldest mean annual temperature at the base of the ACE was 21.3°F from the plowed-closed model. The mean annual model temperatures across the base of the thermal berm and ACE are summarized in Table 6.12.

The mean monthly modeling temperatures at the base of the embankment for the plowed-closed and snow-closed models were compared to measured temperatures from the TAC. Modeling results for the plowed-open and snow-open models were not included in the comparison since they are believed to be incorrect. The mean monthly temperatures at the base of the embankment for the plowed-closed model, snow-closed model, and TAC for Oct., Nov., Dec., Jan., Feb., Mar., Apr., May, and Jun. are presented in Figures 6.49 through 6.57, respectively.

For the months of Oct. and Nov. (see Figures 6.49 and 6.50) the temperatures beneath the ACE are colder for the models than measured temperatures, which is expected since the model results are at thermal equilibrium while the ACE has not yet experienced its first year of convection. Beneath the thermal berm the modeled temperatures are similar to the measured temperatures in Oct.; however, the modeled temperatures become much colder than the measured temperatures for Nov. through Apr., at which time the trend shifts and the modeled temperatures for Jun. are much warmer than what was measured.

The plowed-closed model temperatures beneath the ACE for all the months are typically much colder than those measured, while the snow-closed model temperatures are slightly colder and generally more comparable; however, there appears to be a lack of multiple convection cells in the measured data compared to the models. It was expected that the snow-closed model temperatures would be more comparable to the measured temperatures since the

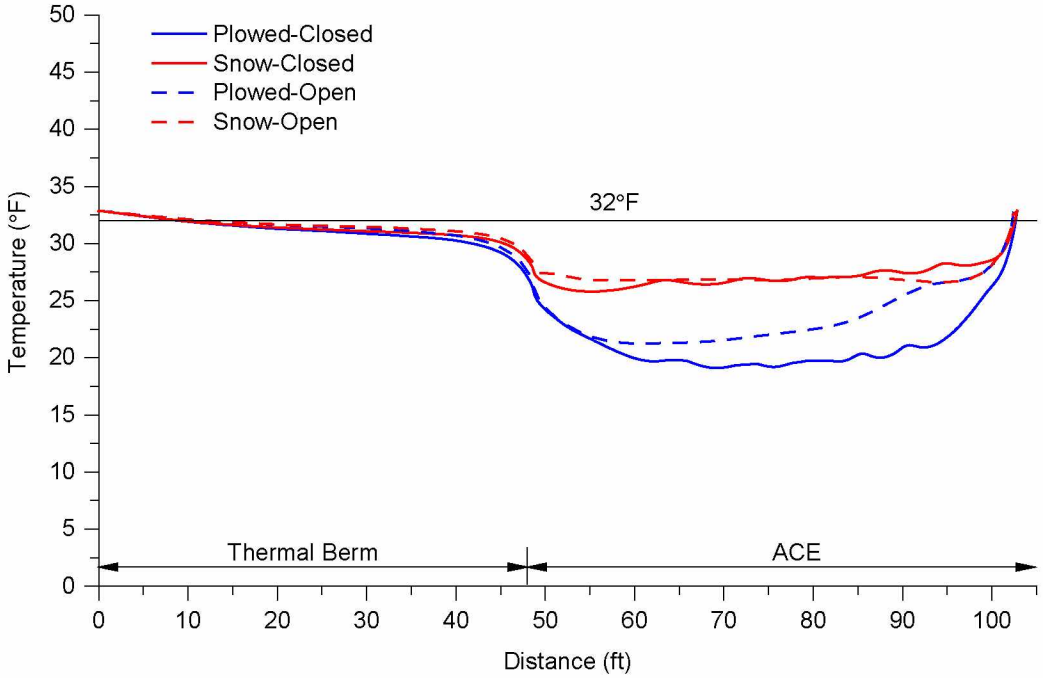

Figure 6.48 Mean annual model temperatures at base of embankment.

Table 6.12 Mean annual model temperatures across base of thermal berm and ACE.

Model Description	Thermal Berm (°F)	ACE (°F)
Plowed-Closed	31.1	21.3
Plowed-Open	31.4	23.6
Snow-Closed	31.3	27.1
Snow-Open	31.6	27.1

highway at the site is not maintained in the winter and snow is left to accumulate on the embankment surface. The apparent lack of multiple convection cells in the measured data could be due to an attenuating effect from the sand backfill over the TAC casing as well as averaging the data for each month; however, there does appear to be at least two convection cells in the measured data for Dec. (see Figure 6.51), which also more closely match the snow-closed model temperatures.

The average temperatures at the base of the embankment for the plowed-closed and snow-closed models and average temperatures measured by the TAC for Oct. through Jun. are presented in Figure 6.58. The results indicate that the modeled temperatures beneath the entire embankment are significantly colder than those measured, although the average snow-closed model temperatures are closer to the measured temperatures from 58 to 63 ft.

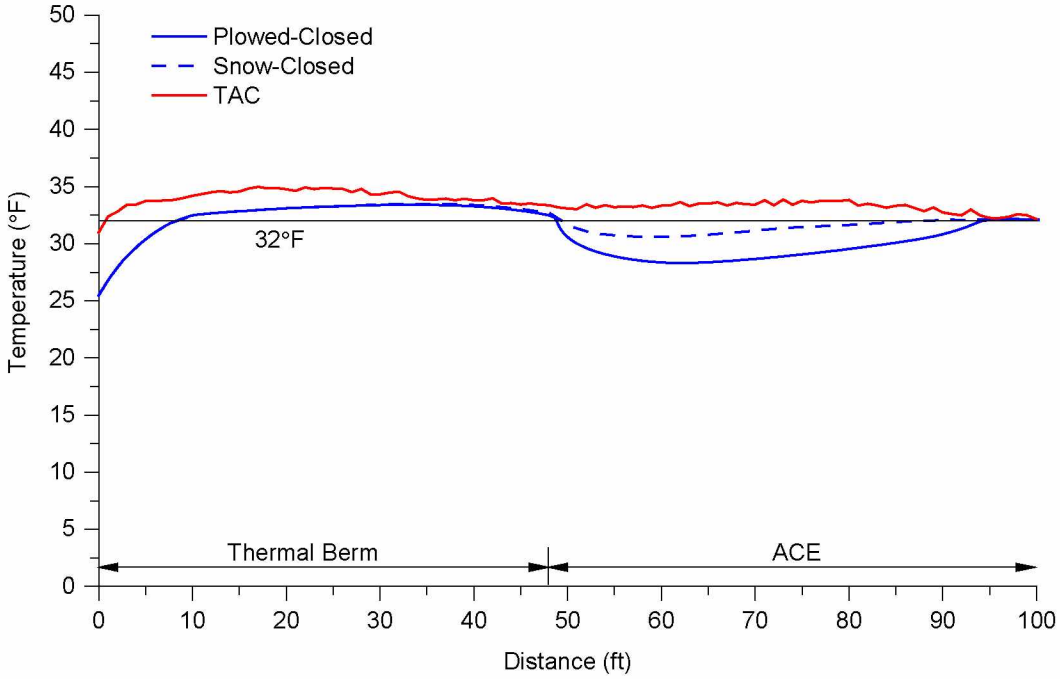

Figure 6.49 A comparison of modeled temperatures to measured TAC temperatures for Oct.

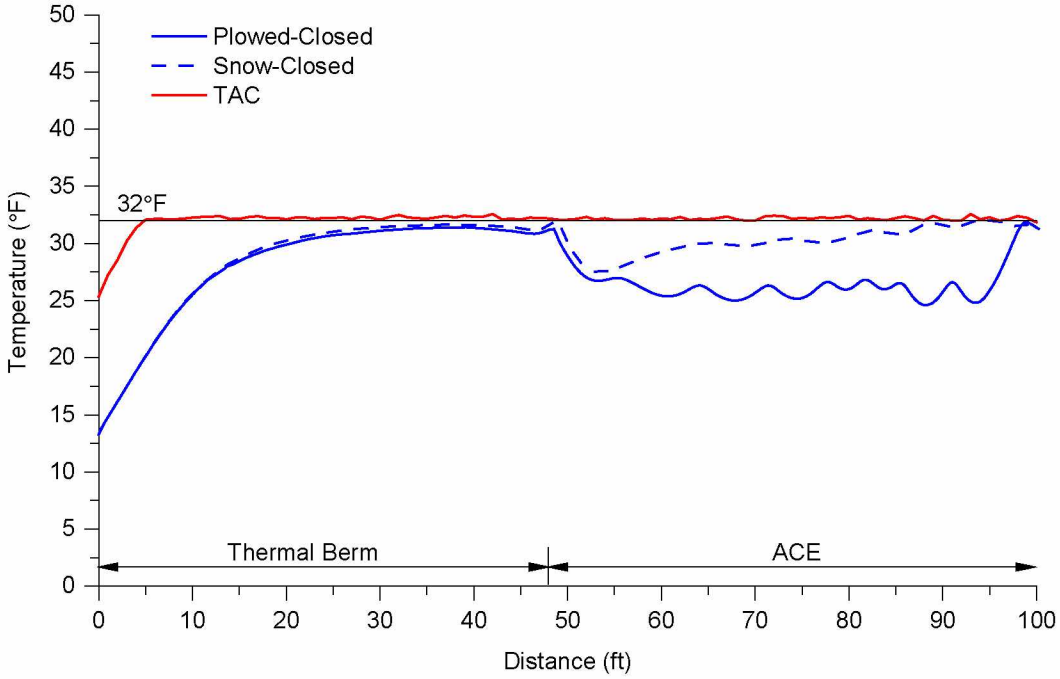

Figure 6.50 A comparison of modeled temperatures to measured TAC temperatures for Nov.

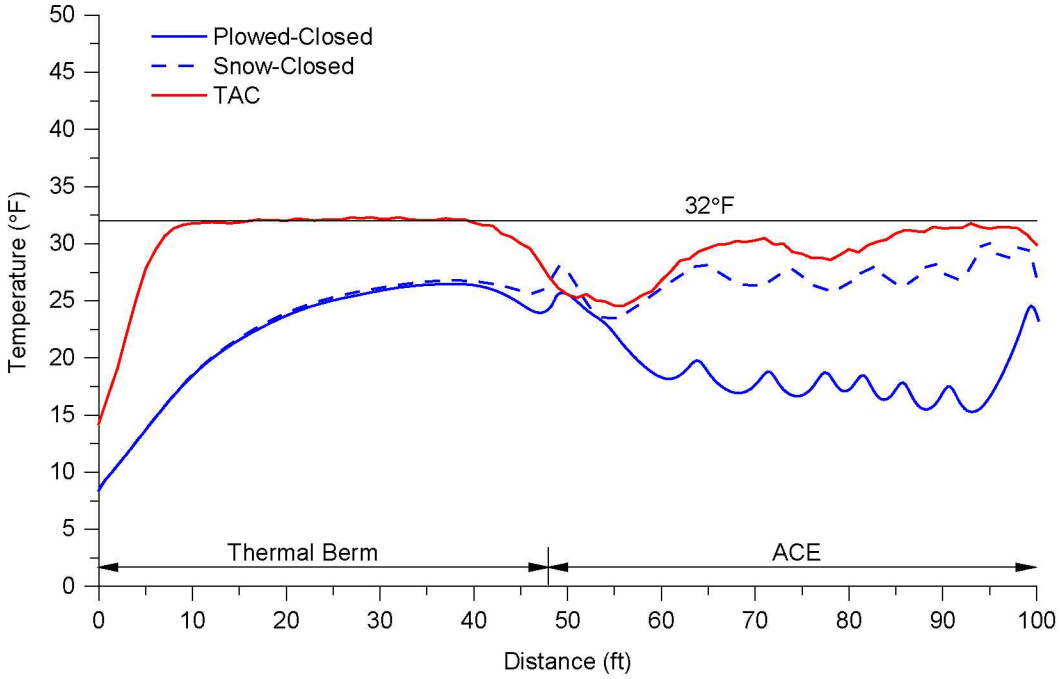

Figure 6.51 A comparison of modeled temperatures to measured TAC temperatures for Dec.

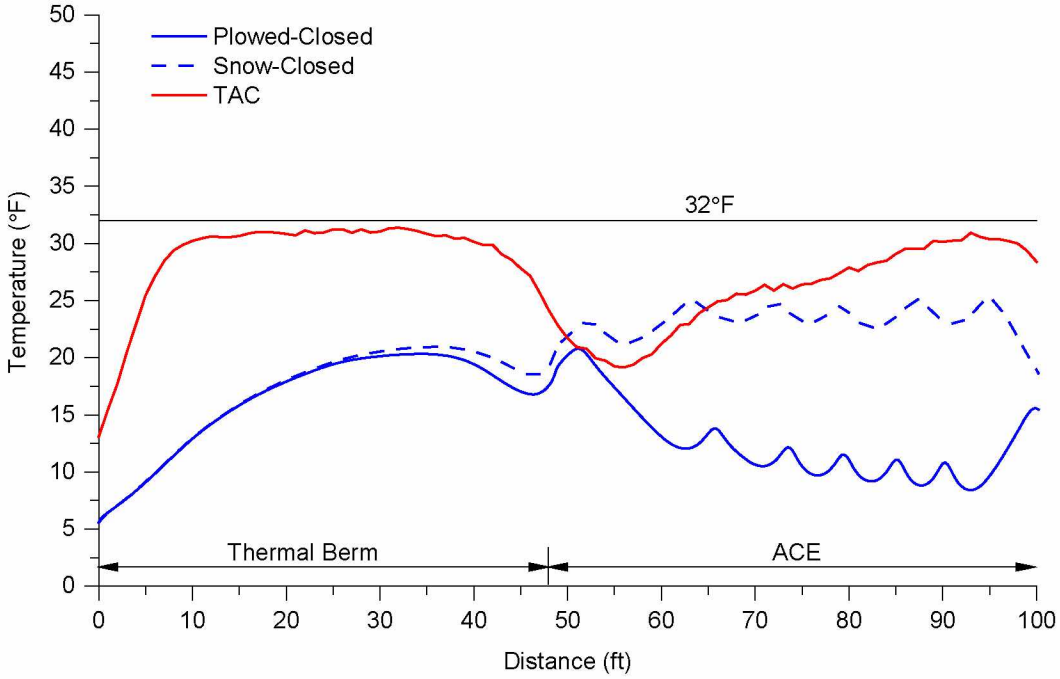

Figure 6.52 A comparison of modeled temperatures to measured TAC temperatures for Jan.

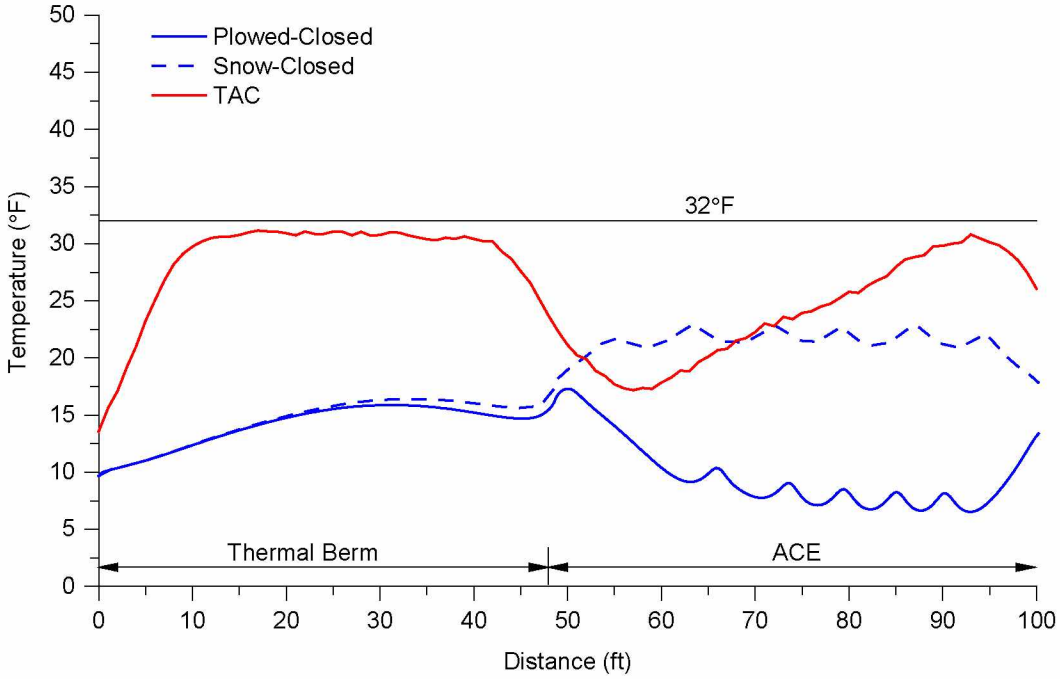

Figure 6.53 A comparison of modeled temperatures to measured TAC temperatures for Feb.

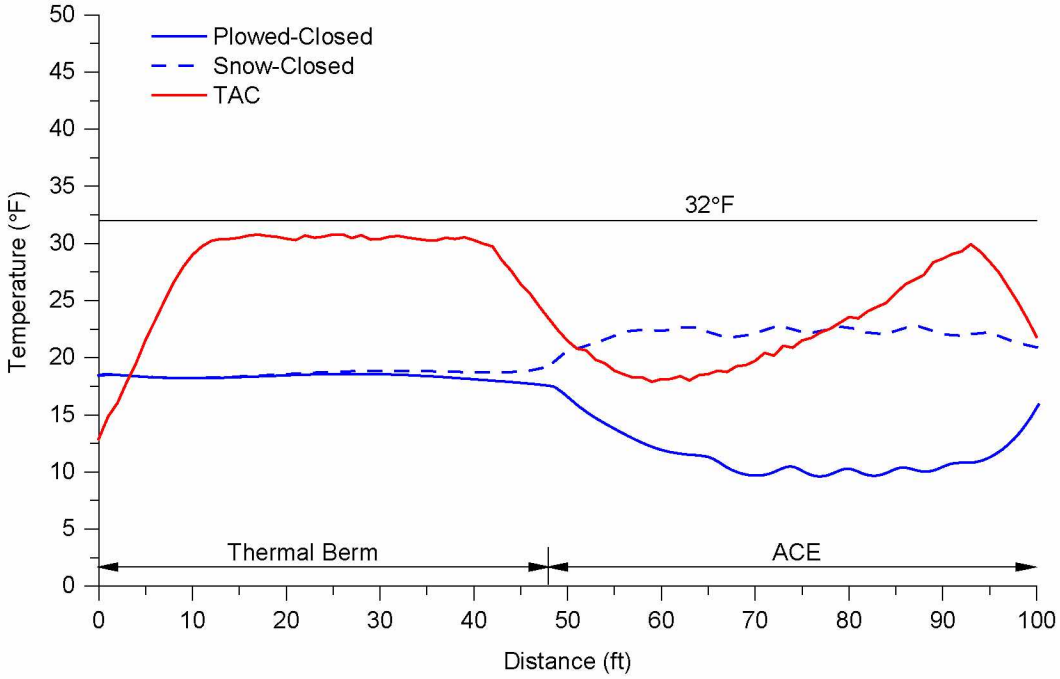

Figure 6.54 A comparison of modeled temperatures to measured TAC temperatures for Mar.

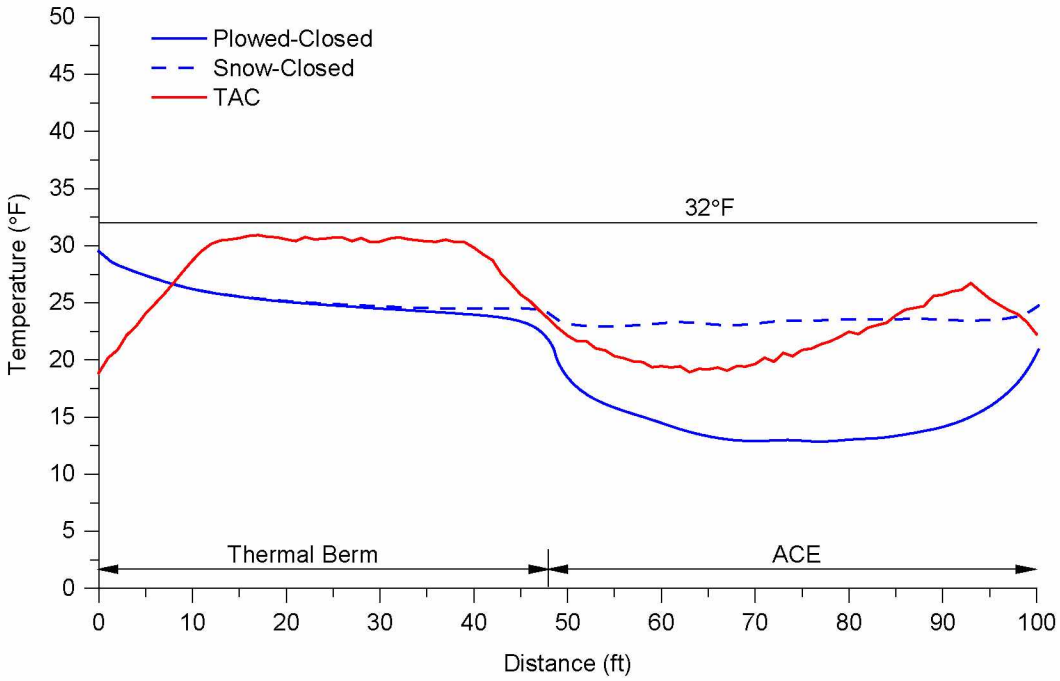

Figure 6.55 A comparison of modeled temperatures to measured TAC temperatures for Apr.

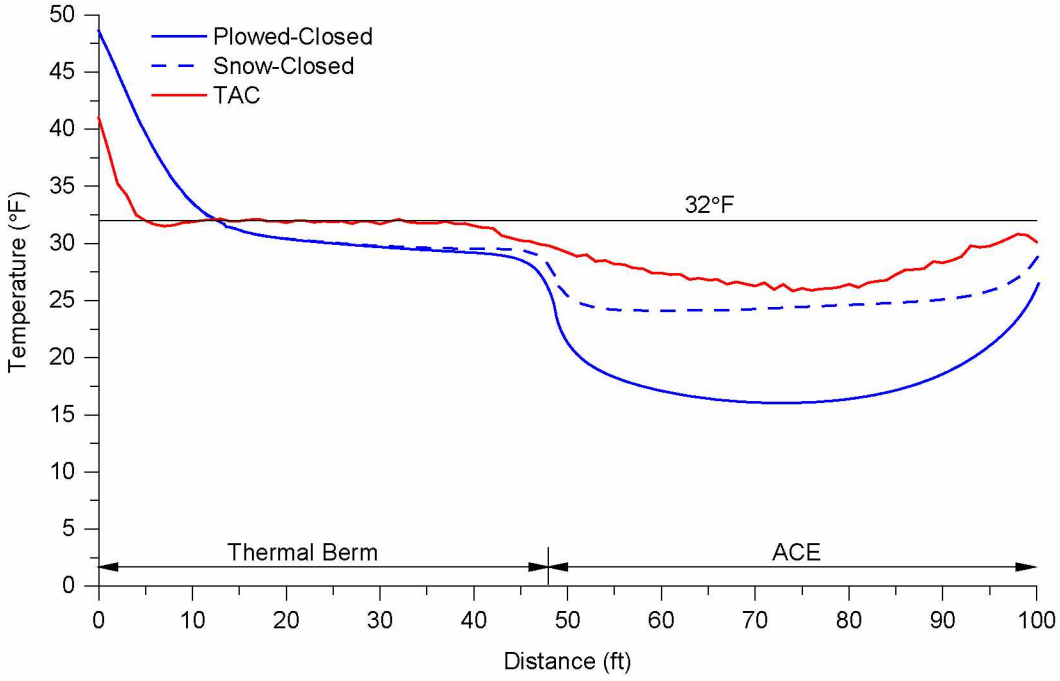

Figure 6.56 A comparison of modeled temperatures to measured TAC temperatures for May.

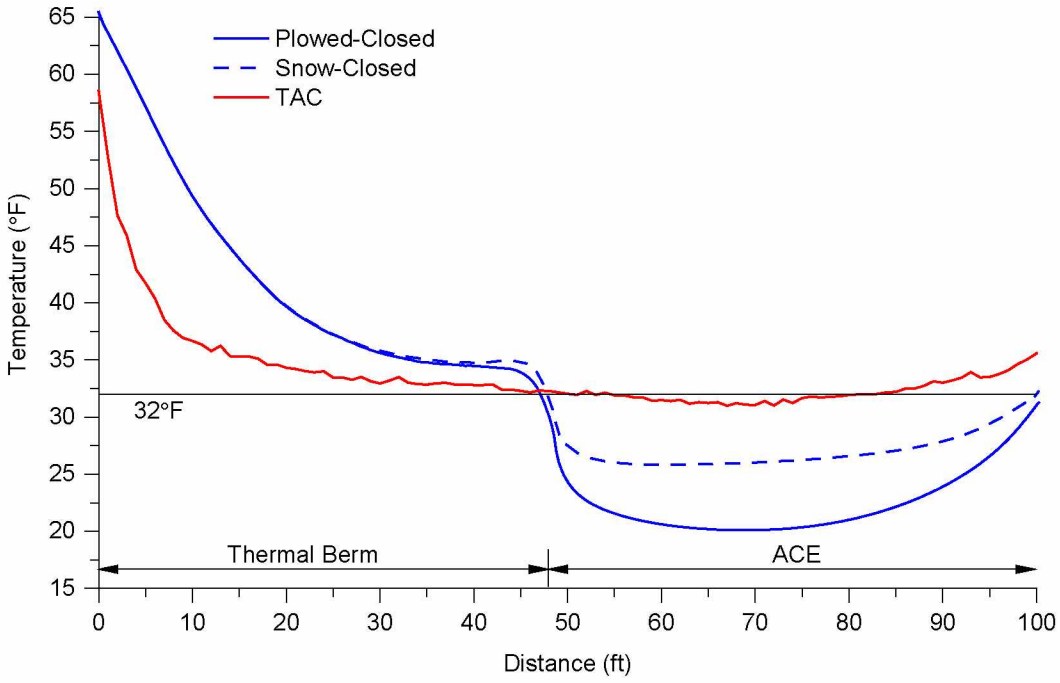

Figure 6.57 A comparison of modeled temperatures to measured TAC temperatures for Jun.

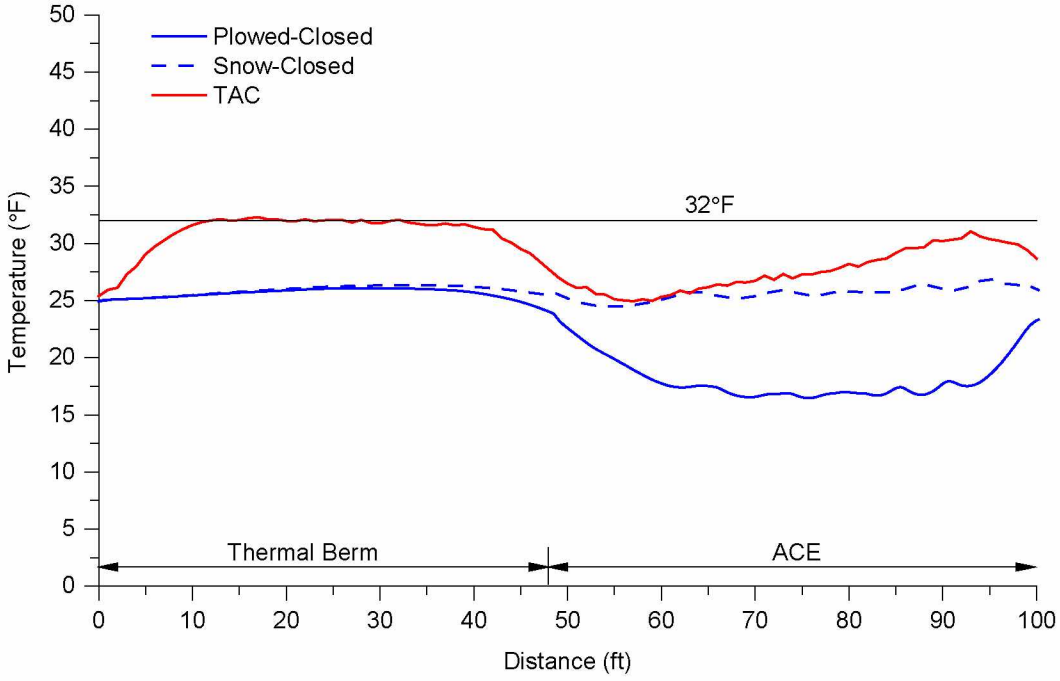

Figure 6.58 A comparison of averaged modeled temperatures to averaged measured TAC temperatures for Oct. through Jun.

To provide a quantitative analysis of the differences between the plowed-closed modeled temperatures, snow-closed modeled temperatures, and TAC measured temperatures, the average monthly temperatures at the base of the embankment were calculated by averaging all points beneath the thermal berm and ACE. Figure 6.59 illustrates the mean monthly temperatures at the base of the thermal berm from Oct. 2012 to Jun. 2013. The results indicate that the temperatures beneath the thermal berm for the plowed-closed and snow-open models are nearly identical, which is expected since the same surface boundary condition was applied to the thermal berm in both modeling scenarios. When compared to the measured temperatures, the modeled temperatures are slightly lower in Oct., becoming significantly lower throughout the winter. In Jun. the modeled temperatures are higher than the measured temperatures. In general, there is a greater change in the modeled temperatures than what was measured by the TAC.

Figure 6.60 illustrates the mean monthly temperatures at the base of the ACE for the TAC measured temperatures, and the snow-closed and plowed-closed modeled temperatures from Oct. 2012 to Jun. 2013. The results indicate that the temperatures beneath the ACE for the plowed-closed model were much lower than those measured, with the greatest difference in temperature occurring in Feb. The snow-closed model, on the other hand, produced temperatures that were comparable to the measured temperatures, although typically slightly lower. The use of a slightly smaller freezing *n*-factor for the snow-closed model may have resulted in mean monthly temperatures even more comparable to those measured. The mean monthly temperature values used to develop Figures 6.59 and 6.60 are provided in Table C-1 of Appendix C, and differences between the average monthly measured temperatures, and snow-closed and plowed-closed model temperatures are provided in Table C-2.

The mean plowed-closed modeled temperatures from Oct. 2012 to Jun. 2013 at the base of the thermal berm and ACE were 25.6°F and 18.2°F, respectively. For the snow-closed model, the temperatures at the base of the thermal berm and ACE were 25.9°F and 25.6°F, respectively. Finally, the measured temperatures at the base of the thermal berm and ACE were 30.8°F and 27.6°F, respectively. These results indicate that on average the temperatures beneath the ACE for the snow-closed model more closely match the measured temperatures. In addition, the average temperatures beneath the thermal berm for both models were significantly colder than those measured.

The seemingly larger seasonal temperature fluctuations in the models could be the result of the chosen *n*-factors. A freezing *n*-factor of 0.5 and thawing *n*-factor of 1.5 were used for the snow-covered gravel. In reality, the site specific freezing and thawing *n*-factors most

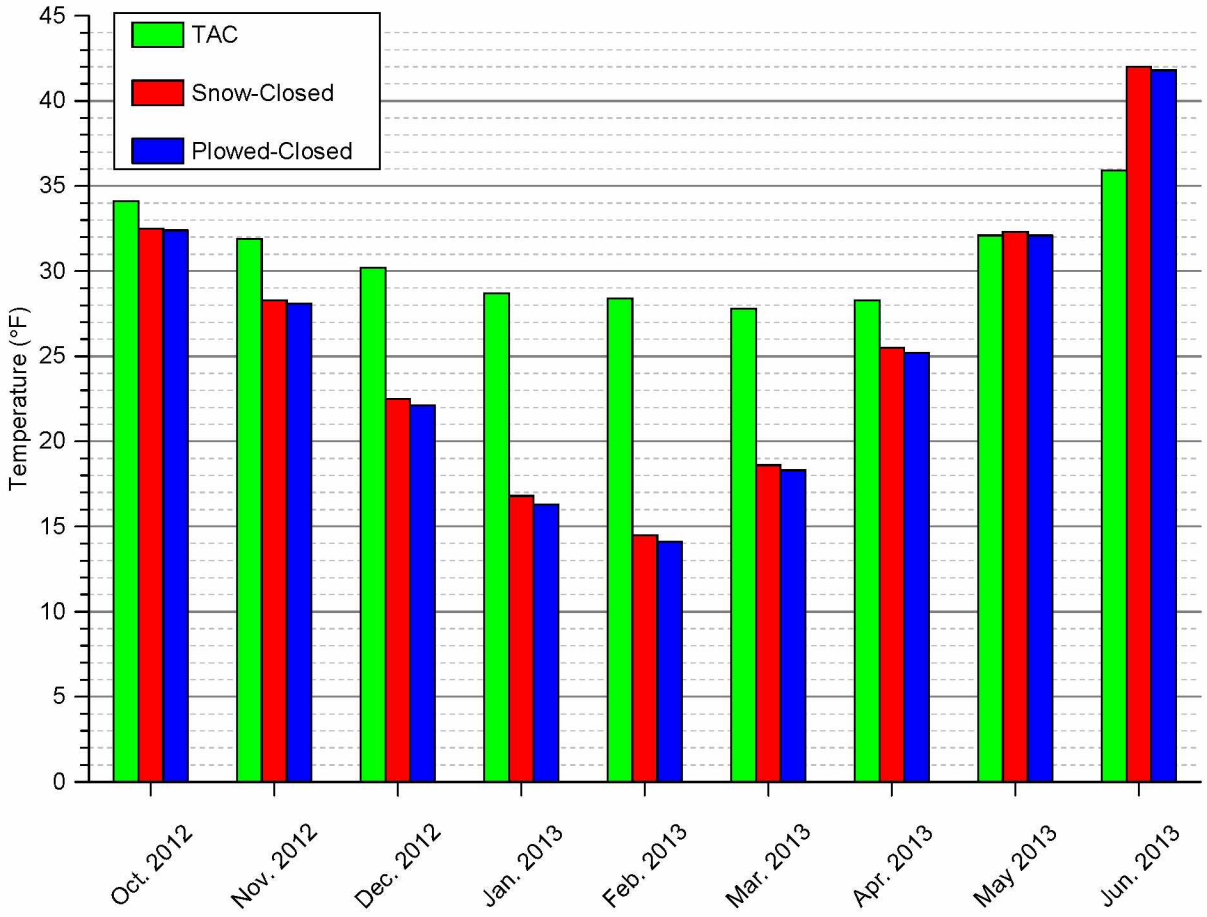

Figure 6.59 Mean monthly temperatures at base of thermal berm.

likely differed from those chosen for modeling. Another factor that could account for the differences in the modeled and measured embankment temperatures are differences in the air temperature at the site and historical air temperature used for modeling. To evaluate the differences in air temperature, the average monthly air temperature measured at Lost Chicken was compared to the average monthly historical air temperature used in the models. Figure 6.61 illustrates the differences between the historical and measured air temperatures for Oct. 2012 to Jun. 2013. The data used to create Figure 6.61 can be found in Table C-3 of Appendix C. The results show that for Oct. to Dec. the measured air temperature was colder than the model air temperature, yet the average modeled temperature at the base of the embankment was colder. This indicates that the model freezing *n*-factor was too large, or there was still heat trapped beneath the newly constructed embankment.

For Jan. and Feb. the average model air temperatures were colder than the measured air temperatures. This coincides with the much colder modeled embankment temperatures compared to the measured temperatures for the same months; thus the difference in model and

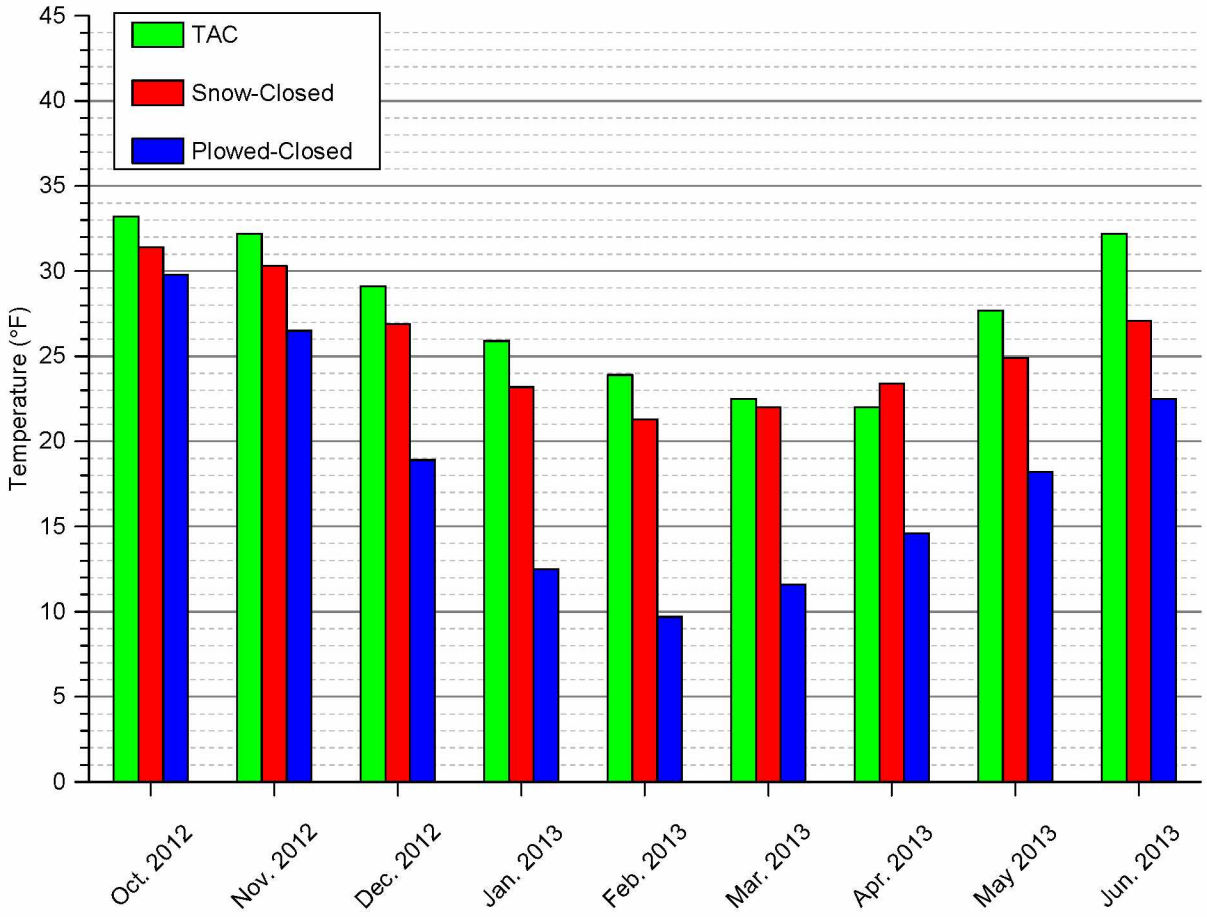

Figure 6.60 Mean monthly temperatures at base of ACE.

measured air temperatures likely contributed to the extreme difference. From Mar. to May the average model air temperatures were warmer than the measured temperatures, yet the modeled embankment temperatures were colder; however, the difference between the model and measured air temperatures was less in May, as was the difference between the modeled and measured embankment temperatures. Finally, the average measured air temperatures in Jun. were warmer than the model air temperatures, yet the modeled embankment temperatures were warmer than those measured. This could be due to a too large thawing *n*-factor.

In general, it appears that there is no single element that accounts for the differences between the modeled and measured embankment temperatures. Instead, the differences are likely due to a combination of the differences between modeled and site specific *n*-factors, differences between model and measured air temperatures, and the fact that the embankment was newly constructed and not yet at thermal equilibrium, while the model was run for 27 years and had more time to reach equilibrium.

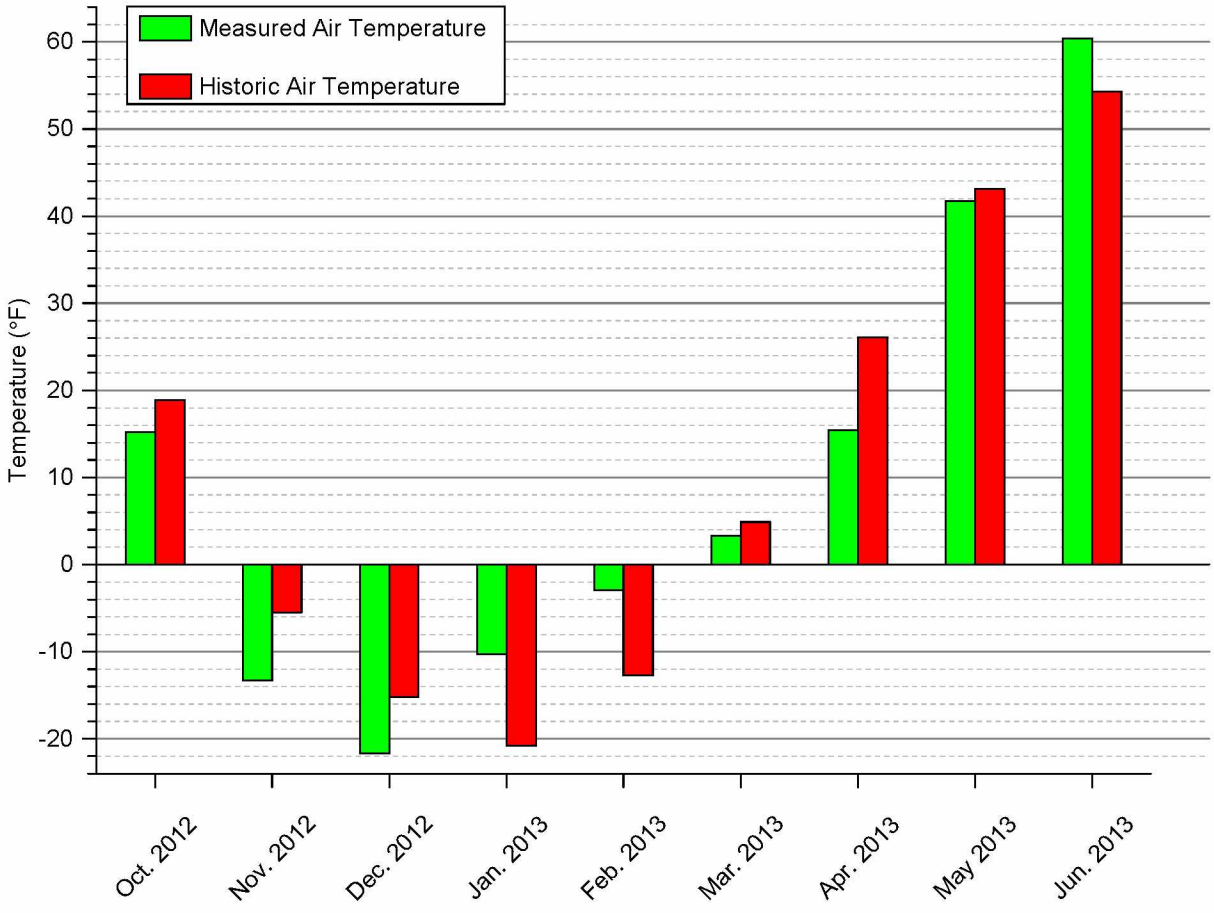

Figure 6.61 Mean monthly measured and historic air temperatures.

CHAPTER 7 SUMMARY AND CONCLUSIONS

The primary goals of this research were to: 1) evaluate geotechnical instrumentation performance for measuring deformation and temperature; 2) analyze embankment thermal performance and deformation; and 3) develop a two-dimensional numerical model of the ACE and thermal berm to estimate long-term stability. In evaluating instrument performance, temperature measurements from the relatively new TAC and SAA were compared to those of the well-established thermistor string. In general, the results of the SAA compared favorably to the thermistor string, with measured temperatures well within the manufacturer-stated accuracy for the SAA temperature sensors. The SAA device does not provide very high spatial temperature resolution due to the sensor spacing, which is a drawback in applications where high spatial temperature resolution is necessary, such as determining active layer thickness.

The mean difference between temperature measurements from the TAC and thermistor string exceeded the manufacturer-stated accuracy of the thermistor string by 0.06°F, which is considered small enough that the TAC is still suitable for monitoring temperature change depending on the specific needs of a given project. Another positive feature of the TAC is the potentially high spatial temperature resolution (depending on the specified sensor quantity and spacing), as well as the flexibility and small diameter of the cable. This makes the TAC suitable for use in monitoring temperature changes over both short and long distances where either low or high spatial resolution is required.

The last instrument for which performance was evaluated was the relatively new SAA, which was compared to the well-established SI for monitoring vertical deformation beneath an embankment over ice-rich permafrost. Comparison of bi-weekly deformation measurements during this research revealed that the SAA measurements deviated from the SI measurements over time. Since there was a small amount of differential settlement at the casing ends from which deformation measurements were referenced, it is difficult to ascertain whether or not instrument drift, differential casing settlement, or both are to blame for the difference in readings. Despite the small deviation in measurements, the SAA yielded results comparable to the traditional SI with the added benefit of automation, thus eliminating the need for frequent field trips to take measurements. Automation allows a much higher measurement frequency facilitating the identification of sudden changes in deformation. Results from this research illustrate that it is imperative to have one end of the instrument casing secured to a fixed point, such as a post anchored in the ground, since it is impractical to survey the casing end on a daily basis.

In evaluating the thermal performance of the embankment, temperature changes over time at the base of the thermal berm and ACE were analyzed. The temperature measurements provided strong evidence to suggest that the ACE at Lost Chicken experienced density-driven air convection during the winter months, and that temperatures at the base of the ACE were significantly colder than beneath the thermal berm. Temperature measurements also indicated that the coldest section of the ACE occurred on the downhill side where the ACE fill was the thickest. Warmer temperatures in the uphill direction may be due to the decrease in ACE thickness, resulting in decreased air convection and less heat transfer.

The warmest temperature measurements at the base of the embankment occurred beneath the toe of the thermal berm. Data indicated that temperatures at the base of the thermal berm were above freezing by the middle of May 2013, while temperatures beneath the thickest portion of the ACE did not rise above freezing until the end of Jun. 2013. Based on these temperature measurements, it is expected that thaw settlement will occur beneath the thermal berm and the uphill toe of the ACE.

The last objective of this research was to develop a two-dimensional numerical model of the ACE and thermal berm, which was accomplished using GeoStudio software, including the TEMP/W, SEEP/W, and AIR/W modules. Four different embankment scenarios were modeled to simulate plowed and snow-covered gravel embankments with open airflow boundaries, and plowed and snow-covered gravel embankments with closed airflow boundaries. The final results indicated that the snow-closed and snow-open ACE had significantly higher temperatures at the base and less pronounced air convection eddies than the plowed-closed and plowed-open ACE. This is due primarily to the warmer embankment surface temperatures on account of the snow cover, resulting in weaker air convection.

Results of the plowed-open and snow-open models were not as expected, as the models showed little difference in embankment temperatures from their closed airflow boundary counterparts. The reason for the warmer than expected temperatures is due to the snow-covered gravel boundary condition applied to the side slopes of the ACE, which made the air flowing into the embankment the same temperature as the snow-covered gravel surface.

Comparison of the plowed-closed and snow-closed model temperatures to measured temperatures revealed that the models were colder during winter and warmer during summer than the measured temperatures, and the models did not mimic the decrease in cooling associated with the decrease in ACE thickness as observed in the measured temperatures. Of the two models, the snow-closed modeled temperatures beneath the ACE were the most similar

to measured temperatures, likely due to the fact that the roadway at Lost Chicken is not maintained during the winter.

There are a number of possible reasons for the differences between the modeled and measured temperatures. First, the freezing and thawing *n*-factors may not be correct for the site. Second, historical air temperatures used for the model differed from air temperatures measured at the site. Next, given that the embankment was just constructed in 2012, it did not have time to reach thermal equilibrium and likely had excess heat trapped beneath it after construction. Finally, there may have been differences in the material properties used for the embankment in the models compared to what was actually at the site. Higher moisture contents in the thermal berm would result in higher latent heat and a greater attenuating effect on temperature changes at the base of the embankment. Even though the thermal modeling did not reproduce the temperatures measured at Lost Chicken, it provided an estimate of long-term thermal performance, which is valuable when evaluating an ACE as a design option for a specific project. It is also likely that the model could be modified to represent site specific conditions better with further adjustment of input parameters.

Given the results of geotechnical instrumentation and numerical modeling at Lost Chicken, it is expected that thaw settlement will continue to occur beneath the thermal berm until thermal equilibrium is eventually reached. Based on temperature measurements, the exposed, uphill toe of the ACE also may experience some settlement that could translate to longitudinal cracking along the shoulder of the roadway; however, most of the ACE is expected to remain stable. Finally, foundation soil temperatures beneath the thermal berm are expected to grow warmer while temperatures beneath the ACE are expected to grow colder until thermal equilibrium is reached.

Based on the results of this research, the following are recommendations for future research and modeling.

- It is highly recommended that all temperature measurement devices be checked for calibration in an ice bath prior to field installation. It is also recommended that any instruments used be checked for calibration at the end of the monitoring period to assess how well they maintain calibration over time. This would enable evaluation of long-term sensor performance and reliability.
- ACE design should incorporate the existing ground slope, thus ensuring that a minimum fill thickness is maintained at the thinnest parts of the embankment.
- For continued research in monitoring temperature change beneath an ACE, it is recommended to use temperature sensors with high spatial resolution to identify the

potential location of air convection eddies and to observe the extreme temperature shifts that occur at the embankment toes.

- For a non-symmetric embankment, temperature sensors should be installed across the full width since it appears that ACE fill thickness impacts the uniformity of temperatures across the base of the embankment. The embankment temperatures also should be monitored for a longer period than one year since the initial season's temperatures appear to be impacted by the embankment construction.
- For future research involving the use of an SAA or SI to monitor vertical deformation beneath an embankment over ice-rich permafrost, it is imperative that at least one end of the instrument casing is anchored to a fixed elevation. This could be accomplished by installing a vertical post in the ground to a depth sufficient to resist frost jacking, just beyond the toe of the embankment. The end of the instrument casing should extend beyond the embankment toe and be secured to the wooden post. Periodic survey measurements of the post should be conducted to check for any vertical movement over time.
- For future research involving numerical modeling of ACE, emphasis should be placed on evaluation of site specific surface *n*-factors for model calibration.
- Measured air temperatures could be used in modeling to better reproduce measured embankment temperatures and aid in model calibration; however, the historical average air temperatures should be used for estimation of long term embankment temperatures.
- Finally, for modeling an ACE with open air boundary conditions, the side slopes must be assigned a surface boundary temperature function equal to the modeled air temperature where the open airflow boundary exists, thus allowing the temperature of the air that flows into the embankment to be unaffected. To be more realistic, the ACE side slopes during winter should have some points with open airflow boundaries and freezing *n*-factor of 1 to represent "holes" through the snow, while the rest of the side slope should be assigned a zero airflow boundary and a freezing *n*-factor for snow-covered gravel. During the thawing season, the airflow boundary should be open for the entire side slope since there is no snow.

REFERENCES

Adl-Zarrabi, B. (2006). *Forsmark Site Investigation Borehole KFM01C, Thermal Properties of Rocks Using Calorimeter and TPS Method,* SP Swedish National Testing and Research Institute Report No. P-06-66, Stockholm, Sweden, 34 p.

Ager, T. A. (2003). "Late Quaternary vegetation and climate history of the central Bering Land Bridge from St. Michael Island, western Alaska." *Quaternary Research*, 60, 19-32.

Alaska History & Cultural Studies. (2014). "Alaska's Heritage." <http://www.akhistorycourse.org/articles/article.php?artID=145> (Sep. 25, 2012).

ASTM International. (1999). *Standard Test Method for Laboratory Determination of Water (Moisture) Content of Soil and Rock by Mass,* ASTM International Standard D2216, West Conshohocken, PA, 1135-1139.

Barney, S. W. (2010). *Taylor Highway MP 70 Lost Chicken Slide*, Design Study Report State Project No. 63379, ADOT&PF Northern Region Preconstruction, Fairbanks, AK, 15 p.

BeadedStream LLC. (2010). *BeadedStream TAC Sensor Specifications*, BeadedStream LLC., Anchorage, AK.

Bjella, K. (2013). *Thule Air Base Airfield White Painting and Permafrost Investigation*, Cold Regions Research and Engineering Laboratory Report No. TR-13-8, US Army Corps of Engineers, Hanover, NH, 89 p.

Bureau of Land Management (BLM). (2007). "Taylor Highway Fortymile gold country travel guide," U.S. Department of the Interior, <http://www.blm.gov/style/medialib/blm/ak/aktest/brochures.Par.71908.File.dat/Taylor_Highway_brochure.pdf> (Sep. 25, 2012).

Campbell Scientific, Inc. (2011). *Model 109 Temperature Probe Instruction Manual,* Campbell Scientific, Inc., Logan, UT, 22 p.

Darrow, M. (2008). *Taylor Hwy MP 64 to Canadian Border Rehabilitation,* ADOT&PF Geotechnical Report State Project No. 66446, ADOT&PF Northern Region, Fairbanks, AK, 137 p.

Darrow, M. (2011). "Thermal modeling of roadway embankments over permafrost." *Cold Regions Science and Technology*, 65(3), 474-487.

Darrow, M., and Xu, L. (2011). *UAF Support for Shishmaref Airport Master Plan, Stage II, Wind Study and Climate Data Collection Project: Shishmaref Thermal Modeling,* UAF Institute of Northern Engineering, 40 p.

Decagon Devices, Inc. (2012). *KD2 Pro Thermal Properties Analyzer: Operator's Manual*, Decagon Devices Inc., Pullman, WA, 68 p.

Esch, D. C. (1982). "Thawing of Permafrost by passive solar means." *Proc., 4th Can. Permafrost Conference,* Ottawa, Canada, 560-569.

Esch, D. C. (1986). "Insulation performance beneath roads and airfields in Alaska." *Transportation Research Board Record,* 1146, 23-27.

Esch, D. C., and Livingston, H. R. (1978). *Performance of a Roadway with a Peat Underlay Over Permafrost,* Interim Report for Period 1973-1977, Report No. AK-RD-78-1, State of Alaska Department of Transportation and Public Facilities, 62 p.

Farouki, O. T. (1981). *Thermal Properties of Soils*, Monograph 81-1, U.S. Army Cold Regions Research and Engineering Laboratory, Hanover, NH, 151 p.

Gallant, A. L., Binnian, E. F., Omernik, J. M., Shasby, M. B. (1995). "Level III Ecoregions of Alaska." <ftp://ftp.epa.gov/wed/ecoregions/ak/ak_eco.pdf> (Oct. 12, 2012).

GEO-SLOPE International Ltd. (2012a). *Air Flow Modeling with AIR/W Engineering Methodology Book,* GEO-SLOPE International Ltd., Calgary, Canada, 88 p.

GEO-SLOPE International Ltd. (2012b). *Passive Cooling of Permafrost by Air Convection*: *Case History,* GEO-SLOPE International Ltd., Calgary, Canada, 11 p.

GEO-SLOPE International Ltd. (2012c). *Seepage Modeling with SEEP/W Engineering Methodology Book,* GEO-SLOPE International Ltd., Calgary, Canada, 199 p.

GEO-SLOPE International Ltd. (2012d). *Thermal Modeling with TEMP/W Engineering Methodology Book,* GEO-SLOPE International Ltd., Calgary, Canada, 175 p.

Goering, D. J. (1998). "Experimental investigation of air convection embankments for permafrost-resistant roadway design." *Proc., Seventh International Conference on Permafrost*: Yellowknife, Canada, 319-326.

Goering, D. J. (2003). "Passively cooled railway embankments for use in permafrost areas." *Journal of Cold Regions Engineering*: 17(3), 119-133.

Goering, D. J., and Kumar, P. (1996). "Winter-time convection in open-graded embankments." *Cold Regions Science and Technology*: 24(1), 57-74.

Goering, D. J., and Kumar, P. (1999). "Permeability effects on winter-time natural convection in gravel embankments." In Kolumban, H., Wang, Y., Beer, H. (Editors), *Advances in Cold-Region Thermal Engineering and Sciences Lecture Notes in Physics*, Springer, Berlin, Germany, 455-464.

Golden Gate Weather Services. (2011). "Alaska Climate Normals (1981-2010)." <http://ggweather.com/normals/daily_AK.html>. (Dec. 10, 2012).

International Permafrost Association. (2014). "What is Permafrost?" <http://ipa.arcticportal.org/resources/what-is-permafrost>. (Jun. 20, 2012).

Johansen, O. (1977). *Thermal Conductivity of Soils*, U.S. Army, Cold Regions Research and Engineering Laboratory Report No. 637, Hanover, NH, 291 p.

Jorgenson T, Yoshikawa K, Kanevskiy M, Shur Y, Romanovsky V, Marchenko S, Grosse G, Brown J, Jones B (2008). "Permafrost Characteristics of Alaska – A new permafrost map of Alaska." *Proc.*, *Ninth International Conference on Permafrost*, Fairbanks, AK, 2 p.

Latham, J. P., Newberry, S., Mannion, M., Simm, J., Stewart, T. (2002). "The void porosity of rock armour in coastal structures." *Water & Maritime Engineering*, 154(3), 189-198.

Lindeburg, M. R. (2012). *Civil Engineering Reference Manual for the PE Exam*, 13th Ed., Professional Publications Incorporated, Belmont, CA, 1552 p.

McFadden, T. (1989). *Bethel Airport Thermosyphon Study Final Report*, State of Alaska Department of Transportation and Public Facilities Statewide Research, Fairbanks, AK, 19 p.

Measurand, Inc. (2013). *ShapeAccelArray Product Manual,* Measurand, Inc., Fredericton, Canada, 113 p.

Muhll, V. D., and Haeberli, W. (1990). "Thermal characteristics of the permafrost within an active rock glacier." *Journal of Glaciology*, 36(123), 151-158.

Reger, R. D., Hubbard, T. D., Gallagher, P. E. (2012). *Reconnaissance Interpretation of 1978-1981 Permafrost, Alaska Highway Corridor, Tetlin Junction to Canada Border, Alaska*, Alaska Department of Natural Resources Division of Geological & Geophysical Surveys, Preliminary Interpretive Report 2012-1c, Fairbanks, AK, 27 p.

Saboundjian, S., and Goering, D. J. (2003). "Air convection embankment for roadways: a field experimental study in Alaska." *Proc., 82nd Annual Meeting of the Transportation Research Board* Paper #03-2603, Washington, D.C., 25 p.

Slope Indicator (2006). *Horizontal Digitilt Inclinometer Probe Manual,* Slope Indicator, Mukilteo, WA, 15 p.

Slope Indicator (2010). *Horizontal Digitilt Inclinometer Probe Datasheet*, Slope Indicator, Mukilteo, WA, 2 p.

Speeter, G. (2010). *Taylor Hwy MP 70 Lost Chicken Creek Slide Realignment*, ADOT&PF Geotechnical Memorandum State Project No. 63379, ADOT&PF Northern Region, Fairbanks, AK, 23 p.

StormTech International. (2012). *Porosity of Structural Backfill: Tech Sheet*, StormTech International, Rocky Hill, CT, 2 p.

U.S. Geological Survey (USGS) (1956). *Eagle A-2 Quadrangle*, U.S. Department of the Interior USGS, 1 sheet, scale 1:63,360.

Vinson, T. S., Rooney, J. W., Haas, W. H. (1996). *Roads and Airfields in Cold Regions: A State of the Practice Report*, ASCE Publications 0-7844-0191-8, Technology and Engineering, 321 p.

Wahrhaftig, C. (1965). *Physiographic Divisions of Alaska*, U.S. Geological Survey Professional Paper 482, 52 p.

Waples, D. W., and Waples, J. S. (2004). "A review and evaluation of specific heat capacities of rocks, minerals, and subsurface fluids. Part 1: minerals and nonporous rocks." *Natural Resources Research*, 13(2), 97-122.

Werdon, M. B., Newberry, R. J., Szumigala, D. J., Pinney, D. S. (2001) *Geologic Map of the Eagle A-2 Quadrangle, Fortymile Mining District, Alaska,* Alaska Division of Geological & Geophysical Surveys Preliminary Interpretive Report 2001-3A, 1 sheet, scale 1:63,360.

Western Regional Climate Center (WRCC). (2012). "Chicken Alaska" <http://www.raws.dri.edu/cgi-bin/rawMAIN.pl?akACKN> (Jul. 20, 2012).

Williams, C. F., Galanis, S. P., Grubb, F. V. Sass, J. H. (2006). "Heat flow and geothermal resources of the Alaskan interior." *Proc., Abstracts with Programs – Geological Society of America*: 38(5), 14-15.

Williams, P. J., and Smith, M. W. (1989). *The Frozen Earth*, Cambridge University Press, Cambridge, UK, 306 p.

YSI. (1998). *YSI Precision Thermistors & Probes*, YSI Catalog 1998, YSI Inc., Yellow Springs, OH.

Zarling, J. P., and Braley, A. W. (1986). *Thaw Stabilization of Roadway Embankments Constructed Over Permafrost,* Final Report No. FHWA-AK-87-20, University of Alaska Fairbanks Engineering Research Center, Institute of Northern Engineering, Fairbanks, AK, 34 p.

Zarling, J. P., Connor, B., Goering, D. J. (1984). *Air Duct Systems for Roadway Stabilization Over Permafrost Areas,* Report No. FHWA-AK-RD-84-10, State of Alaska Department of Transportation and Public Facilities Division of Planning, Fairbanks, AK, 55p.

APPENDIX A

ADOT&PF LOST CHICKEN TEST HOLE LOGS AND LABORATORY REPORTS (SPEETER 2010)

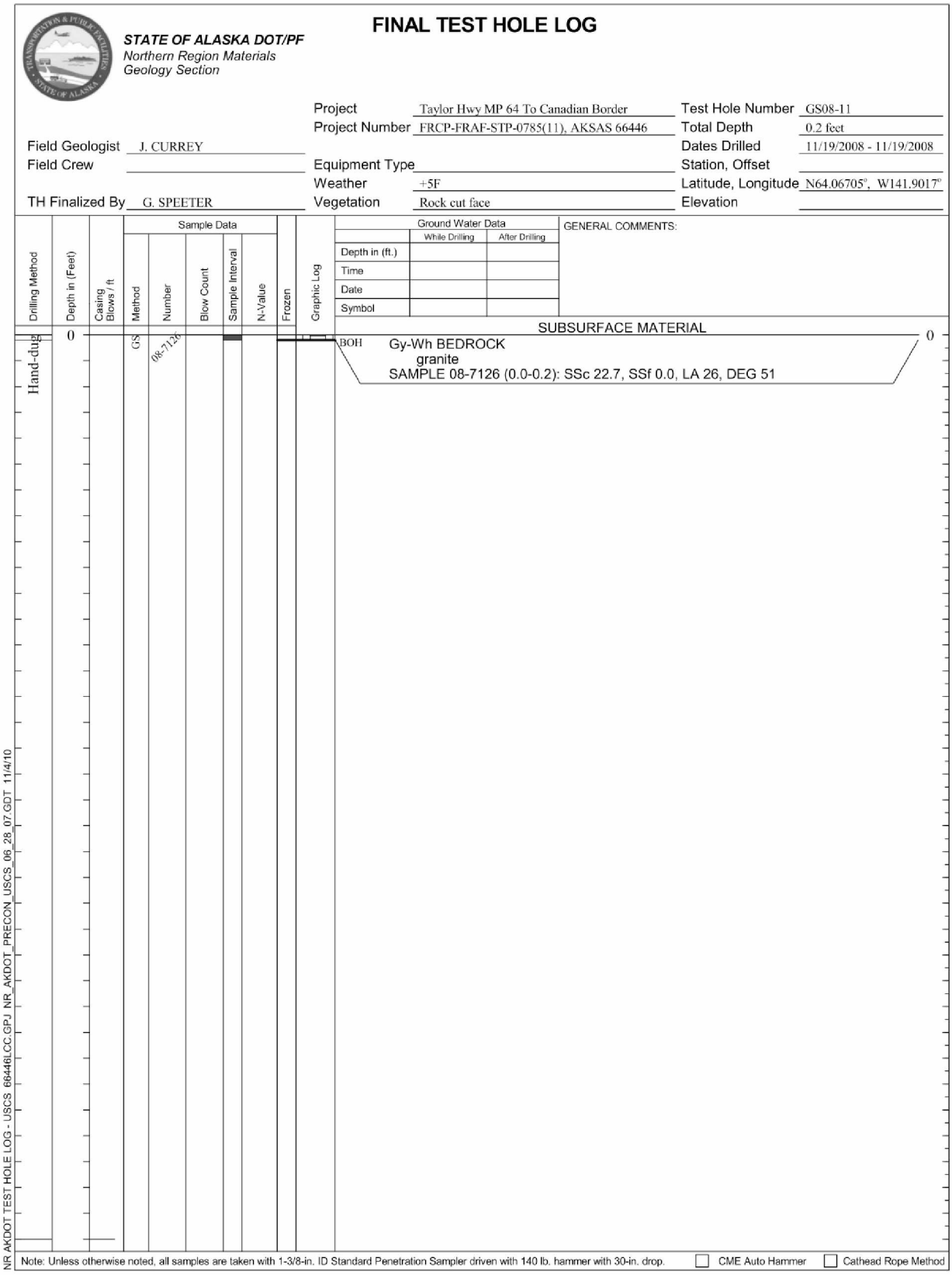

Figure A-1 GS08-11 test hole log.

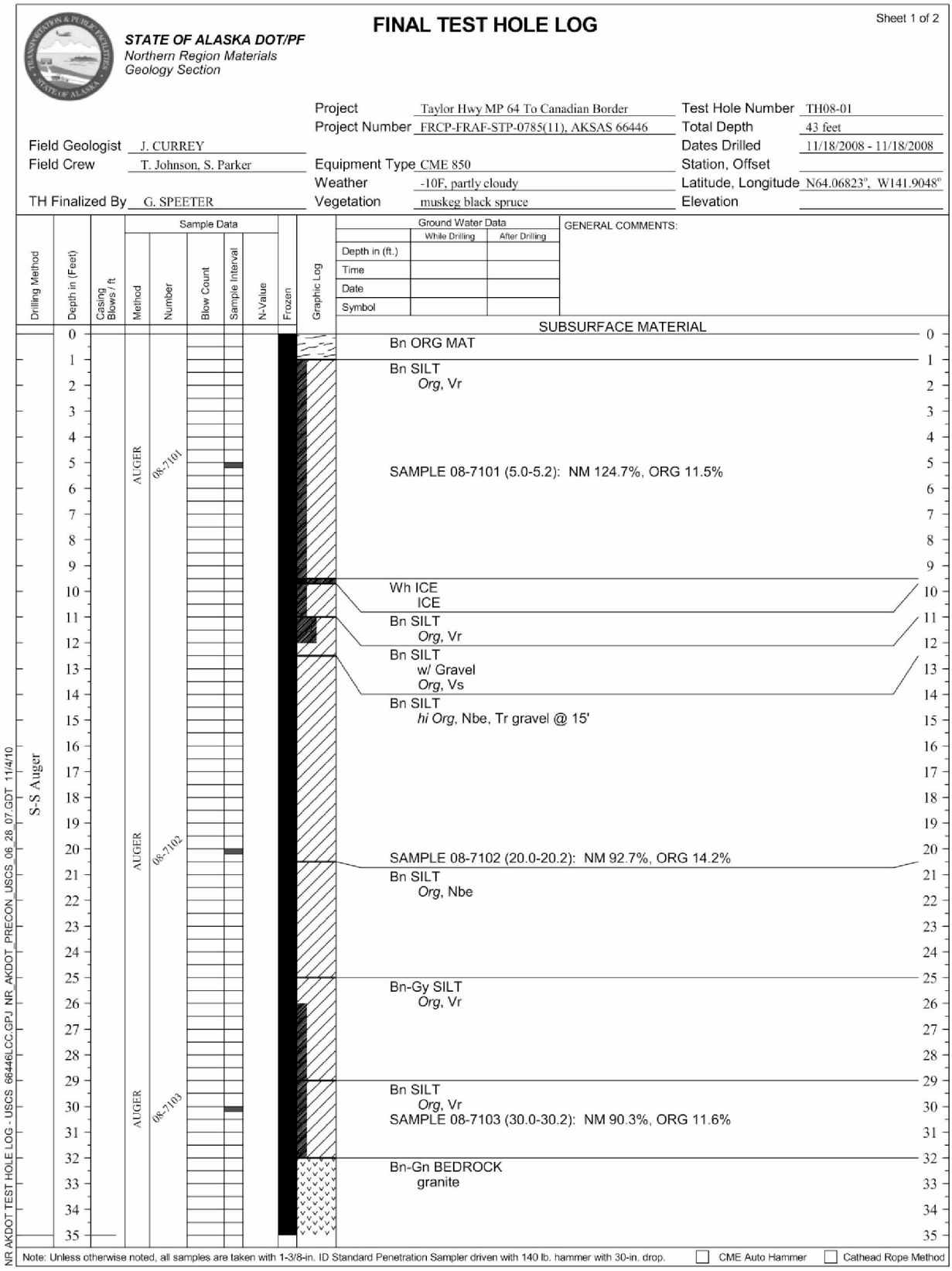

Figure A-2 TH08-01 test hole log.

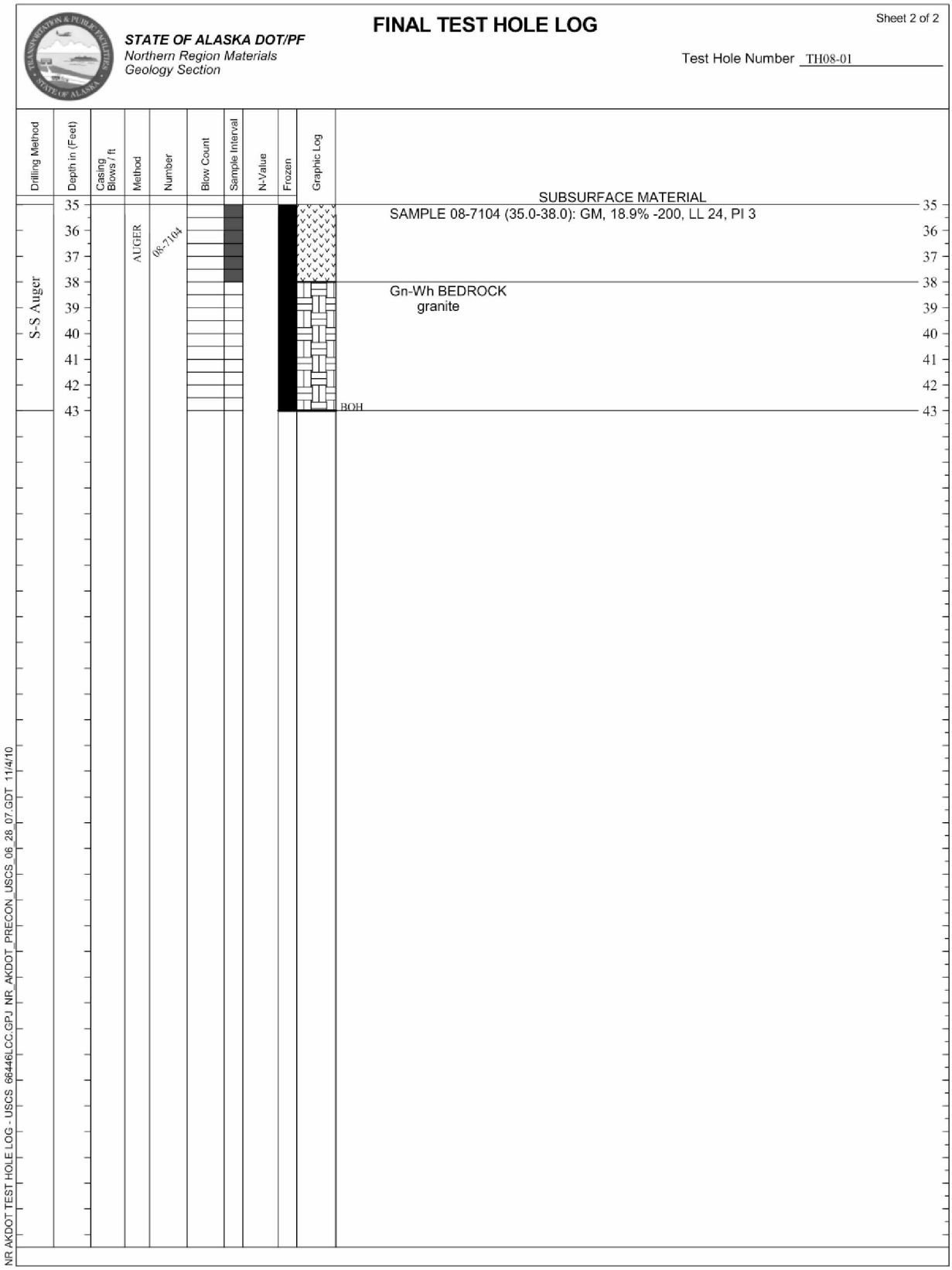

Figure A-2 (continued) TH08-01 test hole log.

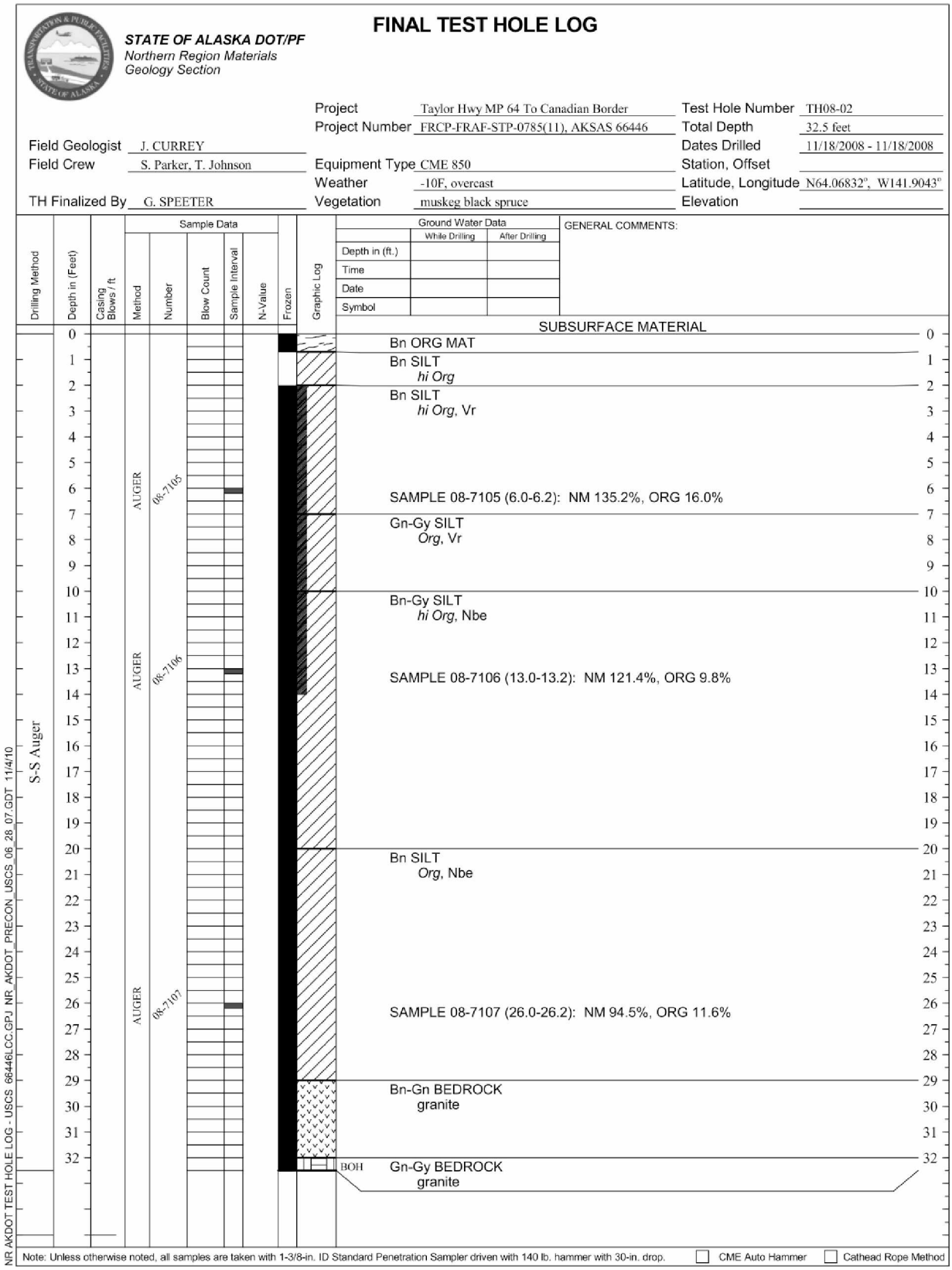

Figure A-3 TH08-02 test hole log.

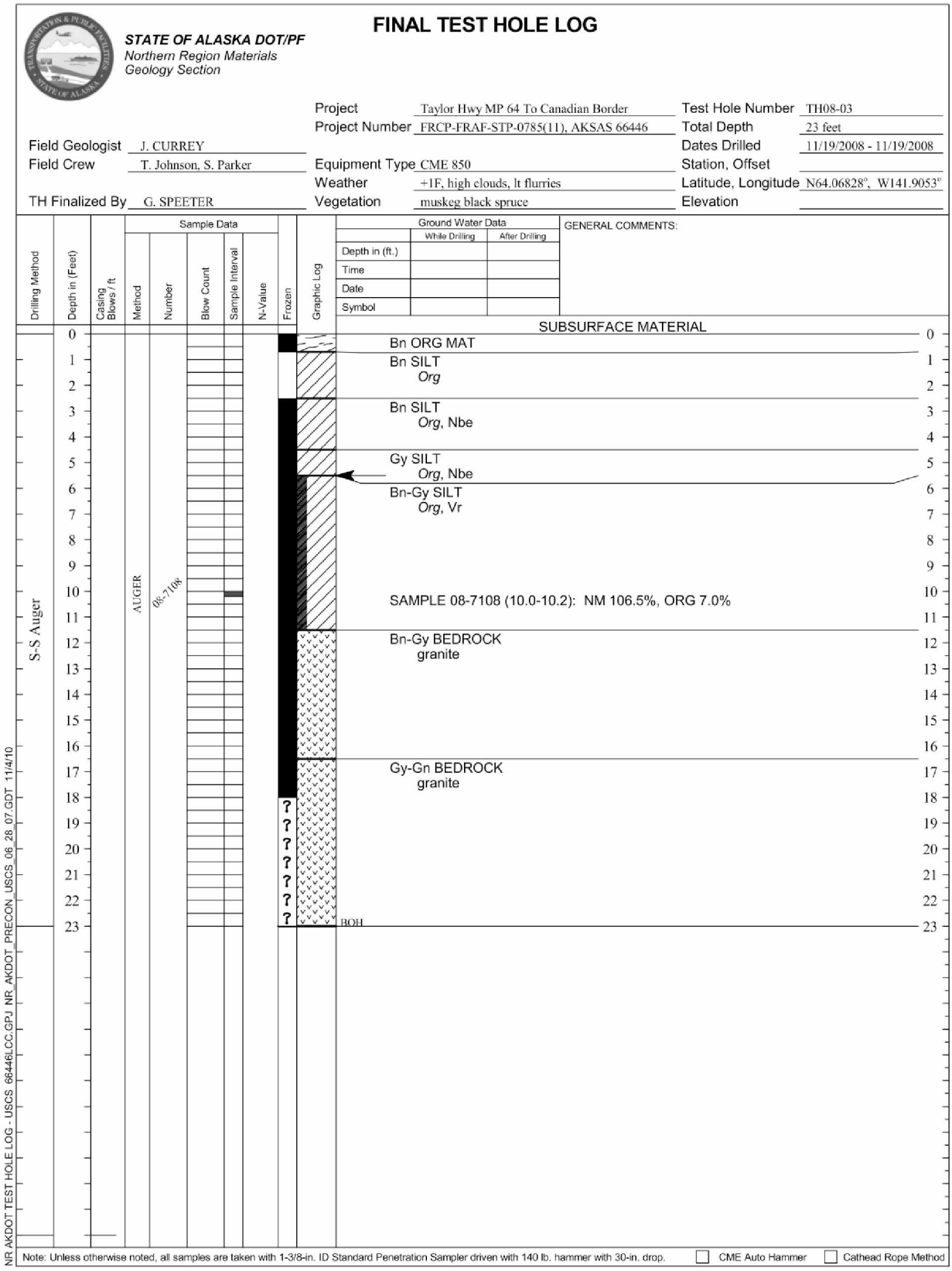

Figure A-4 TH08-03 test hole log.

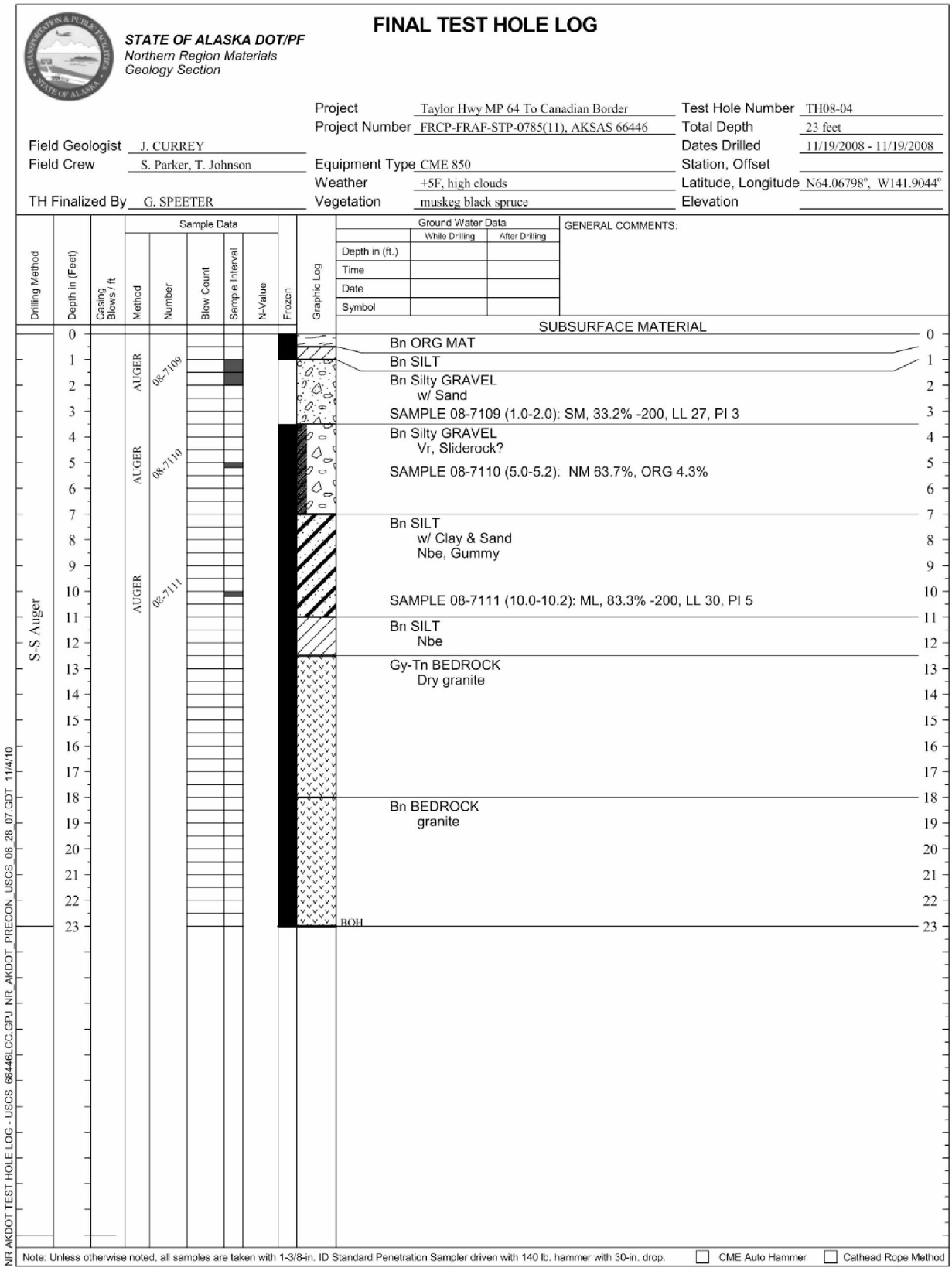

Figure A-5 TH08-04 test hole log.

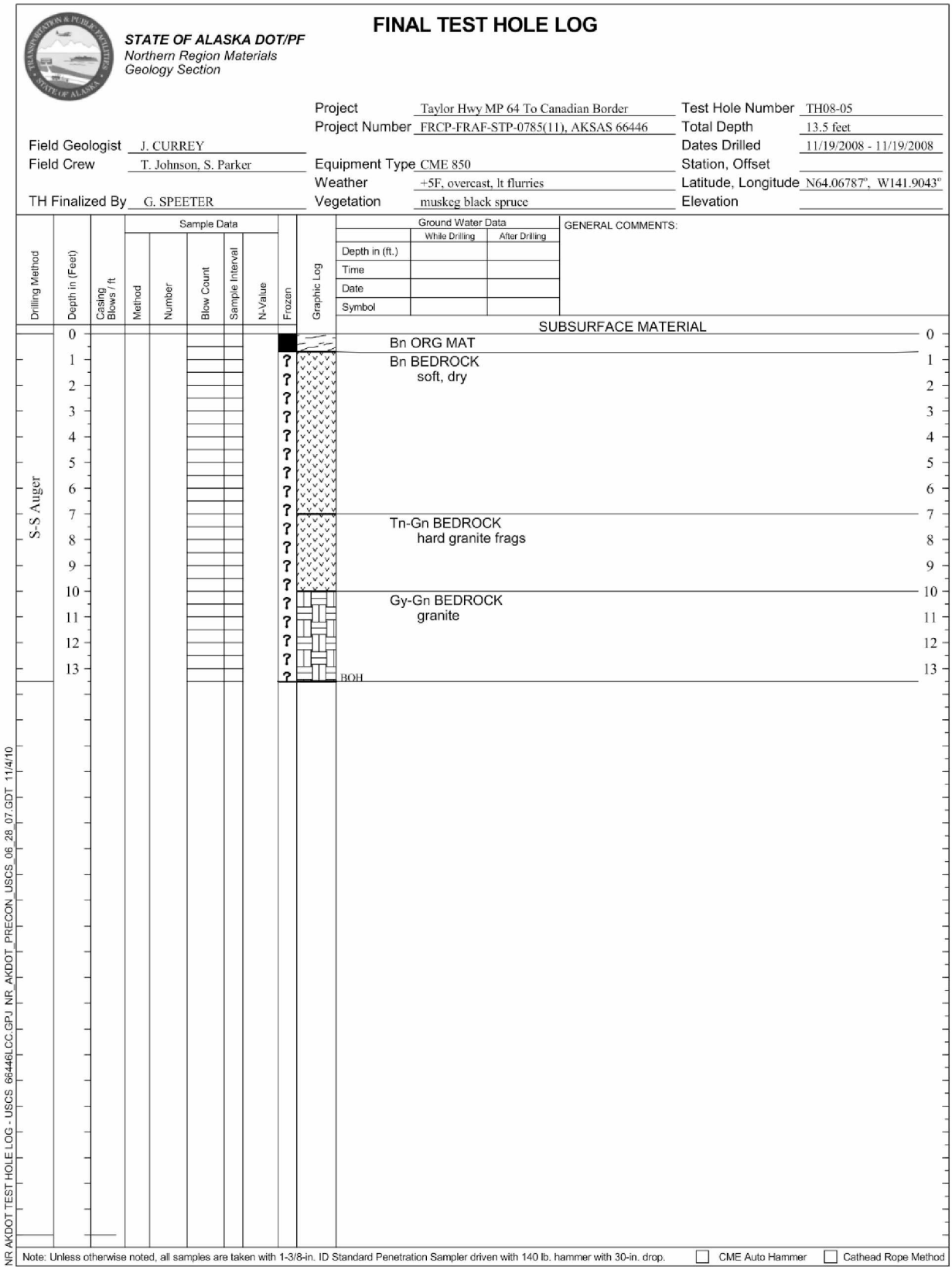

Figure A-6 TH08-05 test hole log.

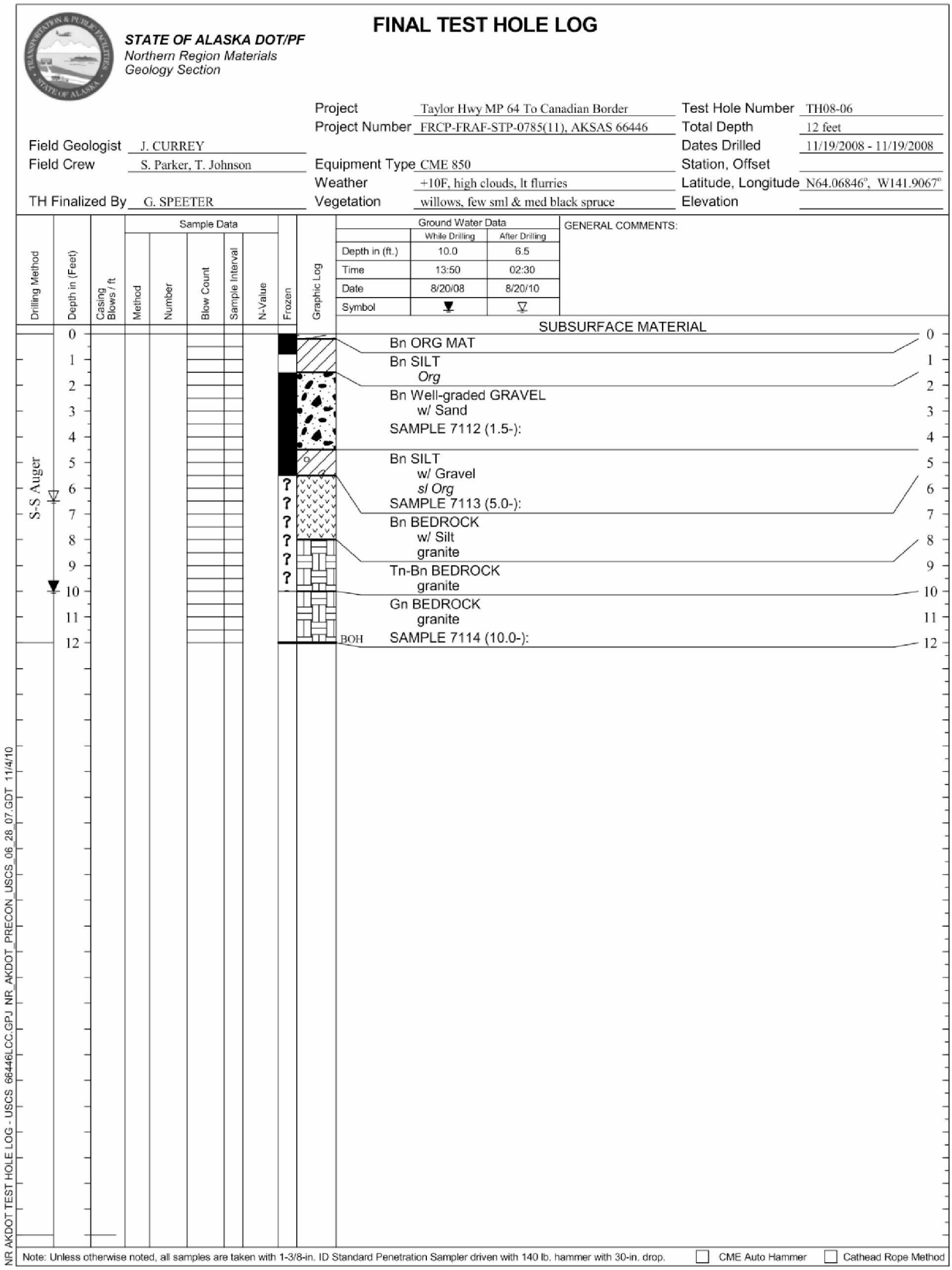

Figure A-7 TH08-06 test hole log.

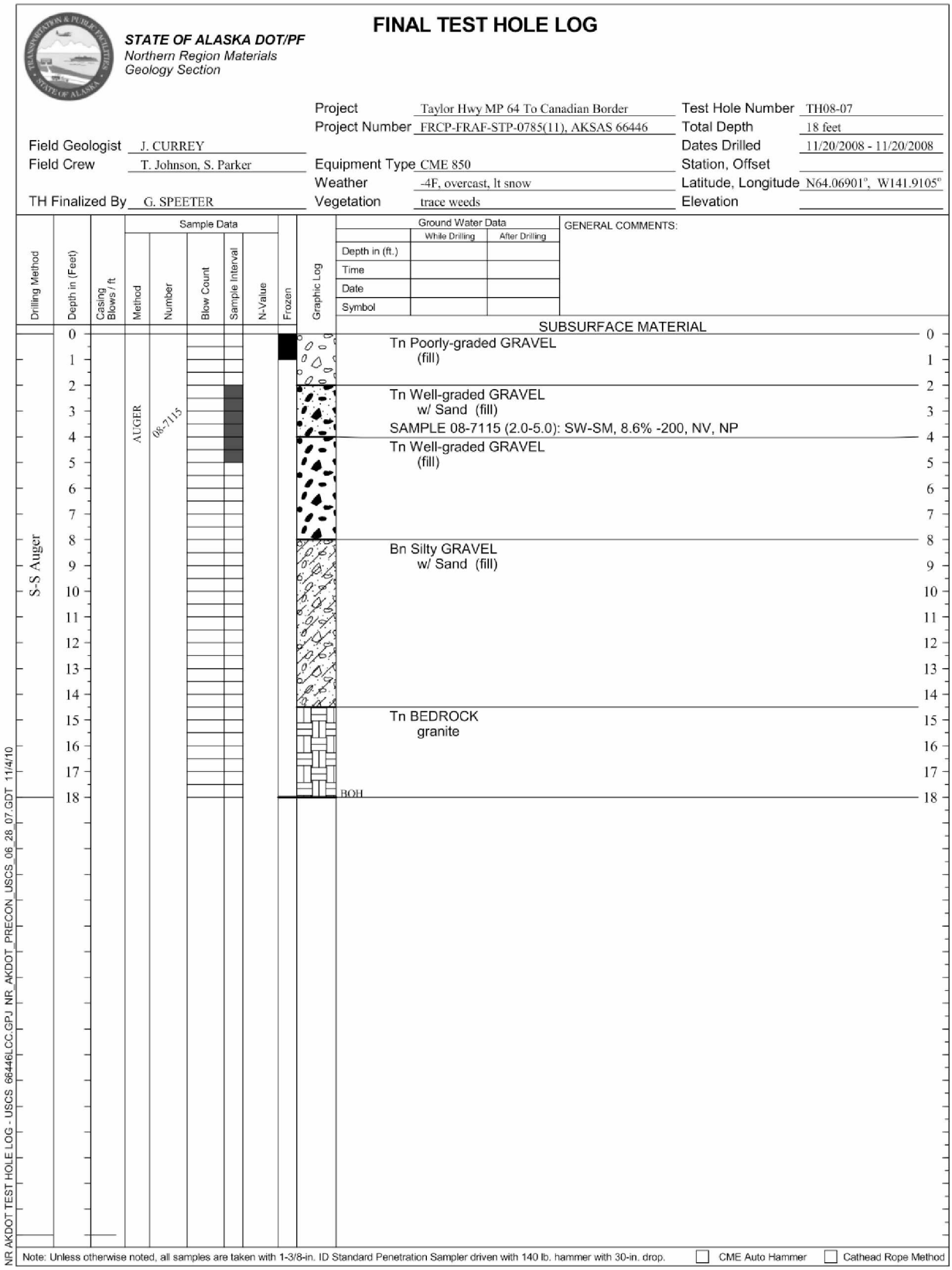

Figure A-8 TH08-07 test hole log.

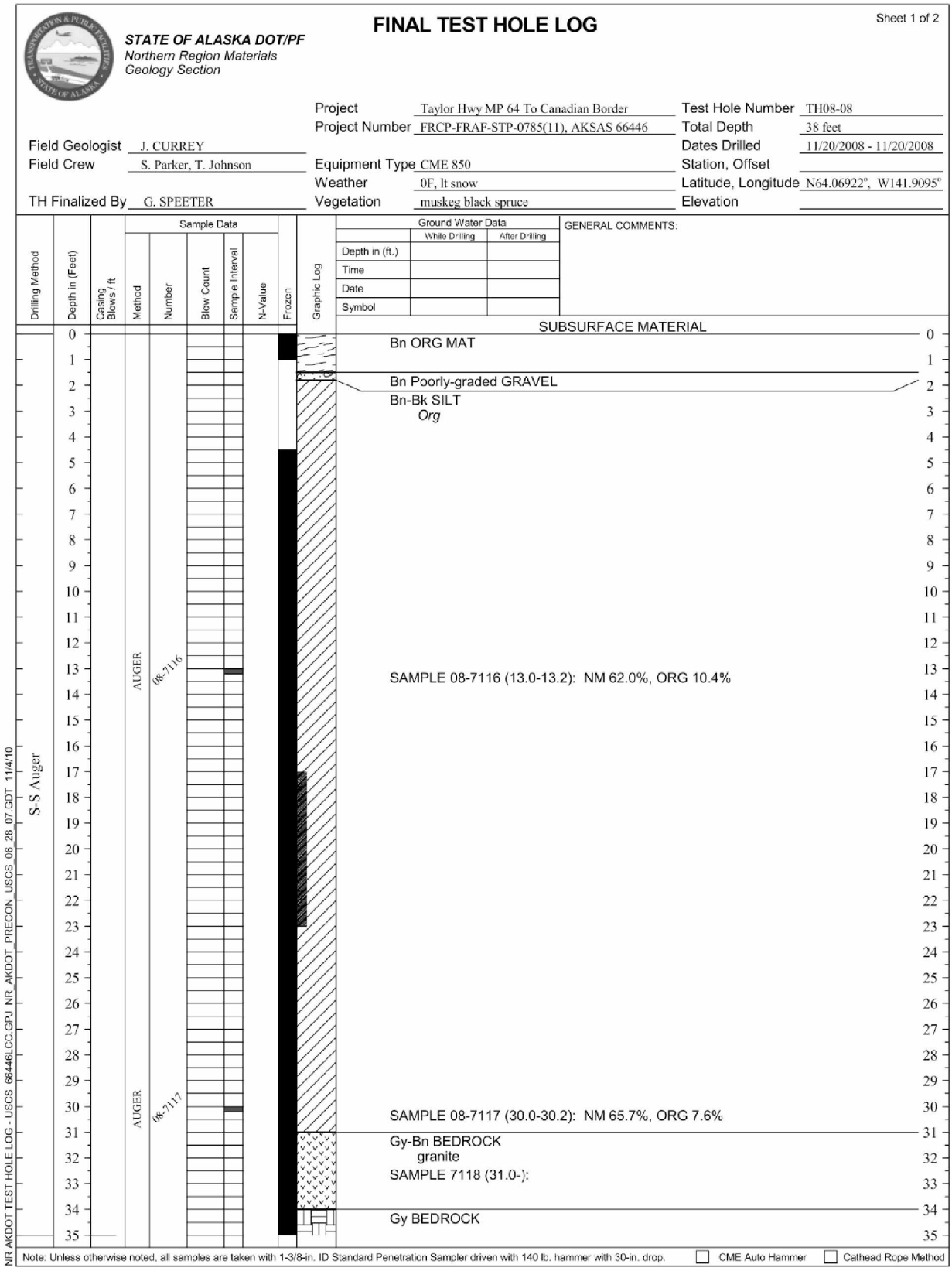

Figure A-9 TH08-08 test hole log.

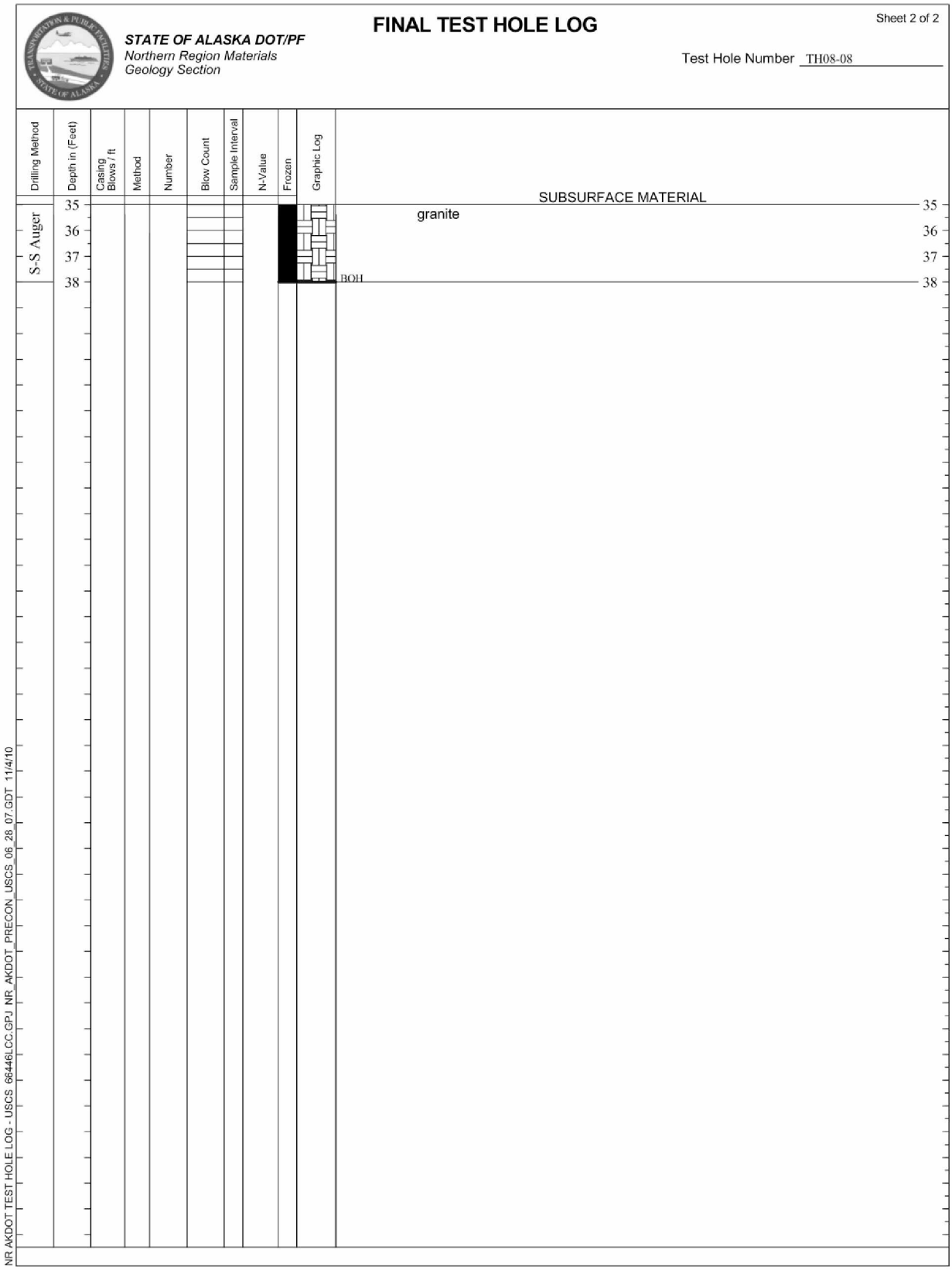

Figure A-9 (continued) TH08-08 test hole log.

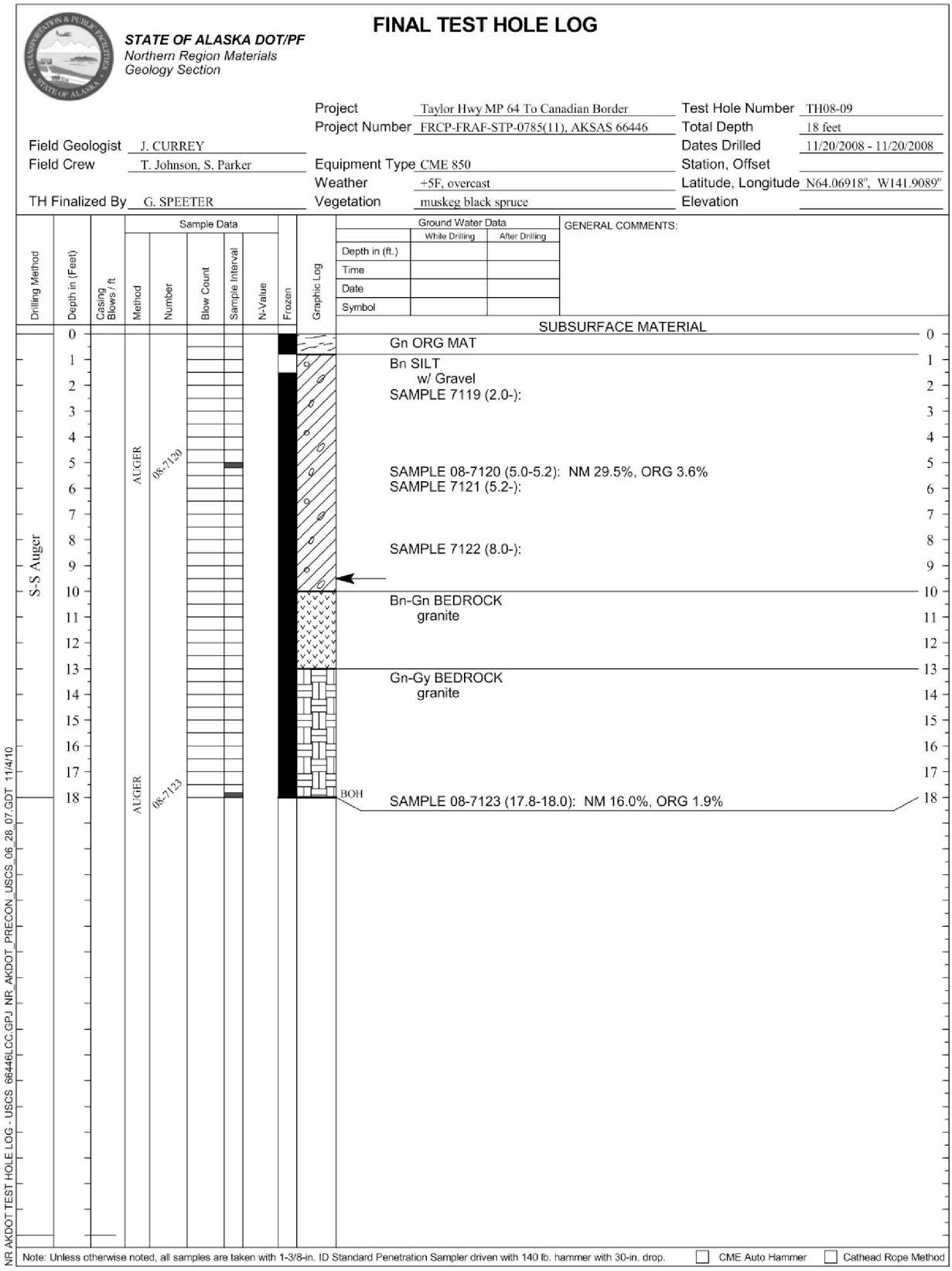

Figure A-10 TH08-09 test hole log.

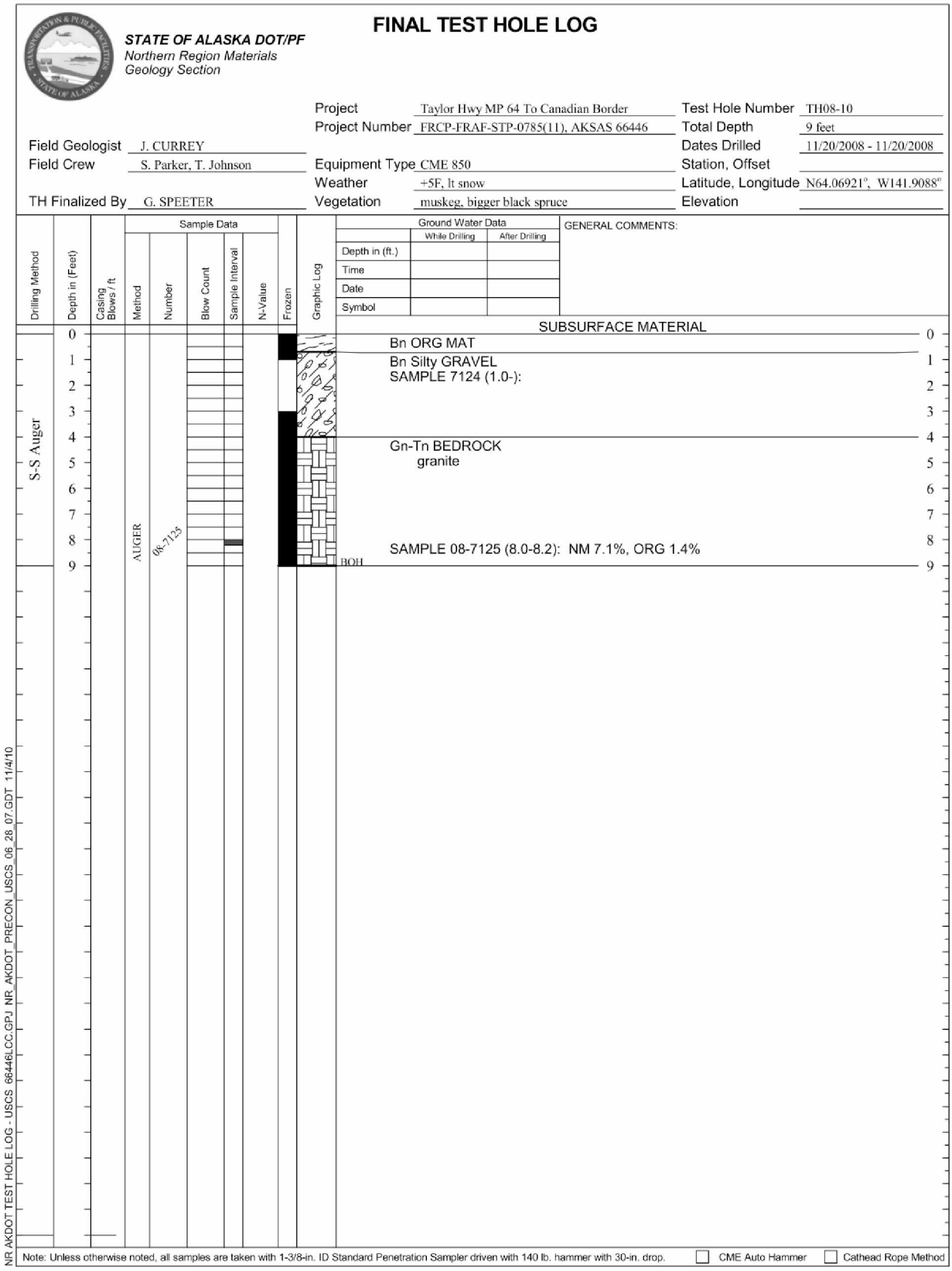

Figure A-11 TH08-10 test hole log.

STATE OF ALASKA DEPARTMENT OF TRANSPORTATION
NORTHERN REGION
LABORATORY TESTING REPORT

PROJECT NAME:	Taylor Hwy MP 64 To Canadian Border
PROJECT NUMBER:	FRCP-FRAF-STP-0785(11)
AKSAS NUMBER:	66446
SAMPLED BY:	J. CURREY
MATERIAL SOURCE:	CENTERLINE

TEST HOLE NUMBER		TH08-01	TH08-01	TH08-01	TH08-01	TH08-02	TH08-02	TH08-02
DEPTH (feet)		5.0-5.2	20.0-20.2	30.0-30.2	35.0-38.0	6.0-6.2	13.0-13.2	26.0-26.2
LATITUDE		N64.06823°	N64.06823°	N64.06823°	N64.06823°	N64.06832°	N64.06832°	N64.06832°
LONGITUDE		W141.9048°	W141.9048°	W141.9048°	W141.9048°	W141.9043°	W141.9043°	W141.9043°
LAB NUMBER		**08-7101**	**08-7102**	**08-7103**	**08-7104**	**08-7105**	**08-7106**	**08-7107**
DATE SAMPLED		18-Nov-08	18-Nov-08	18-Nov-08	18-Nov-08	18-Nov-08	18-Nov-08	18-Nov-08
% Passing	**3"**							
	2"							
	1.5"				100			
Gravel	**1.0"**				99			
	0.75"				97			
	0.5"				90			
	0.375"				83			
	#4				58			
	#8				48			
	#10				46			
	#16				41			
	#30				34			
Sand	**#40**				31			
	#50				28			
	#60				27			
	#80				25			
	#100				23			
Silt/Clay	**#200**				18.9			
	0.02							
	0.005							
Hydro	**0.002**							
	0.001							
LIQUID LIMIT					24			
PLASTIC INDEX					3			
USCS CLASSIFICATION					GM			
USCS SOIL DESCRIPTION								
NATURAL MOISTURE		124.7	92.7	90.3		135.2	121.4	94.5
ORGANICS		11.5	14.2	11.6		16.0	9.8	11.6
SP. GR. (FINE)								
SP. GR. (COARSE)								
MAX. DRY DENSITY								
OPTIMUM MOISTURE								
L.A. ABRASION								
DEGRAD. FACTOR								
SODIUM SULF. (CRSE)								
SODIUM SULF. (FINE)								
NORDIC ABRASION								
REMARKS		Org[1]	Org[1]	Org[1]		hi Org[1]	Org[1]	Org[1]

GENERAL COMMENTS

Gradation is based on material passing the 3" sieve, according to Alaska Test Method T-7.

[1] Organic content determination is based on the results of the ATM T-6 test method.

(Soil descriptions shown in parentheses are based on field determinations.)

USCS Soil Description Abbreviations: WG = Well-graded; PG = Poorly-graded; E = Elastic; L = Lean; F = Fat

Figure A-12 Laboratory testing report.

STATE OF ALASKA DEPARTMENT OF TRANSPORTATION
NORTHERN REGION
LABORATORY TESTING REPORT

PROJECT NAME:	Taylor Hwy MP 64 To Canadian Border
PROJECT NUMBER:	FRCP-FRAF-STP-0785(11)
AKSAS NUMBER:	66446
SAMPLED BY:	J. CURREY
MATERIAL SOURCE:	CENTERLINE

TEST HOLE NUMBER		TH08-03	TH08-04	TH08-04	TH08-04	TH08-07	TH08-08	TH08-08
DEPTH (feet)		10.0-10.2	1.0-2.0	5.0-5.2	10.0-10.2	2.0-5.0	13.0-13.2	30.0-30.2
LATITUDE		N64.06828°	N64.06798°	N64.06798°	N64.06798°	N64.06901°	N64.06922°	N64.06922°
LONGITUDE		W141.9053°	W141.9044°	W141.9044°	W141.9044°	W141.9105°	W141.9095°	W141.9095°
LAB NUMBER		**08-7108**	**08-7109**	**08-7110**	**08-7111**	**08-7115**	**08-7116**	**08-7117**
DATE SAMPLED		19-Nov-08	19-Nov-08	19-Nov-08	19-Nov-08	20-Nov-08	20-Nov-08	20-Nov-08
% Passing	**3"**							
	2"							
	1.5"					100		
Gravel	**1.0"**					95		
	0.75"		100			91		
	0.5"		98			81		
	0.375"		96			74		
	#4		90			58		
	#8		81			44		
	#10		79		100	41		
	#16		71		99	31		
	#30		60		97	22		
Sand	**#40**		55		96	19		
	#50		50		94	16		
	#60		48		94	15		
	#80		43		92	13		
	#100		41		90	12		
Silt/Clay	**#200**		33.2		83.3	8.6		
	0.02							
Hydro	**0.005**							
	0.002							
	0.001							
LIQUID LIMIT			27		30	NV		
PLASTIC INDEX			3		5	NP		
USCS CLASSIFICATION			SM		ML	SW-SM		
USCS SOIL DESCRIPTION								
NATURAL MOISTURE		106.5		63.7			62.0	65.7
ORGANICS		7.0		4.3			10.4	7.6
SP. GR. (FINE)								
SP. GR. (COARSE)								
MAX. DRY DENSITY								
OPTIMUM MOISTURE								
L.A. ABRASION								
DEGRAD. FACTOR								
SODIUM SULF. (CRSE)								
SODIUM SULF. (FINE)								
NORDIC ABRASION								
REMARKS		Org[1]		sl Org[1]			Org[1]	Org[1]

GENERAL COMMENTS

Gradation is based on material passing the 3" sieve, according to Alaska Test Method T-7.

[1] Organic content determination is based on the results of the ATM T-6 test method.

(Soil descriptions shown in parentheses are based on field determinations.)

USCS Soil Description Abbreviations: WG = Well-graded; PG = Poorly-graded; E = Elastic; L = Lean; F = Fat

Figure A-12 (continued) Laboratory testing report.

STATE OF ALASKA DEPARTMENT OF TRANSPORTATION
NORTHERN REGION
LABORATORY TESTING REPORT

PROJECT NAME:	Taylor Hwy MP 64 To Canadian Border
PROJECT NUMBER:	FRCP-FRAF-STP-0785(11)
AKSAS NUMBER:	66446
SAMPLED BY:	J. CURREY
MATERIAL SOURCE:	CENTERLINE

TEST HOLE NUMBER		TH08-09	TH08-09	TH08-10	GS08-11			
DEPTH (feet)		5.0-5.2	17.8-18.0	8.0-8.2	0.0-0.2			
LATITUDE		N64.06918°	N64.06918°	N64.06921°	N64.06705°			
LONGITUDE		W141.9089°	W141.9089°	W141.9088°	W141.9017°			
LAB NUMBER		**08-7120**	**08-7123**	**08-7125**	**08-7126**			
DATE SAMPLED		20-Nov-08	20-Nov-08	20-Nov-08	19-Nov-08			
% Passing	**3"**							
	2"							
	1.5"							
Gravel	**1.0"**							
	0.75"							
	0.5"							
	0.375"							
	#4							
	#8							
	#10							
	#16							
	#30							
Sand	**#40**							
	#50							
	#60							
	#80							
	#100							
Silt/Clay	**#200**							
	0.02							
	0.005							
Hydro	**0.002**							
	0.001							
LIQUID LIMIT								
PLASTIC INDEX								
USCS CLASSIFICATION								
USCS SOIL DESCRIPTION								
NATURAL MOISTURE		29.5	16.0	7.1				
ORGANICS		3.6	1.9	1.4				
SP. GR. (FINE)								
SP. GR. (COARSE)								
MAX. DRY DENSITY								
OPTIMUM MOISTURE								
L.A. ABRASION					26			
DEGRAD. FACTOR					51			
SODIUM SULF. (CRSE)					23			
SODIUM SULF. (FINE)					0			
NORDIC ABRASION								
REMARKS		sl Org[1]						

GENERAL COMMENTS

Gradation is based on material passing the 3" sieve, according to Alaska Test Method T-7.

[1] Organic content determination is based on the results of the ATM T-6 test method.

(Soil descriptions shown in parentheses are based on field determinations.)

USCS Soil Description Abbreviations: WG = Well-graded; PG = Poorly-graded; E = Elastic; L = Lean; F = Fat

Figure A-12 (continued) Laboratory testing report.

APPENDIX B
SOIL LABORATORY TEST RESULTS

Table B-1 Soil thaw strain and frozen and unfrozen thermal conductivity for each sample. Consolidated samples are indicated by "(cons)", "–" indicates no data, ε_v is thaw strain, K_f is frozen thermal conductivity, and K_u is unfrozen thermal conductivity.

Soil Type	Sample ID	ε_v (%)	K_f BTU/(hr·ft·°F)	K_u BTU/(hr·ft·°F)
Peat w/ silt	01-002	53.6	0.962	-
(cons)	01-002	-	0.871	0.428
Peat w/ silt	02-004	-	0.908	0.340
Peat w/ silt	02-006	-	0.801	0.335
Peat w/ silt	04-001	-	0.829	0.418
Peat w/ silt	04-002	-	0.988	0.390
Peat w/ silt	05-003	-	0.917	0.346
(cons)	05-003	-	0.911	0.435
Coarse sand w/ silt	01-004	-	1.081	0.574
Coarse sand w/ silt	02-003	17.8	1.183	-
(cons)	02-003	-	-	0.594
Silt w/ sand & org.	01-003	-	0.898	0.502
Silt w/ sand & org.	03-001	24.3	0.946	-
(cons)	03-001	-	0.894	0.529
Silt w/ sand & org.	03-003	-	1.102	0.703
(cons)	03-003	-	-	0.744
Silt w/ sand & org.	03-004	-	1.011	0.613
(cons)	03-004	-	-	0.655
Silt w/ sand & org.	03-005	-	1.087	0.388
Silt w/ sand & org.	04-003	32.0	0.845	0.350
(cons)	04-003	-	-	0.388
Silt w/ sand & org.	04-005	51.4	0.920	-
(cons)	04-005	-	-	0.394
Silt w/ sand & org.	04-006	40.8	0.953	-
(cons)	04-006	-	0.839	0.413
Silt w/ sand & org.	05-001	-	1.094	0.490
Silt w/ sand & org.	05-002	51.4	0.939	-
(cons)	05-002	-	-	0.394
Silt w/ sand & org.	05-004	-	0.989	0.715

Table B-2 Water content and wet and dry unit weight for each sample. Consolidated samples are indicated by "(cons)", "–" indicates no data, w is gravimetric water content, θ is volumetric water content, γ is unit weight, and γ_d is dry unit weight.

Soil Type	Sample ID	w (%)	θ (%)	γ (lb/ft^3)	γ_d (lb/ft^3)
Peat w/ silt	01-001	254.9	83.7	72.8	20.5
Peat w/ silt (cons)	01-002	111.2	71.9	85.3	40.4
Peat w/ silt	02-005	307.2	77.2	63.8	15.7
Peat w/ silt	04-004	344.4	82.8	66.7	15.0
Peat w/ silt	05-003	74.1	–	–	–
Peat w/ silt (cons)	05-003	65.5	61.2	96.5	58.3
Coarse sand w/ silt	01-004	49.2	58.7	111.1	74.4
Coarse sand w/ silt	02-002	32.2	48.7	124.8	94.4
Silt w/ sand & org.	02-001	105.6	62.6	76.1	37.0
Silt w/ sand & org.	03-002	100.8	68.8	85.5	42.6
Silt w/ sand & org.	03-003	83.4	64.7	88.8	48.4
Silt w/ sand & org.	03-004	93.8	65.6	84.6	43.7
Silt w/ sand & org.	03-005	121.7	70.2	79.8	36.0
Silt w/ sand & org.	04-003	117.5	64.5	74.5	34.2
Silt w/ sand & org. (cons)	04-003	73.4	59.2	87.3	50.4
Silt w/ sand & org.	04-005	135.5	68.2	73.9	31.4
Silt w/ sand & org. (cons)	04-005	50.6	52.4	97.3	64.7
Silt w/ sand & org.	04-006	73.5	62.6	92.1	53.1
Silt w/ sand & org. (cons)	04-006	34.5	49.6	120.6	89.7

Table B-2 (continued) Water content and wet and dry unit weight for each sample. Consolidated samples are indicated by "(cons)", "–" indicates no data, w is gravimetric water content, θ is volumetric water content, γ is unit weight, and γ_d is dry unit weight.

Soil Type	Sample ID	w (%)	θ (%)	γ (lb/ft^3)	γ_d (lb/ft^3)
Silt w/ sand & org.	05-001	116.9	68.6	79.4	36.6
Silt w/ sand & org.	05-002	130.0	69.7	77.0	33.5
Silt w/ sand & org.	05-004	87.4	64.5	86.3	46.0
Road Surface Course	10-1009	6.2	11.7	124.3	117.0
Road Surface Course	10-1006	5.0	8.9	117.4	111.8
Road Surface Course	10-1010	4.3	7.8	118.3	113.4
Organic Mat	LC12-07	344.0	82.8	66.7	15.0
Organic Mat	LC12-04	101.0	68.8	85.5	42.6
Thermal Berm	10-1000	10.9	–	–	–
Thermal Berm	10-1007	10.5	–	–	–
Thermal Berm	10-1010	8.3	–	–	–

APPENDIX C
MODELING RESULTS

Table C-1 Mean monthly measured TAC and modeled temperatures beneath thermal berm and ACE.

Month	Thermal Berm (°F)			ACE (°F)		
	TAC	Snow-Closed	Plowed-Closed	TAC	Snow-Closed	Plowed-Closed
Oct. 2012	34.1	32.5	32.4	33.2	31.4	29.8
Nov. 2012	31.9	28.3	28.1	32.2	30.3	26.5
Dec. 2012	30.2	22.5	22.1	29.1	26.9	18.9
Jan. 2013	28.7	16.8	16.3	25.9	23.2	12.5
Feb. 2013	28.4	14.5	14.1	23.9	21.3	9.7
Mar. 2013	27.8	18.6	18.3	22.5	22.0	11.6
Apr. 2013	28.3	25.5	25.2	22.0	23.4	14.6
May 2013	32.1	32.3	32.1	27.7	24.9	18.2
Jun. 2013	35.9	42.0	41.8	32.2	27.1	22.5
Annual Mean	30.8	25.9	25.6	27.6	25.6	18.2

Table C-2 Difference between mean monthly measured TAC and modeled temperatures beneath thermal berm and ACE.

Description	Thermal Berm (°F)		ACE (°F)	
	Snow-Closed	Plowed-Closed	Snow-Closed	Plowed-Closed
Oct. 2012	-17.3	-17.8	-10.4	-20.7
Nov. 2012	-17.4	-17.8	-11.2	-22.3
Dec. 2012	-11.6	-11.9	-7.1	-17.2
Jan. 2013	-3.2	-3.5	-2.4	-10.8
Feb. 2013	3.9	3.7	1.4	-5.0
Mar. 2013	14.2	14.0	5.4	1.0
Apr. 2013	4.2	4.1	9.4	7.8
May 2013	-3.8	-4.0	2.4	-1.2
Jun. 2013	-13.4	-13.8	-5.6	-13.4
Annual Mean	-4.9	-5.2	-2.0	-9.0

Table C-3 Average monthly historical and measured air temperatures at Lost Chicken.

Month	Measured Air Temperature (°F)	Historical Air Temperature (°F)	Difference (°F)
Oct 2012	15.2	18.9	-3.7
Nov 2012	-13.3	-5.5	-7.8
Dec 2012	-21.7	-15.2	-6.5
Jan 2013	-10.3	-20.8	10.6
Feb 2013	-2.9	-12.7	9.8
Mar 2013	3.3	4.9	-1.6
Apr 2013	15.4	26.1	-10.7
May 2013	41.7	43.1	-1.4
Jun 2013	60.4	54.3	6.1